

Numerical Investigation of Fermion Mass Generation in QED

A thesis submitted for the degree of
Doctor of Philosophy
by

Jacques Christophe Rodolphe Bloch

University of Durham
Department of Physics
November 1995

Abstract

We investigate the dynamical generation of fermion mass in quantum electrodynamics (QED). This non-perturbative study is performed using a truncated set of Schwinger-Dyson equations for the fermion and the photon propagator.

First, we study dynamical fermion mass generation in quenched QED with the Curtis-Pennington vertex, which satisfies the Ward-Takahashi identity and moreover ensures the multiplicative renormalizability of the fermion propagator. We apply bifurcation analysis to determine the critical point for a general covariant gauge.

In the second part of this work we investigate the dynamical generation of fermion mass in full, unquenched QED. We develop a numerical method to solve the system of three coupled non-linear equations for the dynamical fermion mass, the fermion wavefunction renormalization and the photon renormalization function. Much care is taken to ensure the high accuracy of the solutions. Moreover, we discuss in detail the proper numerical cancellation of the quadratic divergence in the vacuum polarization integral and the requirement of using smooth approximations to the solutions. To achieve this, we improve the numerical method by introducing the Chebyshev expansion method. We apply this method to the bare vertex approximation to unquenched QED to determine the critical coupling for a variety of approximations. This culminates in the detailed, highly accurate, solution of the Schwinger-Dyson equations for dynamical fermion mass generation in QED including both, the photon renormalization function and the fermion wavefunction renormalization in a consistent way, in the bare vertex approximation and, for the first time, using improved vertices. We introduce new improvements to the numerical method, to achieve the accuracy necessary to avoid unphysical quadratic divergences in the vacuum polarization with the Ball-Chiu vertex.

Declaration

I declare that no material in this thesis has previously been submitted for a degree at this or any other university.

All the research in this work has been carried out in collaboration with Dr. M.R. Pennington.

Part of Chapter 3 has been published in

Critical coupling in strong QED with weak gauge dependence

D. Atkinson, J.C.R. Bloch, V.P. Gusynin, M.R. Pennington and M. Reenders, Phys.Lett. **B329** (1994) 117.

The discussion of Chapter 6 has been published in

Can the photon quadratic divergence be cancelled numerically?

J.C.R. Bloch and M.R. Pennington, Mod. Phys. Lett. **A10** (1995) 1225.

©*The copyright of this thesis rests with the author. No quotation from it should be published without his prior written consent and information derived from it should be acknowledged.*

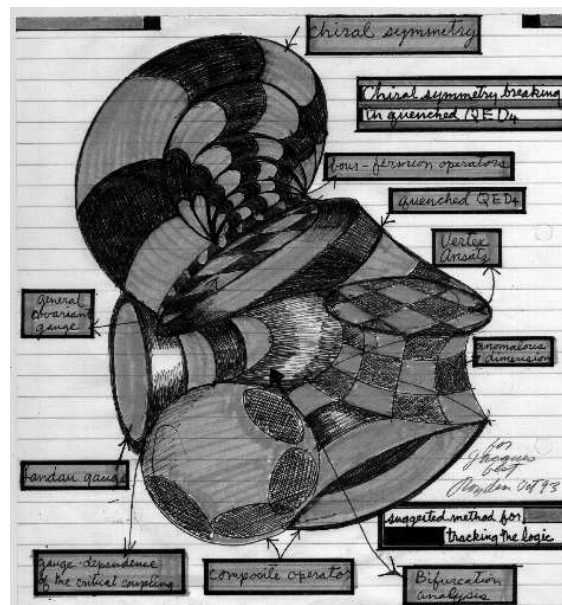
Acknowledgements

I would like to acknowledge Mike Pennington for his supervision during my research work.

This thesis would not have been possible without the endless patience, encouragements and love of Caroline, Manon and Raphaël. Many thanks to my parents for their unconditional support throughout my education and especially during our stay in Durham. I am also very grateful to my parents-in-law for being so helpful and hospitable, even after I abducted their daughter to the high north of England.

I would not have started this research was it not for my friend and artist Royden Rabinowitch whose enthusiasm gave me the confidence I needed. I remember very well the very first of our many absorbing discussions, in his studio in front of numerous cups of tea (premonition?) with his wife Liz.

I wish to thank my non-perturbative friends Adnan, Ayse, and Kirsten for keeping me efficiently from working, for baby-sitting for our little devils and most importantly for their support in difficult moments. Thanks also to my first-year office mate Richard for the entertaining discussions in our first steps in elementary particle theory, to Charlie for putting up with me for three years in Room 303 and finally, to all my colleague students and staff members of the physics department for the agreeable working atmosphere they contributed to.



'Chiral symmetry breaking in quenched $(QED)_4$ - suggested method for tracking the logic', R. Rabinowitch, Oct 93.

Contents

| | | |
|----------|--|-----------|
| 1 | Introduction | 1 |
| 2 | Schwinger-Dyson equations | 7 |
| 2.1 | QED Lagrangian | 7 |
| 2.2 | Fermion SD equation | 9 |
| 2.3 | Photon SD equation | 11 |
| 2.4 | Fermion mass generation | 12 |
| 2.5 | The bare vertex approximation | 14 |
| 2.5.1 | The fermion equations | 14 |
| 2.5.2 | The photon equation | 17 |
| 2.6 | Improving the vertex Ansatz | 19 |
| 2.6.1 | Ball-Chiu Vertex | 19 |
| 2.6.2 | Curtis-Pennington vertex | 20 |
| 2.7 | The Curtis-Pennington equations | 21 |
| 2.7.1 | The fermion equations | 21 |
| 2.7.2 | The photon equation | 27 |
| 2.7.3 | Summary | 31 |
| 3 | Fermion mass generation in quenched QED | 32 |
| 3.1 | Introduction | 32 |
| 3.2 | Bare vertex | 33 |

| | | |
|----------|--|-----------|
| 3.3 | Curtis-Pennington vertex | 34 |
| 3.3.1 | Introduction | 34 |
| 3.3.2 | Gauge independence of fermion mass and critical coupling | 35 |
| 3.3.3 | Bifurcation analysis and critical point | 36 |
| 3.4 | Scaling law: mass generation versus coupling | 44 |
| 3.4.1 | Bare vertex | 45 |
| 3.4.2 | Curtis-Pennington vertex | 49 |
| 3.4.3 | Summary | 53 |
| 4 | Fermion mass generation in unquenched QED: a survey | 54 |
| 5 | Numerical Solution of Schwinger-Dyson Equations | 60 |
| 5.1 | Linear Fredholm equation of the second kind | 61 |
| 5.1.1 | Linear Fredholm equation and the Neumann series | 61 |
| 5.1.2 | Numerical solution using the Neumann series | 63 |
| 5.1.3 | The Nystrom method | 64 |
| 5.2 | Non-linear Fredholm equation of the second kind | 67 |
| 5.3 | Schwinger-Dyson equations | 71 |
| 5.3.1 | The 3 coupled equations | 71 |
| 5.3.2 | Simplified approach: the Σ equation | 73 |
| 5.4 | Newton's iterative method | 77 |
| 5.5 | Numerical integration rules | 83 |
| 5.6 | Implementation of the quadrature rule | 86 |
| 5.6.1 | Estimate of computing time | 86 |
| 5.6.2 | Influence of infrared cutoff | 88 |
| 5.6.3 | Influence of grid spacing, kink in the integrand | 89 |
| 5.6.4 | Smooth toy kernel | 93 |

| | | |
|----------|---|------------|
| 5.6.5 | Toy kernel with kink | 96 |
| 5.6.6 | Split Simpson's rule and the integral equation | 98 |
| 5.6.7 | Heuristic improvement of the split Simpson's rule | 100 |
| 5.7 | Critical coupling in the 1-loop approximation to Π | 103 |
| 6 | Solving the coupled (Σ, \mathcal{G})-system: first attempt | 106 |
| 6.1 | Numerical method to solve the coupled (Σ, \mathcal{G}) -system | 106 |
| 6.2 | Numerical cancellation of the photon quadratic divergence | 112 |
| 7 | Chebyshev expansion method | 121 |
| 7.1 | Chebyshev polynomials | 121 |
| 7.2 | Chebyshev approximation | 123 |
| 7.3 | Evaluation of Chebyshev approximation | 124 |
| 7.4 | Chebyshev expansions for Σ , \mathcal{F} and \mathcal{G} | 125 |
| 7.5 | Σ -equation and Chebyshev expansion | 126 |
| 7.6 | Splitting the integral | 129 |
| 7.7 | Gaussian quadrature | 129 |
| 7.8 | Gaussian quadrature and the integral equations | 131 |
| 8 | Numerical results with Chebyshev expansion method | 134 |
| 8.1 | The 1-loop approximation | 134 |
| 8.1.1 | The LAK-approximation | 135 |
| 8.1.2 | The $\mathcal{F} \equiv 1$ approximation | 136 |
| 8.1.3 | The coupled (Σ, \mathcal{F}) -system | 139 |
| 8.1.4 | Summary | 144 |
| 8.2 | Coupled (Σ, \mathcal{G}) -system: revisited | 145 |
| 8.3 | Coupled $(\Sigma, \mathcal{F}, \mathcal{G})$ -system | 153 |
| 8.4 | Summary | 160 |

| | | |
|-----------|---|------------|
| 9 | Improving the vertex Ansatz | 162 |
| 9.1 | $1/\mathcal{F}$ -corrected vertex | 163 |
| 9.2 | Ball-Chiu vertex | 166 |
| 9.2.1 | Improper cancellation of quadratic divergences | 167 |
| 9.2.2 | Small- x expansion of angular functions | 172 |
| 9.2.3 | Subtracting the leading order term | 175 |
| 9.2.4 | Recurrence formula for difference of Chebyshev expansions | 181 |
| 9.2.5 | Alternative logarithm calculation | 185 |
| 9.2.6 | Numerical results | 191 |
| 9.3 | Curtis-Pennington vertex | 195 |
| 9.4 | Hybrid method | 197 |
| 9.5 | About the renormalization of the SD equations | 200 |
| 9.6 | Summary | 202 |
| 10 | Conclusions | 203 |
| A | Angular integrals | 207 |
| | Bibliography | 211 |

Chapter 1

Introduction

The fundamental laws of nature are believed to be described by quantum field theory and with the exception of gravity are embodied in the Standard Model (SM) of strong, weak and electromagnetic interactions. Despite the enormous success of the model when comparing its predictions with experimental data, one can argue about its large number of parameters. One of the outstanding problems in particle physics is the *origin of mass*. Is it just a parameter which has to be measured experimentally and then inserted in the theoretical model describing the particles and their interactions or is there an underlying mechanism through which these particles acquire their mass ?

For the first possibility to be consistent with the quantum field theory of the Standard Model things are not as easy as they may seem at first sight. Merely inserting the experimentally determined fermion masses in the Lagrangian of the SM is not allowed because such mass terms would break the gauge invariance and hence ruin the renormalizability of the theory. For fermions to be massive the concept of spontaneous symmetry breaking has to be introduced. The original Lagrangian is $SU(2)_L \times U(1)_Y$ symmetric but a new, fundamental scalar, *Higgs* field is introduced which explicitly breaks this symmetry to $U(1)_{EM}$. The non-zero vacuum expectation value of this field is directly responsible for the mass of the W and Z intermediate bosons. To generate a mass for the fermions we have to introduce additional Yukawa interaction terms between the fermions and the Higgs boson in the Lagrangian. Then, the vacuum expectation value of the Higgs field yields fermion masses which are proportional to the Yukawa coupling.

Although the Standard Model remains renormalizable after the introduction of the Higgs field, the idea is somehow unattractive because of new quadratic mass divergences. Renormalizing these requires a very sharp fine tuning to keep the fermion masses to the scales at which they

are experimentally measured. Without such fine tuning the quantum corrections would raise the fermion masses to the scale of new physics which is expected to be between 10^{15} GeV and 10^{19} GeV.

An attractive alternative to the spontaneous symmetry breaking mechanism engendered by the Higgs field is that of fermion mass generation through dynamical symmetry breaking. There, the initially massless fermions acquire their mass through a non-perturbative dynamical mechanism without the need for any fundamental scalar field with a non-zero vacuum expectation value to be introduced. We know from quantum field theory that the mass of a particle receives loop corrections because of its interactions with the gauge field. In perturbation theory each term in the perturbative expansion of the corrected fermion mass is proportional to its bare mass. Hence, if the theory is originally massless, it remains so at each order in perturbation theory. Of course this argument is only valid as long as the perturbative series makes sense. One can imagine that when the coupling is of order unity, an expansion in powers of the coupling constant does not necessarily give us relevant information about the theory. Indeed, it has been shown [1] that provided the coupling is larger than some critical value one can generate a non-zero fermion mass dynamically, even in a theory without any bare mass in the Lagrangian.

Furthermore, not only the fermions but also the intermediate gauge bosons can acquire mass by the dynamical breaking of chiral symmetry. Unfortunately, in quantum chromodynamics (QCD), the only strong interaction in the SM, the running coupling becomes strong at a scale which is far too low to account for the measured W and Z masses. Therefore, the mechanism of dynamical mass generation can only explain the experimentally measured masses if a new interaction, with a higher scale, is introduced, as has been proposed in the Technicolor (TC) [2] and Extended Technicolor theories (ETC) [3]. One of the major problems encountered by these theories is the excess of flavour changing neutral currents(FCNC). A possible solution for this has been suggested by Holdom in the Walking Technicolor theory [4]. To make realistic predictions in these theories, the non-perturbative phenomenon of dynamical fermion mass generation in gauge field theories has to be well understood. The research undertaken for this purpose can be divided into two main categories: phenomenological studies where the basic concepts of dynamical fermion mass generation are applied to realistic models of gauge groups, constructed to reproduce the experimental results; and theoretical studies, concerned with the fundamental aspects of the dynamical generation of fermion mass, which are needed to provide the correct ideas and numbers for phenomenologists to refine their calculations.

The research presented in this thesis belongs to these theoretical studies. We will investigate the dynamical generation of fermion mass in strong coupling quantum electrodynamics (QED), the simplest gauge field theory in nature. There are several motivations for this study. In the realm of TC and ETC theories it can serve as a toy model for more complicated gauge theories. However, it is also important in its own right, to study the consistency of QED as a quantum field theory, as discussed by Landau [5] as early as in 1955. Furthermore, it could be of interest considering the possibility of a new phase transition of nature's QED in strong electromagnetic fields, as might be suggested by some unexplained narrow peaks in e^+e^- coincidence spectra in heavy ion collision experiments [6, 7].

Because of the intrinsically non-perturbative nature of dynamical fermion mass generation, we need an appropriate framework to conduct our investigation. The two methods most frequently used to study non-perturbative aspects of quantum field theory are the continuum method using the Schwinger-Dyson equations and lattice gauge theory, where the field theory is solved on a discretized lattice. In these lattice studies one cannot take the bare mass identically to zero. Therefore, one has to compute results for various, finite values of this mass, in order to extrapolate to the zero-mass situation. This extrapolation procedure can be a source of difficulties in the correct interpretation of the lattice results.

The Schwinger-Dyson (SD) equations are an infinite set of coupled integral equations derived from the functional integral formalism, relating all the Green's functions of the quantum field theory. If these equations could be solved, all the Green's functions would be known and the S-matrix for all physical processes could be calculated exactly. However, because there are an infinite number of coupled equations, such solution is not possible and one must truncate the system in some way. The most common procedure is to expand the equations in powers of the coupling and to truncate the series at a certain order. This method is just perturbation theory. However, if we are to investigate the non-perturbative aspects of the theory, this clearly will not suffice and we have to devise other ways of truncating the infinite tower of equations. In the study of the dynamical generation of fermion mass, one is primarily interested in the behaviour of the fermion propagator. The fermion SD equation determines how the fermion propagator is altered by the self-energy generated by the interactions. In this equation the fermion propagator is related to the photon propagator and the QED-vertex. The photon SD equation describes how the vacuum polarization corrects the photon propagator and again relates the fermion and photon propagator and the vertex. An infinity of other SD equations relate higher order Green's

functions. To study the fermion mass generation we will decouple the first two equations from all the others by choosing some suitable vertex Ansatz and investigate the possibility of these equations having a non-trivial mass solution in a theory without bare mass.

Several studies of fermion mass generation in QED have been performed in the rainbow approximation, where the full photon propagator and the full vertex are replaced by their bare quantities. In this approximation, it has been shown that QED does undergo a phase transition and the originally massless fermions acquire a mass, when the value of the fixed coupling is larger than a critical value, which is of order unity in the Landau gauge [8]-[11]. However the bare vertex does not satisfy the Ward-Takahashi identity, which is a consequence of gauge invariance. Therefore, in the first part of this work, we will study the dynamical generation of fermion mass in quenched QED with the Curtis-Pennington vertex Ansatz [12], which satisfies the Ward-Takahashi identity and moreover ensures the multiplicative renormalizability of the fermion propagator. We will apply bifurcation analysis to determine the critical point for a general covariant gauge.

In the second part of the study we will investigate the dynamical generation of fermion mass in full, unquenched QED. All studies performed so far in the Landau gauge have used the bare vertex approximation. Furthermore, various additional approximations were introduced to simplify the analytical and numerical calculations [13]-[20]. The most frequently encountered approximations are: replacing the full photon propagator by its 1-loop perturbative result, removing the angular dependence of the vacuum polarization and setting the fermion wavefunction renormalization to one. To avoid these approximations we will develop a numerical method to solve the system of coupled, non-linear integral equations for the fermion and the photon propagator, paying special attention to achieve high degree of accuracy. We will also give a detailed discussion about the proper numerical cancellation of the quadratic divergence in the vacuum polarization integral. We will apply this method to the bare vertex approximation to unquenched QED to determine the critical coupling for a variety of approximations to the system of coupled integral equations, and will compare our results with those found in the literature. We will give detailed, highly accurate results of dynamical fermion mass generation in QED, including both the photon renormalization function and the fermion wavefunction renormalization in a consistent way. Finally, we will produce the first results of fermion mass generation in unquenched QED using improved vertices and will discuss in detail how to avoid unphysical quadratic divergences in the vacuum polarization integral, with the Ball-Chiu vertex.

In Chapter 2 we formulate the Schwinger-Dyson equations for the fermion and photon propagator. We discuss how fermion mass can be generated dynamically from these equations when the QED coupling is sufficiently large. We derive three coupled non-linear integral equations for the dynamical fermion mass Σ , the fermion wavefunction renormalization \mathcal{F} and the photon renormalization function \mathcal{G} , in the bare vertex approximation to the full vertex and with the Curtis-Pennington vertex Ansatz.

In Chapter 3 we study the dynamical fermion mass generation in quenched QED, where the full photon propagator is replaced by the bare one. We determine the critical point in the Curtis-Pennington approximation using bifurcation analysis. We also derive the Miransky scaling law, specific to quenched QED, for the bare vertex approximation and with the Curtis-Pennington vertex.

In Chapter 4 we give a literature survey of the various approximations introduced in the investigation of dynamical fermion mass generation in unquenched QED.

In Chapter 5 we develop a numerical method to solve the system of coupled non-linear integral equations, describing fermion mass generation in QED, taking special care to achieve high accuracy and convergence rate. This is done by discretizing the unknown functions and solving a system of non-linear algebraic equations for the function values at a finite number of points, using the natural iterative procedure. After a first attempt to apply the method to the problem of fermion mass generation in QED, simplified to the solution of a sole non-linear integral equation for Σ , the poor convergence of the procedure will be improved by introducing Newton's iterative method. We discuss how the numerical method can only be satisfactory if a suitable choice of integration rule is made. The scene being set, we apply the numerical method to the Σ -equation and show the main results.

In Chapter 6 we apply this method to the system of coupled integral equations for Σ and \mathcal{G} (neglecting the corrections to the wavefunction renormalization \mathcal{F}). We compare our results with those of Kondo et al. [20] and discuss the improper cancellation of the quadratic divergence in the vacuum polarization, which generates an unphysical behaviour in the photon renormalization function \mathcal{G} . We suggest that this could be remedied by introducing smooth approximations to the functions Σ , \mathcal{F} and \mathcal{G} .

In Chapter 7 we realize this by introducing Chebyshev expansions for the unknown functions and modifying the numerical method of Chapter 5 accordingly.

In Chapter 8 we apply the Chebyshev expansion method to various approximations to the system of coupled non-linear integral equations for Σ , \mathcal{F} and \mathcal{G} in the bare vertex approximation. In the 1-loop approximation to the vacuum polarization we first solve the Σ -equation with and without the LAK-approximation, then we solve the coupled (Σ, \mathcal{F}) -system. Consequently, we redo the calculation of Chapter 6 for the coupled (Σ, \mathcal{G}) -system, finding that indeed the unphysical behaviour of \mathcal{G} disappears. Finally, we solve the complete $(\Sigma, \mathcal{F}, \mathcal{G})$ -system of integral equations.

In Chapter 9 we perform the first calculations of fermion mass generation in unquenched QED using improved vertices. We solve the coupled $(\Sigma, \mathcal{F}, \mathcal{G})$ -system with various vertex approximations. The specific structure of the Ball-Chiu vertex leads to accuracy problems to cancel the quadratic photon divergence properly. These problems are dealt with in detail, since this is crucial for further numerical studies.

Finally, in Chapter 10 we summarize our results and give some suggestions for future studies.

Chapter 2

Schwinger-Dyson equations

In this chapter we formulate the Schwinger-Dyson equations for the fermion and photon propagator. These equations are just two of the infinite tower of integral equations relating the Green's functions of the quantum field theory [21]. We discuss how fermion mass generation can be studied using these equations and derive three coupled, non-linear algebraic integral equations for the dynamical mass Σ , the fermion wavefunction renormalization \mathcal{F} and the photon renormalization function \mathcal{G} , first using the bare vertex approximation, then with the Curtis-Pennington vertex Ansatz.

2.1 QED Lagrangian

The Lagrangian for a free Dirac field with bare mass m_0 is:

$$\mathcal{L}_0 = i\bar{\psi}\gamma^\mu\partial_\mu\psi - m_0\bar{\psi}\psi. \quad (2.1)$$

The fermion field ψ will transform under a local U(1) gauge transformation as:

$$\psi \rightarrow \psi'(x) = e^{-ie\lambda(x)}\psi(x). \quad (2.2)$$

The Lagrangian of Eq. (2.1) is not invariant under the transformation Eq. (2.2).

Local U(1) gauge invariance of the Lagrangian can be achieved by introducing a vector field A_μ , called the gauge field, which transforms as:

$$A_\mu \rightarrow A'_\mu = A_\mu + \partial_\mu\lambda \quad (2.3)$$

and replacing the ordinary derivative ∂_μ in the free Lagrangian of Eq. (2.1) by a covariant

derivative D_μ :

$$D_\mu = \partial_\mu + ieA_\mu. \quad (2.4)$$

The new Lagrangian is now given by:

$$\mathcal{L} = i\bar{\psi}\gamma^\mu\partial_\mu\psi - e\bar{\psi}\gamma^\mu A_\mu\psi - m_0\bar{\psi}\psi. \quad (2.5)$$

To this Lagrangian one has to add a kinetic term for the gauge field A_μ , which has to be invariant under the transformation Eq. (2.3). The full QED Lagrangian for a fermion field ψ with charge e in an electromagnetic field A_μ is given by:

$$\mathcal{L} = i\bar{\psi}\gamma^\mu\partial_\mu\psi - e\bar{\psi}\gamma^\mu A_\mu\psi - m_0\bar{\psi}\psi - \frac{1}{4}F_{\mu\nu}F^{\mu\nu} \quad (2.6)$$

where

$$F_{\mu\nu} = \partial_\mu A_\nu - \partial_\nu A_\mu. \quad (2.7)$$

The quantum field theory defined by this Lagrangian can be derived by applying the functional integral method [21, 22, 23] using the following generating functional:

$$Z[\bar{\eta}, \eta, J] = \frac{1}{N} \int \mathcal{D}\bar{\psi} \mathcal{D}\psi \mathcal{D}A \exp \left[i \int d^4x (\mathcal{L} + \bar{\psi}\eta + \bar{\eta}\psi + J^\mu A_\mu) \right] \quad (2.8)$$

where $\bar{\eta}$, η and J are the source fields for the fermion, antifermion and gauge boson, and the normalization factor N is given by:

$$N = \int \mathcal{D}\bar{\psi} \mathcal{D}\psi \mathcal{D}A \exp \left[i \int d^4x \mathcal{L} \right].$$

A peculiarity of gauge theories is that there are orbits of gauge fields A_μ which are just gauge transforms of each other. Since the Lagrangian is gauge invariant the functional integral over a complete orbit of gauge fields will automatically be infinite. To avoid this we must pick out one representative on each orbit and integrate over these representative gauge fields. To do this we impose a gauge condition which is only satisfied by one field per orbit. In QED this is done by introducing a gauge fixing term in the Lagrangian. A common choice for this is the covariant gauge fixing term $-1/2\xi(\partial_\mu A^\mu)^2$. The full QED Lagrangian then becomes:

$$\mathcal{L}_{QED} = i\bar{\psi}\gamma^\mu\partial_\mu\psi - e\bar{\psi}\gamma^\mu A_\mu\psi - m_0\bar{\psi}\psi - \frac{1}{4}F_{\mu\nu}F^{\mu\nu} - \frac{1}{2\xi}(\partial^\mu A_\mu)^2. \quad (2.9)$$

It can be shown [21] that the generating functional of connected Green's functions, $G[\bar{\eta}, \eta, J^\mu]$ can be defined from the generating functional, Eq. (2.8), by:

$$Z[\bar{\eta}, \eta, J] = \exp(G[\bar{\eta}, \eta, J]). \quad (2.10)$$

Let us now define effective fields $\hat{\psi}$, $\hat{\bar{\psi}}$, \hat{A} by:

$$\hat{\psi} \equiv \frac{\delta G}{i\delta\bar{\eta}}; \quad \hat{\bar{\psi}} \equiv -\frac{\delta G}{i\delta\eta}; \quad \hat{A}_\nu \equiv \frac{\delta G}{i\delta J^\nu}. \quad (2.11)$$

Next we define an effective action $\Gamma[\hat{\psi}, \hat{\bar{\psi}}, \hat{A}]$, as the Legendre transform of the generating functional of connected Green's functions $G[\bar{\eta}, \eta, J]$:

$$i\Gamma[\hat{\psi}, \hat{\bar{\psi}}, \hat{A}] \equiv G[\bar{\eta}, \eta, J] - i \int d^4y (\bar{\eta}\hat{\psi} + \hat{\bar{\psi}}\eta + J^\mu \hat{A}_\mu). \quad (2.12)$$

One can prove that the effective action $\Gamma[\hat{\psi}, \hat{\bar{\psi}}, \hat{A}]$ is the generating functional of the one-particle-irreducible (1PI) Green's functions (see pp. 289-294 of Ref. [21]).

We now define the Green's functions which will be used in the investigation of fermion mass generation. The connected 2-point fermion Green's function or *fermion propagator* $iS(x, y)$ is:

$$iS_{ab}(x, y) \equiv -\frac{\delta^2 G}{\delta\eta_b(y)\delta\bar{\eta}_a(x)} \Big|_{\eta, \bar{\eta}, J=0}. \quad (2.13)$$

We define the connected 2-point photon Green's function or *photon propagator* $iD^{\mu\nu}(x, y)$ as:

$$iD_{\mu\nu}(x, y) \equiv -\frac{\delta^2 G}{\delta J^\nu(y)\delta J^\mu(x)} \Big|_{\eta, \bar{\eta}, J=0}. \quad (2.14)$$

The 1PI 3-points Green's function or *vertex* $e\Gamma(x, y; z)$ is defined by:

$$e\Gamma_{ab}^\mu(x, y; z) \equiv -\frac{\delta^3 \Gamma}{\delta \hat{A}_\mu(z)\delta \hat{\psi}_b(y)\delta \hat{\bar{\psi}}_a(x)} \Big|_{\eta, \bar{\eta}, J=0}. \quad (2.15)$$

The Schwinger-Dyson equations can be derived by applying the functional integral formalism to the QED Lagrangian (see pp. 475-481 of Ref. [21]).

2.2 Fermion SD equation

The Schwinger-Dyson equation for the fermion propagator in coordinate space is given by:

$$\left[S^{-1} \right] (x, y) = (i\gamma^\mu \partial_\mu - m_0) \delta^4(x - y) - ie^2 \int d^4x_1 d^4x_2 \gamma^\mu S(x, x_1) \Gamma^\nu(x_1, y; x_2) D_{\nu\mu}(x_2, x). \quad (2.16)$$

After Fourier transforming the various Green's functions, the Schwinger-Dyson equation for the fermion propagator in momentum space is given by:

$$\boxed{\left[S^{-1} \right] (p) = p_\mu \gamma^\mu - m_0 - E_f(p)} \quad (2.17)$$

where the fermion self-energy $E_f(p)$ is defined by:

$$\boxed{E_f(p) \equiv \frac{ie^2}{(2\pi)^4} \int d^4k \gamma^\mu S(k) \Gamma^\nu(k, p) D_{\nu\mu}(k - p)}. \quad (2.18)$$

Here, we simplified the notation with:

$$\begin{aligned} S(p) &\equiv S(p, -p) \\ D^{\mu\nu}(q) &\equiv D^{\mu\nu}(q, -q) \\ \Gamma^\mu(k, p) &\equiv \Gamma^\mu(k, p; k - p), \end{aligned} \quad (2.19)$$

where in the vertex, $\Gamma^\mu(k, p)$, k is the incoming fermion momentum, p is the outgoing fermion momentum and the photon momentum is taken outgoing.

Eq. (2.17) is represented diagrammatically in Fig. 2.1.

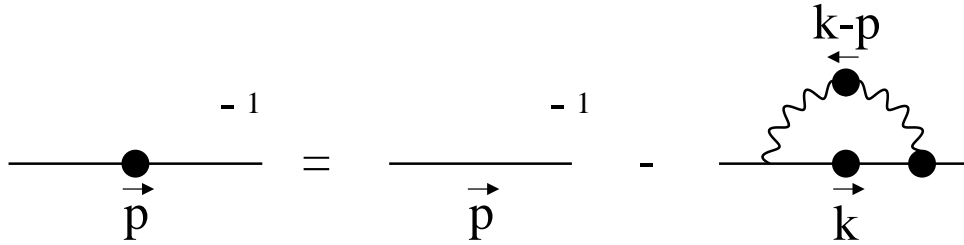


Figure 2.1: Schwinger-Dyson equation for the fermion propagator.

Because of the spinor structure of the fermion propagator $S(p)$, its most general form is:

$$S(p) = A(p^2) p_\mu \gamma^\mu + B(p^2). \quad (2.20)$$

We rewrite this as:

$$S(p) = \frac{\mathcal{F}(p^2)}{\not{p} - \Sigma(p^2)} = \frac{\mathcal{F}(p^2)}{p^2 - \Sigma^2(p^2)} (\not{p} + \Sigma(p^2)), \quad (2.21)$$

where $\mathcal{F}(p^2)$ is called the *fermion wavefunction renormalization*, $\Sigma(p^2)$ is the *dynamical fermion mass* and we introduced the notation $\not{p} \equiv p_\mu \gamma^\mu$.

From Eq. (2.17) we see that the fermion propagator for a free fermion field or *bare fermion propagator* is given by:

$$S^0(p) = \frac{1}{\not{p} - m_0}. \quad (2.22)$$

2.3 Photon SD equation

The Schwinger-Dyson equation for the photon propagator in coordinate space is:

$$\begin{aligned} [D^{-1}]^{\rho\lambda}(x, y) &= \left[g^{\rho\lambda} \partial^2 + \left(\frac{1}{\xi} - 1 \right) \partial^\rho \partial^\lambda \right] \delta^4(x - y) \\ &+ iN_f e^2 \int d^4x_1 d^4x_2 \text{Tr} \left[\gamma^\rho S(x, x_1) \Gamma^\lambda(x_1, x_2; y) S(x_2, x) \right]. \end{aligned} \quad (2.23)$$

To derive this equation in momentum space we Fourier transform the various Green's functions.

The Schwinger-Dyson equation for the photon propagator in momentum space is:

$$\boxed{[D^{-1}]^{\mu\nu}(q) = -q^2 \left[g^{\mu\nu} + \left(\frac{1}{\xi} - 1 \right) \frac{q^\mu q^\nu}{q^2} \right] + \Pi^{\mu\nu}(q)} \quad (2.24)$$

where the vacuum polarization tensor $\Pi^{\mu\nu}(q)$ is defined by:

$$\boxed{\Pi^{\mu\nu}(q) \equiv \frac{iN_f e^2}{(2\pi)^4} \int d^4k \text{Tr} [\gamma^\mu S(k) \Gamma^\nu(k, k - q) S(k - q)]}. \quad (2.25)$$

This equation is represented diagrammatically in Fig. 2.2.

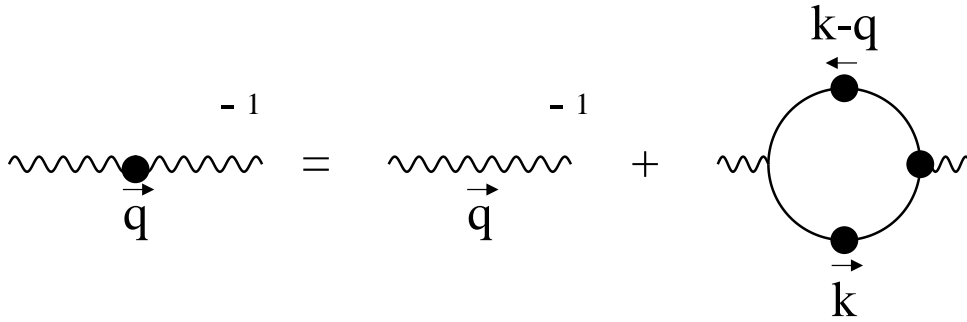


Figure 2.2: Schwinger-Dyson equation for the photon propagator.

The number of fermion flavours N_f in the vacuum polarization integral, Eq. (2.25), accounts for the number of distinct flavour loops which can occur in the photon propagator. We assume here that all fermion flavours couple with the same strength e to the electromagnetic field. Because of fermion flavour conservation, there is no factor of N_f multiplying the fermion self-energy integral, Eq. (2.18).

To study further the structure of the photon propagator, we will use the following Ward-Takahashi identity, which tells us that the vacuum polarization is transverse to the photon momentum:

$$q_\mu \Pi^{\mu\nu}(q) = 0. \quad (2.26)$$

Therefore the vacuum polarization tensor can be written as:

$$\Pi^{\mu\nu}(q) = -q^2 \left[g^{\mu\nu} - \frac{q^\mu q^\nu}{q^2} \right] \Pi(q^2). \quad (2.27)$$

Substituting Eq. (2.27) in Eq. (2.24) gives:

$$\left[D^{-1} \right]^{\mu\nu}(q) = -q^2 \left[\left(g^{\mu\nu} - \frac{q^\mu q^\nu}{q^2} \right) \left(1 + \Pi(q^2) \right) + \frac{1}{\xi} \frac{q^\mu q^\nu}{q^2} \right]. \quad (2.28)$$

To find the photon propagator we must invert the previous expression. The definition of inverse in momentum space (which can be deduced by Fourier transforming the definition for inverse in coordinate space) is:

$$D_{\mu\lambda}(q) \left[D^{-1} \right]^{\lambda\nu}(q) = \delta_{\mu}^{\nu}. \quad (2.29)$$

Substituting the most general tensor form $D_{\mu\nu}(q) = A g_{\mu\nu} + B q_\mu q_\nu / q^2$ in Eq. (2.29) and using Eq. (2.28) we find:

$$D_{\mu\nu}(q) = -\frac{1}{q^2} \left[\mathcal{G}(q^2) \left(g_{\mu\nu} - \frac{q_\mu q_\nu}{q^2} \right) + \xi \frac{q_\mu q_\nu}{q^2} \right], \quad (2.30)$$

where we defined the *photon renormalization function* $\mathcal{G}(q^2)$ as:

$$\mathcal{G}(q^2) \equiv \frac{1}{1 + \Pi(q^2)}. \quad (2.31)$$

From Eq. (2.30) one finds that the photon propagator in a pure gauge theory or *bare photon propagator* is given by:

$$D_{\mu\nu}^0(q) = -\frac{1}{q^2} \left[\left(g_{\mu\nu} - \frac{q_\mu q_\nu}{q^2} \right) + \xi \frac{q_\mu q_\nu}{q^2} \right]. \quad (2.32)$$

2.4 Fermion mass generation

From the Schwinger-Dyson equations we now derive the algebraic integral equations necessary for the investigation of dynamical fermion mass generation in QED.

After inserting the fermion propagator, Eq. (2.21), in the fermion SD equation, Eq. (2.17) we can write:

$$\frac{\not{p} - \Sigma(p^2)}{\mathcal{F}(p^2)} = \not{p} - m_0 - E_f(p). \quad (2.33)$$

This integral equation contains the two unknown propagator functions, $\mathcal{F}(p^2)$ and $\Sigma(p^2)$, and the unknown vertex $\Gamma^\nu(k, p)$. From the spinor equation Eq. (2.33) one can derive two algebraic integral equations. Taking the trace of Eq. (2.33) and dividing the equation by (-4) gives:

$$\frac{\Sigma(p^2)}{\mathcal{F}(p^2)} = m_0 + \frac{1}{4} \text{Tr} [E_f(p)]. \quad (2.34)$$

A second, independent equation is derived by multiplying Eq. (2.33) with \not{p} , taking the trace and dividing by $4p^2$:

$$\frac{1}{\mathcal{F}(p^2)} = 1 - \frac{1}{4p^2} \text{Tr} \left[\not{p} E_f(p) \right], \quad (2.35)$$

where we recall the fermion self-energy, Eq. (2.18):

$$E_f(p) \equiv \frac{ie^2}{(2\pi)^4} \int d^4k \gamma^\mu S(k) \Gamma^\nu(k, p) D_{\nu\mu}(k - p). \quad (2.36)$$

We will now derive the equation for the photon renormalization function $\mathcal{G}(q^2)$. We have seen in Eq. (2.27) that the photon Ward-Takahashi identity requires the vacuum polarization tensor to have the following form:

$$\Pi^{\mu\nu}(q) = -q^2 \left[g^{\mu\nu} - \frac{q^\mu q^\nu}{q^2} \right] \Pi(q^2). \quad (2.37)$$

It is important to note that unless the vertex $\Gamma^\mu(k, p)$ satisfies the fermion Ward-Takahashi identity and the regularization of the loop integrals is translation invariant, the vacuum polarization integral, Eq. (2.25), will **not** have the correct Lorentz structure of Eq. (2.37) with the coefficients of $g^{\mu\nu}$ and $q^\mu q^\nu$ being related to a single function $\Pi(q^2)$. When these conditions are satisfied, we can extract the vacuum polarization function $\Pi(q^2)$ by contracting Eq. (2.37) with the operator $\mathcal{P}_{\mu\nu} = g_{\mu\nu} - nq_\mu q_\nu / q^2$ (with any value of n):

$$\mathcal{P}_{\mu\nu} \Pi^{\mu\nu}(q) = -3q^2 \Pi(q^2). \quad (2.38)$$

The integral equation for $\Pi(q^2)$ can then be derived by applying the operator $\mathcal{P}_{\mu\nu}$ to the vacuum polarization integral, Eq. (2.25), and equating this to Eq. (2.38). This gives:

$$\Pi(q^2) = -\frac{iN_f e^2 \mathcal{P}_{\mu\nu}}{3(2\pi)^4 q^2} \int d^4k \text{Tr} \left[\gamma^\mu S(k) \Gamma^\nu(k, p) S(p) \right], \quad (2.39)$$

where we defined the fermion momentum $p \equiv k - q$.

From the photon SD equation and the WT-identity we know that the photon renormalization function \mathcal{G} can be written as (Eq. (2.31)):

$$\mathcal{G}(q^2) \equiv \frac{1}{1 + \Pi(q^2)}. \quad (2.40)$$

Combining Eqs. (2.39, 2.40) yields the integral equation for \mathcal{G} :

$$\frac{1}{\mathcal{G}(q^2)} = 1 - \frac{iN_f e^2 \mathcal{P}_{\mu\nu}}{3(2\pi)^4 q^2} \int d^4k \text{Tr} \left[\gamma^\mu S(k) \Gamma^\nu(k, p) S(p) \right]. \quad (2.41)$$

We want to investigate the dynamical generation of fermion mass with the use of the coupled integral equations, Eqs. (2.34, 2.35, 2.41), for Σ , \mathcal{F} and \mathcal{G} when $m_0 = 0$. However, these three integral equations still contain the full QED vertex, which is itself coupled to higher order Green's functions through other SD equations. To make the problem tractable, we want to decouple the three equations for Σ , \mathcal{F} and \mathcal{G} from the rest of the infinite tower of SD equations. This can be achieved by introducing an Ansatz for the QED vertex. The choice of vertex Ansatz can be dictated by reasons of simplicity or better by physical motivations. In the past, many additional approximations have been introduced in the $(\Sigma, \mathcal{F}, \mathcal{G})$ -system of equations to simplify the search for its solution. The key equation for the study of dynamical fermion mass generation is the Σ -equation also called gap-equation, Eq. (2.34), as this is the one which generates the purely non-perturbative solution for the fermion mass when the coupling constant is sufficiently large. It is easy to verify that the trivial solution, $\Sigma \equiv 0$, is always a solution of Eq. (2.34), when the bare mass is zero. This is the solution which corresponds with perturbation theory. However, it has been demonstrated that a non-trivial solution exists in the quenched approximation to QED ($N_f = 0$), when the coupling constant is sufficiently large [8]. When the coupling exceeds a certain critical value, the non-zero mass solution bifurcates away from the trivial one. Above this critical point, the generated fermion mass will increase further with increasing values of the coupling. In this work we will investigate the dynamical generation of fermion mass and determine the value of the critical coupling for quenched QED with the Curtis-Pennington vertex and in unquenched QED in a variety of approximations. For this purpose we will now derive the three coupled integral equations for the bare vertex approximation and with the Curtis-Pennington vertex.

2.5 The bare vertex approximation

2.5.1 The fermion equations

In the bare vertex approximation the fermion self-energy, Eq. (2.36), becomes:

$$E_f(p) = \frac{ie^2}{(2\pi)^4} \int d^4k \gamma^\mu S(k) \gamma^\nu D_{\nu\mu}(k-p). \quad (2.42)$$

In this approximation Eqs. (2.34, 2.35) now are:

$$\frac{\Sigma(p^2)}{\mathcal{F}(p^2)} = m_0 + \frac{ie^2}{4(2\pi)^4} \int d^4k \text{Tr}[\gamma^\mu S(k) \gamma^\nu] D_{\nu\mu}(k-p) \quad (2.43)$$

$$\frac{1}{\mathcal{F}(p^2)} = 1 - \frac{ie^2}{4p^2(2\pi)^4} \int d^4k \operatorname{Tr}[\not{p} \gamma^\mu S(k) \gamma^\nu] D_{\nu\mu}(k-p). \quad (2.44)$$

Substituting the fermion propagator, Eq. (2.21), in Eqs. (2.43, 2.44) yields:

$$\frac{\Sigma(p^2)}{\mathcal{F}(p^2)} = m_0 + \frac{ie^2}{4(2\pi)^4} \int d^4k \frac{\mathcal{F}(k^2)}{k^2 - \Sigma^2(k^2)} \operatorname{Tr}[\gamma^\mu (\not{k} + \Sigma(k^2)) \gamma^\nu] D_{\nu\mu}(k-p) \quad (2.45)$$

$$\frac{1}{\mathcal{F}(p^2)} = 1 - \frac{ie^2}{4p^2(2\pi)^4} \int d^4k \frac{\mathcal{F}(k^2)}{k^2 - \Sigma^2(k^2)} \operatorname{Tr}[\not{p} \gamma^\mu (\not{k} + \Sigma(k^2)) \gamma^\nu] D_{\nu\mu}(k-p). \quad (2.46)$$

where the photon momentum is given by $q = k - p$.

To evaluate the traces in Eqs. (2.45, 2.46) we will need to compute traces of products of gamma matrices. The Dirac gamma matrices obey the anticommutation relation:

$$\{\gamma^\mu, \gamma^\nu\} = 2g^{\mu\nu}. \quad (2.47)$$

From Eq. (2.47) it is easy to prove that in 4 dimensions:

$$\begin{aligned} \operatorname{Tr}[I] &= 4 \\ \operatorname{Tr}[\gamma^\mu \gamma^\nu] &= 4g^{\mu\nu} \\ \operatorname{Tr}[\not{k} \not{p}] &= 4k \cdot p \\ \operatorname{Tr}[\not{k}_1 \not{k}_2 \not{k}_3 \not{k}_4] &= 4[(k_1 \cdot k_2)(k_3 \cdot k_4) - (k_1 \cdot k_3)(k_2 \cdot k_4) + (k_1 \cdot k_4)(k_2 \cdot k_3)] \\ \operatorname{Tr}[\not{k}_1, \dots, \not{k}_n] &= 0 \quad , \quad \text{if } n \text{ is odd.} \end{aligned} \quad (2.48)$$

Applying those rules to Eqs. (2.45, 2.46) and substituting the photon propagator, Eq. (2.30), gives us:

$$\frac{\Sigma(p^2)}{\mathcal{F}(p^2)} = m_0 + \frac{ie^2}{(2\pi)^4} \int d^4k \frac{\mathcal{F}(k^2)\Sigma(k^2)}{k^2 - \Sigma^2(k^2)} g^{\mu\nu} \left\{ -\frac{1}{q^2} \left[\mathcal{G}(q^2) \left(g_{\mu\nu} - \frac{q_\mu q_\nu}{q^2} \right) + \xi \frac{q_\mu q_\nu}{q^2} \right] \right\} \quad (2.49)$$

$$\begin{aligned} \frac{1}{\mathcal{F}(p^2)} &= 1 - \frac{ie^2}{p^2(2\pi)^4} \int d^4k \frac{\mathcal{F}(k^2)}{k^2 - \Sigma^2(k^2)} (p^\mu k^\nu + k^\mu p^\nu - k \cdot p g^{\mu\nu}) \\ &\quad \times \left\{ -\frac{1}{q^2} \left[\mathcal{G}(q^2) \left(g_{\mu\nu} - \frac{q_\mu q_\nu}{q^2} \right) + \xi \frac{q_\mu q_\nu}{q^2} \right] \right\}. \end{aligned} \quad (2.50)$$

Executing the Lorentz-contractions with the photon propagator and substituting $q = k - p$ yields:

$$\frac{\Sigma(p^2)}{\mathcal{F}(p^2)} = m_0 - \frac{ie^2}{(2\pi)^4} \int d^4k \frac{\mathcal{F}(k^2)\Sigma(k^2)}{q^2(k^2 - \Sigma^2(k^2))} \left\{ 3\mathcal{G}(q^2) + \xi \right\} \quad (2.51)$$

$$\begin{aligned} \frac{1}{\mathcal{F}(p^2)} &= 1 + \frac{ie^2}{p^2(2\pi)^4} \int d^4k \frac{\mathcal{F}(k^2)}{q^2(k^2 - \Sigma^2(k^2))} \\ &\quad \times \left\{ \mathcal{G}(q^2) \left[2 \left(\frac{k^2 p^2 - (k \cdot p)^2}{q^2} \right) - 3k \cdot p \right] + \xi \left[\frac{(k^2 + p^2) k \cdot p - 2k^2 p^2}{q^2} \right] \right\}. \end{aligned} \quad (2.52)$$

In order to enable us to compute the 4-dimensional integral we will now perform a change of coordinates, called *Wick rotation*. The transformation consists of $k_0 \rightarrow ik_0$ and $k_j \rightarrow k_j$, $j = 1, \dots, 3$. By doing so, the phase space is transformed from a Minkowski space to a Euclidean space as the original metric, which was $k^2 = k_0^2 - k_1^2 - k_2^2 - k_3^2$, has been transformed to $-k^2 = -(k_0^2 + k_1^2 + k_2^2 + k_3^2)$. The Wick rotation in fact consists of changing from real time to imaginary time and then rotating back the integration interval over 90° to integrate over the real time axis. One can prove that in most cases the value of the integral remains unchanged after a Wick rotation. In Minkowski space the mass of a particle is defined as the pole of its propagator. From Eq. (2.21) we see that this pole occurs at the timelike momentum m^2 which solves the equation $m^2 = \Sigma^2(m^2)$. After the Wick rotation the mass of the fermion, still defined as pole of the propagator, will be given by $m^2 = -p_E^2 = \Sigma^2(-p_E^2)$, which will be satisfied by some $p_E^2 < 0$. When solving the integral equation in Euclidean space, one only finds solutions for $p_E^2 \geq 0$. To determine the mass of the particle one has to analytically continue the mass function $\Sigma(p_E^2)$ to negative values of p_E^2 . In our study we will refrain from doing so and will only consider $\Sigma(p_E^2)$ for positive values of Euclidean momentum. In the further discussion we will omit the subscript E for Euclidean space to simplify the notation.

After the Wick rotation to Euclidean space, Eqs. (2.51, 2.52) are given by:

$$\frac{\Sigma(p^2)}{\mathcal{F}(p^2)} = m_0 + \frac{e^2}{(2\pi)^4} \int d^4k \frac{\mathcal{F}(k^2)\Sigma(k^2)}{q^2(k^2 + \Sigma^2(k^2))} \{3\mathcal{G}(q^2) + \xi\} \quad (2.53)$$

$$\begin{aligned} \frac{1}{\mathcal{F}(p^2)} &= 1 - \frac{e^2}{p^2(2\pi)^4} \int d^4k \frac{\mathcal{F}(k^2)}{q^2(k^2 + \Sigma^2(k^2))} \\ &\times \left\{ \mathcal{G}(q^2) \left[2 \left(\frac{k^2 p^2 - (k \cdot p)^2}{q^2} \right) - 3k \cdot p \right] + \xi \left[\frac{(k^2 + p^2)k \cdot p - 2k^2 p^2}{q^2} \right] \right\}. \end{aligned} \quad (2.54)$$

Once in Euclidean space we can now change to spherical coordinates:

$$\begin{cases} k_0 &= k \cos \theta \\ k_1 &= k \sin \theta \cos \phi \\ k_2 &= k \sin \theta \sin \phi \cos \psi \\ k_3 &= k \sin \theta \sin \phi \sin \psi, \end{cases} \quad (2.55)$$

where $k = (k_0^2 + k_1^2 + k_2^2 + k_3^2)^{1/2}$ and θ is taken to be the angle between the incoming fermion momentum p and the fermion loop momentum k . The volume element d^4k now becomes $k^3 \sin^2 \theta \sin \phi dk d\theta d\phi d\psi$. The integration ranges of the new variables are: $k \in [0, \infty]$, $\theta, \phi \in [0, \pi]$ and $\psi \in [0, 2\pi]$.

The angular integrals over the angles ϕ and ψ can always be separated yielding:

$$\int_0^\pi d\phi \sin \phi \int_0^{2\pi} d\psi = 4\pi. \quad (2.56)$$

If we now define the coupling constant $\alpha \equiv e^2/4\pi$ and introduce the notation $x = p^2$, $y = k^2$ and $z = q^2$, then Eqs. (2.53, 2.54) in spherical coordinates are given by:

$$\frac{\Sigma(x)}{\mathcal{F}(x)} = m_0 + \frac{\alpha}{2\pi^2} \int dy \frac{y\mathcal{F}(y)\Sigma(y)}{y + \Sigma^2(y)} \int d\theta \frac{\sin^2 \theta}{z} \{3\mathcal{G}(z) + \xi\} \quad (2.57)$$

$$\begin{aligned} \frac{1}{\mathcal{F}(x)} &= 1 - \frac{\alpha}{2\pi^2 x} \int dy \frac{y\mathcal{F}(y)}{y + \Sigma^2(y)} \\ &\times \int d\theta \frac{\sin^2 \theta}{z} \left\{ \mathcal{G}(z) \left[\frac{2xy \sin^2 \theta}{z} - 3\sqrt{yx} \cos \theta \right] + \xi \left[\frac{(y+x)\sqrt{yx} \cos \theta - 2yx}{z} \right] \right\}. \end{aligned} \quad (2.58)$$

Here, the angular integrals of the ξ -part can be computed analytically, as shown in Appendix A. Substituting Eqs. (A.1, A.2, A.5) in Eqs. (2.57, 2.58) yields:

$$\begin{aligned} \frac{\Sigma(x)}{\mathcal{F}(x)} &= m_0 + \frac{3\alpha}{2\pi^2} \int dy \frac{y\mathcal{F}(y)\Sigma(y)}{y + \Sigma^2(y)} \int d\theta \sin^2 \theta \frac{\mathcal{G}(z)}{z} \\ &+ \frac{\alpha\xi}{4\pi} \int dy \frac{\mathcal{F}(y)\Sigma(y)}{y + \Sigma^2(y)} \left[\frac{y}{x}\theta(x-y) + \theta(y-x) \right] \end{aligned} \quad (2.59)$$

$$\begin{aligned} \frac{1}{\mathcal{F}(x)} &= 1 - \frac{\alpha}{2\pi^2 x} \int dy \frac{y\mathcal{F}(y)}{y + \Sigma^2(y)} \int d\theta \sin^2 \theta \mathcal{G}(z) \left[\frac{2xy \sin^2 \theta}{z^2} - \frac{3\sqrt{yx} \cos \theta}{z} \right] \\ &+ \frac{\alpha\xi}{4\pi} \int dy \frac{\mathcal{F}(y)}{y + \Sigma^2(y)} \left[\frac{y^2}{x^2}\theta(x-y) + \theta(y-x) \right]. \end{aligned} \quad (2.60)$$

2.5.2 The photon equation

We introduce the bare vertex approximation in Eq. (2.41):

$$\frac{1}{\mathcal{G}(q^2)} = 1 - \frac{iN_f e^2 \mathcal{P}_{\mu\nu}}{3(2\pi)^4 q^2} \int d^4k \text{Tr} \left[\gamma^\mu S(k) \gamma^\nu S(p) \right]. \quad (2.61)$$

Substituting the fermion propagator, Eq. (2.21), in Eq. (2.61), gives:

$$\frac{1}{\mathcal{G}(q^2)} = 1 - \frac{iN_f e^2}{3(2\pi)^4 q^2} \int d^4k \frac{\mathcal{F}(k^2)\mathcal{F}(p^2)}{(k^2 - \Sigma^2(k^2))(p^2 - \Sigma^2(p^2))} \mathcal{P}_{\mu\nu} T^{\mu\nu} \quad (2.62)$$

where

$$T^{\mu\nu} \equiv \text{Tr} \left[\gamma^\mu (\not{k} + \Sigma(k^2)) \gamma^\nu (\not{p} + \Sigma(p^2)) \right]. \quad (2.63)$$

We now compute the trace, Eq. (2.63), using Eq. (2.48). This gives:

$$T^{\mu\nu} = 4 \left[k^\mu p^\nu + p^\mu k^\nu - (k \cdot p - \Sigma(k^2)\Sigma(p^2)) g^{\mu\nu} \right]. \quad (2.64)$$

To simplify Eq. (2.62) we first work out the Lorentz contraction of $T^{\mu\nu}$ with $\mathcal{P}_{\mu\nu} = g_{\mu\nu} - nq_\mu q_\nu / q^2$, and substitute $p = k - q$:

$$\mathcal{P}_{\mu\nu} T^{\mu\nu} = 4 \left[(n-2)k^2 - \frac{2n(k \cdot q)^2}{q^2} + (n+2)k \cdot q - (n-4)\Sigma(k^2)\Sigma(p^2) \right]. \quad (2.65)$$

Substituting Eq. (2.65) in Eq. (2.62) gives:

$$\begin{aligned} \frac{1}{\mathcal{G}(q^2)} &= 1 - \frac{4iN_f e^2}{3(2\pi)^4 q^2} \int d^4 k \frac{\mathcal{F}(k^2)\mathcal{F}(p^2)}{(k^2 - \Sigma^2(k^2))(p^2 - \Sigma^2(p^2))} \\ &\times \left[(n-2)k^2 - \frac{2n(k \cdot q)^2}{q^2} + (n+2)k \cdot q - (n-4)\Sigma(k^2)\Sigma(p^2) \right]. \end{aligned} \quad (2.66)$$

As for the fermion equation we perform a Wick rotation to Euclidean space. We have:

$$\begin{aligned} \frac{1}{\mathcal{G}(q^2)} &= 1 + \frac{4N_f e^2}{3(2\pi)^4 q^2} \int d^4 k \frac{\mathcal{F}(k^2)\mathcal{F}(p^2)}{(k^2 + \Sigma^2(k^2))(p^2 + \Sigma^2(p^2))} \\ &\times \left[(n-2)k^2 - \frac{2n(k \cdot q)^2}{q^2} + (n+2)k \cdot q + (n-4)\Sigma(k^2)\Sigma(p^2) \right]. \end{aligned} \quad (2.67)$$

Changing to spherical coordinates, substituting $\alpha = e^2/4\pi$ and defining $x \equiv q^2$, $y \equiv k^2$ and $z \equiv p^2$ we find:

$$\begin{aligned} \frac{1}{\mathcal{G}(x)} &= 1 + \frac{2N_f \alpha}{3\pi^2 x} \int dy \frac{y\mathcal{F}(y)}{y + \Sigma^2(y)} \int d\theta \sin^2 \theta \frac{\mathcal{F}(z)}{z + \Sigma^2(z)} \\ &\times \left[(n-2)y - 2ny \cos^2 \theta + (n+2)\sqrt{yx} \cos \theta + (n-4)\Sigma(y)\Sigma(z) \right]. \end{aligned} \quad (2.68)$$

In general, if we regularize the theory using an ultraviolet cutoff, the vacuum polarization integral in Eq. (2.68) contains a quadratic divergence which has to be removed, since such a photon mass term is not allowed in more than 2 dimensions. One can show that the $q_\mu q_\nu / q^2$ term of the vacuum polarization tensor cannot receive any quadratically divergent contribution. Consequently, if we choose the operator $\mathcal{P}_{\mu\nu}$ of Eq. (2.39) with $n = 4$, the resulting integral will be free of quadratic divergences because the contraction $\mathcal{P}_{\mu\nu} g^{\mu\nu}$ vanishes. Setting $n = 4$ in the photon equation Eq. (2.68) yields:

$$\frac{1}{\mathcal{G}(x)} = 1 + \frac{4N_f \alpha}{3\pi^2 x} \int dy \frac{y\mathcal{F}(y)}{y + \Sigma^2(y)} \int d\theta \sin^2 \theta \frac{\mathcal{F}(z)}{z + \Sigma^2(z)} \left[y(1 - 4 \cos^2 \theta) + 3\sqrt{yx} \cos \theta \right]. \quad (2.69)$$

2.6 Improving the vertex Ansatz

In the previous section we have derived the integral equations for the study of dynamical fermion mass generation with the bare vertex approximation. This vertex Ansatz has the advantage of being very simple and therefore it makes the manipulation of the Schwinger-Dyson equations easier. However, this approximation does not satisfy the Ward-Takahashi identity relating the QED vertex with the fermion propagator, which is a consequence of the gauge invariance of the theory. Therefore, the bare vertex approximation does not ensure that the calculated physical quantities are gauge invariant, as they should be.

In this section we will introduce the Ball-Chiu vertex [24] which is the exact longitudinal part of the full QED vertex, uniquely determined by the Ward-Takahashi identity relating the vertex with the fermion propagator. However, the transverse part of the vertex is still arbitrary. We then consider the Curtis-Pennington vertex [12] in which the transverse part of the vertex is constructed by requiring the multiplicative renormalizability of the fermion propagator and the reproduction of the perturbative results in the weak coupling limit.

2.6.1 Ball-Chiu Vertex

The Ward-Takahashi identity relating the QED vertex and the fermion propagator is:

$$(k-p)_\mu \Gamma^\mu(k,p) = S^{-1}(k) - S^{-1}(p). \quad (2.70)$$

In the limit $p \rightarrow k$, Eq. (2.70) becomes the Ward identity:

$$\Gamma^\mu(k,k) = \frac{\partial S^{-1}(k)}{\partial k_\mu}. \quad (2.71)$$

In general, the full QED vertex can be written as the sum of a longitudinal and a transverse part:

$$\Gamma^\mu(k,p) = \Gamma_L^\mu(k,p) + \Gamma_T^\mu(k,p). \quad (2.72)$$

The longitudinal part, $\Gamma_L^\mu(k,p)$, of the vertex is determined by the Ward-Takahashi identity, Eq. (2.70), and the Ward identity, Eq. (2.71), as demonstrated by Ball and Chiu [24], and is given by:

$$\begin{aligned} \Gamma_L^\mu(k,p) &= \frac{1}{2} \left[\frac{1}{\mathcal{F}(k^2)} + \frac{1}{\mathcal{F}(p^2)} \right] \gamma^\mu + \frac{1}{2} \left[\frac{1}{\mathcal{F}(k^2)} - \frac{1}{\mathcal{F}(p^2)} \right] \frac{(k+p)^\mu (k+p)_\nu}{k^2 - p^2} \\ &\quad - \left[\frac{\Sigma(k^2)}{\mathcal{F}(k^2)} - \frac{\Sigma(p^2)}{\mathcal{F}(p^2)} \right] \frac{(k+p)^\mu}{k^2 - p^2}. \end{aligned} \quad (2.73)$$

The transverse part of the vertex, which has to satisfy the transversality condition

$$(k - p)_\mu \Gamma_T^\mu(k, p) = 0, \quad \text{and} \quad \Gamma_T^\mu(p, p) = 0,$$

is not constrained by the Ward-Takahashi identity. However, other properties of gauge theories can be used to restrict its form. These constraints are mainly multiplicative renormalizability, reproduction of perturbative results in weak coupling, absence of kinematical singularities and gauge invariance of physical observables [12, 25, 26].

The most general form for the transverse part of the vertex can be given by [24, 27]:

$$\Gamma_T^\mu(k, p) = \sum_{i=1}^8 \tau_i(k^2, p^2, q^2) T_i^\mu(k, p), \quad (2.74)$$

where the T_i^μ form a tensor basis in spinor space and are defined as:

$$\begin{aligned} T_1^\mu(k, p) &= p^\mu(k \cdot q) - k^\mu(p \cdot q) \\ T_2^\mu(k, p) &= [p^\mu(k \cdot q) - k^\mu(p \cdot q)] (\not{k} + \not{p}) \\ T_3^\mu(k, p) &= q^2 \gamma^\mu - q^\mu \not{q} \\ T_4^\mu(k, p) &= q^2 [\gamma^\mu(\not{p} + \not{k}) - p^\mu - k^\mu] + 2(p - k)^\mu k^\lambda p^\nu \sigma_{\lambda\nu} \\ T_5^\mu(k, p) &= q_\nu \sigma^{\nu\mu} \\ T_6^\mu(k, p) &= \gamma^\mu(k^2 - p^2) - (k + p)^\mu (\not{k} - \not{p}) \\ T_7^\mu(k, p) &= \frac{1}{2}(p^2 - k^2) [\gamma^\mu(\not{p} + \not{k}) - p^\mu - k^\mu] + (k + p)^\mu k^\lambda p^\nu \sigma_{\lambda\nu} \\ T_8^\mu(k, p) &= -\gamma^\mu k^\nu p^\lambda \sigma_{\nu\lambda} + k^\mu \not{p} - p^\mu \not{k} \end{aligned} \quad (2.75)$$

with $q = k - p$ and $\sigma_{\mu\nu} = \frac{1}{2}[\gamma_\mu, \gamma_\nu]$.

2.6.2 Curtis-Pennington vertex

In Ref. [12] Curtis and Pennington have proposed a vertex Ansatz which ensures the multiplicative renormalizability of the fermion propagator, reproduces the perturbative results in the weak coupling limit and is free of kinematical singularities in the massive case. As these requirements do not constrain the transverse part uniquely, they have chosen a simple form satisfying them and which is only composed of T_6^μ :

$$\Gamma_T^\mu(k, p) = \frac{1}{2} \left[\frac{1}{\mathcal{F}(k^2)} - \frac{1}{\mathcal{F}(p^2)} \right] \frac{(k^2 + p^2) [\gamma^\mu(k^2 - p^2) - (k + p)^\mu (\not{k} - \not{p})]}{(k^2 - p^2)^2 + (\Sigma^2(k^2) + \Sigma^2(p^2))^2}. \quad (2.76)$$

Substituting Eqs. (2.73, 2.76) in Eq. (2.72) yields the full *Curtis-Pennington vertex Ansatz*:

$$\begin{aligned} \Gamma_{\text{CP}}^\mu(k, p) &= \frac{1}{2} \left[\frac{1}{\mathcal{F}(k^2)} + \frac{1}{\mathcal{F}(p^2)} \right] \gamma^\mu + \frac{1}{2} \left[\frac{1}{\mathcal{F}(k^2)} - \frac{1}{\mathcal{F}(p^2)} \right] \frac{(k+p)^\mu (\not{k} + \not{p})}{k^2 - p^2} \\ &\quad - \left[\frac{\Sigma(k^2)}{\mathcal{F}(k^2)} - \frac{\Sigma(p^2)}{\mathcal{F}(p^2)} \right] \frac{(k+p)^\mu}{k^2 - p^2} \\ &\quad + \frac{1}{2} \left[\frac{1}{\mathcal{F}(k^2)} - \frac{1}{\mathcal{F}(p^2)} \right] \frac{(k^2 + p^2) [\gamma^\mu (k^2 - p^2) - (k+p)^\mu (\not{k} - \not{p})]}{(k^2 - p^2)^2 + (\Sigma^2(k^2) + \Sigma^2(p^2))^2}. \end{aligned} \quad (2.77)$$

2.7 The Curtis-Pennington equations

2.7.1 The fermion equations

We now derive the equations necessary for the study of dynamical mass generation in QED with the Curtis-Pennington vertex Ansatz. The fermion self-energy integral, Eq. (2.36), with the Curtis-Pennington vertex is:

$$E_f(p) = \frac{ie^2}{(2\pi)^4} \int d^4k \gamma^\mu S(k) \Gamma_{\text{CP}}^\nu(k, p) D_{\nu\mu}(k-p). \quad (2.78)$$

If we substitute the photon propagator, Eq. (2.30), in the self-energy integral, Eq. (2.78), we find:

$$E_f(p) = -\frac{ie^2}{(2\pi)^4} \int d^4k \gamma^\mu S(k) \Gamma_{\text{CP}}^\nu(k, p) \left[\frac{\mathcal{G}(q^2)}{q^2} \left(g_{\nu\mu} - \frac{q_\nu q_\mu}{q^2} \right) + \xi \frac{q_\nu q_\mu}{q^4} \right], \quad (2.79)$$

where we defined $q \equiv k - p$.

Because the CP-vertex satisfies the Ward-Takahashi identity, Eq. (2.70), in the same way as the full vertex does, it is useful to substitute this identity in the ξ -part of Eq. (2.79), to ensure translational invariance. This yields:

$$E_f(p) = -\frac{ie^2}{(2\pi)^4} \int d^4k \left\{ \frac{\mathcal{G}(q^2)}{q^2} \left(g_{\nu\mu} - \frac{q_\nu q_\mu}{q^2} \right) \gamma^\mu S(k) \Gamma_{\text{CP}}^\nu(k, p) + \frac{\xi}{q^4} \not{q} \left[1 - S(k) S^{-1}(p) \right] \right\}. \quad (2.80)$$

From translational invariance we know:

$$\int_{-\infty}^{+\infty} d^4k \frac{\not{q}}{q^4} = \int_{-\infty}^{+\infty} d^4q \frac{\not{q}}{q^4} = 0. \quad (2.81)$$

So that Eq. (2.80) becomes:

$$E_f(p) = -\frac{ie^2}{(2\pi)^4} \int d^4k \left\{ \frac{\mathcal{G}(q^2)}{q^2} \left(g_{\nu\mu} - \frac{q_\nu q_\mu}{q^2} \right) \gamma^\mu S(k) \Gamma_{\text{CP}}^\nu(k, p) - \frac{\xi}{q^4} \not{q} S(k) S^{-1}(p) \right\}. \quad (2.82)$$

Substituting Eq. (2.82) in the Σ -equation, Eq. (2.34), and introducing $\alpha \equiv e^2/4\pi$ we find

$$\frac{\Sigma(p^2)}{\mathcal{F}(p^2)} = m_0 - \frac{i\alpha}{16\pi^3} \int d^4k \left\{ \frac{\mathcal{G}(q^2)}{q^2} \left(g_{\nu\mu} - \frac{q_\nu q_\mu}{q^2} \right) \text{Tr} \left[\gamma^\mu S(k) \Gamma_{\text{CP}}^\nu(k, p) \right] - \frac{\xi}{q^4} \text{Tr} \left[\not{q} S(k) S^{-1}(p) \right] \right\}. \quad (2.83)$$

We now substitute the fermion propagator, Eq. (2.21), in the integral of Eq. (2.83), yielding

$$\frac{\Sigma(p^2)}{\mathcal{F}(p^2)} = m_0 - \frac{i\alpha}{16\pi^3} \int d^4k \frac{\mathcal{F}(k^2)}{k^2 - \Sigma^2(k^2)} \left\{ \frac{\mathcal{G}(q^2)}{q^2} \left(g_{\nu\mu} - \frac{q_\nu q_\mu}{q^2} \right) T_{\mathcal{G}}^{\mu\nu} - \frac{\xi}{\mathcal{F}(p^2)q^4} T_\xi \right\} \quad (2.84)$$

where we defined

$$T_{\mathcal{G}}^{\mu\nu} \equiv \text{Tr} \left[\gamma^\mu (\not{k} + \Sigma(k^2)) \Gamma_{\text{CP}}^\nu(k, p) \right] \quad (2.85)$$

$$T_\xi \equiv \text{Tr} \left[\not{q} (\not{k} + \Sigma(k^2)) (\not{p} - \Sigma(p^2)) \right]. \quad (2.86)$$

We first consider the ξ -part of the integral in Eq. (2.84), which we call I_ξ :

$$I_\xi \equiv \frac{i\alpha\xi}{16\pi^3\mathcal{F}(p^2)} \int d^4k \frac{\mathcal{F}(k^2)}{(k^2 - \Sigma^2(k^2))q^4} T_\xi. \quad (2.87)$$

We compute the trace, Eq. (2.86), using Eq. (2.48), and substitute $q = k - p$. This gives:

$$T_\xi = 4 \left[(\Sigma(k^2) + \Sigma(p^2)) k \cdot p - \Sigma(k^2) p^2 - \Sigma(p^2) k^2 \right]. \quad (2.88)$$

Substituting the trace, Eq. (2.88), in the ξ -integral, Eq. (2.87), we find:

$$I_\xi = \frac{i\alpha\xi}{4\pi^3\mathcal{F}(p^2)} \int d^4k \frac{\mathcal{F}(k^2)}{k^2 - \Sigma^2(k^2)} \frac{1}{q^4} \left[(\Sigma(k^2) + \Sigma(p^2)) k \cdot p - \Sigma(k^2) p^2 - \Sigma(p^2) k^2 \right]. \quad (2.89)$$

Performing a Wick rotation to go from Minkowski to Euclidean space, as explained in Section 2.5, gives:

$$I_\xi = -\frac{\alpha\xi}{4\pi^3\mathcal{F}(p^2)} \int d^4k \frac{\mathcal{F}(k^2)}{k^2 + \Sigma^2(k^2)} \frac{1}{q^4} \left[(\Sigma(k^2) + \Sigma(p^2)) k \cdot p - \Sigma(k^2) p^2 - \Sigma(p^2) k^2 \right]. \quad (2.90)$$

We can now change to spherical coordinates. Two angles can be integrated out straight away leaving us with one angle, θ , and a Jacobian which is $2\pi dy y d\theta \sin^2 \theta$ where we denoted $y \equiv k^2$. If we also define $x \equiv p^2$ and $z \equiv q^2$, Eq. (2.90) becomes:

$$I_\xi = -\frac{\alpha\xi}{2\pi^2\mathcal{F}(x)} \int dy \frac{y\mathcal{F}(y)}{y + \Sigma^2(y)} \int d\theta \frac{\sin^2 \theta}{z^2} \left[(\Sigma(y) + \Sigma(x)) \sqrt{yx} \cos \theta - \Sigma(y) x - \Sigma(x) y \right]. \quad (2.91)$$

The angular integrals of Eq. (2.91) can be computed analytically as shown in Appendix A. Substituting Eqs. (A.2, A.5) in Eq. (2.91) finally gives:

$$I_\xi = \frac{\alpha\xi}{4\pi\mathcal{F}(x)} \int dy \frac{\mathcal{F}(y)}{y + \Sigma^2(y)} \left[\frac{y\Sigma(y)}{x} \theta(x - y) + \Sigma(x) \theta(y - x) \right]. \quad (2.92)$$

We now consider the \mathcal{G} -part of the integral in the Σ -equation, Eq. (2.84):

$$I_{\mathcal{G}} \equiv -\frac{i\alpha}{16\pi^3} \int d^4k \frac{\mathcal{F}(k^2)}{k^2 - \Sigma^2(k^2)} \frac{\mathcal{G}(q^2)}{q^2} \left(g_{\nu\mu} - \frac{q_\nu q_\mu}{q^2} \right) T_{\mathcal{G}}^{\mu\nu} \quad (2.93)$$

where we defined $T_{\mathcal{G}}^{\mu\nu}$ in Eq. (2.85) as:

$$T_{\mathcal{G}}^{\mu\nu} \equiv \text{Tr} \left[\gamma^\mu (\not{k} + \Sigma(k^2)) \Gamma_{\text{CP}}^\nu(k, p) \right]. \quad (2.94)$$

In contrast to the ξ -part of the Σ -equation, the \mathcal{G} -part depends on the specific vertex Ansatz used. We recall the CP-vertex, Eq. (2.77):

$$\begin{aligned} \Gamma_{\text{CP}}^\mu(k, p) &= A(k^2, p^2) \gamma^\mu + B(k^2, p^2) (k+p)^\mu (\not{k} + \not{p}) + C(k^2, p^2) (k+p)^\mu \\ &\quad + \tau_6(k^2, p^2) \left[\gamma^\mu (k^2 - p^2) - (k+p)^\mu (\not{k} - \not{p}) \right] \end{aligned} \quad (2.95)$$

where we define:

$$\begin{aligned} A(k^2, p^2) &\equiv \frac{1}{2} \left[\frac{1}{\mathcal{F}(k^2)} + \frac{1}{\mathcal{F}(p^2)} \right] \\ B(k^2, p^2) &\equiv \frac{1}{2(k^2 - p^2)} \left[\frac{1}{\mathcal{F}(k^2)} - \frac{1}{\mathcal{F}(p^2)} \right] \\ C(k^2, p^2) &\equiv -\frac{1}{k^2 - p^2} \left[\frac{\Sigma(k^2)}{\mathcal{F}(k^2)} - \frac{\Sigma(p^2)}{\mathcal{F}(p^2)} \right] \\ \tau_6(k^2, p^2) &\equiv \frac{(k^2 + p^2)}{2 \left[(k^2 - p^2)^2 + (\Sigma^2(k^2) + \Sigma^2(p^2)) \right]} \left[\frac{1}{\mathcal{F}(k^2)} - \frac{1}{\mathcal{F}(p^2)} \right]. \end{aligned} \quad (2.96)$$

Substituting the CP-vertex, Eq. (2.95), in Eq. (2.94) and computing the traces using Eq. (2.48) yields:

$$\begin{aligned} T_{\mathcal{G}}^{\mu\nu} &= 4\Sigma(k^2) \left\{ A(k^2, p^2) g^{\mu\nu} + B(k^2, p^2) (k+p)^\mu (k+p)^\nu \right. \\ &\quad \left. + \tau_6(k^2, p^2) \left[(k^2 - p^2) g^{\mu\nu} - (k-p)^\mu (k+p)^\nu \right] \right\} + 4C(k^2, p^2) k^\mu (k+p)^\nu. \end{aligned} \quad (2.97)$$

We now contract $T_{\mathcal{G}}^{\mu\nu}$ with the transverse tensor, $g_{\mu\nu} - q_\mu q_\nu / q^2$, of the photon propagator. This gives:

$$\begin{aligned} \left(g_{\mu\nu} - \frac{q_\mu q_\nu}{q^2} \right) T_{\mathcal{G}}^{\mu\nu} &= 4 \left\{ 3\Sigma(k^2) \left[A(k^2, p^2) + \tau_6(k^2, p^2) (k^2 - p^2) \right] \right. \\ &\quad \left. + 2 \left[2B(k^2, p^2) \Sigma(k^2) + C(k^2, p^2) \right] \left[\frac{k^2 p^2 - (k \cdot p)^2}{q^2} \right] \right\}. \end{aligned} \quad (2.98)$$

Substituting Eq. (2.98) in the integral, Eq. (2.93), we find:

$$I_G = -\frac{i\alpha}{4\pi^3} \int d^4k \frac{\mathcal{F}(k^2)}{k^2 - \Sigma^2(k^2)} \frac{\mathcal{G}(q^2)}{q^2} \left\{ 3\Sigma(k^2) \left[A(k^2, p^2) + \tau_6(k^2, p^2)(k^2 - p^2) \right] \right. \\ \left. + 2 \left[2B(k^2, p^2)\Sigma(k^2) + C(k^2, p^2) \right] \left[\frac{k^2 p^2 - (k.p)^2}{q^2} \right] \right\}. \quad (2.99)$$

We now perform a Wick rotation to Euclidean space. Note, from Eq. (2.96), that $A \rightarrow A$, $B \rightarrow -B$, $C \rightarrow -C$ and $\tau_6 \rightarrow -\tau_6$. This gives:

$$I_G = \frac{\alpha}{4\pi^3} \int d^4k \frac{\mathcal{F}(k^2)}{k^2 + \Sigma^2(k^2)} \frac{\mathcal{G}(q^2)}{q^2} \left\{ 3\Sigma(k^2) \left[A(k^2, p^2) + \tau_6(k^2, p^2)(k^2 - p^2) \right] \right. \\ \left. + 2 \left[2B(k^2, p^2)\Sigma(k^2) + C(k^2, p^2) \right] \left[\frac{k^2 p^2 - (k.p)^2}{q^2} \right] \right\}. \quad (2.100)$$

Introducing spherical coordinates and defining $x = p^2$, $y = k^2$, $z = q^2$ yields:

$$I_G = \frac{\alpha}{2\pi^2} \int dy \frac{y\mathcal{F}(y)}{y + \Sigma^2(y)} \int d\theta \sin^2 \theta \frac{\mathcal{G}(z)}{z} \left\{ 3\Sigma(y) \left[A(y, x) + \tau_6(y, x)(y - x) \right] \right. \\ \left. + [2B(y, x)\Sigma(y) + C(y, x)] \frac{2yx \sin^2 \theta}{z} \right\}. \quad (2.101)$$

From Eq. (2.96) we check that:

$$2B(y, x)\Sigma(y) + C(y, x) = -\frac{1}{\mathcal{F}(x)} \left[\frac{\Sigma(y) - \Sigma(x)}{y - x} \right]. \quad (2.102)$$

Substituting Eqs. (2.92, 2.101, 2.102) in the Σ -equation, Eq. (2.84), yields:

$$\boxed{\begin{aligned} \frac{\Sigma(x)}{\mathcal{F}(x)} &= m_0 + \frac{\alpha}{2\pi^2} \int dy \frac{y\mathcal{F}(y)}{y + \Sigma^2(y)} \int d\theta \sin^2 \theta \frac{\mathcal{G}(z)}{z} \\ &\times \left\{ 3\Sigma(y) \left[A(y, x) + \tau_6(y, x)(y - x) \right] - \frac{1}{\mathcal{F}(x)} \left[\frac{\Sigma(y) - \Sigma(x)}{y - x} \right] \frac{2yx \sin^2 \theta}{z} \right\} \\ &+ \frac{\alpha\xi}{4\pi\mathcal{F}(x)} \int dy \frac{\mathcal{F}(y)}{y + \Sigma^2(y)} \left[\frac{y\Sigma(y)}{x} \theta(x - y) + \Sigma(x)\theta(y - x) \right]. \end{aligned}} \quad (2.103)$$

Next, we derive the \mathcal{F} -equation in a similar way. Substituting the self-energy, Eq. (2.82), in the \mathcal{F} -equation, Eq. (2.35), and introducing $\alpha \equiv e^2/4\pi$ we have

$$\frac{1}{\mathcal{F}(p^2)} = 1 + \frac{i\alpha}{16p^2\pi^3} \int d^4k \left\{ \frac{\mathcal{G}(q^2)}{q^2} \left(g_{\nu\mu} - \frac{q_\nu q_\mu}{q^2} \right) \text{Tr} \left[\not{p} \gamma^\mu S(k) \Gamma_{\text{CP}}^\nu(k, p) \right] - \frac{\xi}{q^4} \text{Tr} \left[\not{p} \not{q} S(k) S^{-1}(p) \right] \right\}. \quad (2.104)$$

After introducing the fermion propagator, Eq. (2.21), in Eq. (2.104) we find:

$$\frac{1}{\mathcal{F}(p^2)} = 1 + \frac{i\alpha}{16p^2\pi^3} \int d^4k \frac{\mathcal{F}(k^2)}{k^2 - \Sigma^2(k^2)} \left\{ \frac{\mathcal{G}(q^2)}{q^2} \left(g_{\nu\mu} - \frac{q_\nu q_\mu}{q^2} \right) T_G^{\mu\nu} - \frac{\xi}{\mathcal{F}(p^2)q^4} T_\xi \right\} \quad (2.105)$$

where we defined the traces:

$$T_G^{\mu\nu} \equiv \text{Tr} \left[\not{p} \gamma^\mu (\not{k} + \Sigma(k^2)) \Gamma_{\text{CP}}^\nu(k, p) \right] \quad (2.106)$$

$$T_\xi \equiv \text{Tr} \left[\not{p} \not{q} (\not{k} + \Sigma(k^2)) (\not{p} - \Sigma(p^2)) \right]. \quad (2.107)$$

We first compute the ξ -part of the integral in Eq. (2.105), which we call I_ξ :

$$I_\xi \equiv -\frac{i\alpha\xi}{16p^2\mathcal{F}(p^2)\pi^3} \int d^4k \frac{\mathcal{F}(k^2)}{(k^2 - \Sigma^2(k^2))q^4} T_\xi. \quad (2.108)$$

We compute the trace, Eq. (2.107), using Eq. (2.48) and substitute $q = k - p$:

$$T_\xi = 4 \left[p^2(k^2 - k.p) - \Sigma(k^2)\Sigma(p^2)(k.p - p^2) \right]. \quad (2.109)$$

Substituting this trace in Eq. (2.108) gives:

$$I_\xi = -\frac{i\alpha\xi}{4\pi^3\mathcal{F}(p^2)} \int d^4k \frac{\mathcal{F}(k^2)}{(k^2 - \Sigma^2(k^2))q^4} \left[k^2 - k.p - \Sigma(k^2)\Sigma(p^2) \left(\frac{k.p}{p^2} - 1 \right) \right]. \quad (2.110)$$

After performing a Wick rotation on Eq. (2.110), we find in Euclidean space:

$$I_\xi = \frac{\alpha\xi}{4\pi^3\mathcal{F}(p^2)} \int d^4k \frac{\mathcal{F}(k^2)}{(k^2 + \Sigma^2(k^2))q^4} \left[k^2 - k.p + \Sigma(k^2)\Sigma(p^2) \left(\frac{k.p}{p^2} - 1 \right) \right]. \quad (2.111)$$

We can now change the integration variables to spherical coordinates, again introducing $x = p^2$, $y = k^2$ and $z = q^2$. This gives:

$$I_\xi = \frac{\alpha\xi}{2\pi^2\mathcal{F}(x)} \int dy \frac{y\mathcal{F}(y)}{y + \Sigma^2(y)} \int d\theta \frac{\sin^2\theta}{z^2} \left[y - \sqrt{yx} \cos\theta + \Sigma(y)\Sigma(x) \left(\sqrt{\frac{y}{x}} \cos\theta - 1 \right) \right]. \quad (2.112)$$

The angular integrals of Eq. (2.112) can be computed analytically and are given in Appendix A.

Substituting Eqs. (A.2, A.5) in Eq. (2.112) yields:

$$I_\xi = -\frac{\alpha\xi}{4\pi\mathcal{F}(x)} \int dy \frac{\mathcal{F}(y)}{y + \Sigma^2(y)} \left[\frac{y\Sigma(y)\Sigma(x)}{x^2} \theta(x - y) - \theta(y - x) \right]. \quad (2.113)$$

Next, we consider the \mathcal{G} -part of the integral in Eq. (2.105):

$$I_G \equiv \frac{i\alpha}{16p^2\pi^3} \int d^4k \frac{\mathcal{F}(k^2)}{k^2 - \Sigma^2(k^2)} \frac{\mathcal{G}(q^2)}{q^2} \left(g_{\nu\mu} - \frac{q_\nu q_\mu}{q^2} \right) T_G^{\mu\nu} \quad (2.114)$$

where the trace $T_G^{\mu\nu}$ has been defined in Eq. (2.106) as:

$$T_G^{\mu\nu} = \text{Tr} \left[\not{p} \gamma^\mu (\not{k} + \Sigma(k^2)) \Gamma_{\text{CP}}^\nu(k, p) \right]. \quad (2.115)$$

Substituting the vertex expression, Eq. (2.95), in Eq. (2.115), and computing the traces using Eq. (2.48), gives:

$$\begin{aligned} T_G^{\mu\nu} &= 4A(k^2, p^2)(p^\mu k^\nu + p^\nu k^\mu - k.p g^{\mu\nu}) + 4B(k^2, p^2)(k+p)^\nu(p^2 k^\mu + k^2 p^\mu) \\ &+ 4\tau_6(k^2, p^2) \left[(k-p)^\mu(p^2 k^\nu + k^2 p^\nu) - (k^2 - p^2)k.p g^{\mu\nu} \right] + 4C(k^2, p^2)\Sigma(k^2)p^\mu(k+p)^\nu. \end{aligned} \quad (2.116)$$

We now contract $T_G^{\mu\nu}$ of Eq. (2.116) with the transverse tensor $g_{\mu\nu} - q_\mu q_\nu / q^2$ and substitute $q = k - p$. This gives:

$$\begin{aligned} \left(g_{\mu\nu} - \frac{q_\mu q_\nu}{q^2} \right) T_G^{\mu\nu} &= 4 \left\{ A(k^2, p^2) \left[2 \left(\frac{k^2 p^2 - (k.p)^2}{q^2} \right) - 3k.p \right] \right. \\ &\left. + 2 \left[B(k^2, p^2)(k^2 + p^2) + C(k^2, p^2)\Sigma(k^2) \right] \left(\frac{k^2 p^2 - (k.p)^2}{q^2} \right) - 3\tau_6(k^2, p^2)(k^2 - p^2)k.p \right\}. \end{aligned} \quad (2.117)$$

Substituting Eq. (2.117) in the integral Eq. (2.114) yields:

$$\begin{aligned} I_G &= \frac{i\alpha}{4p^2\pi^3} \int d^4k \frac{\mathcal{F}(k^2)}{k^2 - \Sigma^2(k^2)} \frac{\mathcal{G}(q^2)}{q^2} \left\{ A(k^2, p^2) \left[2 \left(\frac{k^2 p^2 - (k.p)^2}{q^2} \right) - 3k.p \right] \right. \\ &\left. + 2 \left[B(k^2, p^2)(k^2 + p^2) + C(k^2, p^2)\Sigma(k^2) \right] \left(\frac{k^2 p^2 - (k.p)^2}{q^2} \right) - 3\tau_6(k^2, p^2)(k^2 - p^2)k.p \right\}. \end{aligned} \quad (2.118)$$

After a Wick rotation to Euclidean space, Eq. (2.118) becomes:

$$\begin{aligned} I_G &= -\frac{\alpha}{4p^2\pi^3} \int d^4k \frac{\mathcal{F}(k^2)}{k^2 + \Sigma^2(k^2)} \frac{\mathcal{G}(q^2)}{q^2} \left\{ A(k^2, p^2) \left[2 \left(\frac{k^2 p^2 - (k.p)^2}{q^2} \right) - 3k.p \right] \right. \\ &\left. + 2 \left[B(k^2, p^2)(k^2 + p^2) - C(k^2, p^2)\Sigma(k^2) \right] \left(\frac{k^2 p^2 - (k.p)^2}{q^2} \right) - 3\tau_6(k^2, p^2)(k^2 - p^2)k.p \right\}. \end{aligned} \quad (2.119)$$

Introducing spherical coordinates and defining $x = p^2$, $y = k^2$, $z = q^2$ yields:

$$\begin{aligned} I_G &= -\frac{\alpha}{2x\pi^2} \int dy \frac{y\mathcal{F}(y)}{y + \Sigma^2(y)} \int d\theta \sin^2 \theta \frac{\mathcal{G}(z)}{z} \left\{ A(y, x) \left[\frac{2yx \sin^2 \theta}{z} - 3\sqrt{yx} \cos \theta \right] \right. \\ &\left. + [B(y, x)(y + x) - C(y, x)\Sigma(y)] \left(\frac{2yx \sin^2 \theta}{z} \right) - 3\tau_6(y, x)(y - x) \sqrt{yx} \cos \theta \right\}. \end{aligned} \quad (2.120)$$

Substituting Eqs. (2.113, 2.120) in the \mathcal{F} -equation, Eq. (2.105), finally gives:

$$\begin{aligned}
\frac{1}{\mathcal{F}(x)} &= 1 - \frac{\alpha}{2x\pi^2} \int dy \frac{y\mathcal{F}(y)}{y + \Sigma^2(y)} \int d\theta \sin^2 \theta \frac{\mathcal{G}(z)}{z} \\
&\times \left\{ A(y, x) \left[\frac{2yx \sin^2 \theta}{z} - 3\sqrt{yx} \cos \theta \right] \right. \\
&+ [B(y, x)(y + x) - C(y, x)\Sigma(y)] \frac{2yx \sin^2 \theta}{z} - 3\tau_6(y, x)(y - x) \sqrt{yx} \cos \theta \left. \right\} \\
&- \frac{\alpha\xi}{4\pi\mathcal{F}(x)} \int dy \frac{\mathcal{F}(y)}{y + \Sigma^2(y)} \left[\frac{y\Sigma(y)\Sigma(x)}{x^2} \theta(x - y) - \theta(y - x) \right].
\end{aligned} \tag{2.121}$$

2.7.2 The photon equation

We will now derive the integral equation for the photon renormalization function using the Curtis-Pennington vertex Ansatz. We introduce the CP-vertex in the integral equation for \mathcal{G} , Eq. (2.41):

$$\frac{1}{\mathcal{G}(q^2)} = 1 - \frac{iN_f e^2 \mathcal{P}_{\mu\nu}}{3(2\pi)^4 q^2} \int d^4k \operatorname{Tr} \left[\gamma^\mu S(k) \Gamma_{\text{CP}}^\nu(k, p) S(p) \right]. \tag{2.122}$$

When substituting the fermion propagator, Eq. (2.21), in Eq. (2.122), we find:

$$\frac{1}{\mathcal{G}(q^2)} = 1 - \frac{iN_f e^2}{3(2\pi)^4 q^2} \int d^4k \frac{\mathcal{F}(k^2)\mathcal{F}(p^2)}{(k^2 - \Sigma^2(k^2))(p^2 - \Sigma^2(p^2))} \mathcal{P}_{\mu\nu} T^{\mu\nu} \tag{2.123}$$

where

$$T^{\mu\nu} \equiv \operatorname{Tr} \left[\gamma^\mu (\not{k} + \Sigma(k^2)) \Gamma_{\text{CP}}^\nu(k, p) (\not{p} + \Sigma(p^2)) \right]. \tag{2.124}$$

Now, insert the CP-vertex, Eq. (2.95) in Eq. (2.124):

$$\begin{aligned}
T^{\mu\nu} &= 4 \left\{ A(k^2, p^2) \left[k^\mu p^\nu + p^\mu k^\nu - k \cdot p g^{\mu\nu} + \Sigma(k^2)\Sigma(p^2) g^{\mu\nu} \right] \right. \\
&+ B(k^2, p^2) \left[p^2 k^\mu + k^2 p^\mu + \Sigma(k^2)\Sigma(p^2)(k + p)^\mu \right] (k + p)^\nu \\
&+ C(k^2, p^2) \left[\Sigma(p^2)k^\mu + \Sigma(k^2)p^\mu \right] (k + p)^\nu \\
&+ \tau_6(k^2, p^2) \left[(k - p)^\mu (k^2 p^\nu + p^2 k^\nu) - (k^2 - p^2)k \cdot p g^{\mu\nu} \right. \\
&\quad \left. + \Sigma(k^2)\Sigma(p^2)((k^2 - p^2) g^{\mu\nu} - (k - p)^\mu (k + p)^\nu) \right] \left. \right\}.
\end{aligned} \tag{2.125}$$

When contracting $T^{\mu\nu}$ with the operator $\mathcal{P}_{\mu\nu} = g_{\mu\nu} - nq_\mu q_\nu / q^2$ and substituting $p = k - q$, we

find:

$$\begin{aligned}
\mathcal{P}_{\mu\nu}T^{\mu\nu} = & 4 \left\{ A(k^2, p^2) \left[(n-2)k^2 + (n+2)k \cdot q - \frac{2n(k \cdot q)^2}{q^2} + (4-n)\Sigma(k^2)\Sigma(p^2) \right] \right. \\
& + B(k^2, p^2) \left[(k^2 + p^2 + 2\Sigma(k^2)\Sigma(p^2)) \left(2k^2 - \frac{2n(k \cdot q)^2}{q^2} + (n-1)k \cdot q \right) \right. \\
& \quad \left. \left. + (n-1)(k^2 - p^2)(k^2 + \Sigma(k^2)\Sigma(p^2)) \right] \right. \\
& + C(k^2, p^2) \left[(\Sigma(k^2) + \Sigma(p^2)) \left(2k^2 - \frac{2n(k \cdot q)^2}{q^2} + (n-1)k \cdot q \right) \right. \\
& \quad \left. \left. + (n-1)(k^2 - p^2)\Sigma(k^2) \right] \right. \\
& \left. - 3\tau_6(k^2, p^2)(k^2 - p^2)(k^2 - k \cdot q - \Sigma(k^2)\Sigma(p^2)) \right\}. \tag{2.126}
\end{aligned}$$

Now, substitute Eq. (2.126) in the \mathcal{G} -equation, Eq. (2.123):

$$\begin{aligned}
\frac{1}{\mathcal{G}(q^2)} = & 1 - \frac{4iN_f e^2}{3(2\pi)^4 q^2} \int d^4k \frac{\mathcal{F}(k^2)\mathcal{F}(p^2)}{(k^2 - \Sigma^2(k^2))(p^2 - \Sigma^2(p^2))} \\
& \times \left\{ A(k^2, p^2) \left[(n-2)k^2 + (n+2)k \cdot q - \frac{2n(k \cdot q)^2}{q^2} + (4-n)\Sigma(k^2)\Sigma(p^2) \right] \right. \\
& + B(k^2, p^2) \left[(k^2 + p^2 + 2\Sigma(k^2)\Sigma(p^2)) \left(2k^2 - \frac{2n(k \cdot q)^2}{q^2} + (n-1)k \cdot q \right) \right. \\
& \quad \left. \left. + (n-1)(k^2 - p^2)(k^2 + \Sigma(k^2)\Sigma(p^2)) \right] \right. \\
& + C(k^2, p^2) \left[(\Sigma(k^2) + \Sigma(p^2)) \left(2k^2 - \frac{2n(k \cdot q)^2}{q^2} + (n-1)k \cdot q \right) \right. \\
& \quad \left. \left. + (n-1)(k^2 - p^2)\Sigma(k^2) \right] \right. \\
& \left. - 3\tau_6(k^2, p^2)(k^2 - p^2)(k^2 - k \cdot q - \Sigma(k^2)\Sigma(p^2)) \right\}. \tag{2.127}
\end{aligned}$$

After performing a Wick rotation to Euclidean space, Eq. (2.127) becomes:

$$\begin{aligned}
\frac{1}{\mathcal{G}(q^2)} &= 1 + \frac{4N_f e^2}{3(2\pi)^4 q^2} \int d^4 k \frac{\mathcal{F}(k^2)\mathcal{F}(p^2)}{(k^2 + \Sigma^2(k^2))(p^2 + \Sigma^2(p^2))} \\
&\times \left\{ A(k^2, p^2) \left[(n-2)k^2 + (n+2)k \cdot q - \frac{2n(k \cdot q)^2}{q^2} - (4-n)\Sigma(k^2)\Sigma(p^2) \right] \right. \\
&+ B(k^2, p^2) \left[(k^2 + p^2 - 2\Sigma(k^2)\Sigma(p^2)) \left(2k^2 - \frac{2n(k \cdot q)^2}{q^2} + (n-1)k \cdot q \right) \right. \\
&\quad \left. \left. + (n-1)(k^2 - p^2)(k^2 - \Sigma(k^2)\Sigma(p^2)) \right] \right. \\
&- C(k^2, p^2) \left[(\Sigma(k^2) + \Sigma(p^2)) \left(2k^2 - \frac{2n(k \cdot q)^2}{q^2} + (n-1)k \cdot q \right) \right. \\
&\quad \left. \left. + (n-1)(k^2 - p^2)\Sigma(k^2) \right] \right. \\
&\left. - 3\tau_6(k^2, p^2)(k^2 - p^2)(k^2 - k \cdot q + \Sigma(k^2)\Sigma(p^2)) \right\}. \tag{2.128}
\end{aligned}$$

Finally, we introduce spherical coordinates and substitute $\alpha = e^2/4\pi$ in Eq. (2.128). The equation for the photon renormalization function \mathcal{G} becomes:

$$\begin{aligned}
\frac{1}{\mathcal{G}(x)} &= 1 + \frac{2N_f \alpha}{3\pi^2 x} \int dy \frac{y\mathcal{F}(y)}{y + \Sigma^2(y)} \int d\theta \sin^2 \theta \frac{\mathcal{F}(z)}{z + \Sigma^2(z)} \\
&\times \left\{ A(y, z) \left[(n-2)y + (n+2)\sqrt{yx} \cos \theta - 2ny \cos^2 \theta - (4-n)\Sigma(y)\Sigma(z) \right] \right. \\
&+ B(y, z) \left[(y + z - 2\Sigma(y)\Sigma(z)) (2y - 2ny \cos^2 \theta + (n-1)\sqrt{yx} \cos \theta) \right. \\
&\quad \left. \left. + (n-1)(y-z)(y - \Sigma(y)\Sigma(z)) \right] \right. \\
&- C(y, z) \left[(\Sigma(y) + \Sigma(z)) (2y - 2ny \cos^2 \theta + (n-1)\sqrt{yx} \cos \theta) \right. \\
&\quad \left. \left. + (n-1)(y-z)\Sigma(y) \right] \right. \\
&\left. - 3\tau_6(y, z)(y-z)(y - \sqrt{yx} \cos \theta + \Sigma(y)\Sigma(z)) \right\}. \tag{2.129}
\end{aligned}$$

As discussed in Section 2.5.2, if we take $n = 4$ in the operator $\mathcal{P}_{\mu\nu}$, the vacuum polarization

integral should be free of quadratic divergences. Then, Eq. (2.129) becomes:

$$\begin{aligned}
\frac{1}{\mathcal{G}(x)} &= 1 + \frac{2N_f\alpha}{3\pi^2x} \int dy \frac{y\mathcal{F}(y)}{y + \Sigma^2(y)} \int d\theta \sin^2 \theta \frac{\mathcal{F}(z)}{z + \Sigma^2(z)} \\
&\times \left\{ 2A(y, z) \left[y(1 - y \cos^2 \theta) + 3\sqrt{yx} \cos \theta \right] \right. \\
&\quad + B(y, z) \left[(y + z - 2\Sigma(y)\Sigma(z)) (2y(1 - 4 \cos^2 \theta) + 3\sqrt{yx} \cos \theta) \right. \\
&\quad \quad \left. \left. + 3(y - z)(y - \Sigma(y)\Sigma(z)) \right] \right. \\
&\quad - C(y, z) \left[(\Sigma(y) + \Sigma(z)) (2y(1 - 4 \cos^2 \theta) + 3\sqrt{yx} \cos \theta) + 3(y - z)\Sigma(y) \right] \\
&\quad \left. - 3\tau_6(y, z)(y - z)(y - \sqrt{yx} \cos \theta + \Sigma(y)\Sigma(z)) \right\}.
\end{aligned} \tag{2.130}$$

2.7.3 Summary

The set of coupled integral equations (in Euclidean space) using the Curtis-Pennington vertex Ansatz, Eqs. (2.103, 2.121, 2.130) are now summarized:

$$\begin{aligned} \frac{\Sigma(x)}{\mathcal{F}(x)} &= m_0 + \frac{\alpha}{2\pi^2} \int dy \frac{y\mathcal{F}(y)}{y + \Sigma^2(y)} \int d\theta \sin^2 \theta \frac{\mathcal{G}(z)}{z} \\ &\times \left\{ 3\Sigma(y) [A(y, x) + \tau_6(y, x)(y - x)] - \frac{1}{\mathcal{F}(x)} \left[\frac{\Sigma(y) - \Sigma(x)}{y - x} \right] \frac{2yx \sin^2 \theta}{z} \right\} \\ &+ \frac{\alpha\xi}{4\pi\mathcal{F}(x)} \int dy \frac{\mathcal{F}(y)}{y + \Sigma^2(y)} \left[\frac{y\Sigma(y)}{x} \theta(x - y) + \Sigma(x)\theta(y - x) \right] \end{aligned} \quad (2.131)$$

$$\begin{aligned} \frac{1}{\mathcal{F}(x)} &= 1 - \frac{\alpha}{2x\pi^2} \int dy \frac{y\mathcal{F}(y)}{y + \Sigma^2(y)} \int d\theta \sin^2 \theta \frac{\mathcal{G}(z)}{z} \\ &\times \left\{ A(y, x) \left[\frac{2yx \sin^2 \theta}{z} - 3\sqrt{yx} \cos \theta \right] \right. \\ &+ [B(y, x)(y + x) - C(y, x)\Sigma(y)] \frac{2yx \sin^2 \theta}{z} - 3\tau_6(y, x)(y - x) \sqrt{yx} \cos \theta \left. \right\} \\ &- \frac{\alpha\xi}{4\pi\mathcal{F}(x)} \int dy \frac{\mathcal{F}(y)}{y + \Sigma^2(y)} \left[\frac{y\Sigma(y)\Sigma(x)}{x^2} \theta(x - y) - \theta(y - x) \right] \end{aligned} \quad (2.132)$$

$$\begin{aligned} \frac{1}{\mathcal{G}(x)} &= 1 + \frac{2N_f\alpha}{3\pi^2x} \int dy \frac{y\mathcal{F}(y)}{y + \Sigma^2(y)} \int d\theta \sin^2 \theta \frac{\mathcal{F}(z)}{z + \Sigma^2(z)} \\ &\times \left\{ 2A(y, z) [y(1 - y \cos^2 \theta) + 3\sqrt{yx} \cos \theta] \right. \\ &+ B(y, z) \left[(y + z - 2\Sigma(y)\Sigma(z)) (2y(1 - 4 \cos^2 \theta) + 3\sqrt{yx} \cos \theta) \right. \\ &\quad \left. \left. + 3(y - z)(y - \Sigma(y)\Sigma(z)) \right] \right. \\ &- C(y, z) \left[(\Sigma(y) + \Sigma(z)) (2y(1 - 4 \cos^2 \theta) + 3\sqrt{yx} \cos \theta) + 3(y - z)\Sigma(y) \right] \\ &\left. - 3\tau_6(y, z)(y - z)(y - \sqrt{yx} \cos \theta + \Sigma(y)\Sigma(z)) \right\} \end{aligned} \quad (2.133)$$

$$\begin{aligned} \text{where} \quad A(y, x) &= \frac{1}{2} \left[\frac{1}{\mathcal{F}(y)} + \frac{1}{\mathcal{F}(x)} \right] \\ B(y, x) &= \frac{1}{2(y - x)} \left[\frac{1}{\mathcal{F}(y)} - \frac{1}{\mathcal{F}(x)} \right] \\ C(y, x) &= -\frac{1}{y - x} \left[\frac{\Sigma(y)}{\mathcal{F}(y)} - \frac{\Sigma(x)}{\mathcal{F}(x)} \right] \\ \tau_6(y, x) &= \frac{y + x}{2[(y - x)^2 + (\Sigma^2(y) + \Sigma^2(x))^2]} \left[\frac{1}{\mathcal{F}(y)} - \frac{1}{\mathcal{F}(x)} \right]. \end{aligned} \quad (2.134)$$

Chapter 3

Fermion mass generation in quenched QED

3.1 Introduction

In the previous chapter we derived the system of equations describing the dynamical generation of fermion mass in QED. To truncate the infinite set of integral equations we introduced a suitable vertex Ansatz which reduces the system of equations to three integral equations relating Σ , \mathcal{F} and \mathcal{G} . A way to reduce the number of simultaneous equations even more is to consider what is called the *quenched* approximation to QED. In this approximation the full photon propagator is replaced by the bare one, neglecting any fermion loops, and the two fermion equations now form an independent system of two coupled integral equations for Σ and \mathcal{F} .

Formally, this approximation is obtained by setting the number of flavours N_f equal to zero. Then, the vacuum polarization contribution to the photon propagator, Eq. (2.24), will vanish and the full photon propagator will be identical to the bare one. In this way the photon equation is now decoupled from the fermion equation and the photon propagator occurring in the fermion self-energy integral, Eq. (2.36), is known. Although it can seem bizarre to put $N_f \equiv 0$ and still consider the behaviour of the fermion propagator and its self-energy, this limit is mathematically perfectly sound (in the same way as N_f could be given any non-integer value) as N_f is a free parameter, which occurs only in the photon equation, while it is absent from the fermion equation. However, one can wonder to what extent the results obtained in the quenched approximation will reflect the physical reality of the theory with one or more fermion flavours. In this context it is useful to note that in gauge theories, the coupling will run with momentum as a consequence of quantum corrections. This, in turn, brings about the need to renormalize

the theory. It is exactly this renormalization procedure which introduces a scale in the theory, to which the generated fermion mass will be related. An important consequence of quenching the theory is that the running of the coupling disappears, the coupling in quenched QED is constant and no renormalization is needed. It is therefore not clear what can set the scale of the generated fermion mass, other than the ultraviolet cutoff, in quenched QED without bare mass.

3.2 Bare vertex

In the simplest calculation in quenched QED, we replace the full vertex $\Gamma^\mu(k, p)$ by the bare vertex γ^μ . This is called the *rainbow* approximation, which is obvious if we look at the Feynman diagram decomposition of the fermion self-energy $E_f(p)$ shown in Fig. 3.1. It is well known from the literature that fermion mass is generated dynamically in the Rainbow approximation to QED provided that the coupling is larger than a critical value, which is $\alpha_c = \pi/3$ in the Landau gauge [8, 9, 10, 11]. Because the bare vertex violates the Ward-Takahashi identity, the critical coupling varies wildly if we go to other gauges as shown in Ref. [28] by Curtis and Pennington. They find $\alpha_c = 1.69$ in the Feynman gauge ($\xi = 1$) and $\alpha_c = 2.04$ in the Yennie gauge ($\xi = 3$). Because of this strong dependence of α_c on the covariant gauge parameter, we will investigate the behaviour of the critical coupling using the Curtis-Pennington vertex Ansatz in the next section.

$$E_f(p) = \text{---} \text{---} \text{---} + \text{---} \text{---} \text{---} + \text{---} \text{---} \text{---} + \dots$$

Figure 3.1: Fermion self-energy in the rainbow approximation.

Comparing these results with those of numerical lattice studies is not straightforward. In fact the study of the SD equations of quenched QED shows that the large anomalous dimension of the $\bar{\psi}\psi$ operator makes this operator renormalizable [29]. Therefore a four-fermion interaction should in principle be included in the Lagrangian of quenched QED. In Ref. [30] Kondo et al. found the critical line, describing the phase transition in quenched QED, in the (α, G) -plane where α is the usual QED coupling constant and G is the strength of a four-fermion interaction, and in Ref. [31] Bardeen et al. studied the corresponding critical scaling laws. This is important for the comparison with lattice studies as the numerical simulation of quenched non-compact QED appears to automatically incorporate the four-fermion interaction in the calculation. The

lattice calculations also find a phase transition but the critical point is situated somewhere on the critical line [32] rather than in the pure QED point ($G = 0$). Therefore the critical coupling found in the lattice calculations is not directly comparable with the value of $\pi/3$ found in the SD treatment of “pure” quenched QED. This is also true for the scaling law which is of Miransky type for the SD treatment of quenched QED while the power-law scaling in the lattice calculation coincides with a mixture of QED and four fermion interaction. Moreover, there is an additional problem as the chiral limit, $m_0 \rightarrow 0$, can only be retrieved through extrapolation in lattice studies. Recently Kogut et al. [33] have introduced the momentum space lattice method in contrast to the conventional position space formulation. They indicate that the method could avoid the contamination of QED by four-fermion interactions and that it would then be possible to locate the critical point of pure QED.

3.3 Curtis-Pennington vertex

3.3.1 Introduction

In this section we will discuss the dynamical generation of fermion mass in quenched QED with the Curtis-Pennington vertex. This study has been performed independently in Durham and in Groningen and the common results obtained, have been merged and published in *Critical Coupling in Strong QED with Weak Gauge Dependence* by D. Atkinson, J.C.R. Bloch, V.P. Gusynin, M.R. Pennington and M. Reenders in Ref. [34]. As observed by Dong et al. [35], the regularization scheme used in that paper was not translationally invariant and a spurious additional term appeared in the equation for the fermion wavefunction renormalization. In this section we will use the corrected equations.

The Curtis-Pennington vertex not only ensures satisfaction of the Ward-Takahashi identity and avoids singularities that would imply the existence of a scalar, massless particle, but it also respects the requirement of multiplicative renormalizability, a property of exact QED that is destroyed by the rainbow approximation. It agrees moreover with perturbative results in the weak coupling limit.

Our study has been motivated by the previous numerical work performed by Curtis and Pennington in Ref. [28] where the system of non-linear equations for Σ and \mathcal{F} was solved numerically in the Landau, Feynman and Yennie gauge. They find a critical coupling $\alpha_c \approx 0.92$ which is almost exactly gauge independent, in complete contrast to the rainbow approximation. In

Ref. [36] Atkinson et al. use bifurcation analysis to determine the critical coupling analytically using the Curtis-Pennington vertex Ansatz in the Landau gauge. They introduce various approximations to simplify the bifurcation equations and find similar results, although with a much larger inaccuracy, with a critical coupling ranging from 0.910 to 1.047, depending on the approximation.

We will consider the Schwinger-Dyson equations in a general covariant gauge, with the Curtis-Pennington Ansatz, and apply bifurcation analysis to them. This involves calculating the functional derivative of the nonlinear mapping of the mass function into itself. Thanks to the scale-invariance of the problem, the bifurcation equation can be solved by inspection, in the limit that the ultraviolet cutoff is taken to infinity. A solution for the mass function is a power of the momentum that has to satisfy a certain transcendental equation. The onset of criticality is heralded by the coming together of two solutions of this transcendental equation, for that is the indication that oscillatory takes over from non-oscillatory behaviour.

We find the gauge dependence of the critical coupling to be slight, varying by only a few percent over a relatively large range of the gauge parameter. This confirms the previous wholly numerical findings of Curtis and Pennington [28], which covered only small changes of gauge. This weak gauge dependence is in marked contrast to the rainbow approximation, for which the critical coupling changes by 60% between just the Landau and Feynman gauges [28].

3.3.2 Gauge independence of fermion mass and critical coupling

The physical mass of the fermion is defined to be the lowest position at which the denominator function in the fermion propagator,

$$S(p) = \mathcal{F}(p^2) \frac{\gamma^\mu p_\mu + \Sigma(p^2)}{p^2 - \Sigma^2(p^2)},$$

has a zero, which is therefore a solution, m , of

$$m = \Sigma(m^2).$$

On physical grounds, this singularity should be on the real timelike axis of p^2 and should be gauge-independent. When we work in Euclidean space we can either choose to determine the ‘Euclidean mass’, which is the lowest solution of $M = \Sigma(M^2)$, and is not the same as the physical mass m , or one might perhaps take $\Sigma(0)$ as an ersatz *effective mass*. Both approximations are not expected to be exactly gauge-invariant, but one might hope them to be approximately so, on

the grounds that they should be close to the physical mass m , which is gauge-invariant, at least in exact QED, or in a quenched approximation in which the first two Ward-Takahashi identities are respected [37].

The value of the wavefunction at an arbitrarily selected renormalization point, μ , is defined to be the wavefunction renormalization constant, which is conventionally dubbed Z_2 :

$$Z_2 = \mathcal{F}(\mu^2).$$

It is convenient to choose the renormalization point to be Euclidean; the renormalized wave function is specified by

$$\tilde{\mathcal{F}}(x) = Z_2^{-1} \mathcal{F}(x). \quad (3.1)$$

The Curtis-Pennington Ansatz defines a renormalizable scheme, so that in it $\tilde{\mathcal{F}}(x)$ has a finite limit as the ultraviolet regularization is removed. The renormalized wavefunction contains no explicit cutoff, but it is dependent on the renormalization point, and on the gauge parameter.

Chiral symmetry breaking occurs if the coupling, α , is greater than a certain critical value, α_c . This critical coupling is potentially a physically measurable quantity, since it signals a change of phase, and so it should be gauge invariant. Although this is not exactly true in the Curtis-Pennington system, it is approximately so. Indeed, the requirement that α_c be gauge-invariant could perhaps be used to specify further the form of the Ansatz for the vertex function. The transverse part of the vertex is not uniquely determined, and the above requirement might with profit be used to refine this transverse part of the vertex as discussed in Ref. [25].

3.3.3 Bifurcation analysis and critical point

The basic coupled integral equations for quenched QED with the Curtis-Pennington vertex Ansatz are now derived by putting $N_f = 0$ in Eqs. (2.131, 2.132, 2.133). The photon equation, Eq. (2.133), yields $\mathcal{G}(x) = 1$, so Eqs. (2.131, 2.132) now become:

$$\begin{aligned} \frac{\Sigma(x)}{\mathcal{F}(x)} &= m_0 + \frac{\alpha}{2\pi^2} \int dy \frac{y\mathcal{F}(y)}{y + \Sigma^2(y)} \int d\theta \frac{\sin^2 \theta}{z} \\ &\quad \times \left\{ 3\Sigma(y) [A(y, x) + \tau_6(y, x)(y - x)] - \frac{1}{\mathcal{F}(x)} \left[\frac{\Sigma(y) - \Sigma(x)}{y - x} \right] \frac{2yx \sin^2 \theta}{z} \right\} \\ &\quad + \frac{\alpha\xi}{4\pi\mathcal{F}(x)} \int dy \frac{\mathcal{F}(y)}{y + \Sigma^2(y)} \left\{ \frac{y\Sigma(y)}{x} \theta(x - y) + \Sigma(x) \theta(y - x) \right\} \end{aligned} \quad (3.2)$$

$$\begin{aligned}
\frac{1}{\mathcal{F}(x)} &= 1 - \frac{\alpha}{2\pi^2 x} \int dy \frac{y\mathcal{F}(y)}{y + \Sigma^2(y)} \int d\theta \sin^2 \theta \\
&\times \left\{ A(y, x) \left[\frac{2yx \sin^2 \theta}{z^2} - \frac{3\sqrt{yx} \cos \theta}{z} \right] \right. \\
&\quad + [B(y, x)(y + x) - C(y, x)\Sigma(y)] \frac{2yx \sin^2 \theta}{z^2} \\
&\quad \left. - \tau_6(y, x)(y - x) \frac{3\sqrt{yx} \cos \theta}{z} \right\} \\
&- \frac{\alpha\xi}{4\pi\mathcal{F}(x)} \int dy \frac{\mathcal{F}(y)}{y + \Sigma^2(y)} \left\{ \frac{y\Sigma(x)\Sigma(y)}{x^2} \theta(x - y) - \theta(y - x) \right\}.
\end{aligned} \tag{3.3}$$

The complicated kernels are explicit functions of Σ and \mathcal{F} . In the quenched case the angular integrals of the fermion equations, Eqs. (3.2, 3.3), can be computed analytically and are given in Appendix A. Substituting Eqs. (A.1, A.3) in Eq. (3.2) and putting the bare mass $m_0 = 0$, yields:

$$\begin{aligned}
\frac{\Sigma(x)}{\mathcal{F}(x)} &= \frac{3\alpha}{8\pi} \int dy \frac{y\mathcal{F}(y)}{y + \Sigma^2(y)} \\
&\times \left\{ 2[A(y, x) + \tau_6(y, x)(y - x)] \Sigma(y) \left[\frac{\theta(x - y)}{x} + \frac{\theta(y - x)}{y} \right] \right. \\
&\quad \left. - \frac{1}{\mathcal{F}(x)} \frac{\Sigma(y) - \Sigma(x)}{y - x} \left[\frac{y}{x} \theta(x - y) + \frac{x}{y} \theta(y - x) \right] \right\} \\
&+ \frac{\alpha\xi}{4\pi\mathcal{F}(x)} \int dy \frac{\mathcal{F}(y)}{y + \Sigma^2(y)} \left\{ \frac{y\Sigma(y)}{x} \theta(x - y) + \Sigma(x) \theta(y - x) \right\}.
\end{aligned} \tag{3.4}$$

When substituting Eqs. (A.3, A.4) in Eq. (3.3), the $A(y, x)$ term vanishes (which is similar to the bare vertex case) and Eq. (3.3) now becomes:

$$\begin{aligned}
\frac{1}{\mathcal{F}(x)} &= 1 - \frac{3\alpha}{8\pi x} \int dy \frac{y\mathcal{F}(y)}{y + \Sigma^2(y)} \\
&\times \left\{ [B(y, x)(y + x) - C(y, x)\Sigma(y) - \tau_6(y, x)(y - x)] \left[\frac{y}{x} \theta(x - y) + \frac{x}{y} \theta(y - x) \right] \right\} \\
&- \frac{\alpha\xi}{4\pi\mathcal{F}(x)} \int dy \frac{\mathcal{F}(y)}{y + \Sigma^2(y)} \left[\frac{y\Sigma(x)\Sigma(y)}{x^2} \theta(x - y) - \theta(y - x) \right].
\end{aligned} \tag{3.5}$$

As can be seen from Eqs. (3.4, 3.5), the complete Curtis-Pennington equations are nonlinear and complicated. Clearly $\Sigma(x) \equiv 0$ is always a possible solution; but it is not the one in which we are interested. However, the equations simplify at the critical point, where a nontrivial solution *bifurcates* away from the trivial one. To investigate this critical point, we have to take the functional derivative of the nonlinear operators with respect to $\Sigma(x)$ and evaluate it at the trivial ‘point’, $\Sigma(x) \equiv 0$. This amounts in fact simply to throwing away all terms

that are quadratic or higher in the mass function. It must be emphasized that this is *not* an approximation: it is a precise manner to locate the critical point by applying bifurcation theory.

We now apply bifurcation analysis to Eqs. (3.4, 3.5). After substitution of the expressions for A , B , C and τ_6 , Eq. (2.134), and neglecting the terms of $\mathcal{O}(\Sigma^2)$, the \mathcal{F} -equation, Eq. (3.5), is reduced to

$$\frac{1}{\mathcal{F}(x)} = 1 + \frac{\alpha\xi}{4\pi} \int_0^{\Lambda^2} \frac{dy}{y} \frac{\mathcal{F}(y)}{\mathcal{F}(x)} \theta(y-x) \quad (3.6)$$

where the UV-cutoff Λ^2 has been introduced to regularize the integral. It is important to note that now the \mathcal{F} -equation is independent of Σ . After multiplying both sides with $\mathcal{F}(x)$ and applying the step function, this gives:

$$\mathcal{F}(x) = 1 - \frac{\alpha\xi}{4\pi} \int_x^{\Lambda^2} dy \frac{\mathcal{F}(y)}{y}. \quad (3.7)$$

It is easy to check that the unique solution to this equation is:

$$\mathcal{F}(x) = \left(\frac{x}{\Lambda^2} \right)^\nu \quad (3.8)$$

where

$$\nu = \frac{\alpha\xi}{4\pi}. \quad (3.9)$$

Next we apply the bifurcation analysis to the Σ -equation, Eq. (3.4), neglecting terms of $\mathcal{O}(\Sigma^2)$, and find:

$$\begin{aligned} \frac{\Sigma(x)}{\mathcal{F}(x)} &= \frac{3\alpha}{8\pi} \int_0^{\Lambda^2} dy \left\{ \left(1 + \frac{\mathcal{F}(y)}{\mathcal{F}(x)} + \frac{y+x}{y-x} \left[1 - \frac{\mathcal{F}(y)}{\mathcal{F}(x)} \right] \right) \Sigma(y) \left[\frac{\theta(x-y)}{x} + \frac{\theta(y-x)}{y} \right] \right. \\ &\quad \left. - \frac{\mathcal{F}(y)}{\mathcal{F}(x)} \frac{\Sigma(y) - \Sigma(x)}{y-x} \left[\frac{y}{x} \theta(x-y) + \frac{x}{y} \theta(y-x) \right] \right\} \\ &\quad + \frac{\alpha\xi}{4\pi} \int_0^{\Lambda^2} \frac{dy}{y} \frac{\mathcal{F}(y)}{\mathcal{F}(x)} \left\{ \frac{y}{x} \Sigma(y) \theta(x-y) + \Sigma(x) \theta(y-x) \right\}. \end{aligned} \quad (3.10)$$

The second term of the ξ -part of Eq. (3.10) is identical to the integral in the \mathcal{F} -equation, Eq. (3.6), and can be replaced by $(1/\mathcal{F}(x) - 1)$. Then, the left hand side of Eq. (3.10) cancels, the integrals are now finite and need not be regularized anymore, as a consequence of the multiplicative renormalizability of the fermion propagator in the Curtis-Pennington approximation. However, the limit $\Lambda \rightarrow \infty$ has to be taken in a proper way to respect the axial current conservation [9, 28, 38]. If not, one will wrongly find that chiral symmetry breaking occurs for all values of the coupling [39]. Therefore the UV-cutoff can only be taken to infinity if the boundary conditions imposed by Eq. (3.10) at $x = \Lambda^2$ are satisfied, as will be ensured later in this section. After

substituting the solution Eq. (3.8) for $\mathcal{F}(x)$ and eliminating α using $\alpha = 4\pi\nu/\xi$, the Σ -equation, Eq. (3.10), becomes:

$$\begin{aligned} \Sigma(x) = & \frac{3\nu}{2\xi} \int_0^\infty dy \left\{ \left(1 + \left(\frac{y}{x} \right)^\nu + \frac{y+x}{y-x} \left[1 - \left(\frac{y}{x} \right)^\nu \right] \right) \Sigma(y) \left[\frac{\theta(x-y)}{x} + \frac{\theta(y-x)}{y} \right] \right. \\ & \left. - \left(\frac{y}{x} \right)^\nu \frac{\Sigma(y) - \Sigma(x)}{y-x} \left[\frac{y}{x} \theta(x-y) + \frac{x}{y} \theta(y-x) \right] \right\} + \nu \int_0^\infty dy \left(\frac{y}{x} \right)^\nu \Sigma(y) \frac{\theta(x-y)}{x}. \end{aligned} \quad (3.11)$$

The last equation is scaling invariant, and is solved by

$$\Sigma(x) = x^{-s} \quad (3.12)$$

as will be shown below.

After substituting Eq. (3.12) in Eq. (3.11) we find:

$$\begin{aligned} x^{-s} = & \frac{3\nu}{2\xi} \int_0^\infty dy \left\{ \left(y^{-s} + \frac{y^{\nu-s}}{x^\nu} + \frac{y+x}{y-x} \left[y^{-s} - \frac{y^{\nu-s}}{x^\nu} \right] \right) \left[\frac{\theta(x-y)}{x} + \frac{\theta(y-x)}{y} \right] \right. \\ & \left. - \left(\frac{y}{x} \right)^\nu \frac{y^{-s} - x^{-s}}{y-x} \left[\frac{y}{x} \theta(x-y) + \frac{x}{y} \theta(y-x) \right] \right\} + \nu \int_0^\infty dy \frac{y^{\nu-s}}{x^{\nu+1}} \theta(x-y). \end{aligned} \quad (3.13)$$

We now divide Eq. (3.13) by x^{-s} , change variables to $t = y/x$, and apply the step functions, giving:

$$\begin{aligned} 1 = & \frac{3\nu}{2\xi} \int_0^1 dt \left\{ [t^{-s} + t^{\nu-s}] + \frac{t^{-s+1} + t^{-s} - 2t^{\nu-s+1} - t^{\nu-s} + t^{\nu+1}}{t-1} \right\} \\ & + \frac{3\nu}{2\xi} \int_1^\infty dt \left\{ [t^{-s-1} + t^{\nu-s-1}] + \frac{t^{-s} + t^{-s-1} - t^{\nu-s} - 2t^{\nu-s-1} + t^{\nu-1}}{t-1} \right\} \\ & + \nu \int_0^1 dt t^{\nu-s}. \end{aligned} \quad (3.14)$$

After putting the terms on a common denominator, we get:

$$\begin{aligned} 1 = & \frac{3\nu}{2\xi} \int_0^1 dt \left\{ \frac{2t^{-s+1} - t^{\nu-s+1} - 2t^{\nu-s} + t^{\nu+1}}{t-1} \right\} \\ & + \frac{3\nu}{2\xi} \int_1^\infty dt \left\{ \frac{2t^{-s} - 3t^{\nu-s-1} + t^{\nu-1}}{t-1} \right\} + \nu \int_0^1 dt t^{\nu-s}. \end{aligned} \quad (3.15)$$

To solve these integrals we will use Eq. (3.231.5) of Ref. [40], which can be written as:

$$\int_0^1 dt \frac{t^{\mu-1} - t^{\nu-1}}{t-1} = \psi(\mu) - \psi(\nu) \quad [\operatorname{Re}(\mu) > 0, \operatorname{Re}(\nu) > 0]. \quad (3.16)$$

From this integral we also derive the following integral:

$$\int_1^\infty du \frac{u^{-\mu} - u^{-\nu}}{u-1} = -\psi(\mu) + \psi(\nu) \quad [\operatorname{Re}(\mu) > 0, \operatorname{Re}(\nu) > 0]. \quad (3.17)$$

To show this, we change variables $t = 1/u$ in Eq. (3.17):

$$\int_1^\infty du \frac{u^{-\mu} - u^{-\nu}}{u-1} = \int_1^0 -\frac{dt}{t^2} \frac{t^\mu - t^\nu}{t^{-1} - 1} = -\int_0^1 dt \frac{t^{\mu-1} - t^{\nu-1}}{t-1} \quad (3.18)$$

and apply Eq. (3.16) to Eq. (3.18), yielding Eq. (3.17).

We now substitute the integral evaluations Eqs. (3.16, 3.17) in Eq. (3.15). This gives:

$$1 = \frac{3\nu}{2\xi} \left[2\psi(-s+2) - \psi(\nu-s+2) - 2\psi(\nu-s+1) + \psi(\nu+2) \right. \\ \left. - 2\psi(s) + 3\psi(-\nu+s+1) - \psi(-\nu+1) \right] + \frac{\nu}{\nu-s+1} \quad (3.19)$$

where the region of the (s, ν) -plane for the convergence of the integrals in Eq. (3.15) is specified by:

$$\begin{aligned} 0 < s < 2 \\ -2 < \nu < 1 \\ -1 < \nu - s < 1. \end{aligned} \quad (3.20)$$

We note that each of these inequalities has one limit imposed by requiring the integrals to be infrared finite, while the other comes from the ultraviolet side.

We now mention two properties of the ψ -function (see Eq. (8.365.1, 8.365.8) of Ref. [40]):

$$\psi(z+1) = \psi(z) + \frac{1}{z} \quad (3.21)$$

$$\psi(1-z) = \psi(z) + \pi \cot z\pi. \quad (3.22)$$

Applying Eqs. (3.21, 3.22) to Eq. (3.19) and bringing the term in the left hand side to the right gives:

$$f(\xi, \nu, s) \equiv \frac{3\nu}{2\xi} \left[2\pi \cot s\pi - \pi \cot \nu\pi + 3\pi \cot(\nu-s)\pi \right. \\ \left. + \frac{2}{1-s} + \frac{1}{\nu+1} + \frac{1}{\nu} - \frac{3}{\nu-s} - \frac{1}{\nu-s+1} \right] - \frac{1-s}{\nu-s+1} = 0. \quad (3.23)$$

This means that Eq. (3.12) is a solution to Eq. (3.11) if s satisfies Eq. (3.23) together with the convergence conditions Eq. (3.20).

In a chosen gauge specified by ξ , this equation defines roots s for any value of the coupling α . Bifurcation occurs when two of these roots (with ν and s satisfying Eq. (3.20)) are equal. Then $\alpha \equiv \alpha_c$. A necessary condition for equality of two roots is $\partial f(\xi, s, \nu)/\partial s = 0$, i.e.

$$g(\xi, s, \nu) \equiv \frac{\partial f(\xi, s, \nu)}{\partial s} = \frac{3\nu}{2\xi} \left[-2\pi^2 \csc^2 s\pi + 3\pi^2 \csc^2(\nu-s)\pi \right. \\ \left. + \frac{2}{(1-s)^2} - \frac{3}{(\nu-s)^2} - \frac{1}{(\nu-s+1)^2} \right] + \frac{\nu}{(\nu-s+1)^2} = 0. \quad (3.24)$$

To find the critical point we have to solve the coupled system of transcendental equations Eqs. (3.23, 3.24) for ν_c and s_c , together with the convergence conditions Eq. (3.20). The numerical program [41] used to solve this system of equations requires a realistic starting guess in order to find the solution. For this purpose, as well as to understand how and when bifurcation happens, it is useful to consider first the situation in the Landau gauge, $\xi = 0$ i.e. $\nu = 0$ and $\nu/\xi = \alpha/4\pi$. Then Eq. (3.23) simplifies to:

$$f(\xi = 0, \nu, s) \equiv f_0(\alpha, s) = \frac{3\alpha}{8\pi} \left[-\pi \cot s\pi + \frac{1}{1-s} + \frac{3}{s} + 1 \right] - 1 = 0, \quad (3.25)$$

and the conditions, Eq. (3.20), with $\nu = 0$, are reduced to $0 < s < 1$.

From the plot of this function for $0 < s < 1$, Fig. 3.2, we see that it has just two real roots in this interval when α is small. As α is increased, they approach one another, becoming equal at criticality. To find this critical point we take the derivative of Eq. (3.25) with respect to s :

$$g(\xi = 0, s, \nu) \equiv g_0(s) = \pi^2 \csc^2 s\pi + \frac{1}{(1-s)^2} - \frac{3}{s^2} = 0. \quad (3.26)$$

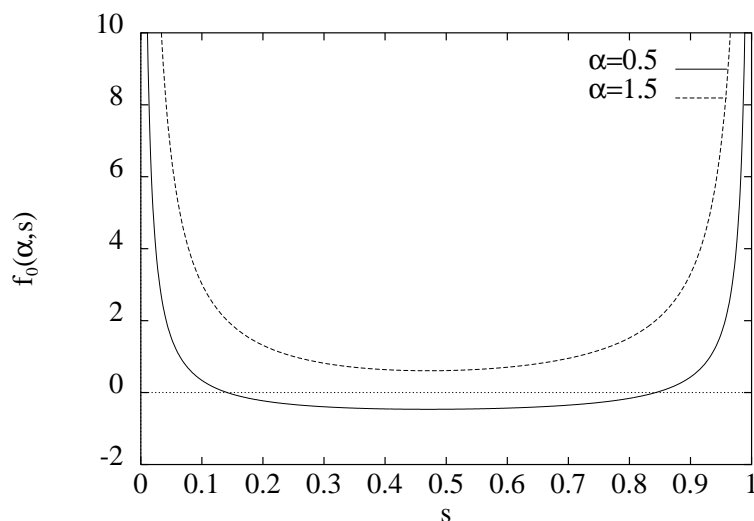


Figure 3.2: Function $f_0(\alpha, s)$ versus exponent s . To satisfy the integral equation Eq. (3.11) in the Landau gauge, the exponent s has to satisfy $f_0(\alpha, s) = 0$.

We plot the function $g_0(s)$ from Eq. (3.26) in Fig. 3.3. Eq. (3.26) is a single transcendental equation which determines the exponent s_c in the critical point. The numerical program used to solve it, finds $s_c = 0.470966$. Substituting this value for s_c in Eq. (3.25) allows us to compute

the value of the critical coupling, which is $\alpha_c(\xi = 0) = 0.933667$. The boundary conditions imposed by Eq. (3.10) at $x = \Lambda^2$ demand that the behaviour of the mass function be oscillatory, and that implies that the roots in Eq. (3.25) are complex. Thus only for α greater than α_c does Eq. (3.10) have a non-zero solution for $\Sigma(x)$: only then can chiral symmetry breaking occur.

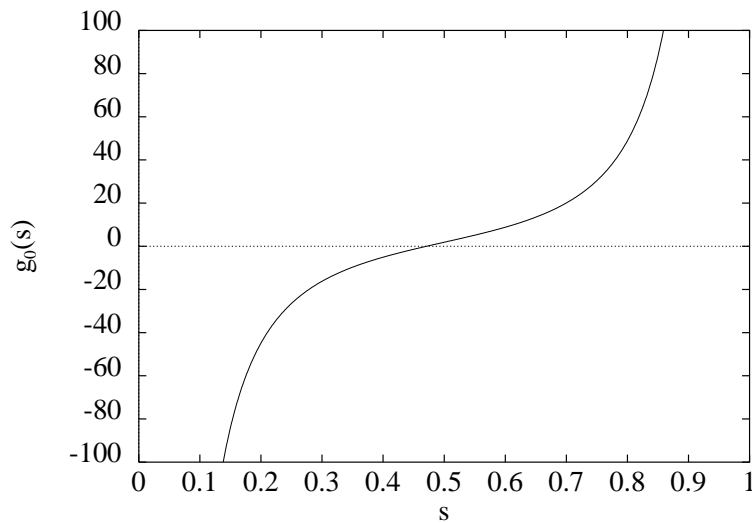


Figure 3.3: Function $g_0(s)$ versus exponent s . To determine the critical point of the integral equation Eq. (3.11) in the Landau gauge, the exponent s_c has to satisfy $g_0(s_c) = 0$.

To find the solutions in other than the Landau gauge we will look for solutions of the system of equations, Eqs. (3.23, 3.24), which are continuously connected to the one found in the Landau gauge. We will start from values of the gauge close to zero and work our way up and down to positive and negative values of ξ , using the solution at the previous ξ -value as starting guess for the new calculation.

The solutions for ν_c and s_c are shown in Fig. 3.4. We only find solutions satisfying the convergence conditions, Eq. (3.20), as long as $\xi > -3$. For $\xi = -3$ one can show from Eq. (3.15) that the ξ -term causes an additional cancellation and the integrals of Eq. (3.11) are still convergent. Below this, for $\xi < -3$, the condition $\nu - s > -1$ is not satisfied anymore: the transcendental equation, Eq. (3.23), is not equivalent anymore to the integral equation, Eq. (3.11), which becomes infrared divergent. For positive values of ξ , however large, we always find a solution which satisfies the conditions, Eq. (3.20), needed for the convergence of the integrals of Eq. (3.11).

From the solution ν_c and Eq. (3.9) we compute $\alpha_c(\xi)$ as a function of ξ . The variation of the

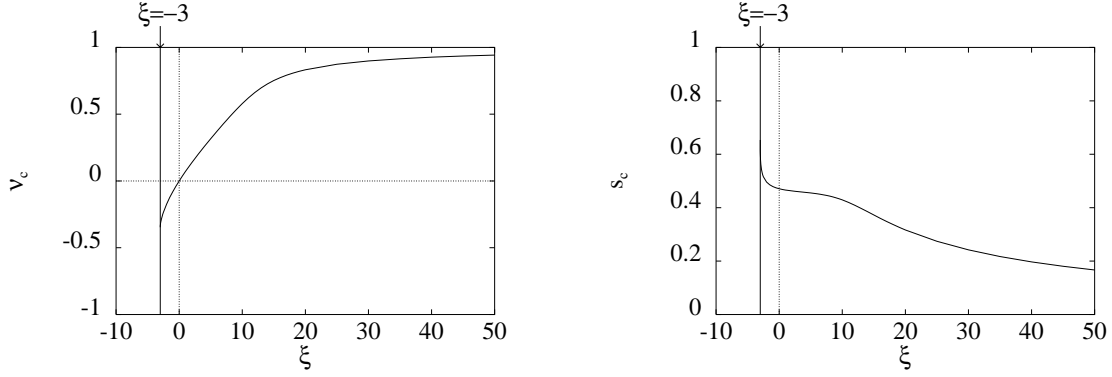


Figure 3.4: Solutions ν_c and s_c versus covariant gauge parameter ξ .

critical coupling with the covariant gauge parameter is shown in Fig. 3.5, where we have plotted the critical coupling α_c against ξ over the rather large domain $-3 \leq \xi \leq 50$. The results are in agreement with those of Ref. [28] where the system of non-linear coupled equations, Eqs. (3.4, 3.5), was solved numerically at $\xi = 0, 1$ and 3. We can compare these results with those obtained in the rainbow approximation [28], where the bare vertex is used instead of the Curtis-Pennington vertex. The values of the critical coupling for $\xi = 0, 1, 3$ are compared in Table 3.1. We note the reassuringly weak gauge dependence of the critical coupling in the CP-case.

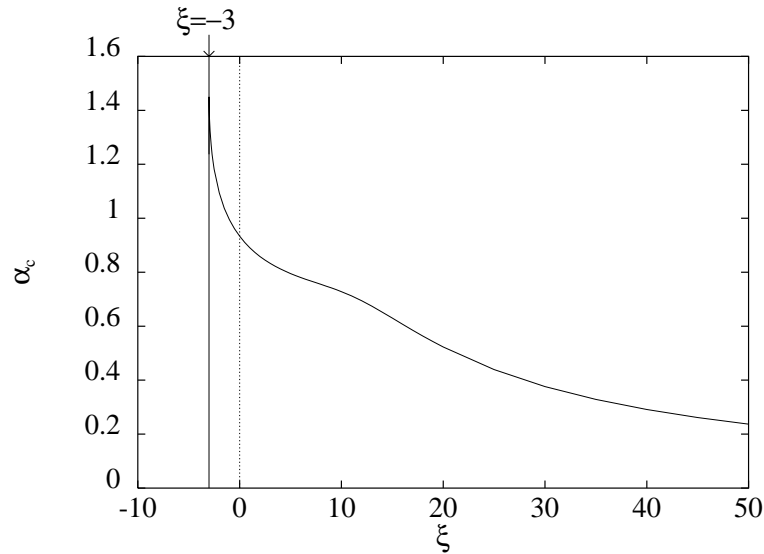


Figure 3.5: Critical coupling, α_c , as a function of the covariant gauge parameter, ξ .

| ξ | CP-vertex | Rainbow |
|-------|-----------|---------|
| 0 | 0.933667 | 1.047 |
| 1 | 0.890712 | 1.690 |
| 3 | 0.832927 | 2.040 |

Table 3.1: Critical coupling, α_c , for $\xi = 0, 1, 3$ with the Curtis-Pennington vertex and in the rainbow approximation.

In solving the bifurcation equation, we have at the same time found the exponent s of Eq. (3.12). This too is only weakly gauge dependent in a sizeable region of ξ , as can be seen in Fig. 3.4. For instance, in the Landau gauge ($\xi = 0$), $s = 0.4710$, while with $\xi = 5$, $s = 0.4551$. This exponent determines the ultraviolet behaviour of the mass-function $\Sigma(x)$ and is consequently related to γ_m , the anomalous dimension of the $\bar{\psi}\psi$ operator by $\gamma_m = 2(1 - s)$. Thus in the Landau gauge $\gamma_m = 1.058$, close to the value 1 that holds in the rainbow approximation and Holdom claims is exactly true in all gauges [42].

The fact that the variation of the critical coupling is small over a sizeable region of the gauge parameter indicates the superiority of the Curtis-Pennington vertex over the bare vertex as well as over previous Ansätze for the vertex function [43, 44, 45, 46] made in the past in an attempt to improve on the ladder approximation.

In this section we have determined the critical point, where the generation of fermion mass sets in, in quenched QED with the Curtis-Pennington vertex. In the next section we will investigate how this generated mass scales when we increase the coupling above its critical value.

3.4 Scaling law: mass generation versus coupling

One of the most interesting features in the study of mass generation as a consequence of chiral symmetry breaking is the scaling law relating the scale of the generated fermion mass M to the coupling α , when this coupling is larger than, but still very close to its critical value α_c . It is generally thought that this scaling in quenched QED can be described by what is often referred to as the *Miransky scaling law* [11]:

$$\frac{\Lambda}{M} = \exp \left(\frac{A}{\sqrt{\frac{\alpha}{\alpha_c} - 1}} - B \right). \quad (3.27)$$

The scaling law is important as it can be related to the triviality of the theory. It is thought

that a mean field scaling law indicates that the theory is trivial, while any departure from it opens the possibility for the continuum theory to remain interactive. From the Miransky scaling law, one can show that the critical coupling α_c can be interpreted as an ultraviolet fixed point of the continuum theory.

We will first prove this formula in the rainbow approximation. Then, we will apply the same method to the Curtis-Pennington vertex to show that Eq. (3.27) remains valid and to determine the coefficients A and B .

3.4.1 Bare vertex

In the rainbow approximation to QED we know that $\mathcal{F}(x) \equiv 1$ and the mass equation is given by:

$$\Sigma(x) = \frac{3\alpha}{4\pi} \left[\frac{1}{x} \int_0^x dy \frac{y\Sigma(y)}{y + \Sigma^2(y)} + \int_x^{\Lambda^2} dy \frac{\Sigma(y)}{y + \Sigma^2(y)} \right]. \quad (3.28)$$

We now want to linearize this equation to make it tractable. By doing this Eq. (3.28) becomes scale invariant and all information about the scale of the generated mass is lost. This can be remedied by introducing an IR-cutoff in the linearized equation. To retain the correct scale of the generated mass in the linearized equation, the IR-cutoff κ has to satisfy $\Sigma(\kappa^2) = \kappa$. This can be understood by noting that below this cutoff the original integral in Eq. (3.28) is negligible while the linearized equation would give a big contribution; above the cutoff both integrals will be similar. The linearized Σ -equation is:

$$\Sigma(x) = \frac{3\alpha}{4\pi} \left[\frac{1}{x} \int_{\kappa^2}^x dy \Sigma(y) + \int_x^{\Lambda^2} dy \frac{\Sigma(y)}{y} \right]. \quad (3.29)$$

To solve this integral equation it is usual to transform it to a differential equation, through successive differentiation, with boundary conditions derived from the integral equation. Differentiating Eq. (3.29) once with respect to x gives:

$$\Sigma'(x) = -\frac{3\alpha}{4\pi} \frac{1}{x^2} \int_{\kappa^2}^x dy \Sigma(y). \quad (3.30)$$

Multiplying Eq. (3.30) by x^2 and differentiating once more with respect to x gives the following differential equation:

$$x^2 \Sigma''(x) + 2x \Sigma'(x) + \frac{3\alpha}{4\pi} \Sigma(x) = 0. \quad (3.31)$$

This is a standard differential equation which has solutions of the form:

$$\Sigma(x) = x^{-s}. \quad (3.32)$$

Substituting the solution (3.32) in Eq. (3.31) gives the following condition for s :

$$s^2 - s + \frac{3\alpha}{4\pi} = 0 . \quad (3.33)$$

Therefore, the exponent s of the solution Eq. (3.32) has the following values:

$$s_{1,2} = \frac{1}{2} \pm \frac{1}{2} \sqrt{1 - \frac{\alpha}{\alpha_c}} \quad (3.34)$$

with $\alpha_c = \pi/3$.

The general solution for $\Sigma(x)$ can thus be written as:

$$\Sigma(x) = C_1 x^{-s_1} + C_2 x^{-s_2} . \quad (3.35)$$

If the value of the coupling α is larger than the critical value α_c this solution can be written as:

$$\Sigma(x) = C_1 x^{-\frac{1}{2} - \frac{i}{2}\tau} + C_2 x^{-\frac{1}{2} + \frac{i}{2}\tau} \quad (3.36)$$

where $\tau = \sqrt{\frac{\alpha}{\alpha_c} - 1}$ is real.

The coefficients C_1 and C_2 of Eq. (3.36) have to be determined from the boundary conditions which are derived from Eqs. (3.29, 3.30). These boundary conditions are:

$$[x\Sigma(x)]'(\Lambda^2) = 0 \quad (3.37)$$

and

$$\Sigma'(\kappa^2) = 0 . \quad (3.38)$$

Substituting the solution, Eq. (3.36), in the UV and IR boundary conditions, Eqs. (3.37, 3.38), yields:

$$C_1 \left(\frac{1}{2} - \frac{i\tau}{2} \right) \Lambda^{-i\tau} + C_2 \left(\frac{1}{2} + \frac{i\tau}{2} \right) \Lambda^{i\tau} = 0 \quad (3.39)$$

and

$$C_1 \left(-\frac{1}{2} - \frac{i\tau}{2} \right) \kappa^{-i\tau} + C_2 \left(-\frac{1}{2} + \frac{i\tau}{2} \right) \kappa^{i\tau} = 0 . \quad (3.40)$$

Eliminating C_1 and C_2 from Eqs. (3.39, 3.40) gives:

$$\left(\frac{\Lambda}{\kappa} \right)^{2i\tau} = \frac{\left(\frac{1}{2} - \frac{i\tau}{2} \right)^2}{\left(\frac{1}{2} + \frac{i\tau}{2} \right)^2} = \frac{r^2 \exp(-2i\theta)}{r^2 \exp(2i\theta)} = \exp(-4i\theta) \quad (3.41)$$

where $r = \frac{1}{2}\sqrt{1 + \tau^2}$ and $\theta = \arctan(\tau)$.

From Eq. (3.41) we find:

$$2\tau \ln \left(\frac{\Lambda}{\kappa} \right) = -4 \arctan(\tau) + 2k\pi. \quad (3.42)$$

If α is close to α_c we can expand the arctan in a Taylor series, this yields:

$$\ln \left(\frac{\Lambda}{\kappa} \right) = \frac{k\pi}{\tau} - 2. \quad (3.43)$$

The ground state of the system is found for $k=1$, and so the generated mass is related to the coupling as:

$$\frac{\Lambda}{\kappa} = \exp \left(\frac{\pi}{\sqrt{\frac{\alpha}{\alpha_c} - 1}} - 2 \right). \quad (3.44)$$

The use of a hard IR-cutoff κ in Eq. (3.29) is in fact quite crude, as the low momentum behaviour of the mass function, Eq. (3.28), is not approximated very well. A better approximation consists in replacing the quadratic term $\Sigma^2(y)$ in the denominator of Eq. (3.28) by a constant term $m^2 = \Sigma^2(0)$. This seems more realistic, as the mass term is approximately constant at low momentum and is negligible at large momentum:

$$\Sigma(x) = \frac{3\alpha}{4\pi} \left[\frac{1}{x} \int_0^x dy \frac{y\Sigma(y)}{y+m^2} + \int_x^{\Lambda^2} dy \frac{\Sigma(y)}{y+m^2} \right]. \quad (3.45)$$

From this integral equation one derives the following differential equation:

$$x^2 \Sigma''(x) + 2x \Sigma'(x) + \frac{3\alpha}{4\pi} \frac{x}{x+m^2} \Sigma(x) = 0. \quad (3.46)$$

To find the solutions of this differential equation we introduce the new variable $z = -x/m^2$ and find:

$$z(1-z) \Sigma''(z) + 2(1-z) \Sigma'(z) - \frac{3\alpha}{4\pi} \Sigma(z) = 0. \quad (3.47)$$

From Section 9.15 of Ref. [40] we know that the hypergeometric function $F(a, b; c; z)$ satisfies the following differential equation:

$$\left[z(1-z) \frac{d^2}{dz^2} + [c - (a+b+1)z] \frac{d}{dz} - ab \right] F(a, b; c; z) = 0. \quad (3.48)$$

This means that, using the normalization condition $\Sigma(0) = m$, the mass function is given by:

$$\Sigma(x) = m F \left(\frac{1}{2} + \sigma, \frac{1}{2} - \sigma; 2; -\frac{x}{m^2} \right) \quad (3.49)$$

where $\sigma = \frac{1}{2} \sqrt{1 - \frac{\alpha}{\alpha_c}}$.

From Eq. (3.46) we derive the UV boundary condition, which is

$$[x\Sigma(x)]'(\Lambda^2) = 0. \quad (3.50)$$

A property of hypergeometric functions is [47]:

$$\frac{d}{dz}[z^{c-1}F(a, b; c; z)] = (c-1)z^{c-2}F(a, b; c-1; z). \quad (3.51)$$

Substituting the solution, Eq. (3.49), in the boundary condition, Eq. (3.50), and applying the property, Eq. (3.51), gives:

$$mF\left(\frac{1}{2} + \sigma, \frac{1}{2} - \sigma; 1; -\frac{\Lambda^2}{m^2}\right) = 0. \quad (3.52)$$

To simplify this last expression we will make use the following equality [47]:

$$\begin{aligned} F(a, b, c; z) &= \frac{\Gamma(c)\Gamma(b-a)}{\Gamma(b)\Gamma(c-a)}(-z)^{-a}F(a, 1+a-c; 1+a-b; z^{-1}) \\ &+ \frac{\Gamma(c)\Gamma(a-b)}{\Gamma(a)\Gamma(c-b)}(-z)^{-b}F(1+b-c, b; 1+b-a; z^{-1}). \end{aligned} \quad (3.53)$$

Applying Eq. (3.53) to the UV boundary condition, Eq. (3.52), when $\Lambda^2 \gg m^2$ and keeping the leading order terms yields:

$$m \frac{\Gamma(-2\sigma)}{\Gamma^2(\frac{1}{2}-\sigma)} \left(\frac{\Lambda^2}{m^2}\right)^{-\frac{1}{2}-\sigma} + m \frac{\Gamma(2\sigma)}{\Gamma^2(\frac{1}{2}+\sigma)} \left(\frac{\Lambda^2}{m^2}\right)^{-\frac{1}{2}+\sigma} = 0. \quad (3.54)$$

When $\alpha > \alpha_c$ we write $\sigma = \frac{i}{2}\tau$ where $\tau = \sqrt{\frac{\alpha}{\alpha_c} - 1}$. Eq. (3.54) then becomes:

$$\left(\frac{\Lambda^2}{m^2}\right)^{i\tau} = -\frac{\Gamma(-i\tau)\Gamma^2(\frac{1}{2} + \frac{i}{2}\tau)}{\Gamma(i\tau)\Gamma^2(\frac{1}{2} - \frac{i}{2}\tau)}. \quad (3.55)$$

Using the equality $\Gamma(\bar{z}) = \overline{\Gamma(z)}$ and defining $\Gamma(i\tau) \equiv r_1 \exp(i\theta_1)$ and $\Gamma(\frac{1}{2} + \frac{i}{2}\tau) \equiv r_2 \exp(i\theta_2)$ we get:

$$\left(\frac{\Lambda^2}{m^2}\right)^{i\tau} = \exp(i\theta) \quad (3.56)$$

where $\theta = \pi - 2\theta_1 + 4\theta_2$ and $\theta_1 = \arg(\Gamma(i\tau))$, $\theta_2 = \arg(\Gamma(\frac{1}{2} + \frac{i}{2}\tau))$.

We want to approximate θ for small values of τ . Therefore, we Taylor expand the Gamma functions:

$$\Gamma(i\tau) \approx \frac{1}{i\tau}(1 + i\tau\psi(1)) = \psi(1) - \frac{i}{\tau} \quad (3.57)$$

and

$$\Gamma\left(\frac{1}{2} + \frac{i}{2}\tau\right) \approx \Gamma\left(\frac{1}{2}\right) \left(1 + \frac{i}{2}\tau\psi\left(\frac{1}{2}\right)\right). \quad (3.58)$$

Thus, the argument θ from Eq. (3.56) becomes:

$$\begin{aligned}
\theta &= \pi - 2\arg(\Gamma(i\tau)) + 4\arg\left(\Gamma\left(\frac{1}{2} + \frac{i}{2}\tau\right)\right) \\
&\approx \pi - 2\arctan\left(-\frac{1}{\tau\psi(1)}\right) + 4\arctan\left(\frac{\tau}{2}\psi\left(\frac{1}{2}\right)\right) \\
&\approx \pi - 2\left(\frac{\pi}{2} + \tau\psi(1)\right) + 2\tau\psi\left(\frac{1}{2}\right) \\
&\approx -4\tau \ln 2
\end{aligned} \tag{3.59}$$

knowing that $\psi(1) = -\gamma$ and $\psi(\frac{1}{2}) = -\gamma - 2 \ln 2$.

After substituting Eq. (3.59) in Eq. (3.56) and inverting the exponential, we find:

$$\ln\left(\frac{\Lambda}{m}\right) = \frac{1}{2\tau}(-4\tau \ln 2 + 2k\pi). \tag{3.60}$$

The ground state of the system is found for $k=1$, and so the generated mass is related to the coupling as:

$$\frac{\Lambda}{m} = \exp\left(\frac{\pi}{\sqrt{\frac{\alpha}{\alpha_c} - 1}} - 2 \ln 2\right) \tag{3.61}$$

where we note that $2 \ln 2 \approx 1.386$.

We see from Eqs. (3.44, 3.61) that both cutoff methods yield a similar scaling law, in agreement with Eq. (3.27). The coefficients of the scaling law are $A = \pi$ in both approximations, but $B = 2$ in the first case and $B = 2 \ln 2$ in the second, more realistic, case.

3.4.2 Curtis-Pennington vertex

We now want to make an analogous calculation using the Curtis-Pennington vertex Ansatz. In this case, the linearized equation for the fermion mass in an arbitrary covariant gauge is given by the bifurcation equation, Eq. (3.11). In the Landau gauge ($\xi = 0$), the Σ -equation becomes:

$$\Sigma(x) = \frac{3\alpha}{8\pi} \int_{\kappa^2}^{\Lambda^2} \left\{ 2\Sigma(y) \left[\frac{\theta(x-y)}{x} + \frac{\theta(y-x)}{y} \right] - \frac{\Sigma(y) - \Sigma(x)}{y-x} \left[\frac{y}{x}\theta(x-y) + \frac{x}{y}\theta(y-x) \right] \right\} \tag{3.62}$$

where we introduced again an infrared cutoff κ^2 , satisfying $\kappa = \Sigma(\kappa^2)$, to retain the scale of the generated fermion mass when α is larger, but very close, to the critical coupling α_c . We know from the discussion of Section 3.3 that in the critical point, where the infrared cutoff κ is zero, the solution of this equation has a power behaviour. Therefore we assume that close to the critical point, the solution to Eq. (3.62) is still power behaved:

$$\Sigma(x) \sim x^{-s}. \tag{3.63}$$

After substituting this solution in Eq. (3.62) we get:

$$x^{-s} = \frac{3\alpha}{8\pi} \left\{ \left[-\pi \cot \pi s + \frac{3}{s} + \frac{1}{1-s} + 1 \right] x^{-s} - \frac{2}{1-s} \frac{(\kappa^2)^{1-s}}{x} + \int_0^{\kappa^2} dy \frac{y y^{-s} - x^{-s}}{x y - x} - \frac{2}{s} (\Lambda^2)^{-s} + \int_{\Lambda^2}^{\infty} dy \frac{x y^{-s} - x^{-s}}{y y - x} \right\}. \quad (3.64)$$

The exponent s has to satisfy the transcendental equation derived by equating the terms in x^{-s} in Eq. (3.64) ($\kappa \rightarrow 0$ and $\Lambda \rightarrow \infty$):

$$1 = \frac{3\alpha}{8\pi} \left[-\pi \cot \pi s + \frac{3}{s} + \frac{1}{1-s} + 1 \right]. \quad (3.65)$$

We want to investigate the behaviour of s in the neighbourhood of the critical point. Therefore we rewrite Eq. (3.65) as:

$$\frac{3\alpha}{8\pi} = h(s) = \frac{1}{f(s)} \quad (3.66)$$

where

$$f(s) = -\pi \cot \pi s + \frac{3}{s} + \frac{1}{1-s} + 1. \quad (3.67)$$

We now make a Taylor expansion of the function $h(s)$ around the critical point:

$$h(s) = h(s_c) + (s - s_c)h'(s_c) + \frac{1}{2}(s - s_c)^2 h''(s_c) + \mathcal{O}(s - s_c)^3. \quad (3.68)$$

From Eq. (3.66) we know that $h(s_c) = 3\alpha_c/8\pi$ and in Section 3.3 we have shown that $h'(s_c) = 0$ in the critical point. Therefore, Eq. (3.68) becomes:

$$\frac{3\alpha}{8\pi} = \frac{3\alpha_c}{8\pi} - \frac{1}{2}(s - s_c)^2 \frac{f''(s_c)}{f^2(s_c)}. \quad (3.69)$$

The behaviour of s in the neighbourhood of the critical point is thus given by,

$$s_{1,2} = s_c \pm \beta_c \sqrt{1 - \frac{\alpha}{\alpha_c}} \quad (3.70)$$

where

$$\beta_c \equiv \sqrt{\frac{2f(s_c)}{f''(s_c)}}. \quad (3.71)$$

Differentiating Eq. (3.67) twice yields:

$$f''(s) = -2\pi^3 \csc^2 \pi s \cot \pi s + \frac{6}{s^3} + \frac{2}{(1-s)^3}. \quad (3.72)$$

Substituting the value $s_c = 0.4710$, found in Section 3.3, in the previous equations, Eqs. (3.67, 3.72, 3.71), gives $\boxed{\beta_c = 0.5246}$.

The general solution of Eq. (3.64), in the neighbourhood of the critical point is:

$$\Sigma(x) = C_1 x^{-s_c - i\beta_c \tau} + C_2 x^{-s_c + i\beta_c \tau}. \quad (3.73)$$

The scale of the generated mass will be determined by the boundary conditions which are derived from Eq. (3.64). The IR boundary condition is found by taking $x = \kappa^2$ in Eq. (3.64) ($\Lambda \rightarrow \infty$):

$$\begin{aligned} & C_1 \left[-\frac{2}{1-s_1} (\kappa^2)^{-s_1} + \int_0^{\kappa^2} dy \frac{y}{\kappa^2} \frac{y^{-s_1} - (\kappa^2)^{-s_1}}{y - \kappa^2} \right] \\ & + C_2 \left[-\frac{2}{1-s_2} (\kappa^2)^{-s_2} + \int_0^{\kappa^2} dy \frac{y}{\kappa^2} \frac{y^{-s_2} - (\kappa^2)^{-s_2}}{y - \kappa^2} \right] = 0. \end{aligned} \quad (3.74)$$

Substituting $t = y/\kappa^2$ in the integral of Eq. (3.74) yields:

$$C_1 (\kappa^2)^{-s_1} \left[-\frac{2}{1-s_1} + \int_0^1 dt \frac{t^{-s_1+1} - t}{t-1} \right] + C_2 (\kappa^2)^{-s_2} \left[-\frac{2}{1-s_2} + \int_0^1 dt \frac{t^{-s_2+1} - t}{t-1} \right] = 0. \quad (3.75)$$

The integrals in Eq. (3.75) are given in Eq. (3.16). Substituting these, we find:

$$C_1 (\kappa^2)^{-s_1} \left[-\frac{2}{1-s_1} + \psi(-s_1+2) - \psi(2) \right] + C_2 (\kappa^2)^{-s_2} \left[-\frac{2}{1-s_2} + \psi(-s_2+2) - \psi(2) \right] = 0. \quad (3.76)$$

Taking $x = \Lambda^2$ in Eq. (3.64) gives the UV boundary condition ($\kappa \rightarrow 0$):

$$\begin{aligned} & C_1 \left[-\frac{2}{s_1} (\Lambda^2)^{-s_1} + \int_{\Lambda^2}^{\infty} dy \frac{\Lambda^2}{y} \frac{y^{-s_1} - (\Lambda^2)^{-s_1}}{y - \Lambda^2} \right] \\ & + C_2 \left[-\frac{2}{s_2} (\Lambda^2)^{-s_2} + \int_{\Lambda^2}^{\infty} dy \frac{\Lambda^2}{y} \frac{y^{-s_2} - (\Lambda^2)^{-s_2}}{y - \Lambda^2} \right] = 0. \end{aligned} \quad (3.77)$$

Substituting $t = y/\kappa^2$ in the integral of Eq. (3.77) yields:

$$C_1 (\Lambda^2)^{-s_1} \left[-\frac{2}{s_1} + \int_1^{\infty} dt \frac{t^{-s_1-1} - t^{-1}}{t-1} \right] + C_2 (\Lambda^2)^{-s_2} \left[-\frac{2}{s_2} + \int_1^{\infty} dt \frac{t^{-s_2-1} - t^{-1}}{t-1} \right] = 0. \quad (3.78)$$

Substituting the integral Eq. (3.17) in Eq. (3.78) yields:

$$C_1 (\Lambda^2)^{-s_1} \left[-\frac{2}{s_1} - \psi(s_1+1) + \psi(1) \right] + C_2 (\Lambda^2)^{-s_2} \left[-\frac{2}{s_2} - \psi(s_2+1) + \psi(1) \right] = 0. \quad (3.79)$$

Now, eliminate C_1 and C_2 from the boundary conditions, Eqs. (3.76, 3.79), and substitute $s_{1,2}$ from Eq. (3.70):

$$\left(\frac{\Lambda^2}{\kappa^2} \right)^{2i\beta_c \tau} = \frac{\left[-\frac{2}{s_c + i\beta_c \tau} - \psi(s_c + i\beta_c \tau + 1) + \psi(1) \right] \left[-\frac{2}{1-s_c + i\beta_c \tau} + \psi(-s_c + i\beta_c \tau + 2) - \psi(2) \right]}{\left[-\frac{2}{s_c - i\beta_c \tau} - \psi(s_c - i\beta_c \tau + 1) + \psi(1) \right] \left[-\frac{2}{1-s_c - i\beta_c \tau} + \psi(-s_c - i\beta_c \tau + 2) - \psi(2) \right]}. \quad (3.80)$$

After noting that $\psi(\bar{z}) = \overline{\psi(z)}$, we rewrite Eq. (3.80) as:

$$\left(\frac{\Lambda^2}{\kappa^2}\right)^{2i\beta_c\tau} = \exp(i\theta) = \exp\left(2i(\theta_1 + \theta_2)\right), \quad (3.81)$$

where

$$\theta_1 \equiv \arg\left[-\frac{2}{s_c + i\beta_c\tau} - \psi(s_c + i\beta_c\tau + 1) + \psi(1)\right] \quad (3.82)$$

$$\theta_2 \equiv \arg\left[-\frac{2}{1 - s_c + i\beta_c\tau} + \psi(-s_c + i\beta_c\tau + 2) - \psi(2)\right]. \quad (3.83)$$

For small values of τ , we compute θ_1 and θ_2 to $\mathcal{O}(\tau)$:

$$\begin{aligned} \theta_1 &\approx \arg\left[-\frac{2}{s_c} - \psi(s_c + 1) + \psi(1) + i\beta_c\tau\left(\frac{2}{s_c^2} - \psi'(s_c + 1)\right)\right] \\ &\approx \left[\frac{\frac{2}{s_c^2} - \psi'(s_c + 1)}{-\frac{2}{s_c} - \psi(s_c + 1) + \psi(1)}\right] \beta_c\tau \end{aligned} \quad (3.84)$$

$$\begin{aligned} \theta_2 &\approx \arg\left[-\frac{2}{1 - s_c} + \psi(-s_c + 2) - \psi(2) + i\beta_c\tau\left(\frac{2}{(1 - s_c)^2} + \psi'(-s_c + 2)\right)\right] \\ &\approx \left[\frac{\frac{2}{(1 - s_c)^2} + \psi'(-s_c + 2)}{-\frac{2}{1 - s_c} + \psi(-s_c + 2) - \psi(2)}\right] \beta_c\tau. \end{aligned} \quad (3.85)$$

We compute θ by inserting Eqs. (3.84, 3.85) in Maple:

$$\theta = 2(\theta_1 + \theta_2) = -7.2269 \beta_c\tau. \quad (3.86)$$

From Eq. (3.81) we find:

$$\frac{\Lambda}{\kappa} = \exp\left(\frac{k\pi}{2\beta_c\tau} + \frac{\theta}{4\beta_c\tau}\right), \quad (3.87)$$

and substituting Eq. (3.86) for θ in this equation yields precisely the Miransky scaling law, close to the critical point, where $\tau \ll 1$ ($k=1$):

$$\frac{\Lambda}{\kappa} = \exp\left(\frac{A}{\sqrt{\frac{\alpha}{\alpha_c} - 1}} - B\right) \quad (3.88)$$

where

$$\boxed{A = \frac{\pi}{2\beta_c} = 0.9531 \pi} \quad \text{and} \quad \boxed{B = 1.8067}. \quad (3.89)$$

3.4.3 Summary

The previous results can be compared with the numerical results of Curtis and Pennington [28] who solve the non-linear integral equation for various values of α and fit their results to the form of Eq. (3.27), in the rainbow approximation and with the Curtis-Pennington vertex. In the rainbow approximation they find $A = 0.9886\pi$, $B = 1.4883$, while, in Section 3.4.1, we found $A = \pi$ and $B = 2$ or $B = 2 \ln 2 \approx 1.386$, depending on the IR treatment of the linearized integral. There is good agreement between our analytical and their numerical results. The parameter A agrees extremely well and seems independent of the way the IR part of the integral is treated. The deviations for the parameter B can be explained as it sets the scale of the generated mass and is therefore sensitive to the IR approximation introduced in the linearized equation.

This is confirmed for the CP-vertex where Curtis and Pennington find $A = 0.9326\pi$ and $B = 1.2606$. Again, the parameter A is in very good agreement with our analytical results, Eq. (3.89), while the parameter B deviates from it. It is clear from our discussion in Section 3.4.2 that the parameter A is independent of the boundary conditions and the IR treatment of the linearized integral, and will therefore have the correct value of the true scaling law for the original non-linear equation.

Chapter 4

Fermion mass generation in unquenched QED: a survey

In the previous chapter we discussed dynamical fermion mass generation in quenched QED. We found that, provided the coupling is larger than some critical value, this indeed happens. The value of the critical coupling depends on the vertex Ansatz used to truncate the infinite set of SD equations. Furthermore, the scale of the generated mass in quenched QED seems to follow the Miransky scaling law.

As the phenomenon of mass generation is thought to be governed by the dynamics at low momentum it has long been the question if it also occurs in unquenched QED. Here, the coupling runs as a consequence of screening effects due to fermion-antifermion pair productions, such that the interaction becomes weak at long distances. It is this opposition between short and long distance aspects which makes the study of fermion mass generation in unquenched QED essentially different from that in quenched QED.

We will now give a review of the work accomplished prior to this study. It is not so long ago since the first studies about fermion mass generation in unquenched QED, using the Schwinger-Dyson equation approach, were published. The integral equations describing the dynamical generation of fermion mass, Eqs. (2.34, 2.35, 2.41), are given by:

$$\frac{\Sigma(p^2)}{\mathcal{F}(p^2)} = m_0 + \frac{ie^2}{4(2\pi)^4} \int d^4k \operatorname{Tr} \left[\gamma^\mu S(k) \Gamma^\nu(k, p) \right] D_{\nu\mu}(k-p) \quad (4.1)$$

$$\frac{1}{\mathcal{F}(p^2)} = 1 - \frac{ie^2}{4p^2(2\pi)^4} \int d^4k \operatorname{Tr} \left[\not{p} \gamma^\mu S(k) \Gamma^\nu(k, p) \right] D_{\nu\mu}(k-p) \quad (4.2)$$

$$\frac{1}{\mathcal{G}(q^2)} = 1 - \frac{iN_f e^2 \mathcal{P}_{\mu\nu}}{3(2\pi)^4 q^2} \int d^4k \operatorname{Tr} \left[\gamma^\mu S(k) \Gamma^\nu(k, p) S(p) \right]. \quad (4.3)$$

In many studies the full vacuum polarization is replaced by its 1-loop approximation, replacing all the full quantities in the integral of Eq. (4.3) by bare quantities. The integral can then be computed analytically and the 1-loop vacuum polarization function is given by:

$$\Pi(q^2) = \frac{N_f \alpha}{3\pi} \left[\ln \frac{\Lambda^2}{q^2} + C \right] \quad (4.4)$$

where C a constant dependent on the regularization scheme. As we can write the photon renormalization function as

$$\mathcal{G}(q^2) \equiv \frac{1}{1 + \Pi(q^2)},$$

the full photon propagator itself is then approximated by an infinite sum of bare loops.

In Ref. [13] Kondo et al. perform an analytical calculation using the 1-loop approximation to the vacuum polarization. Furthermore they introduce the so-called LAK-approximation (in analogy to Landau, Abrikosov and Khalatnikov [48]):

$$\Pi((k-p)^2) \approx \Pi(\max(k^2, p^2)) \quad (4.5)$$

to allow them to compute the angular integrals of the fermion equations analytically. The full vertex $\Gamma^\mu(k, p)$ is approximated by the bare vertex γ^μ . To determine the *critical point* in the Landau gauge they then linearize the mass equation, applying bifurcation analysis. Consequently, they derive a differential equation with boundary conditions, which cannot be solved by any known special functions. Therefore they use an asymptotic expansion method which is only valid for the number of flavours $N_f = 1, 2$. The main results published in this paper are $\alpha_c(N_f = 1) = 1.99972$, $\alpha_c(N_f = 2) = 2.71482$. The generated dynamical mass and the order parameter $\langle \bar{\psi}\psi \rangle$ scale according to the mean field scaling law (in contrast with the Miransky scaling in the quenched case):

$$\frac{m}{\Lambda} \sim \sqrt{\frac{\alpha}{\alpha_c} - 1}, \quad (4.6)$$

and the anomalous dimension of the composite operator is $\gamma_m = 0$.

In another analytical paper, Gusynin [14] follows almost the same path as Kondo et al. [13]. He introduces the same approximations and hence, finds the same differential equation as they do. His treatment differs in the way he solves the differential equation. His solution method is only valid when $3\pi/N_f\alpha \gg 1$ and is thus limited to $N_f = 1$. For the critical coupling he finds $\alpha_c(N_f = 1) \approx 1.95$. Also, the scale of the generated mass follows the mean field law, Eq. (4.6).

In Ref. [44], Kondo discusses how to recover the gauge invariance of the critical coupling and the scaling law in quenched and unquenched QED by a specific choice of vertex. The vertex

is constructed such that the Landau gauge results, in quenched and unquenched QED, remain unchanged in any arbitrary gauge. However, it is clear, in the light of the most recent investigations about the construction of the full QED vertex [24, 25, 35], that Kondo's choice of vertex shows unphysical properties.

As mentioned before, all the analytical studies of unquenched QED required the introduction of several approximations to make the problem tractable. Therefore, new, numerical studies were undertaken as in Ref. [16] and its preliminary report, Ref. [15], by Kondo et al. They solve the integral equations numerically in the Landau gauge. Again, they use the bare vertex approximation, while the vacuum polarization is still taken at 1-loop, Eq. (4.4). In the first part of their calculation they introduce the LAK-approximation, Eq. (4.5), as in the analytical calculations. This is useful to verify the analytical results and to simplify the numerical calculation. In this approximation the \mathcal{F} -equation decouples, yielding $\mathcal{F}(x) = 1$. The angular integrals of the Σ -equation can be calculated analytically leaving a one-dimensional non-linear integral equation for $\Sigma(x)$ to be solved numerically. They plot the variation of the generated mass and the order parameter, $\langle \bar{\psi}\psi \rangle$, versus coupling for $N_f = 1, 2, 3, 4$. According to them, all the scaling laws are of the mean field type. The values of the critical couplings are: $\alpha_c(N_f = 1) = 1.9989$, $\alpha_c(N_f = 2) = 2.7517$, $\alpha_c(N_f = 3) = 3.5062$, $\alpha_c(N_f = 4) = 4.3177$. The numerical results very much agree with the analytical results of Ref. [13]. In the second part of Ref. [16] they relax the LAK-approximation, keeping the angular dependence of the vacuum polarization. Then, the two-dimensional integrals, i.e. radial and angular, in the fermion equations have to be solved numerically and the two coupled integral equations for \mathcal{F} and Σ have to be solved simultaneously. As an intermediate step they again take $\mathcal{F}(x) \equiv 1$ (as this is a good approximation in the Landau gauge) and solve the integral equation for $\Sigma(x)$. They find $\alpha_c(N_f = 1) = 2.0728$ and $\alpha_c(N_f = 2) = 2.8209$. Finally, they solve the system of coupled equations for Σ and \mathcal{F} . They do not mention any critical coupling but observe that indeed $\mathcal{F}(x) \approx 1$. They state that the scaling laws remain of the mean field type. However, surprisingly, they only find a phase transition for $N_f = 1, 2$. Their iterative procedure does not converge for $N_f \geq 3$. The reason for this, is that the positivity of the vacuum polarization $\Pi(q^2)$ is not guaranteed anymore as can be seen from Eq. (4.4). If $k^2, p^2 \in [0, \Lambda^2]$ then $(k - p)^2 \in [0, 4\Lambda^2]$. It seems inconsistent to use the vacuum polarization for momenta up to $4\Lambda^2$ when the integrals used to compute the vacuum polarization were computed using an UV cutoff Λ^2 . The trouble only occurs for $N_f \geq 3$ because then the photon momentum in the integral of the fermion equation becomes larger than

the Landau pole.

In Ref. [17] Oliensis and Johnson derive a non-linear differential equation from the integral equations and solve this numerically. They use the bare vertex approximation, but their vacuum polarization is slightly different from Eq. (4.4), being

$$\Pi(q^2) = \frac{N_f \alpha}{3\pi} \ln \frac{\Lambda^2}{q^2 + \Sigma^2(0)}, \quad (4.7)$$

where they incorporated an infrared cutoff through the term $\Sigma^2(0)$, which suppresses the effects of the vacuum polarization below this scale. They fix $\Sigma(0)$ and solve their differential equation for increasing values of Λ , finding a critical coupling $\alpha_c(N_f = 1) = 1.999534163$. Furthermore, the generated mass follows a mean field scaling law.

In Ref. [18] Rakow investigates the renormalization group flow in QED using the Schwinger-Dyson equations. He includes the effect of fermion loops in the photon propagator by considering the fermion and photon SD equations simultaneously. The full vertex is still approximated by the bare one. He solves the coupled set of non-linear integral equations numerically. He determines the critical coupling by investigating the dependence of the chiral condensate $\langle \bar{\psi}\psi \rangle$ on the coupling α and the bare mass m_0 . He finds a second order phase transition for $\alpha_c(N_f = 1) = 2.25$. However, we think that this value has not been determined accurately as can be inferred from the data of Ref. [18] and we will show in our own calculations later on. He then goes on to show that the renormalized coupling is zero at the critical point. We note that Rakow renormalizes the coupling at zero momentum. It is clear that the unrenormalized, running coupling goes to zero at zero momentum in the critical point, when the fermion mass generation disappears, and therefore it seems obvious that his renormalized coupling, defined as $\alpha_r = \alpha \mathcal{G}(0) \mathcal{F}^2(0)$, is zero. Nevertheless, we do not agree with Rakow's claim that this proves the triviality of QED, as will be explained later.

In Ref. [19] Atkinson et al. solve the coupled integral equations in the Landau gauge. They use the bare vertex approximation and assume $\mathcal{F}(x) \equiv 1$. Furthermore they use the LAK-approximation, Eq. (4.5), for the vacuum polarization. They make an analogous approximation for the mass function in the vacuum polarization integral to allow the analytic calculation of the angular integrals. The integral equations for Σ and Π are transformed into differential equations (using some more simplifications) which are then solved numerically. They find $\alpha_c(N_f = 1) = 2.100286$ and a mean field type scaling law.

A more detailed numerical investigation of fermion mass generation can be found in Ref. [20].

There, Kondo et al. start from the coupled system of integral equations for Σ , \mathcal{F} and \mathcal{G} . They simplify the numerical problem by assuming $\mathcal{F}(x) \equiv 1$, as this is thought to be a good approximation. Then the system of two coupled integral equations for Σ and \mathcal{G} is solved by an iterative procedure. Their discussion of the numerical aspect of the calculation is very interesting as this is often disregarded in publications. They compare the results obtained for $\Sigma(x)$ and $\mathcal{G}(x)$ in the self-consistent treatment and in the 1-loop approximation to the vacuum polarization. The scaling law is consistent with the mean field type scaling, although they very pertinently point out that the exact scaling law is very difficult to pin down numerically because the scaling window is very narrow, i.e. the scaling law is only valid very close to the critical point. Analytical studies seem more appropriate for this purpose. They find a critical coupling $\alpha_c(N_f = 1) = 2.084$. We note the peculiar behaviour of the full photon renormalization function compared to its 1-loop approximation, as we will discuss later.

We will end our review with alternative methods to the Schwinger-Dyson approach. In Ref. [49] Ukita et al. suggest a gauge invariant way to study the strong coupling phase of QED by applying the inversion method to the chiral condensate $\langle \bar{\psi}\psi \rangle$. The lowest order inversion method leads to the gauge-independent critical point $\alpha_c = 2\pi/3 = 2.094395$. To the lowest order inversion this value is independent of the number of flavours N_f . Although α_c seems reasonably well approximated for $N_f = 1$, it is wrong by a factor two for the quenched case. In Ref. [50] Kondo et al. compare the inversion method with their SD approach from Ref. [51]. They show that their asymptotic solution to the lowest order is the same as that of the inversion method. They then go on showing that including higher orders in the asymptotic solution recovers the known result in quenched QED, i.e. $\alpha_c = \pi/3$, for which the series converges. For $N_f = 1$ the series is asymptotic and they find $\alpha_c(N_f = 1) = 1.9995$. They conclude that therefore the inversion method, which is very useful because gauge invariance is guaranteed and no approximations to vertex nor vacuum polarization are necessary, has to be computed to higher orders to find a critical coupling which depends on the number of flavours.

Finally we will want to know what lattice studies can tell us about the dynamical generation of fermion mass. In Section 3.2 we discussed briefly the lattice calculations in quenched QED. There have been quite few lattice investigations of unquenched QED. In Ref. [52] Dagotto et al. showed that there is a second order phase transition from a massless to a massive phase. Since then, the discussion about the scaling law, which is related to the triviality of the theory, is still active [53, 54].

The values of the critical coupling α_c for $N_f=1, 2$, determined in the above discussed papers are tabulated in Table 4.1.

| Ref. | $\alpha_c(N_f = 1)$ | $\alpha_c(N_f = 2)$ |
|---------|---------------------|---------------------|
| [13] | 1.99972 | 2.71482 |
| [14] | 1.95 | |
| [16] a) | 1.9989 | 2.7517 |
| [16] b) | 2.0728 | 2.8209 |
| [17] | 1.999534163 | |
| [18] | 2.25 | |
| [19] | 2.100286 | |
| [20] | 2.084 | |
| [49] | 2.094395 | |
| [50] | 1.9995 | |

Table 4.1: Literature survey of critical couplings for $N_f = 1$ and $N_f = 2$ in unquenched QED.

We have seen that various approximations have been introduced, in the analytical as well as in the numerical calculations, producing results with varying accuracy. In the next chapters, we will develop a numerical method to make a unified, **highly accurate** numerical study of the various approximations to the Schwinger-Dyson equations for dynamical fermion mass generation in unquenched QED. The final aim is the solution of the system of three coupled, non-linear integral equations for Σ , \mathcal{F} and \mathcal{G} . This will first be achieved with the bare vertex, then, we will for the first time take the study of fermion mass generation in unquenched QED beyond the bare vertex approximation by introducing improved vertices.

Chapter 5

Numerical Solution of Schwinger-Dyson Equations

The aim of this chapter is to set up the formalism needed to solve the integral equations numerically. We will start by considering a single integral equation determining one unknown function. The type of integral equations which are of interest to us are called *non-linear Fredholm equations of the second kind* [55]:

$$x(s) = y(s) + \lambda \int_a^b K(s, t, x(s), x(t)) dt, \quad (5.1)$$

where $y(s)$ is a known function and $x(s)$ is the unknown function we want to determine.

Unfortunately, the major part of the literature about numerical methods to solve integral equations is only concerned with linear integral equations. The linear Fredholm equation of the second kind is:

$$x(s) = y(s) + \lambda \int_a^b K(s, t) x(t) dt. \quad (5.2)$$

For these linear equations there exists convergence criteria related to the behaviour of the kernel $K(s, t)$. Moreover several different solution approaches exist: Nystrom method, expansion methods as Ritz-Galerkin method, ... Very little can be found in the literature about non-linear equations so that the researcher confronted with such an equation has to gather together bits and pieces from a number of different areas of numerical analysis to tackle this problem.

The basic approximation introduced to solve an integral equation numerically resides in the numerical method used to evaluate the integrals involved in the problem.

If one needs to calculate numerically the integral $I[f]$ of some function $f(s)$ given by:

$$I[f] = \int_a^b f(s) ds, \quad (5.3)$$

one will generally use a *quadrature formula* to approximate the exact value of the integral. Most quadrature formulae approximating the integral value by the value $R[f]$ can be expressed as:

$$R[f] = \sum_{i=1}^N w_i f(t_i). \tag{5.4}$$

The error $E[f]$ introduced by this approximation is:

$$E[f] = I[f] - R[f]. \tag{5.5}$$

Well-known quadrature formulae are for instance the Newton-Cotes formulae as the midpoint rule, the trapezoidal rule, Simpson’s rule, ... , or the various Gauss rules of which the Gauss-Legendre rule is the best-known. Several other quadrature formulae exist which can be used depending on the behaviour of the integration kernel.

5.1 Linear Fredholm equation of the second kind

5.1.1 Linear Fredholm equation and the Neumann series

Let us consider a linear Fredholm equation of the second kind:

$$x(s) = y(s) + \lambda \int_a^b K(s,t) x(t) dt. \tag{5.6}$$

Formally this can also be written in operator form as:

$$x = y + \lambda Kx. \tag{5.7}$$

Starting from an initial guess $x_0 = y$ for the function x we will define an iterative procedure:

$$x_{n+1} = y + \lambda Kx_n. \tag{5.8}$$

If this procedure converges when $n \rightarrow \infty$, then from Eq. (5.8) this limit can be written as a series called the *Neumann series*. One can show that the Neumann series converges to the solution of Eq. (5.7):

$$x = \lim_{n \rightarrow \infty} x_n = \sum_{i=0}^{\infty} \lambda^i K^i y. \tag{5.9}$$

If the integral $Kx_n = \int_a^b K(s,t)x_n(t)dt$ can be computed analytically, the iterative procedure Eq. (5.8) can be used to find a good approximation to the function x by truncating it after n iterations and taking $x \approx x_n$.

Can we compute an error bound on the approximate solution ? Let us define the error function e_n on the n^{th} approximation by:

$$e_n = x - x_n. \quad (5.10)$$

If we subtract Eq. (5.8) from Eq. (5.7) we find:

$$x - x_{n+1} = \lambda K(x - x_n) \quad (5.11)$$

or

$$e_{n+1} = \lambda K e_n. \quad (5.12)$$

However we also find:

$$x_{n+1} - x_n = (x_{n+1} - x) + (x - x_n) = e_n - e_{n+1}, \quad (5.13)$$

giving

$$e_n = e_{n+1} + (x_{n+1} - x_n). \quad (5.14)$$

Taking the norm (using some appropriate function norm) of the previous equation gives:

$$\|e_n\| \leq \|e_{n+1}\| + \|x_{n+1} - x_n\|. \quad (5.15)$$

If we now substitute Eq. (5.12) in Eq. (5.15),

$$\|e_n\| \leq \|\lambda K\| \|e_n\| + \|x_{n+1} - x_n\|. \quad (5.16)$$

After rearranging terms,

$$(1 - \|\lambda K\|) \|e_n\| \leq \|x_{n+1} - x_n\|, \quad (5.17)$$

and provided $\|\lambda K\| < 1$,

$$\|e_n\| \leq \frac{\|x_{n+1} - x_n\|}{1 - \|\lambda K\|}. \quad (5.18)$$

One can show that the condition $\|\lambda K\| < 1$ is sufficient for the Neumann series to converge to the solution of the integral equation Eq. (5.7). Furthermore Eq. (5.18) then gives an *a posteriori* error bound which can be computed given two successive iterations x_n and x_{n+1} .

5.1.2 Numerical solution using the Neumann series

In the previous section we defined an iterative procedure to solve the integral equation Eq. (5.6) assuming that the integrals $Kx_n = \int_a^b K(s, t) x_n(t) dt$ could be computed analytically,

$$x_{n+1}(s) = y(s) + \lambda \int_a^b K(s, t) x_n(t) dt. \quad (5.19)$$

In most problems this will not be possible and the integrals will have to be evaluated using some numerical quadrature formula. If we use the quadrature formula R on the interval [a,b] with weights w_i and nodes t_i the integral will be written as:

$$I[f] \equiv \int_a^b f(t) dt = \sum_{i=1}^N w_i f(t_i) + E[f]. \quad (5.20)$$

To compute the Neumann series numerically we approximate the integral of Eq. (5.19) by introducing some suitable quadrature formulae and truncating the error term $E[f]$:

$$\int_a^b K(s, t) x(t) dt \approx \sum_{j=1}^N w_j K(s, t_j) x(t_j). \quad (5.21)$$

The iterative procedure Eq. (5.19) can now be replaced by:

$$x_{n+1}(s) = y(s) + \lambda \sum_{j=1}^N w_j K(s, t_j) x_n(t_j). \quad (5.22)$$

It is interesting to note from this last equation that if we confine ourselves to values $s = t_j$, the nodes of the integration formula, Eq. (5.22) only involves the function values $x_n(t_j)$ in the successive iteration steps. The notation can then be simplified by introducing vector notation,

$$\mathbf{x}_{n+1} = \mathbf{y} + \lambda K \mathbf{x}_n, \quad (5.23)$$

where we define,

$$\begin{aligned} (\mathbf{x}_n)_i &= x_n(t_i) \\ \mathbf{y}_i &= y(t_i) \\ K_{ij} &= w_j K(t_i, t_j), \end{aligned} \quad (5.24)$$

with $i, j = 1, \dots, N$.

One can show that if the iterative procedure Eq. (5.23) converges, it converges to the solution of the set of linear algebraic equations

$$(I - \lambda K) \mathbf{x}_R = \mathbf{y}, \quad (5.25)$$

where the subscript R shows the explicit dependence of the solutions of Eq. (5.25) on the quadrature rule R .

If we now define an error vector \mathbf{e}_n

$$\mathbf{e}_n = \mathbf{x}_R - \mathbf{x}_n, \tag{5.26}$$

then, repeating the error analysis from Eqs. (5.10-5.18), on Eqs. (5.25, 5.23) and replacing the function norm by some suitable matrix norm gives us an error bound on the truncated solution:

$$\|\mathbf{e}_n\| \leq \frac{\|\mathbf{x}_{n+1} - \mathbf{x}_n\|}{1 - \|\lambda K\|}, \tag{5.27}$$

provided $\|\lambda K\| < 1$. This error is the error on the solution \mathbf{x}_R to the set of linear algebraic equations introduced by truncating the iterative procedure and approximating the solution by \mathbf{x}_n , it is **not** the error with respect to the exact solution $x(s)$ from the integral equation.

5.1.3 The Nystrom method

In the previous section we have shown how to find an approximate solution to the integral equation Eq. (5.6) by applying the Neumann series and the corresponding iterative procedure, truncating the procedure after n steps and approximating the integrals in each step by a quadrature rule R .

Instead one could approximate the integral equation Eq. (5.6) straight away by replacing the integral in Eq. (5.6) by a quadrature rule R ,

$$x(s) = y(s) + \lambda \sum_{j=1}^N w_j K(s, t_j) x(t_j). \tag{5.28}$$

If we only consider Eq. (5.28) in the integration nodes $s = t_i$, Eq. (5.28) becomes a system of N linear equations with N unknowns $x_i = x(t_i)$ with solution vector \mathbf{x}_R ,

$$(x_R)_i = y_i + \lambda \sum_{j=1}^N w_j K(t_i, t_j) (x_R)_j, \tag{5.29}$$

which is equivalent to Eq. (5.25). This is called the *Nystrom* method.

The iterative procedure from Section 5.1.2 is, if it converges, just one possible numerical method which can be used to solve the set of linear algebraic equations Eq. (5.29). As a matter of fact there are several other methods to solve sets of linear algebraic equations and one applies the method which suits the problem best. If we denote the approximate numerical solution of the

set of linear equations Eq. (5.29) by \mathbf{x}_S (generalizing the notation \mathbf{x}_n of Section 5.1.2 to an arbitrary convergent method), then the error estimate \mathbf{e}_S on the solution \mathbf{x}_R of Eq. (5.29) is defined as,

$$\mathbf{e}_S = \mathbf{x}_R - \mathbf{x}_S. \quad (5.30)$$

The error \mathbf{e}_S will have to be determined by analysing the specific numerical method used to solve the set of linear algebraic equations.

Of course this error estimate is only part of the error if we want to use the solution \mathbf{x}_S as an approximation to the solution $x(s)$ of the integral equation at the nodes $s = t_i$. For this purpose we will also have to investigate the error caused when replacing the integral by a finite sum using the quadrature formula R . If we could solve the set of linear equations Eq. (5.25) exactly, then $(\mathbf{x}_R)_i$ are approximations to the function $x(s)$ at the grid points $s = t_i$. Eq. (5.28) then defines an approximating function $x_R(s)$ to $x(s)$ for all s occurring in the left hand side of the equation. Can we find an error estimate on this approximation ?

We define the error function $e_R(s)$ as,

$$e_R(s) = x(s) - x_R(s). \quad (5.31)$$

Using Eq. (5.20) in Eq. (5.28) we see that the function $x_R(s)$ satisfies the integral equation

$$x_R(s) = y(s) + \lambda \int_a^b K(s, t)x_R(t)dt - E[\lambda Kx_R](s). \quad (5.32)$$

Subtracting Eq. (5.32) from the original integral equation Eq. (5.6) yields:

$$x(s) - x_R(s) = \lambda \int_a^b K(s, t) (x(t) - x_R(t)) dt + E[\lambda Kx_R](s), \quad (5.33)$$

or

$$e_R(s) = \lambda \int_a^b K(s, t) e_R(t) dt + E[\lambda Kx_R](s). \quad (5.34)$$

This means that the error function $e_R(s)$ introduced by the quadrature rule R also satisfies a linear Fredholm integral equation of the second kind. The kernel is the same as in Eq. (5.6) but the driving term is now $E[\lambda Kx_R](s)$ instead of $y(s)$. Taking the function norm of Eq. (5.34) gives

$$\|e_R\| \leq \|\lambda K\| \cdot \|e_R\| + \|E[\lambda Kx_R]\|, \quad (5.35)$$

thus,

$$\|e_R\| \leq \frac{\|E[\lambda Kx_R]\|}{1 - \|\lambda K\|}, \quad (5.36)$$

provided $|\lambda K| < 1$.

A more practical error formula can be derived in vector form. We rewrite Eq. (5.6) using Eq. (5.20):

$$x(s) = y(s) + \lambda \sum_{j=1}^N w_j K(s, t_j) x(t_j) + E[\lambda K x](s). \quad (5.37)$$

Now subtract Eq. (5.28) for \mathbf{x}_R from Eq. (5.37),

$$x(s) - x_R(s) = \lambda \sum_{j=1}^N w_j K(s, t_j) (x(t_j) - x_R(t_j)) + E[\lambda K x](s), \quad (5.38)$$

or

$$e_R(s) = \lambda \sum_{j=1}^N w_j K(s, t_j) e_R(t_j) + E[\lambda K x](s). \quad (5.39)$$

Evaluating this last equation at the nodes t_i gives:

$$e_R(t_i) = \lambda \sum_{j=1}^N w_j K(t_i, t_j) e_R(t_j) + E[\lambda K x](t_i), \quad (5.40)$$

or in vector notation,

$$(I - \lambda K) \mathbf{e}_R = \mathbf{E}[\lambda K x]. \quad (5.41)$$

This set of equation for \mathbf{e}_R has the same coefficients as Eq. (5.25) for \mathbf{x}_R but with a different constant vector. The solution to Eq. (5.41) is given by:

$$\mathbf{e}_R = (I - \lambda K)^{-1} \mathbf{E}[\lambda K x]. \quad (5.42)$$

After taking the vector and matrix norm,

$$\|\mathbf{e}_R\| = \|(I - \lambda K)^{-1}\| \cdot \|\mathbf{E}[\lambda K x]\|, \quad (5.43)$$

which only requires that we can solve Eq. (5.25) and so is applicable even in the case $\|\lambda K\| \geq 1$. Of course this is a formal result where we note that the error term $\|\mathbf{E}[\lambda K x]\|$ is a function of the unknown solution $x(s)$. To use this formula in practice one could approximate $x(s)$ by $x_R(s)$ to evaluate the error term.

We can now combine the error estimates Eq. (5.31) and Eq. (5.30) (neglecting precision errors) to give a total error bound when approximating the solution $x(t_i)$ of the original integral equation Eq. (5.6) at the grid points by the approximated solution $(\mathbf{x}_S)_i$ of the system of equations derived using the quadrature rule R . The error vector \mathbf{e} is defined as:

$$\mathbf{e} = \mathbf{x} - \mathbf{x}_S. \quad (5.44)$$

This can be written as:

$$\mathbf{e} = (\mathbf{x} - \mathbf{x}_R) + (\mathbf{x}_R - \mathbf{x}_S) = \mathbf{e}_R + \mathbf{e}_S. \quad (5.45)$$

Taking the norm:

$$\|\mathbf{e}\| \leq \|\mathbf{e}_R\| + \|\mathbf{e}_S\|, \quad (5.46)$$

where both error terms have been bounded in Eq. (5.43) and Eq. (5.27) (for the iterative procedure).

5.2 Non-linear Fredholm equation of the second kind

We will use the method described in the previous section to build a numerical solution for the *non-linear* Fredholm equation of the second kind. The equation to solve is:

$$x(s) = y(s) + \lambda \int_a^b K(s, t, x(s), x(t)) dt. \quad (5.47)$$

Applying the *Nystrom* method developed in the previous section, we again will approximate the integral by some quadrature formula R , replacing the integral equation Eq. (5.47) by the approximate equation:

$$\hat{x}(s) = y(s) + \lambda \sum_{j=1}^N w_j K(s, t_j, \hat{x}(s), \hat{x}(t_j)). \quad (5.48)$$

If we require that this equation should hold at the points $s = t_i$, Eq. (5.48) becomes a set of N non-linear algebraic equations with N unknowns x_i where $x_i = \hat{x}(t_i)$:

$$x_i = y_i + \lambda \sum_{j=1}^N w_j K(t_i, t_j, x_i, x_j). \quad (5.49)$$

In matrix form this equation can be written as:

$$\mathbf{x} = \mathbf{y} + \lambda \mathbf{K}(\mathbf{t}, \mathbf{x}). \quad (5.50)$$

It is this system of non-linear algebraic equations we want to solve numerically to approximate the solution of the integral equation Eq. (5.47). A straightforward way to try to solve such a set of non-linear algebraic equations is to start from an initial guess \mathbf{x}_0 and to define the *natural* iterative procedure:

$$\mathbf{x}_{n+1} = \mathbf{y} + \lambda \mathbf{K}(\mathbf{t}, \mathbf{x}_n). \quad (5.51)$$

One can assume that if this procedure converges when $n \rightarrow \infty$, it will converge to one of the solutions of Eq. (5.50). The achievement of convergence as well as its rate depend on the behaviour of the kernel $\mathbf{K}(\mathbf{t}, \mathbf{x})$.

From the previous description one sees that two major numerical approximations are involved in solving the original equation. First we have to make a proper choice of numerical quadrature formula and second we truncate the iterative procedure Eq. (5.51) after a finite number of steps. It is important in order to assess the approximate solution to have a good idea of the size of the errors introduced by both approximations. We will return to this in detail in future sections.

To be able to discuss the size of the errors when solving Eq. (5.50) we will first introduce a suitable vector norm on our solution space (pp. 2-17 of Ref. [56]). In general the p -norm of a vector is defined as,

$$\|\mathbf{x}\|_p \equiv \left(\sum_j |x_j|^p \right)^{1/p}. \quad (5.52)$$

Some of the most frequently used vector norms derived from Eq. (5.52) are:

$$\|\mathbf{x}\|_1 \equiv \sum_i |x_i|, \quad (5.53)$$

$$\|\mathbf{x}\|_2 \equiv \sqrt{\sum_i |x_i|^2}, \quad (5.54)$$

$$\|\mathbf{x}\|_\infty \equiv \max_i |x_i|. \quad (5.55)$$

The norm $\|\mathbf{x}\|_2$ is called the *Euclidean norm*, while the norm $\|\mathbf{x}\|_\infty$ is called the *maximum norm*.

To investigate the error on the solution to our problem we will use the maximum norm, defining,

$$\|\mathbf{x}\| \equiv \|\mathbf{x}\|_\infty \equiv \max_i |x_i|. \quad (5.56)$$

The maximum norm is quite interesting because it makes sure that no deviation in any point is larger than $\|\mathbf{x}\|_\infty$. To discuss the error bounds on the solution we also need the *matrix norm* induced by the corresponding vector norm. The matrix norm induced by the maximum norm is,

$$\|A\|_\infty \equiv \max_i \sum_j |A_{ij}|, \quad (5.57)$$

i.e., the *maximum absolute row sum* of the matrix, which is straightforward to compute.

The matrix norm $\|A\|_1$ is given by the *maximum absolute column sum* of the matrix:

$$\|A\|_1 \equiv \max_j \sum_i |A_{ij}|, \quad (5.58)$$

while the matrix norm induced by the *Euclidean norm* is,

$$\|A\|_2 \equiv \sqrt{\rho(A^\dagger A)}, \quad (5.59)$$

where A^\dagger is the hermitian conjugate of A and $\rho(M)$ is the spectral radius of the matrix M defined by

$$\rho(M) \equiv \max_s |\lambda_s(M)|, \quad (5.60)$$

where $\lambda_s(M)$ denotes the eigenvalues of M . From this it is obvious that the Euclidean norm of a matrix is not easily computable and therefore we opt for the maximum norm in our treatment.

The induced matrix norm ensures that the norm of the vector $A\mathbf{x}$ satisfies:

$$\|A\mathbf{x}\| \leq \|A\| \cdot \|\mathbf{x}\|. \quad (5.61)$$

The error \mathbf{e}_n on the approximate solution \mathbf{x}_n to the exact solution \mathbf{x} is,

$$\|\mathbf{e}_n\| = \|\mathbf{x} - \mathbf{x}_n\| = \max_i |x_i - (x_n)_i|. \quad (5.62)$$

We will use this vector norm to compute the distance between two successive iterations of Eq. (5.51). In practice we will terminate the iterative procedure when a certain criterion is fulfilled. Normally we will require that 2 successive iterations are no more distant than a tolerance \mathcal{T} from each other,

$$\|\mathbf{x}_{n+1} - \mathbf{x}_n\| \leq \mathcal{T}. \quad (5.63)$$

We must be careful however if we want to translate $\|\mathbf{x}_{n+1} - \mathbf{x}_n\|$ to the error $\|\mathbf{e}_n\|$ on the exact solution of the vector equation Eq. (5.50). Can we find a relation between those two quantities ?

In the case of a linear Fredholm equation of the second kind, Eq. (5.27) gave us a bound on the error,

$$\|\mathbf{e}_n\| \leq \frac{\|\mathbf{x}_{n+1} - \mathbf{x}_n\|}{1 - \|\lambda K\|}. \quad (5.64)$$

This expression is very useful because it relates the error on the solution to the distance between two successive iterations. Can we derive an analogous expression in the non-linear case ?

We can write:

$$\mathbf{e}_n - \mathbf{e}_{n+1} = (\mathbf{x} - \mathbf{x}_n) - (\mathbf{x} - \mathbf{x}_{n+1}) = \mathbf{x}_{n+1} - \mathbf{x}_n, \quad (5.65)$$

or

$$\mathbf{e}_n = \mathbf{e}_{n+1} + (\mathbf{x}_{n+1} - \mathbf{x}_n). \quad (5.66)$$

Taking the norm,

$$\|\mathbf{e}_n\| \leq \|\mathbf{e}_{n+1}\| + \|\mathbf{x}_{n+1} - \mathbf{x}_n\|. \quad (5.67)$$

Let us write the set of non-linear equations as:

$$\mathbf{x} = \mathbf{g}(\mathbf{x}), \quad (5.68)$$

or

$$x_i = g_i(x_1, \dots, x_N), \quad i = 1, \dots, N. \quad (5.69)$$

The iterative procedure is:

$$\mathbf{x}_{n+1} = \mathbf{g}(\mathbf{x}_n). \quad (5.70)$$

Subtracting Eq. (5.70) from Eq. (5.68), we have

$$\mathbf{x} - \mathbf{x}_{n+1} = \mathbf{g}(\mathbf{x}) - \mathbf{g}(\mathbf{x}_n), \quad (5.71)$$

or

$$\mathbf{e}_{n+1} = \mathbf{g}(\mathbf{x}) - \mathbf{g}(\mathbf{x}_n). \quad (5.72)$$

We now make a Taylor expansion of $\mathbf{g}(\mathbf{x})$ around $\mathbf{g}(\mathbf{x}_n)$:

$$g_i(\mathbf{x}) = g_i(\mathbf{x}_n) + \sum_{j=1}^N \frac{\partial g_i}{\partial x_j}(\mathbf{x}_n) \cdot (x_j - x_{n,j}) + \mathcal{O}(\mathbf{x} - \mathbf{x}_n)^2, \quad i = 1, \dots, N, \quad (5.73)$$

or in vector notation:

$$\mathbf{g}(\mathbf{x}) = \mathbf{g}(\mathbf{x}_n) + \frac{\partial \mathbf{g}}{\partial \mathbf{x}}(\mathbf{x}_n) \cdot (\mathbf{x} - \mathbf{x}_n) + \mathcal{O}(\mathbf{x} - \mathbf{x}_n)^2. \quad (5.74)$$

Thus,

$$\mathbf{g}(\mathbf{x}) - \mathbf{g}(\mathbf{x}_n) = \frac{\partial \mathbf{g}}{\partial \mathbf{x}}(\mathbf{x}_n) \cdot \mathbf{e}_n + \mathcal{O}(\mathbf{e}_n)^2. \quad (5.75)$$

Substitute Eq. (5.75) in Eq. (5.72),

$$\mathbf{e}_{n+1} = \frac{\partial \mathbf{g}}{\partial \mathbf{x}}(\mathbf{x}_n) \cdot \mathbf{e}_n + \mathcal{O}(\mathbf{e}_n)^2. \quad (5.76)$$

After taking the norm,

$$\begin{aligned} \|\mathbf{e}_{n+1}\| &\leq \left\| \frac{\partial \mathbf{g}}{\partial \mathbf{x}}(\mathbf{x}_n) \cdot \mathbf{e}_n \right\| + \|\mathcal{O}(\mathbf{e}_n)^2\| \\ &\leq \left\| \frac{\partial \mathbf{g}}{\partial \mathbf{x}}(\mathbf{x}_n) \right\| \cdot \|\mathbf{e}_n\| + \|\mathcal{O}(\mathbf{e}_n)^2\|. \end{aligned} \quad (5.77)$$

Substituting Eq. (5.77) in Eq. (5.67),

$$\|\mathbf{e}_n\| \leq \|\mathbf{x}_{n+1} - \mathbf{x}_n\| + \left\| \frac{\partial \mathbf{g}}{\partial \mathbf{x}}(\mathbf{x}_n) \right\| \cdot \|\mathbf{e}_n\| + \|\mathcal{O}(\mathbf{e}_n)^2\|. \quad (5.78)$$

Thus, provided $\left\| \frac{\partial \mathbf{g}}{\partial \mathbf{x}}(\mathbf{x}_n) \right\| < 1$,

$$\|\mathbf{e}_n\| \leq \frac{\|\mathbf{x}_{n+1} - \mathbf{x}_n\| + \|\mathcal{O}(\mathbf{e}_n)^2\|}{1 - \left\| \frac{\partial \mathbf{g}}{\partial \mathbf{x}}(\mathbf{x}_n) \right\|}. \quad (5.79)$$

This again relates the error $\|\mathbf{e}_n\|$ to the distance between two successive iterations $\|\mathbf{x}_{n+1} - \mathbf{x}_n\|$. We can neglect the terms of $\mathcal{O}(\mathbf{e}_n)^2$ if \mathbf{x}_n is sufficiently close to the solution \mathbf{x} .

5.3 Schwinger-Dyson equations

5.3.1 The 3 coupled equations

In this section we will formulate the integral equations for which we have to develop the numerical formalism. There are 3 coupled non-linear integral equations describing 3 unknown functions: the dynamical fermion mass Σ , the wavefunction renormalization \mathcal{F} and the photon renormalization function \mathcal{G} .

We recall the integral equations, Eqs. (2.59, 2.60, 2.69), derived in Euclidean space with the bare vertex approximation. In the Landau gauge ($\xi = 0$) with zero bare mass ($m_0 = 0$), these are:

$$\frac{\Sigma(x)}{\mathcal{F}(x)} = \frac{3\alpha}{2\pi^2} \int dy \frac{y\mathcal{F}(y)\Sigma(y)}{y + \Sigma^2(y)} \int d\theta \sin^2 \theta \frac{\mathcal{G}(z)}{z} \quad (5.80)$$

$$\begin{aligned} \frac{1}{\mathcal{F}(x)} &= 1 - \frac{\alpha}{2\pi^2 x} \int dy \frac{y\mathcal{F}(y)}{y + \Sigma^2(y)} \\ &\times \int d\theta \sin^2 \theta \mathcal{G}(z) \left[\frac{2xy \sin^2 \theta}{z^2} - \frac{3\sqrt{xy} \cos \theta}{z} \right] \end{aligned} \quad (5.81)$$

$$\begin{aligned} \frac{1}{\mathcal{G}(x)} &= 1 + \frac{4N_f \alpha}{3\pi^2 x} \int dy \frac{y\mathcal{F}(y)}{y + \Sigma^2(y)} \\ &\times \int d\theta \sin^2 \theta \frac{\mathcal{F}(z)}{z + \Sigma^2(z)} \left[y(1 - 4 \cos^2 \theta) + 3\sqrt{xy} \cos \theta \right], \end{aligned} \quad (5.82)$$

where $z \equiv x + y - 2\sqrt{xy} \cos \theta$.

If we look at these integral equations, one of the striking features is that the integrals involved are 2-dimensional integrals, the radial and the angular integrals both involve the unknown functions. This is different from quenched QED, where $\mathcal{G}(x) = 1$ implies that the angular integrals in the

\mathcal{F} and Σ equations can be performed analytically, leaving 2 coupled 1-dimensional integral equations to solve. The fact that the problem of unquenched QED involves 2-dimensional integrals is a major problem because it is very computer time consuming.

Symbolically we can write the equations as:

$$\begin{cases} \frac{\Sigma}{\mathcal{F}} = f_1[\Sigma, \mathcal{F}, \mathcal{G}] \\ \frac{1}{\mathcal{F}} = f_2[\Sigma, \mathcal{F}, \mathcal{G}] \\ \frac{1}{\mathcal{G}} = f_3[\Sigma, \mathcal{F}, \mathcal{G}], \end{cases} \quad (5.83)$$

or

$$\frac{\Sigma(x)}{\mathcal{F}(x)} = \int dy \int d\theta K_1(y, \Sigma(y), \mathcal{F}(y), \theta, z, \mathcal{G}(z)) \quad (5.84)$$

$$\frac{1}{\mathcal{F}(x)} = 1 + \int dy \int d\theta K_2(x, y, \Sigma(y), \mathcal{F}(y), \theta, z, \mathcal{G}(z)) \quad (5.85)$$

$$\frac{1}{\mathcal{G}(x)} = 1 + \int dy \int d\theta K_3(x, y, \Sigma(y), \mathcal{F}(y), \theta, z, \Sigma(z), \mathcal{F}(z)). \quad (5.86)$$

A straightforward method is to discretize the problem. This means we will solve the problem for a finite number of function values Σ_i , \mathcal{F}_i and \mathcal{G}_i . In practice these function values are taken at momenta x_i which are the nodes of the quadrature rule used to approximate the integrals. Because of the expected behaviour of the unknown functions and the integration kernels we choose the grid points on a logarithmic scale in momentum squared. For numerical purposes we introduce an infrared cutoff κ as well as an ultraviolet cutoff Λ . We define a grid of $N + 1$ equidistant points t_i , $i = 0, \dots, N$:

$$t_i = \log_{10}(\kappa^2) + \frac{i}{N} \left(\log_{10}(\Lambda^2) - \log_{10}(\kappa^2) \right). \quad (5.87)$$

Discretizing the functions at the integration nodes implies that the function values needed in the numerical approximation of the radial integrals are exactly the tabulated function values. We are thus looking for the function values Σ_i , \mathcal{F}_i and \mathcal{G}_i satisfying,

$$\frac{\Sigma_i}{\mathcal{F}_i} = \sum_j w_j \sum_k w_k K_1(x_j, \Sigma_j, \mathcal{F}_j, \theta_k, z_k, \mathcal{G}_k) \quad (5.88)$$

$$\frac{1}{\mathcal{F}_i} = 1 + \sum_j w_j \sum_k w_k K_2(x_i, x_j, \Sigma_j, \mathcal{F}_j, \theta_k, z_k, \mathcal{G}_k) \quad (5.89)$$

$$\frac{1}{\mathcal{G}_i} = 1 + \sum_j w_j \sum_k w_k K_3(x_i, x_j, \Sigma_j, \mathcal{F}_j, \theta_k, z_k, \Sigma_k, \mathcal{F}_k), \quad (5.90)$$

where $z_k = x_i + x_j - 2\sqrt{x_i x_j} \cos \theta_k$.

Unfortunately the angular integrals of the equations will use function values which are not tabulated. In Eqs. (5.88, 5.89) we need the function values for the photon renormalization function \mathcal{G} at the momentum z_k , while analogously in Eq. (5.90) we need the function values of Σ and \mathcal{F} at the momentum z_k . Whatever numerical quadrature formula one uses for the angular integrals, we always need the unknown functions at values which are not tabulated. These untabulated function values can be estimated by interpolating the functions Σ , \mathcal{F} and \mathcal{G} between two tabulated values. The simplest interpolation scheme will be to use linear interpolation on the logarithm of momentum squared:

$$f(z) = f(x) + \frac{\log_{10} z - \log_{10} x}{\log_{10} y - \log_{10} x} [f(y) - f(x)]. \quad (5.91)$$

5.3.2 Simplified approach: the Σ equation

To develop the numerical program we will first introduce a number of approximations to simplify the problem. As we are working in the Landau gauge with the bare vertex we approximate \mathcal{F} by $\mathcal{F}(x) \equiv 1$. This is motivated by the results of quenched QED and can even be found in unquenched QED after introducing the LAK(Landau-Abrikhizov-Khalatnikov)-approximation $\mathcal{G}(z) = \mathcal{G}(\max(y, x))$. In both cases $F(x)$ will be equal to one. A further approximation consists in replacing the full vacuum polarization by its 1-loop perturbative value instead of solving the photon Schwinger-Dyson equation,

$$\Pi(z) = \frac{N_f \alpha}{3\pi} \left(\ln \frac{\Lambda^2}{z} + C \right), \quad (5.92)$$

where C is a renormalization constant. If we choose $C = 0$ such that $\Pi(\Lambda^2) = 0$ the photon renormalization function \mathcal{G} becomes,

$$\mathcal{G}(z) = \left(1 + \frac{N_f \alpha}{3\pi} \ln \frac{\Lambda^2}{z} \right)^{-1}, \quad (5.93)$$

with $\mathcal{G}(\Lambda^2) = 1$.

The coupled set of integral equations, Eqs. (5.80, 5.81, 5.82), now simplifies to a single non-linear integral equation for the dynamical fermion mass Σ :

$$\Sigma(x) = \frac{3\alpha}{2\pi^2} \int dy \frac{y\Sigma(y)}{y + \Sigma^2(y)} \int d\theta \frac{\sin^2 \theta}{z(1 + \frac{N_f \alpha}{3\pi} \ln \frac{\Lambda^2}{z})}. \quad (5.94)$$

To develop the numerical method we could as well start from the Σ -equation in quenched QED, however in the 1-loop approximation the problem is more realistic because the angular integrals cannot be computed analytically as will also be the case in the complete treatment of the coupled system of integral equations.

We now face two problems: firstly how do we choose the quadrature rules to compute the radial and angular integrals, secondly how do we find a solution for $\Sigma(x)$ once the quadrature rules have been introduced ?

To make a sensible choice of integration rule we have to study the behaviour of the integration kernel using some assumption for the unknown function. From previous studies of quenched QED we know that the integration nodes are best chosen on a logarithmic scale in momentum squared. Therefore we will change variables in Eq. (5.94):

$$t = \log_{10} y \quad (5.95)$$

$$dt = \frac{dy}{y \ln 10}. \quad (5.96)$$

Substituting this in Eq. (5.94),

$$\Sigma(x) = \frac{3\alpha \ln 10}{2\pi^2} \int_{-\infty}^{\infty} dt \frac{y^2 \Sigma(y)}{y + \Sigma^2(y)} \int d\theta \frac{\sin^2 \theta}{z(1 + \frac{N_f \alpha}{3\pi} \ln \frac{\Lambda^2}{z})}, \quad (5.97)$$

where $y = 10^t$.

To compute the integrals numerically we will introduce an ultraviolet cutoff Λ^2 and an infrared cutoff κ^2 on the radial integration. The ultraviolet cutoff is introduced to regularize the integrals while the infrared cutoff only serves numerical purposes. When introducing the infrared cutoff one has to ensure that either the neglected part of the integrals, i.e. $\int_0^{\kappa^2}$ is negligible, or else one must evaluate analytically the contribution of the lower part of the integral and add it to the numerical integral. As we will see later we will choose the infrared cutoff κ^2 so that the infrared part of the integral is negligible and Eq. (5.97) can be replaced by:

$$\Sigma(x) = \frac{3\alpha \ln 10}{2\pi^2} \int_{\log_{10} \kappa^2}^{\log_{10} \Lambda^2} dt \frac{y^2 \Sigma(y)}{y + \Sigma^2(y)} \int d\theta \frac{\sin^2 \theta}{z(1 + \frac{N_f \alpha}{3\pi} \ln \frac{\Lambda^2}{z})}. \quad (5.98)$$

We now introduce the quadrature rules to approximate the integrals numerically, Eq. (5.98) is replaced by the approximate equation:

$$\Sigma(x) = \frac{3\alpha \ln 10}{2\pi^2} \sum_{j=0}^N w_j \frac{x_j^2 \Sigma(x_j)}{x_j + \Sigma^2(x_j)} \sum_{k=0}^M w'_k \frac{\sin^2 \theta_k}{z_k(1 + \frac{N_f \alpha}{3\pi} \ln \frac{\Lambda^2}{z_k})}, \quad (5.99)$$

w_j, w'_k are the weights of the quadrature rules R and R' (which can be different) used respectively to compute the radial and angular integrals. The photon momentum is $z_k = x + x_j - 2\sqrt{xx_j} \cos \theta_k$. A simple choice of integration rule could be a closed formula with $N + 1$ equidistant nodes such as a composite Newton-Cotes formula [56]. The nodes are then given by:

$$t_i = \log_{10} \kappa^2 + \frac{i}{N} \left(\log_{10} \Lambda^2 - \log_{10} \kappa^2 \right), \quad (5.100)$$

with corresponding momenta squared,

$$x_i = k_i^2 = 10^{t_i}. \quad (5.101)$$

How do we find a solution $\Sigma(x)$ of Eq. (5.99) ? One possible solution method is the *collocation method* where one only requires the equation Eq. (5.99) to hold at the integration nodes t_i ,

$$\Sigma_i = \frac{3\alpha \ln 10}{2\pi^2} \sum_{j=0}^N w_j \frac{x_j^2 \Sigma_j}{x_j + \Sigma_j^2} \sum_{k=0}^M w'_k \frac{\sin^2 \theta_k}{z_k \left(1 + \frac{N_f \alpha}{3\pi} \ln \frac{\Lambda^2}{z_k} \right)}, \quad i = 0, \dots, N, \quad (5.102)$$

where we denote $\Sigma_i = \Sigma(x_i)$ and $z_k = x_i + x_j - 2\sqrt{x_i x_j} \cos \theta_k$.

This set of equations is self-consistent and only involves the function values of Σ at the integration points; we do not need any information about Σ at any other point in momentum space. Eq. (5.102) is in fact just the application of the Nystrom method for non-linear Fredholm equations Eq. (5.49) to the Σ -equation Eq. (5.98). If we succeed in solving this set of equations, our knowledge about the function $\Sigma(x)$ will completely reside in the knowledge of the function at a finite number of points; $\Sigma(x)$ has been discretized.

Eq. (5.102) is a set of $(N + 1)$ non-linear algebraic equations for the $(N + 1)$ unknowns Σ_i . An evident method to solve Eq. (5.102) would be to use the natural iterative procedure proposed in Eq. (5.51). We start from an initial guess $(\Sigma_0)_i, i = 0, \dots, N$, and define the iterative procedure:

$$(\Sigma_{n+1})_i = \frac{3\alpha \ln 10}{2\pi^2} \sum_{j=0}^N w_j \frac{x_j^2 (\Sigma_n)_j}{x_j + (\Sigma_n)_j^2} \sum_{k=0}^M w'_k \frac{\sin^2 \theta_k}{z_k \left(1 + \frac{N_f \alpha}{3\pi} \ln \frac{\Lambda^2}{z_k} \right)}, \quad i = 0, \dots, N. \quad (5.103)$$

Does this iterative procedure converge ? If it converges, what is the error on the approximate solution if we truncate the procedure after n steps ?

If we use the empirical approach, implementing the iterative procedure in a computer program and turning the handle, we observe that for sufficiently large coupling α and for a suitably chosen starting guess Σ_0 the iterations tend to converge to a non-trivial solution but at an extremely

low rate. For example, if we require that $\|\Sigma_{\mathbf{n}+1} - \Sigma_{\mathbf{n}}\| \leq \mathcal{T}$, with $\mathcal{T} = \Sigma(0)/1000$, the natural iteration scheme requires several thousands iteration steps to reach the convergence criterion.

Furthermore, it seems very difficult to obtain a reasonable error estimate on the truncated solution $\Sigma_{\mathbf{n}}$ as an approximate solution to the solution Σ of Eq. (5.102). To get an idea of the accuracy of the approximation $\Sigma_{\mathbf{n}}$ we now decrease the value of the tolerance to $\mathcal{T}' = \mathcal{T}/10$ and continue the iterative procedure till a solution $\Sigma_{\mathbf{n}'}$ has been found which satisfies the new tolerance condition. For the iterative method to be reliable we expect the new approximate solution $\Sigma_{\mathbf{n}'}$ not to be much more distant from $\Sigma_{\mathbf{n}}$ than \mathcal{T} as the approximation $\Sigma_{\mathbf{n}}$ was found by imposing the tolerance \mathcal{T} . In reality this seems not to be fulfilled, the results of the numerical program show that the difference $\|\Sigma_{\mathbf{n}'} - \Sigma_{\mathbf{n}}\|$ is much larger than \mathcal{T} . This means that we cannot rely on the approximation $\Sigma_{\mathbf{n}}$ to be an approximate solution to Σ of Eq. (5.102) with an accuracy of $\mathcal{O}(\mathcal{T})$ and that we have no definite error estimate of the solution $\Sigma_{\mathbf{n}}$.

To understand this feature we will investigate if the error formula Eq. (5.79) can be used on the system of non-linear equations Eq. (5.102). From Eq. (5.102) we can formulate our system of non-linear equations in a general form:

$$\Sigma_i = \sum_j K_{ij}, \quad (5.104)$$

where the kernel can be written as:

$$K_{ij} = C_{ij} \frac{\Sigma_j}{x_j + \Sigma_j^2}. \quad (5.105)$$

The iterative procedure to solve this will be:

$$(\Sigma_{n+1})_i = \sum_j (K_n)_{ij} = \sum_j C_{ij} \frac{(\Sigma_n)_j}{x_j + (\Sigma_n)_j^2}. \quad (5.106)$$

The error discussion in Section 5.2 led to an error bound Eq. (5.79) on the error $\mathbf{e}_{\mathbf{n}}$, after truncation of the iterative procedure Eq. (5.106), which can be rewritten in the current notation as,

$$\|\mathbf{e}_{\mathbf{n}}\| \leq \frac{\|\Sigma_{\mathbf{n}+1} - \Sigma_{\mathbf{n}}\| + \|\mathcal{O}(\mathbf{e}_{\mathbf{n}})^2\|}{1 - \left\| \frac{\partial \mathbf{K}}{\partial \Sigma}(\Sigma_{\mathbf{n}}) \right\|}, \quad (5.107)$$

provided $\left\| \frac{\partial \mathbf{K}}{\partial \Sigma}(\Sigma_{\mathbf{n}}) \right\| < 1$, where $K_i = \sum_j K_{ij}$.

Taking the partial derivative of Eq. (5.105) with respect to Σ_k , we obtain

$$\frac{\partial K_{ij}}{\partial \Sigma_k} = C_{ij} \left[\frac{x_j - \Sigma_j^2}{(x_j + \Sigma_j^2)^2} \right] \delta_{jk}. \quad (5.108)$$

Thus,

$$\left(\frac{\partial \mathbf{K}}{\partial \Sigma}\right)_{ij} = \left(\frac{\partial K_i}{\partial \Sigma_j}\right) = \sum_k \left(\frac{\partial K_{ik}}{\partial \Sigma_j}\right) = C_{ij} \left[\frac{x_j - \Sigma_j^2}{(x_j + \Sigma_j^2)^2}\right]. \quad (5.109)$$

For Eq. (5.107) to be valid we know that

$$\left\|\frac{\partial \mathbf{K}}{\partial \Sigma}(\Sigma_{\mathbf{n}})\right\| = \max_i \sum_j \left|\frac{\partial K_i}{\partial \Sigma_j}(\Sigma_{\mathbf{n}})\right| < 1, \quad (5.110)$$

or,

$$\max_i \sum_j \left|C_{ij} \left[\frac{x_j - (\Sigma_n)_j^2}{(x_j + (\Sigma_n)_j^2)^2}\right]\right| < 1. \quad (5.111)$$

From the numerical results we learn that $\left\|\frac{\partial \mathbf{K}}{\partial \Sigma}(\Sigma_{\mathbf{n}})\right\| \approx 3$ and thus condition Eq. (5.110) is not satisfied by the kernel of the fermion equation and therefore the error bound Eq. (5.107) cannot be used in this case. This is the reason why the rate of convergence is so slow and the error estimate so unreliable.

5.4 Newton's iterative method

Let us now consider an alternative method to improve the convergence rate of the iterative procedure (pp. 109-119 of Ref. [56]). Consider a general system of non-linear algebraic equations

$$\mathbf{f}(\mathbf{x}) = \mathbf{0}. \quad (5.112)$$

The most natural way to solve this set of equations iteratively consists in rewriting Eq. (5.112) as

$$\mathbf{x} = \mathbf{g}(\mathbf{x}), \quad (5.113)$$

with

$$\mathbf{g}(\mathbf{x}) \equiv \mathbf{x} - \mathbf{f}(\mathbf{x}) \quad (5.114)$$

and then to define the iterative procedure

$$\mathbf{x}_{\mathbf{n}+1} = \mathbf{g}(\mathbf{x}_{\mathbf{n}}) = \mathbf{x}_{\mathbf{n}} + \mathbf{f}(\mathbf{x}_{\mathbf{n}}). \quad (5.115)$$

However, as we saw in the previous section, this iterative procedure does not always converge and if it converges the convergence rate can be very slow and the error estimate unreliable.

In order to define an alternative iterative procedure to Eq. (5.115) we now replace Eq. (5.114) by:

$$\mathbf{g}(\mathbf{x}) \equiv \mathbf{x} - A(\mathbf{x})\mathbf{f}(\mathbf{x}), \quad (5.116)$$

where $A(\mathbf{x})$ is a square matrix of order $N + 1$. If $A(\mathbf{x})$ is non-singular, Eq. (5.113) and Eq. (5.112) will have the same solutions.

The simplest choice for $A(\mathbf{x})$ is a constant non-singular matrix,

$$A(\mathbf{x}) = A. \quad (5.117)$$

Next we define a matrix $J(\mathbf{x})$ by:

$$J(\mathbf{x}) \equiv \left(\frac{\partial f_i(\mathbf{x})}{\partial x_j} \right) \quad (5.118)$$

the determinant of which is the Jacobian of the function $f_i(\mathbf{x})$.

We also define a matrix $G(\mathbf{x})$:

$$G(\mathbf{x}) \equiv \left(\frac{\partial g_i(\mathbf{x})}{\partial x_j} \right). \quad (5.119)$$

Substituting Eqs. (5.116, 5.117, 5.118) in Eq. (5.119) gives,

$$G(\mathbf{x}) = I - AJ(\mathbf{x}). \quad (5.120)$$

We now define an iterative procedure to solve Eq. (5.113):

$$\mathbf{x}_{\mathbf{n}+1} = \mathbf{g}(\mathbf{x}_{\mathbf{n}}), \quad (5.121)$$

or using Eq. (5.116),

$$\mathbf{x}_{\mathbf{n}+1} = \mathbf{x}_{\mathbf{n}} - A\mathbf{f}(\mathbf{x}_{\mathbf{n}}). \quad (5.122)$$

One can prove Eq. (5.122) will converge, for \mathbf{x}_0 sufficiently close to a solution $\tilde{\mathbf{x}}$ of Eq. (5.112), if the elements in the matrix $G(\mathbf{x})$ of Eq. (5.120) are sufficiently small. This could be realized in the case that $J(\tilde{\mathbf{x}})$ is non-singular and taking the constant matrix A to be approximately the inverse of $J(\tilde{\mathbf{x}})$. This naturally suggests a modification where we replace the constant matrix A from Eq. (5.117) by the choice

$$A(\mathbf{x}) \equiv J^{-1}(\mathbf{x}). \quad (5.123)$$

The iterative procedure constructed with the matrix of Eq. (5.123) is called *Newton's method*.

Substituting Eq. (5.123) in Eq. (5.122) gives the following iterative procedure equation:

$$\mathbf{x}_{\mathbf{n}+1} = \mathbf{x}_{\mathbf{n}} - J^{-1}(\mathbf{x}_{\mathbf{n}}) \mathbf{f}(\mathbf{x}_{\mathbf{n}}). \quad (5.124)$$

Although this suggests that we have to invert a matrix of order $N + 1$ at each iteration step, we can transform the procedure from Eq. (5.124) so that we only have to solve a linear system of order $N + 1$ at each iteration step. Multiply both sides of Eq. (5.124) with $J(\mathbf{x}_n)$,

$$J(\mathbf{x}_n) (\mathbf{x}_n - \mathbf{x}_{n+1}) = \mathbf{f}(\mathbf{x}_n). \quad (5.125)$$

If we define

$$\Delta_{n+1} = \mathbf{x}_n - \mathbf{x}_{n+1} \quad (5.126)$$

then Eq. (5.125) is a linear system of order $N + 1$ to be solved for the vector Δ_{n+1} ,

$$\boxed{J(\mathbf{x}_n) \Delta_{n+1} = \mathbf{f}(\mathbf{x}_n)}. \quad (5.127)$$

From \mathbf{x}_n and the solution Δ_{n+1} of Eq. (5.127) we derive the next approximation \mathbf{x}_{n+1} using Eq. (5.126).

One can generally show that provided

$$G(\tilde{\mathbf{x}}) \equiv \left(\frac{\partial g_i(\tilde{\mathbf{x}})}{\partial x_j} \right) = 0, \quad i, j = 0, \dots, N. \quad (5.128)$$

there is a radius ρ for which the iteration procedure $\mathbf{x}_{n+1} = \mathbf{g}(\mathbf{x}_n)$ converges quadratically to the solution $\tilde{\mathbf{x}}$ of Eq. (5.112) for any starting guess \mathbf{x}_0 satisfying:

$$\|\mathbf{x}_0 - \tilde{\mathbf{x}}\| \leq \rho. \quad (5.129)$$

We will now show that Newton's method satisfies Eq. (5.128) so that the method converges quadratically to a solution $\tilde{\mathbf{x}}$ of Eq. (5.112) provided the starting guess \mathbf{x}_0 is sufficiently close to $\tilde{\mathbf{x}}$.

From Eqs. (5.116, 5.123) the j^{th} column of G is given by,

$$\begin{aligned} \frac{\partial \mathbf{g}(\mathbf{x})}{\partial x_j} &= \frac{\partial \mathbf{x}}{\partial x_j} - \frac{\partial}{\partial x_j} [J^{-1}(\mathbf{x}) \mathbf{f}(\mathbf{x})] \\ &= \frac{\partial \mathbf{x}}{\partial x_j} - J^{-1}(\mathbf{x}) \frac{\partial \mathbf{f}(\mathbf{x})}{\partial x_j} - \frac{\partial J^{-1}(\mathbf{x})}{\partial x_j} \mathbf{f}(\mathbf{x}). \end{aligned} \quad (5.130)$$

Setting $\mathbf{x} = \tilde{\mathbf{x}}$ in Eq. (5.130) and recalling that the solution $\tilde{\mathbf{x}}$ satisfies $\mathbf{f}(\tilde{\mathbf{x}}) = \mathbf{0}$ and $J = \partial f_i / \partial x_j$ we get

$$G(\tilde{\mathbf{x}}) = I - J^{-1}(\tilde{\mathbf{x}}) J(\tilde{\mathbf{x}}) - \frac{\partial J^{-1}(\tilde{\mathbf{x}})}{\partial \mathbf{x}} \mathbf{0} = 0, \quad (5.131)$$

provided the matrix $\partial J^{-1}(\tilde{\mathbf{x}})/\partial x_j$ in Eq. (5.130) exists. To determine $\partial J^{-1}(\mathbf{x})/\partial x_j$ we compute:

$$\frac{\partial(J^{-1}J)}{\partial x_j} = J^{-1} \frac{\partial J}{\partial x_j} + \frac{\partial J^{-1}}{\partial x_j} J \quad (5.132)$$

but also,

$$\frac{\partial(J^{-1}J)}{\partial x_j} = \frac{\partial I}{\partial x_j} = 0. \quad (5.133)$$

This means,

$$\frac{\partial J^{-1}(\mathbf{x})}{\partial x_j} = -J^{-1}(\mathbf{x}) \frac{\partial J(\mathbf{x})}{\partial x_j} J^{-1}(\mathbf{x}). \quad (5.134)$$

Thus, Eq. (5.131) will be satisfied and the Newton method will be quadratically convergent if $\mathbf{f}(\mathbf{x})$ has two derivatives and $J(\mathbf{x})$ is non-singular at the root $\tilde{\mathbf{x}}$.

Furthermore one could also show that provided the starting guess \mathbf{x}_0 is close enough to $\tilde{\mathbf{x}}$ the error on the approximate solution is bound by:

$$\|\mathbf{e}_{\mathbf{n}+1}\| \leq \|\mathbf{x}_{\mathbf{n}+1} - \mathbf{x}_{\mathbf{n}}\|. \quad (5.135)$$

Although this bound is hugely overestimated it is very useful for practical purposes as we will now explain. Indeed, this bound tells us that the distance between the approximation $\mathbf{x}_{\mathbf{n}+1}$ and the exact solution cannot exceed the distance between the solutions of the last iteration and that of the previous one.

Let us now apply Newton's method to the system of non-linear equations Eq. (5.102) for the dynamically generated fermion mass. The equations can be written symbolically as:

$$\Sigma_i = \sum_j K_{ij}, \quad i = 0, \dots, N, \quad (5.136)$$

with kernel

$$K_{ij} = C_{ij} \frac{\Sigma_j}{x_j + \Sigma_j^2}, \quad i, j = 0, \dots, N. \quad (5.137)$$

This can be written in the form of Eq. (5.112) by defining $\mathbf{f}(\boldsymbol{\Sigma})$ as,

$$f_i(\boldsymbol{\Sigma}) = \Sigma_i - \sum_j K_{ij} = 0, \quad i = 0, \dots, N. \quad (5.138)$$

Using Eq. (5.138) we derive the matrix J from Eq. (5.118)

$$J_{ij} \equiv \left(\frac{\partial f_i}{\partial \Sigma_j} \right) = \delta_{ij} - \sum_k \frac{\partial K_{ik}}{\partial \Sigma_j}, \quad i, j = 0, \dots, N. \quad (5.139)$$

The derivative of the kernel Eq. (5.137) with respect to Σ_k is,

$$\frac{\partial K_{ij}}{\partial \Sigma_k} = C_{ij} \frac{x_j - \Sigma_j^2}{(x_j + \Sigma_j^2)^2} \delta_{jk}, \quad i, j, k = 0, \dots, N. \quad (5.140)$$

Substituting Eq. (5.140) in Eq. (5.139) yields,

$$J_{ij} = \delta_{ij} - C_{ij} \frac{x_j - \Sigma_j^2}{(x_j + \Sigma_j^2)^2}, \quad i, j = 0, \dots, N. \quad (5.141)$$

Substituting Eqs. (5.138, 5.137, 5.141) in Eq. (5.127) yields:

$$\sum_j \left(\delta_{ij} - C_{ij} \frac{x_j - (\Sigma_n)_j^2}{(x_j + (\Sigma_n)_j^2)^2} \right) (\Delta_{n+1})_j = (\Sigma_n)_i - \sum_j C_{ij} \frac{(\Sigma_n)_j}{x_j + (\Sigma_n)_j^2}, \quad i = 0, \dots, N. \quad (5.142)$$

For each iteration we have to solve Eq. (5.142) for Δ_{n+1} . Then from this solution we compute a new approximation Σ_{n+1} with,

$$\Sigma_{n+1} = \Sigma_n - \Delta_{n+1}. \quad (5.143)$$

From the numerical results we can say that the implementation of Newton's method has given a tremendous improvement as well in convergence rate (number of iteration steps needed to satisfy $\|\Sigma^{n+1} - \Sigma^n\| \leq \mathcal{T}$) as in reliability of the error estimate on the approximate solution (see Eq. (5.135)).

The required accuracy is achieved in less than 10 steps. Although each step requires the solution of a linear system of order $N + 1$ we observe an important decrease of the computer time needed to find the approximate solution satisfying the convergence criterion. Another consequence of the quadratic convergence is that the distance between two successive iteration decrease very rapidly, often as,

$$\|\Sigma_{n+1} - \Sigma_n\| \approx \frac{\|\Sigma_n - \Sigma_{n-1}\|}{10}. \quad (5.144)$$

From the numerical results it is clear that terminating the iterative procedure when two successive iterations are closer than a tolerance \mathcal{T} ensures that the exact solution is within \mathcal{T} of the last iteration and surely even much closer than that.

A straightforward check of the reliability of Newton's method compared to the natural iterative procedure Eq. (5.106) can be performed by varying the starting guess Σ_0 . The convergence of the natural iterative procedure is very sensitive to the starting guess: it only converges (although very slowly) if the starting guess is larger than but close to the exact solution; it will diverge if

the starting guess is too large, i.e. much larger than the exact solution, and it will converge to the trivial solution $\Sigma = \mathbf{0}$ (which is always a solution to the equation) as soon as the starting guess is taken smaller than the exact solution. Even when the method does converge to the non-trivial solution we observe that for varying Σ_0 the natural iteration scheme gives very different approximate solutions Σ_n satisfying the convergence criterion Eq. (5.63) for a fixed \mathcal{T} . This is due to the fact that the error \mathbf{e}_n on the approximate solutions in the natural iterative procedure is much larger than the required tolerance \mathcal{T} between two successive iterations. We could in fact use this information to get some better estimate of the error on the approximate solution, by comparing the solutions reached from different initial guesses Σ_0 .

In contrast to this, the Newton method performs exceptionally well. Its convergence is almost always guaranteed, independent of the starting guess. Only if the starting guess is chosen very far from the exact solution will it just need a couple more iteration steps to reach the solution and if the starting guess is chosen too close to zero, the method will converge to the trivial solution $\Sigma = \mathbf{0}$. In the case of convergence to the non-trivial solution the method is completely independent of the starting guess Σ_0 : the approximate solutions Σ_n satisfying Eq. (5.63) are all equal within this tolerance and even much closer than that.

The iterative procedure Eq. (5.138) can be extended in a straightforward manner to a system of two or more coupled equations with two or more unknown functions. As an example we take the case of the coupling of the integral equations for the fermion wavefunction \mathcal{F} and for the dynamical fermion mass Σ ,

$$f_{1,i}(\Sigma, \mathcal{F}) = 0, \quad i = 0, \dots, N, \quad (5.145)$$

$$f_{2,i}(\Sigma, \mathcal{F}) = 0, \quad i = 0, \dots, N. \quad (5.146)$$

This system can be written in the form of Eq. (5.112),

$$\mathbf{f}(\mathbf{x}) = \begin{pmatrix} \mathbf{f}_1(\mathbf{x}) \\ \mathbf{f}_2(\mathbf{x}) \end{pmatrix} = \begin{pmatrix} f_{1,0}(\mathbf{x}) \\ \vdots \\ f_{1,N}(\mathbf{x}) \\ f_{2,0}(\mathbf{x}) \\ \vdots \\ f_{2,N}(\mathbf{x}) \end{pmatrix} = \mathbf{0} \quad (5.147)$$

with

$$\mathbf{x} = \begin{pmatrix} \boldsymbol{\Sigma} \\ \mathcal{F} \end{pmatrix} = \begin{pmatrix} \Sigma_0 \\ \vdots \\ \Sigma_N \\ \mathcal{F}_0 \\ \vdots \\ \mathcal{F}_N \end{pmatrix}. \quad (5.148)$$

Eq. (5.147) can be solved using Newton's iterative procedure Eq. (5.127),

$$J(\mathbf{x}_n) \boldsymbol{\Delta}_{n+1} = \mathbf{f}(\mathbf{x}_n), \quad (5.149)$$

where

$$J(\mathbf{x}) = \left(\frac{\partial f_i(\mathbf{x})}{\partial x_j} \right), \quad i, j = 0 \dots 2N + 1 \quad (5.150)$$

$$= \begin{pmatrix} \frac{\partial f_{1,i}(\boldsymbol{\Sigma}, \mathcal{F})}{\partial \Sigma_j} & \frac{\partial f_{1,i}(\boldsymbol{\Sigma}, \mathcal{F})}{\partial \mathcal{F}_j} \\ \frac{\partial f_{2,i}(\boldsymbol{\Sigma}, \mathcal{F})}{\partial \Sigma_j} & \frac{\partial f_{2,i}(\boldsymbol{\Sigma}, \mathcal{F})}{\partial \mathcal{F}_j} \end{pmatrix}, \quad i, j = 0, \dots, N. \quad (5.151)$$

$$(5.152)$$

Every iteration now requires the solution of a system of $2N + 2$ linear equations Eq. (5.149) for the $2N + 2$ unknown components of the vector $\boldsymbol{\Delta}_{n+1}$. Successive iterations will yield new function approximations for $\Sigma_0, \dots, \Sigma_N, \mathcal{F}_0, \dots, \mathcal{F}_N$ computed from:

$$\mathbf{x}_{n+1} = \mathbf{x}_n - \boldsymbol{\Delta}_{n+1}, \quad (5.153)$$

or,

$$\begin{pmatrix} \boldsymbol{\Sigma}_{n+1} \\ \mathcal{F}_{n+1} \end{pmatrix} = \begin{pmatrix} \boldsymbol{\Sigma}_n \\ \mathcal{F}_n \end{pmatrix} - \boldsymbol{\Delta}_{n+1}. \quad (5.154)$$

5.5 Numerical integration rules

In the previous sections we replaced the original integral equation by a system of non-linear algebraic equations using some integration rule and derived a method to solve this set of equations. If we look at the error \mathbf{e} on the approximate solution $\boldsymbol{\Sigma}_n$ with respect to the exact solution $\Sigma(x)$ of the original integral equation we have to consider two error sources (neglecting precision errors): the error \mathbf{e}_R due to the approximation of the integrals by a finite sum using some

quadrature rule R and the error \mathbf{e}_n introduced by solving the system of non-linear equations numerically,

$$\|\mathbf{e}\| \leq \|\mathbf{e}_R\| + \|\mathbf{e}_n\|. \quad (5.155)$$

As we saw in the previous section the error $\|\mathbf{e}_n\|$ is well controlled if we use Newton's method, because of its quadratic convergence. The only limitation on the accuracy in Newton's method seems to come from the numerical precision of the computation and the available computer time. Therefore, the major source of error on the solution will be caused by the quadrature rule. It is important to note that the situation is very critical when solving integrals as part of an integral equation problem because the quadrature error gets amplified quite dramatically in the final solution of the integral equation as we will see later. Furthermore the choice of quadrature rule is even more important as the integrals to solve are two-dimensional and therefore the potential errors even bigger.

If we use a quadrature formula with $N + 1$ grid points to approximate the radial integrals we will end up with a system of $N + 1$ non-linear algebraic equations to solve. To reduce the computing time we want to get maximum accuracy with a minimum of grid points.

The best-known quadrature formulae are probably the *Newton-Cotes* formulae, using equidistant grid points. To approximate the integral:

$$\int_a^b f(x)dx, \quad (5.156)$$

the most frequently used Newton-Cotes formulae, with their corresponding error-term are:

the midpoint rule:

$$\int_{x_0}^{x_2} f(x)dx = 2hf_1 + \frac{h^3}{3}f^{(2)}(\xi), \quad x_0 < \xi < x_2 \quad (5.157)$$

the trapezoidal rule:

$$\int_{x_0}^{x_1} f(x)dx = \frac{h}{2}(f_0 + f_1) - \frac{h^3}{12}f^{(2)}(\xi), \quad x_0 < \xi < x_1 \quad (5.158)$$

Simpson's rule:

$$\int_{x_0}^{x_2} f(x)dx = \frac{h}{3}(f_0 + 4f_1 + f_2) - \frac{h^5}{90}f^{(4)}(\xi), \quad x_0 < \xi < x_2 \quad (5.159)$$

3/8-rule:

$$\int_{x_0}^{x_3} f(x)dx = \frac{3h}{8}(f_0 + 3f_1 + 3f_2 + f_3) - \frac{3h^5}{80}f^{(4)}(\xi), \quad x_0 < \xi < x_3 \quad (5.160)$$

where we define $f_j \equiv f(x_j)$ and

$$x_j = x_0 + jh, \quad j = 0, \dots, N, \quad (5.161)$$

with

$$x_0 = a, \quad x_N = b, \quad h = \frac{b-a}{N}. \quad (5.162)$$

To approximate the integral value to a good accuracy it will not be sufficient to use an integration rule with 1, 2, 3 or 4 integration points, we will normally need many more grid points. For this purpose we could use the corresponding $(N + 1)$ -point Newton-Cotes formula. In practice, this is not useful because interpolation theory, upon which the Newton-Cotes formulae are based, tells us that a very high order polynomial does not in general approximate a function well at all. Furthermore for $N \geq 8$ the weights in the quadrature formula start to have different signs so that the numerical precision of the calculation becomes a worry. A much better method to increase the number of points is to use composite integration rules. This consists in dividing the integration interval $[a, b]$ in m subintervals of size H ,

$$H \equiv \frac{b-a}{m}, \quad (5.163)$$

rewriting the total integral as:

$$\int_a^b f(x)dx = \sum_{j=0}^{m-1} \int_{y_j}^{y_{j+1}} f(x)dx, \quad (5.164)$$

with

$$y_j = a + jH, \quad j = 0, \dots, m. \quad (5.165)$$

We apply a low order basic Newton-Cotes formula with $n + 1$ points on each subinterval:

$$\int_a^b f(x)dx = \sum_{j=0}^{m-1} \sum_{k=0}^n w_k f(y_j + kh), \quad (5.166)$$

with the grid spacing h defined as:

$$h \equiv \frac{H}{n} = \frac{b-a}{mn}. \quad (5.167)$$

Substituting Eqs. (5.165, 5.167) in Eq. (5.166) gives,

$$\boxed{\int_a^b f(x)dx = \sum_{j=0}^{m-1} \sum_{k=0}^n w_k f(x_{jn+k}),} \quad (5.168)$$

defining x_k as:

$$x_k = a + kh, \quad k = 0, \dots, mn . \quad (5.169)$$

The composite trapezoidal rule ($n = 1$) is (using Eq. (5.158)):

$$\int_a^b f(x)dx = \sum_{j=0}^{m-1} \frac{h}{2} (f_j + f_{j+1}), \quad (5.170)$$

where $f_k = f(x_k)$, such that:

$$\int_a^b f(x)dx = \frac{h}{2} \left(f_0 + 2 \sum_{j=1}^{m-1} f_j + f_m \right) . \quad (5.171)$$

The error term on this rule is:

$$E_{trap} = -\frac{b-a}{12} h^2 f^{(2)}(\xi), \quad a < \xi < b . \quad (5.172)$$

For $n = 2$ we derive the composite Simpson's rule using Eq. (5.159):

$$\begin{aligned} \int_a^b f(x)dx &= \sum_{j=0}^{m-1} \frac{h}{3} (f_{2j} + 4f_{2j+1} + f_{2j+2}) \\ &= \frac{h}{3} \left(f_0 + 2 \sum_{j=1}^{m-1} f_{2j} + 4 \sum_{j=0}^{m-1} f_{2j+1} + f_{2m} \right) , \end{aligned} \quad (5.173)$$

with error term:

$$E_{Simp} = -\frac{b-a}{180} h^4 f^{(4)}(\xi), \quad a < \xi < b . \quad (5.174)$$

The composite Simpson's rule requires an odd total number of grid points. If for some reason the grid has an even number of points $N + 1$ we can use the basic 3/8-rule of Eq. (5.160) on the four first points:

$$\int_{x_0}^{x_3} f(x)dx = \frac{3h}{8} (f_0 + 3f_1 + 3f_2 + f_3) , \quad (5.175)$$

and use the composite Simpson's rule Eq. (5.173) on the remaining integral which has an odd number of points $N - 2$. From Eqs. (5.159, 5.160) we note that both basic rules are of comparable accuracy so that the global accuracy of this mixed composite rule will be comparable to Eq. (5.174) .

5.6 Implementation of the quadrature rule

5.6.1 Estimate of computing time

In this section we are going to apply the quadrature rules mentioned before to the integral equation Eq. (5.98) describing the dynamical generation of fermion mass in QED. We will at

first use the trapezoidal rule and roughly study the behaviour of the solution of the integral equation and the computing time needed to find this solution using Newton's method from Section 5.4 with an increasing number of grid points in the radial integrals (with a fixed number of points in the angular integrals). Throughout our study we will take an ultraviolet cutoff $\Lambda^2 = 1e10$. In Table 5.1 we increase the number of grid panels, N_R , from 100 to 1000 and tabulate the values of $\Sigma(0)$, because it is representative for the scale of the generated fermion mass, and the real time (min:s) needed to compute the angular integrals. The other parameters are chosen as $\alpha = 2.086$ and the infrared cutoff $\kappa^2 = 0.1$.

| N_R | $\Sigma(0)$ | Δt_θ | $\Delta\Sigma(0)$ |
|-------|-------------|-------------------|-------------------|
| 100 | 112.74 | 0:04 | |
| 200 | 91.90 | 0:15 | 20.84 |
| 300 | 88.78 | 0:32 | 3.12 |
| 400 | 87.88 | 0:55 | 0.90 |
| 500 | 87.50 | 1:27 | 0.38 |
| 1000 | 87.10 | 5:16 | 0.40 |

Table 5.1: $\Sigma(0)$ versus number of radial integration panels N_R using the trapezoidal rule. Δt_θ is the real time (min:s) needed to compute the angular integrals. $\Delta\Sigma(0)$ is the change in $\Sigma(0)$ when increasing the number of points. $\alpha = 2.086$, $\kappa^2 = 0.1$.

Changing the number of radial points $N_R + 1$ to $N'_R + 1$ produces an increase of $[(N'_R + 1)/(N_R + 1)]^2$ angular integrations to be computed as there are $N_R + 1$ equations each with $N_R + 1$ radial points for which to compute angular integrals. We note from Table 5.1 that indeed the time Δt_θ increases as $[(N'_R + 1)/(N_R + 1)]^2$. Δt_θ only gives part of the computer time needed by the program. Once the angular integrals have been calculated, we have to solve the system of $N_R + 1$ non-linear equations. This will be done using Newton's iterative procedure, Eq. (5.142), involving the solution of a system of $N_R + 1$ linear equations at each iteration step. Because of the large size of these linear systems they will be solved numerically. The solution time of this procedure increases with the increasing number of equations. Although the computing time needed to solve the system of linear equations is small compared to Δt_θ for reasonable N_R (< 500), it becomes quite large for larger N_R . For $N_R = 1000$, each iteration step of Newton's method takes about 2 minutes. If we start from a good initial guess for Σ^0 the iterative procedure will converge after 5 iterations; the total computing time will then approximately be $\Delta t(N_R = 1000) \approx 5 + (5 \times 2) \approx 15$ minutes. This is quite long considering the relative simplicity of the integral equation. From $\Delta\Sigma(0)$ in Table 5.1 we see that $\Sigma(0)$ improves significantly for N_R

up to 500. The stagnation when $N_R \rightarrow 1000$ probably means that the accuracy of the angular integrals only permits a global relative accuracy of about 0.45% for the final solution.

5.6.2 Influence of infrared cutoff

In Section 5.3.2 we have mentioned that the introduction of an infrared cutoff κ^2 for numerical purposes requires that we either have an analytic evaluation of the truncated infrared part of the integral or that κ^2 should be chosen so that this part is negligible. In this section we will look at the influence of the variation of the infrared cutoff κ^2 on the numerical results of the calculation. If we plot the radial integrand as in Fig. 5.1 we see that this integrand decreases rapidly for momenta below the scale of the generated fermion mass ($y < \Sigma^2(0)$).

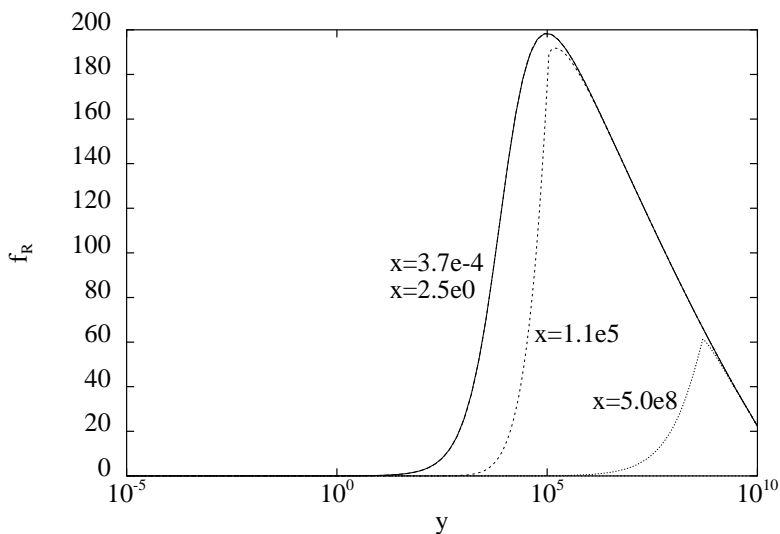


Figure 5.1: Radial integrand $f_R(y)$ for $\alpha = 2.086$ as a function of y for various values of external fermion momentum $x = 3.7e-4, 2.5e0, 1.1e5$ and $5.0e8$.

Consequently, we do not expect any significant contribution from that part of the integral. This means the choice of κ^2 is dependent on the generated fermion mass and thus on the coupling for which we solve the integral equation. If we fix κ^2 at some value, and vary the coupling α we will only get reliable results for couplings down to α_{min} for which the generated fermion mass is larger than κ . In practice we only expect to be able to find accurate solutions down to $\Sigma(0) \approx \mathcal{O}(1)$ (taking $\Lambda^2 = 1e10$) because of the limitations imposed by the numerical precision of the calculation. In Table 5.2 we show $\Sigma(0)$, varying κ^2 from $1e4$ to $1e-5$ for $\alpha = 2.086$. When

changing the value of the infrared cutoff κ^2 , we accordingly modify the number of integration panels N_R in order to have the same grid spacing in every case:

$$h \equiv \frac{\log_{10} \Lambda^2 - \log_{10} \kappa^2}{N_R} = \frac{1}{N_R} \log_{10} \frac{\Lambda^2}{\kappa^2} = \frac{1}{30} . \tag{5.176}$$

| κ^2 | N_R | $\Sigma(0)$ | Δt_θ |
|------------|-------|-------------|-------------------|
| 1e4 | 180 | 69.0990 | 0:11 |
| 1e3 | 210 | 87.0883 | 0:12 |
| 100 | 240 | 88.2892 | 0:19 |
| 10 | 270 | 88.3980 | 0:23 |
| 1 | 300 | 88.4083 | 0:29 |
| 0.1 | 330 | 88.4093 | 0:42 |
| 0.01 | 360 | 88.4094 | 0:46 |
| 1e-5 | 450 | 88.4094 | 1:05 |

Table 5.2: $\Sigma(0)$ versus infrared cutoff κ^2 for $\alpha = 2.086$ using the trapezoidal rule. The number of radial integration panels N_R is chosen to have a fixed grid spacing $h = \frac{1}{30}$. Δt_θ is the real time (min:s) needed to compute the angular integrals.

From Table 5.2 we see that indeed taking the infrared cutoff $\kappa^2 < \mathcal{O}(\frac{\Sigma^2(0)}{100})$ is sufficient to achieve an accuracy of $\approx 0.1\%$. For $\alpha = 2.086$ a suitable choice could be $\kappa^2 \sim 100$. If we are to investigate smaller values of the coupling, closer to its critical value, we will have to choose a smaller value of κ^2 .

5.6.3 Influence of grid spacing, kink in the integrand

Having fixed the infrared cutoff κ^2 , we will now turn our attention to the influence of the grid spacing h , which is inversely proportional to the number of grid panels, N . We performed the calculation using the composite trapezoidal rule and the composite Simpson’s rule. From textbooks it is well known that Simpson’s rule generally yields better results than the trapezoidal rule because the convergence of the composite Simpson’s rule is proportional to $1/N^4$, while the convergence of the trapezoidal rule is proportional to $1/N^2$. With convergence of a quadrature rule we mean the convergence of the finite sum to the exact integral value when $N \rightarrow \infty$. The results from Table 5.3 were computed for $\alpha = 2.086$ with $\kappa^2 = 100$.

The run with $N_R = 5000$ crashed because of memory allocation problems in solving the linear system of equations. From Table 5.3 we see that Simpson’s rule gives worse results than the trapezoidal rule. This is quite puzzling as it has a higher degree of precision. However, for the

| N_R | $1/h$ | $\Sigma_{trap}(0)$ | $\Sigma_{Simp}(0)$ | Δt_θ | Δt_{iter} |
|-------|-------|--------------------|--------------------|-------------------|-------------------|
| 80 | 10 | 107.387 | 172.565 | 0:03 | |
| 120 | 15 | 94.640 | 124.963 | 0:05 | |
| 160 | 20 | 90.773 | 108.192 | 0:09 | |
| 200 | 25 | 89.115 | 100.280 | 0:13 | |
| 240 | 30 | 88.289 | 96.072 | 0:18 | |
| 280 | 35 | 87.844 | 93.555 | 0:26 | |
| 320 | 40 | 87.572 | 91.932 | 0:34 | |
| 360 | 45 | 87.397 | 90.840 | 0:39 | |
| 400 | 50 | 87.276 | 90.056 | 0:51 | |
| 600 | 75 | 87.027 | 88.249 | | |
| 800 | 100 | 86.959 | 87.642 | | 9:00 |
| 1000 | 125 | 86.933 | 87.367 | | 16:00 |
| 2000 | 250 | 86.908 | | | 2:35:25 |
| 5000 | 625 | crash | | | |

Table 5.3: $\Sigma(0)$ versus number of radial integration panels N_R and grid density $1/h$ using the trapezoidal rule and Simpson's rule. Δt_θ is the real time (min:s) needed to compute the angular integrals, Δt_{iter} (h:min:s) is the total real time. $\alpha = 2.086$, $\kappa^2 = 100$.

error formulae to be applicable, the integrand has to be sufficiently smooth. If not, the accuracy of Simpson's rule can be just as good or bad as the one from the trapezoidal rule.

If we look at the radial integrand it becomes clear why this happens. In the quenched case, where the angular integrals can be computed analytically, a typical angular integration will yield:

$$I_\theta \equiv \int_0^\pi d\theta \frac{\sin^2 \theta}{z} = \frac{\pi}{2} \left[\frac{\theta(x-y)}{x} + \frac{\theta(y-x)}{y} \right]. \quad (5.177)$$

The various angular integrals all have this characteristic feature:

$$I_\theta \sim a_{<}(y, x) \theta(x-y) + a_{>}(y, x) \theta(y-x). \quad (5.178)$$

In the unquenched case the angular integrals are solved numerically because of the function $\mathcal{G}(z)$ appearing in the angular integrals of the fermion equation. Still the shape of Eq. (5.178) will remain valid and this will cause a kink in the kernel of the radial integral at $y = x$. This can be seen in Figs. 5.1, 5.2 where we plot the radial integrand for a number of values of external momentum x . Fig. 5.2 shows enlargements of the radial integrands in the neighbourhood of the kink at $y = x$. Although the kernel is continuous, it is not smooth as its first derivative has a discontinuity. This implies that the error formulae on the integration rules, Eqs. (5.157-5.160, 5.172, 5.174), are not applicable. According to Eq. (5.172) the composite trapezoidal rule has

an error decreasing as h^2 if it has a continuous 2^{nd} derivative, while from Eq. (5.174) Simpson's rule goes as h^4 if it has a continuous 4^{th} derivative. Because of the discontinuity in the 1^{st} derivative of the integrand, no higher degree rule applied on the interval $[a, b]$ will be able to give us a better result than the trapezoidal rule.

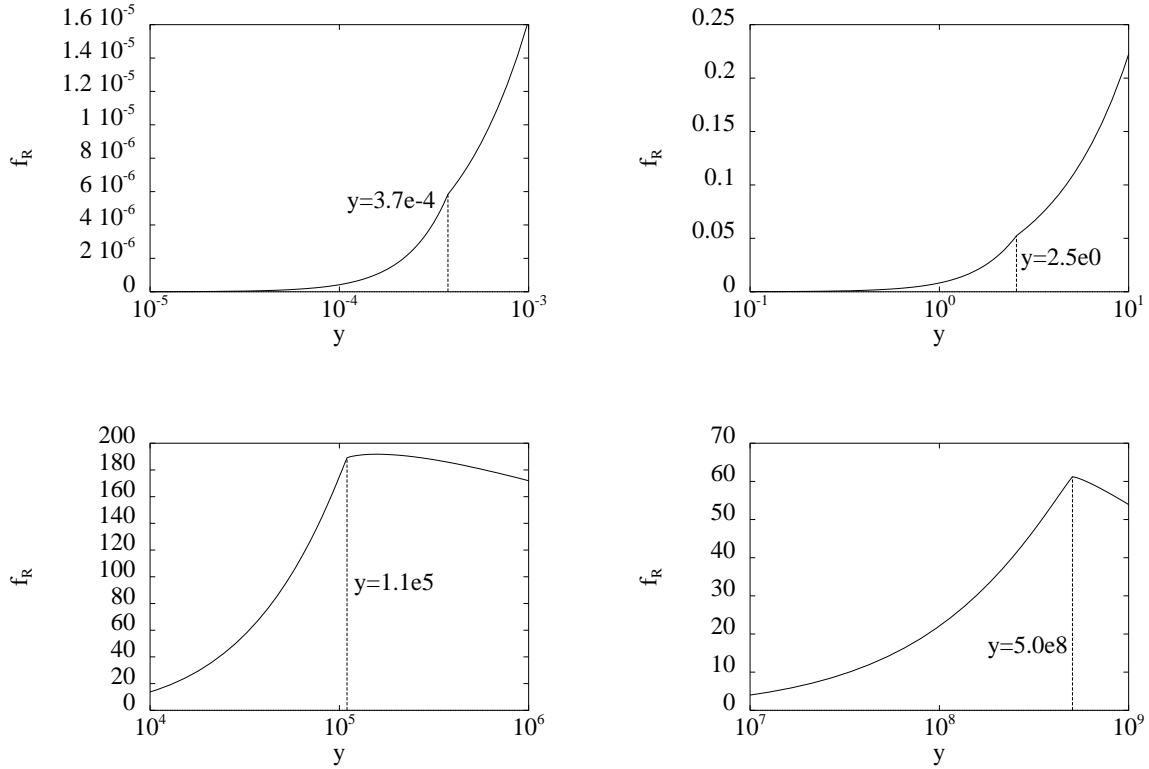


Figure 5.2: Zoomed views of the kink at $y = x$ in the radial integrand $f_R(y)$ for various values of external fermion momentum $x = 3.7e-4, 2.5e0, 1.1e5$ and $5.0e8$, for $\alpha = 2.086$

Even so, we see from Table 5.3 that, for an equal number of grid points, the results of the trapezoidal rule are better than those from Simpson's rule. The reason for this is that Simpson's rule uses three points on each subinterval, while the trapezoidal rule only uses two. If we consider the i^{th} equation from the system, Eq. (5.102), the radial integrand will have a kink at $x_j = x_i$. If x_i is an endpoint of a subinterval the integrands over all the individual subintervals are smooth and Simpson's rule should behave according to its error formula Eq. (5.174). In contrast, if x_i is a midpoint of a subinterval then the integrand over the subinterval $[x_{i-1}, x_{i+1}]$ is not smooth, unlike over the other subintervals, so that the integration rule will generate a considerable error. The trapezoidal rule always has the kink as an endpoint of a subinterval and so its error formula

is always applicable. The numerics of this phenomenon have been checked by comparing the values of the total integrals for various values of external momentum x_i using the trapezoidal rule and Simpson's rule. The integrals with a kink in the middle of a subinterval, i.e. for odd i , definitely yield worse values with Simpson's rule than with the trapezoidal rule. Because the integrals are the building blocks of the integral equation, the error on each individual integral propagates into the final solution of the integral equation. The accuracy of this solution will only be as good as the worst integral evaluation. Therefore the trapezoidal rule will yield a better solution of the integral equation than Simpson's rule. If we are not satisfied with the results computed with the trapezoidal rule (slow convergence when the number of grid points $N_R + 1$ is increased) and would like to use a higher degree rule efficiently, we will have to handle the kink in the radial integrand in an appropriate way.

The evident way to take care of the kink in the radial integrand is to split the integration range into two separate integrals:

$$\begin{aligned} \Sigma_i &= \int_{\kappa^2}^{\Lambda^2} dy K(x_i, y) \\ &= \int_{\kappa^2}^{x_i} dy K(x_i, y) + \int_{x_i}^{\Lambda^2} dy K(x_i, y), \quad i = 0, \dots, N, \end{aligned} \quad (5.179)$$

and approximate each of the integrals by an appropriate integration rule.

Each of these two subintegrals now has an integrand which is smooth over the integration interval. The accuracy of the numerical integration should now respect the theoretical error formula.

When implementing the composite integration rules we have to avoid two pitfalls. Firstly, if the total number of panels (number of grid points minus one) is not a multiple of the number of panels of the basic rule, we have to combine different basic rules preferably of comparable accuracy. Secondly, because of the kink in the radial integrand, the composite rule must have the kink as an endpoint of one of its subintervals if we want to achieve the accuracy predicted by the theoretical error formula. The importance of avoiding these pitfalls will now be demonstrated by considering the numerical integration of functions behaving in a way similar to Eq. (5.94) but for which the exact integral value can be calculated analytically. This will allow us to compare the numerical and analytical results.

5.6.4 Smooth toy kernel

To study the construction of the composite formula in the absence of any kink in the integrand, we will replace the non-smooth radial integrand by a function behaving in a similar way but without any kink:

$$f_R(x, y) = \frac{My}{y + M^2} \frac{2}{y + x}. \tag{5.180}$$

The integral of this function,

$$I(x) = \int_{\kappa^2}^{\Lambda^2} dy f_R(x, y) = \int_{\kappa^2}^{\Lambda^2} dy \frac{My}{y + M^2} \frac{2}{y + x}, \tag{5.181}$$

is readily computed analytically,

$$I(x) = \begin{cases} \frac{2M}{M^2 - x} \left[M^2 \ln \frac{\Lambda^2 + M^2}{\kappa^2 + M^2} - x \ln \frac{\Lambda^2 + x}{\kappa^2 + x} \right], & x \neq M^2 \\ 2M \left[\frac{M^2}{\Lambda^2 + M^2} - \frac{M^2}{\kappa^2 + M^2} + \ln \frac{\Lambda^2 + M^2}{\kappa^2 + M^2} \right], & x = M^2. \end{cases} \tag{5.182}$$

For $M = 100$, $\kappa^2 = 100$ and $\Lambda^2 = 1e10$, we have $I(x = 1e4) = 2563.093$, for instance.

We now apply various composite $(n + 1)$ -point Newton-Cotes rules to this integral for $x = 1e4$ and show the results in Table 5.4.

| N_R | E_1 | E_2 | E_3 | E_4 | E_5 | E_6 | E_7 |
|-------|---------|---------|---------|---------|---------|---------|---------|
| 100 | 4.2e-08 | 3.7e-10 | 1.8e-08 | 1.7e-11 | 7.4e-11 | 7.3e-11 | 3.6e-10 |
| 200 | 1.1e-08 | 2.3e-11 | 6.4e-11 | 2.7e-13 | 5.8e-13 | 9.9e-12 | 2.5e-13 |
| 300 | 4.7e-09 | 4.6e-12 | 1.0e-11 | 2.4e-14 | 5.2e-14 | 2.2e-16 | 5.6e-16 |
| 400 | 2.6e-09 | 1.5e-12 | 2.5e-10 | 4.4e-15 | 9.4e-15 | 1.8e-15 | 2.5e-10 |
| 500 | 1.7e-09 | 5.9e-13 | 1.5e-12 | 8.9e-16 | 1.4e-15 | 9.2e-14 | 3.2e-13 |
| 600 | 1.2e-09 | 2.9e-13 | 6.4e-13 | 5.6e-16 | 1.1e-15 | 2.2e-16 | 4.4e-16 |
| 700 | 8.7e-10 | 1.6e-13 | 4.6e-11 | 0 | 5.6e-16 | 0 | 6.7e-16 |
| 800 | 6.6e-10 | 9.1e-14 | 2.1e-13 | 4.4e-16 | 0 | 8.4e-15 | 8.9e-15 |
| 900 | 5.2e-10 | 5.7e-14 | 1.3e-13 | 3.3e-16 | 6.7e-16 | 0 | 2.2e-16 |
| 1000 | 4.2e-10 | 3.7e-14 | 1.6e-11 | 6.7e-16 | 6.7e-16 | 4.4e-16 | 2.2e-16 |

Table 5.4: Relative error $E_n = |(I_{num} - I_{exact})/I_{exact}|$ from the numerical calculation of $I(x)$ of Eq. (5.181) for $x = 1e4$ using composite $(n + 1)$ -point Newton-Cotes formulae with $n = 1, \dots, 7$ for increasing total number of grid panels N_R .

Comparing the results from Table 5.4 shows that for a fixed total number of grid panels N_R , the higher degree rules perform significantly better than the lower ones (except for $n = 3, 6, 7$). The degree of precision D of a quadrature rule is defined such that all polynomials of degree

at most equal to the degree of precision are integrated exactly by the quadrature formula. The degree of precision of the various rules is given in Table 5.5.

| | | | | | | | |
|-----|---|---|---|---|---|---|---|
| n | 1 | 2 | 3 | 4 | 5 | 6 | 7 |
| D | 1 | 3 | 3 | 5 | 5 | 7 | 7 |

Table 5.5: Degree of precision D of the $(n + 1)$ -point Newton-Cotes formulae with $n = 1, \dots, 7$.

Using a rule with a higher degree of precision seems to yield significantly improved results for the integral evaluation, till the maximum accuracy of about $1e-16$ imposed by the use of double precision arithmetics has been reached.

Also from Table 5.4, we see that increasing the total number of grid panels from N_R to N'_R , using the same basic rule, seems to yield the expected $(N'_R/N_R)^{(D+1)}$ improvement in accuracy, again till the maximum accuracy is reached. This is not true when the number of panels in the basic NC-rule is $n = 3, 6, 7$. To construct a composite formula using a single basic NC-rule, the total number of panels in the integration interval must be a multiple of the number of panels of the basic NC-rule. For $n = 1, 2, 4, 5$ all the total number of panels N_R considered in Table 5.4 are indeed multiples of the number of panels of their basic NC-rule. This is not so for $n = 3, 6, 7$. For $n = 3$ this will be satisfied for $N_R = 300, 600, 900$. For other values of N_R we have to adapt the composite rule by taking as many n -panel rules as will fit in N_R panels and use an n' -panel rule on the remaining interval as shown in Table 5.6. For example, the $n = 3$ case with 400 radial panels will be composed of 133 3-panel or 3/8-rules and one trapezoidal rule.

We now look back at the $n = 3$ results of Table 5.4 using Table 5.6. For $N_R = 300, 600, 900$, the composite rule can be wholly constructed with basic 3/8-rules. For $N_R = 200, 500, 800$, the composite 3/8-rule has to be complemented by one Simpson's rule. Because Simpson's rule and the 3/8-rule have comparable accuracy this does not affect the global accuracy of the composite rule. However, for $N_R = 100, 400, 700, 1000$, the composite 3/8-rule has to be complemented with one trapezoidal rule yielding significantly worse results. From the error term in Eqs. (5.158, 5.160) one can prove theoretically that this mixed composite rule behaves as $1/N^3$, while the pure composite trapezoidal rule goes as $1/N^2$ and the pure Simpson's and 3/8-rule go as $1/N^4$. The results of Table 5.4 for $N_R = 100, 400, 700, 1000$ have indeed a $1/N^3$ convergence rate. We see an analogous pattern for $n = 6, 7$. We can deduce from Tables 5.4, 5.6 that the error on the integral evaluation is determined by the least accurate of the subrules used even if it is only used

| N_R | $n = 3$ | $n = 6$ | $n = 7$ |
|-------|--------------------|--------------------|--------------------|
| 100 | $33 \times 3 + 1$ | $16 \times 6 + 4$ | $14 \times 7 + 2$ |
| 200 | $66 \times 3 + 2$ | $33 \times 6 + 2$ | $28 \times 7 + 4$ |
| 300 | 100×3 | 50×6 | $42 \times 7 + 6$ |
| 400 | $133 \times 3 + 1$ | $66 \times 6 + 4$ | $57 \times 7 + 1$ |
| 500 | $166 \times 3 + 2$ | $83 \times 6 + 2$ | $71 \times 7 + 3$ |
| 600 | 200×3 | 100×6 | $85 \times 7 + 5$ |
| 700 | $233 \times 3 + 1$ | $116 \times 6 + 4$ | 100×7 |
| 800 | $266 \times 3 + 2$ | $133 \times 6 + 2$ | $114 \times 7 + 2$ |
| 900 | 300×3 | 150×6 | $128 \times 7 + 4$ |
| 1000 | $333 \times 3 + 1$ | $166 \times 6 + 4$ | $142 \times 7 + 6$ |

Table 5.6: Structure of the composite $(n + 1)$ -point NC-rules for $n = 3, 6, 7$ for a total number of grid panels N_R , written as m times an n -panel rule complemented by one n' -panel rule.

once in the total evaluation. Further demonstration of this can be found in Table 5.7 where we alter the total number of grid panels in the cases $n = 3, 6, 7$ to make it a multiple of the number of panels of the basic rules. It is clear that for $n = 3$ the error formula is now well respected and that the error is comparable to that of Simpson's rule ($n = 2$) from Table 5.4, as it should be for composite rules of equal degree of precision. For $n = 6, 7$ the improvement of the accuracy with increasing total number of grid points seems to respect the error formula although the maximum accuracy of $O(1e-16)$ is reached very rapidly.

| N_R | E_3 | N_R | E_6 | N_R | E_7 |
|-------|---------|-------|---------|-------|---------|
| 99 | 8.5e-10 | 97 | 2.3e-10 | 99 | 1.0e-09 |
| 198 | 5.4e-11 | 193 | 5.0e-15 | 197 | 8.2e-15 |
| 297 | 1.1e-11 | 289 | 2.2e-16 | 295 | 0 |
| 396 | 3.4e-12 | 385 | 6.7e-16 | 393 | 2.2e-16 |
| 495 | 1.4e-12 | 481 | 4.4e-16 | 491 | 0 |
| 594 | 6.7e-13 | 577 | 5.6e-16 | 589 | 8.9e-16 |
| 693 | 3.6e-13 | 673 | 4.4e-16 | 687 | 3.3e-16 |
| 792 | 2.1e-13 | 769 | 5.6e-16 | 785 | 4.4e-16 |
| 891 | 1.3e-13 | 865 | 3.3e-16 | 883 | 2.2e-16 |
| 990 | 8.7e-14 | 961 | 8.9e-16 | 981 | 2.2e-16 |

Table 5.7: Relative error $E_n = |(I_{num} - I_{exact})/I_{exact}|$ from the numerical calculation of $I(x)$ of Eq. (5.181) for $x = 1e4$, adapting the number of panels N_R to use pure composite $(n + 1)$ -point Newton-Cotes formulae with $n = 3, 6, 7$ for increasing total number of grid panels N_R .

5.6.5 Toy kernel with kink

We will now make an analogous study using a simplified kernel which has a kink in the integration region:

$$f_R(x, y) = \frac{My}{y + M^2} \frac{1}{\max(x, y)}. \tag{5.183}$$

The integration of this function,

$$I(x) = \int_{\kappa^2}^{\Lambda^2} dy f_R(x, y) = \int_{\kappa^2}^{\Lambda^2} dy \frac{My}{y + M^2} \frac{1}{\max(x, y)} \tag{5.184}$$

can be performed analytically yielding:

$$I(x) = M - \frac{M\kappa^2}{x} - \frac{M^3}{x} \ln \frac{x + M^2}{\kappa^2 + M^2} + M \ln \frac{\Lambda^2 + M^2}{x + M^2}. \tag{5.185}$$

For $M = 100$, $\kappa^2 = 100$ and $\Lambda^2 = 1e10$, we compute $I(x = 1e4) = 1342.917$. The numerical results computed with the composite NC-formulae are tabulated in Table 5.8.

| N_R | i_{kink} | E_1 | E_2 | E_3 | E_4 | E_5 | E_6 | E_7 |
|-------|------------|---------|---------|---------|---------|---------|---------|---------|
| 100 | 25 | 1.1e-04 | 2.1e-04 | 1.4e-06 | 2.3e-04 | 5.3e-09 | 4.3e-04 | 7.1e-05 |
| 200 | 50 | 2.6e-05 | 3.7e-08 | 8.4e-08 | 1.4e-05 | 9.8e-11 | 1.1e-11 | 4.6e-05 |
| 300 | 75 | 1.2e-05 | 2.3e-05 | 1.7e-08 | 2.7e-05 | 8.8e-12 | 4.8e-05 | 2.8e-05 |
| 400 | 100 | 6.6e-06 | 2.3e-09 | 5.5e-09 | 7.4e-13 | 1.6e-12 | 7.1e-15 | 1.5e-05 |
| 500 | 125 | 4.2e-06 | 8.4e-06 | 2.1e-09 | 9.5e-06 | 4.2e-13 | 1.7e-05 | 7.9e-06 |
| 600 | 150 | 2.9e-06 | 4.6e-10 | 1.0e-09 | 1.6e-06 | 1.4e-13 | 2.2e-16 | 2.0e-06 |
| 700 | 175 | 2.1e-06 | 4.3e-06 | 6.0e-10 | 4.9e-06 | 5.5e-14 | 8.8e-06 | 0 |
| 800 | 200 | 1.6e-06 | 1.5e-10 | 3.3e-10 | 1.1e-14 | 2.5e-14 | 8.4e-15 | 1.1e-06 |
| 900 | 225 | 1.3e-06 | 2.6e-06 | 2.0e-10 | 2.9e-06 | 1.2e-14 | 5.3e-06 | 2.4e-06 |
| 1000 | 250 | 1.1e-06 | 6.0e-11 | 1.5e-10 | 5.6e-07 | 7.6e-15 | 4.4e-16 | 2.5e-06 |

Table 5.8: Relative error $E_n = |(I_{num} - I_{exact})/I_{exact}|$ from the numerical calculation of $I(x)$ of Eq. (5.184) for $x = 1e4$ using composite $(n + 1)$ -point Newton-Cotes formulae with $n = 1, \dots, 7$ for increasing total number of grid panels N_R . i_{kink} gives the position of the kink within the $N_R + 1$ points of the grid, $i \in [0, N_R]$.

From Table 5.8 we see that increasing the total number of integration panels N_R in the composite trapezoidal rule gives the improvement expected from Eq. (5.172). However, for Simpson's rule ($n = 2$) this is not so. When N_R is such that the index of the kink is odd, the integral evaluation is clearly worse than when it is even. This reflects the fact that an odd index means that the kink is *not* an endpoint of a basic Simpson's rule. The accuracy, in this case, is comparable to the one achieved with the trapezoidal rule. The 3/8-rule ($n = 3$) behaves in a better way than

Simpson’s rule. As we saw in Table 5.6 the composite 3/8-rule is a mixed one. In our exercise we use the first n' ($n' < 3$) panels to apply one n' -point NC-rule, the remaining points are used to apply a pure composite 3/8-rule. One can check that this implies that the kink will always be an endpoint of a basic 3/8-rule for any N_R of Table 5.8. For $n = 5$, it is obvious that the kink will be an endpoint as the index of the kink is a multiple of 5, which is also the number of panels in the basic NC-rule. For $n = 4, 6, 7$ the kink will only be an endpoint for some values of N_R , hence the erratic behaviour of the computed integral value. To improve on the previous calculation we will now split the integral as suggested in Eq. (5.179). The results are shown in Table 5.9.

| N_R | i_{kink} | E_1 | E_2 | E_3 | E_4 | E_5 | E_6 | E_7 |
|-------|------------|---------|---------|---------|---------|---------|---------|---------|
| 100 | 25 | 1.1e-04 | 6.1e-07 | 1.4e-06 | 2.1e-08 | 5.3e-09 | 1.9e-08 | 1.1e-09 |
| 200 | 50 | 2.6e-05 | 3.7e-08 | 8.4e-08 | 5.6e-11 | 9.8e-11 | 1.1e-11 | 2.1e-09 |
| 300 | 75 | 1.2e-05 | 7.9e-09 | 1.7e-08 | 7.1e-12 | 8.8e-12 | 4.5e-12 | 1.3e-12 |
| 400 | 100 | 6.6e-06 | 2.3e-09 | 5.5e-09 | 7.4e-13 | 1.6e-12 | 7.1e-15 | 3.0e-13 |
| 500 | 125 | 4.2e-06 | 1.1e-09 | 2.1e-09 | 1.3e-10 | 4.2e-13 | 1.1e-15 | 1.1e-15 |
| 600 | 150 | 2.9e-06 | 4.6e-10 | 1.0e-09 | 1.0e-13 | 1.4e-13 | 2.2e-16 | 1.3e-13 |
| 700 | 175 | 2.1e-06 | 2.9e-10 | 6.0e-10 | 3.1e-14 | 5.6e-14 | 4.5e-11 | 2.2e-16 |
| 800 | 200 | 1.6e-06 | 1.5e-10 | 3.3e-10 | 1.2e-14 | 2.5e-14 | 8.2e-15 | 3.3e-16 |
| 900 | 225 | 1.3e-06 | 1.1e-10 | 2.0e-10 | 2.1e-11 | 1.2e-14 | 1.7e-14 | 2.1e-11 |
| 1000 | 250 | 1.1e-06 | 6.0e-11 | 1.5e-10 | 7.1e-15 | 7.1e-15 | 6.7e-16 | 3.9e-14 |

Table 5.9: Relative error $E_n = |(I_{num} - I_{exact})/I_{exact}|$ from the numerical calculation of $I(x)$ of Eq. (5.184) for $x = 1e4$, splitting the integral and using composite $(n + 1)$ -point Newton-Cotes formulae with $n = 1, \dots, 7$ for increasing total number of grid panels N_R . i_{kink} gives the position of the kink within the grid with $N_R + 1$ points, $i \in [0, N_R]$.

As expected the results for $n = 1, 3, 5$ are the same as in Table 5.8. For Simpson’s rule ($n = 2$) the results are now significantly better and comparable to the 3/8-rule for the various values of N_R . For the other NC-rules, $n = 4, 6, 7$, although the results have improved because the kink is an endpoint in every case, the behaviour is not consistent for increasing N_R . The explanation for this can be found in the composition of the various *mixed* composite rules, mixing the main n -panel rule with one rule of lower degree of precision.

To improve on those integral evaluations we can modify the number of integration points such that, after splitting the integral in two subintegrals at the kink, the number of panels in both integrals is a multiple of the number of panels of the basic rule. The new results are shown in Table 5.10. The results for $n = 1, 5$ are not shown as they are the same as in Table 5.9. All the

composite rules now have the accuracy predicted by their error formula.

| N_R | i_{kink} | E_2 | E_3 | E_4 | E_6 | N_R | i_{kink} | E_7 |
|-------|------------|---------|---------|---------|---------|-------|------------|---------|
| 96 | 24 | 7.0e-07 | 1.6e-06 | 3.4e-09 | 6.4e-10 | 85 | 21 | 4.7e-09 |
| 192 | 48 | 4.4e-08 | 9.8e-08 | 5.9e-11 | 1.9e-12 | 169 | 42 | 1.2e-11 |
| 288 | 72 | 8.6e-09 | 1.9e-08 | 5.3e-12 | 7.1e-14 | 253 | 63 | 4.5e-13 |
| 384 | 96 | 2.7e-09 | 6.2e-09 | 9.5e-13 | 7.5e-15 | 337 | 84 | 4.4e-14 |
| 480 | 120 | 1.1e-09 | 2.5e-09 | 2.5e-13 | 4.4e-16 | 421 | 105 | 7.5e-15 |
| 576 | 144 | 5.4e-10 | 1.2e-09 | 8.5e-14 | 0 | 505 | 126 | 2.0e-15 |
| 672 | 168 | 2.9e-10 | 6.6e-10 | 3.3e-14 | 4.4e-16 | 589 | 147 | 4.4e-16 |
| 768 | 192 | 1.7e-10 | 3.8e-10 | 1.5e-14 | 4.4e-16 | 673 | 168 | 5.6e-16 |
| 864 | 216 | 1.1e-10 | 2.4e-10 | 7.8e-15 | 3.3e-16 | 757 | 189 | 2.2e-16 |
| 960 | 240 | 7.0e-11 | 1.6e-10 | 4.0e-15 | 1.1e-15 | 841 | 210 | 3.3e-16 |

Table 5.10: Relative error $E_n = |(I_{num} - I_{exact})/I_{exact}|$ from the numerical calculation of $I(x)$ of Eq. (5.184) for $x = 1e4$, splitting the integral and adapting the number of panels N_R to use pure composite $(n + 1)$ -point Newton-Cotes formulae with $n = 2, 3, 4, 6, 7$ for increasing total number of grid panels N_R . i_{kink} gives the position of the kink within the grid with $N_R + 1$ points, $i \in [0, N_R]$.

From the previous discussion it is clear that, even for an integrand with a kink, it is far more advantageous to use a quadrature rule with a higher degree of precision, as the 6-panel or 7-panel rules, than one of lower degree, for an equal total number of integration points.

5.6.6 Split Simpson's rule and the integral equation

Of course the quadrature rules are only building blocks of the integral equation and we must keep in mind how these rules are used in the global solution scheme of the integral equations. The various tables in the previous discussion were all derived for one value of external momentum, $x = 1e4$. Because this also coincides with the kink in the radial integrand, some conclusions drawn from these tables rely specifically on this value or rather on its index in the vector of integration points. If we consider the system of non-linear equations, Eq. (5.102), instead of just an individual integral, we note that the external momentum x_i takes on values corresponding to the momenta of the radial integration nodes, $i = 0, \dots, N_R$. This means that it may be difficult to satisfy the requirements needed to obtain an optimal accuracy, as derived from the previous discussion, for all of them at the same time, as we will now clarify.

When we split the integration interval in two subintervals to avoid the kink in the integrand at the value $x_i, i = 0, \dots, N_R$, we will have i panels in the lower interval and $N_R - i$ panels in the

upper interval. We will then apply some composite integration rule to each of these subintegrals. Unfortunately, we now encounter a problem due to the use of the collocation method to solve the integral equation. In the collocation method, we use the same fixed set of integration points for *all* the radial integrals, independently of the external momentum, as we only know the function values Σ_i and thus the values of the integrands at a fixed number of momenta x_i . We are not able to choose the number of points in the various integrals according to the external momentum and the position of the kink, such that the number of panels is a multiple of that from the basic rules as suggested by the results of Table 5.10. The collocation method *forces* us to use non-optimal *mixed* composite rules.

Let us show this in the following example. We want to apply the composite Simpson's rule to evaluate the integrals. Let us take $N_R = 100$ and vary the position of the kink corresponding to the external momentum in Eq. (5.102). Table 5.11 shows the number of radial integration panels N_{R1} , N_{R2} in each integral after we have split the total integral in two at the kink x_i . It also shows the composition of the integration rule if we use the composite Simpson's rule, complemented with one 3/8-rule or trapezoidal rule when needed.

| x_i | N_{R1} | N_{R2} | Rule 1 | Rule 2 |
|-------------------|----------|----------|---------------|---------------|
| x_0 | 0 | 100 | - | Simpson's |
| x_1 | 1 | 99 | Trapezoidal | Simpson's+3/8 |
| x_2 | 2 | 98 | Simpson's | Simpson's |
| x_3 | 3 | 97 | Simpson's+3/8 | Simpson's+3/8 |
| \vdots | | | | |
| x_{even} | even | even | Simpson's | Simpson's |
| x_{odd} | odd | odd | Simpson's+3/8 | Simpson's+3/8 |
| \vdots | | | | |
| x_{97} | 97 | 3 | Simpson's+3/8 | Simpson's+3/8 |
| x_{98} | 98 | 2 | Simpson's | Simpson's |
| x_{99} | 99 | 1 | Simpson's+3/8 | Trapezoidal |
| x_{100} | 100 | 0 | Simpson's | - |

Table 5.11: Number of radial integration panels N_{R1} , N_{R2} and structure of the mixed composite Simpson's rule in each integral after splitting the total integral in two at the kink x_i ($N_R = 100$).

From Table 5.11 we see that varying x_i leads to different mixed composite rules to be used. Even if we try to combine rules with comparable accuracy, this is never possible for $x_i = x_1$ or x_{N_R-1} where a trapezoidal rule is always involved. This reduces the accuracy to about the same level

as the one achieved with the pure trapezoidal rule. Even using composite rules formed with a basic rule of higher degree of precision does not help because, depending on the position of the kink, the composite rule will have to be complemented with rules of lower degree of precision. There is nothing we can do about this as long as we use the *collocation* method. In a later section, when we will introduce the *polynomial expansion* of the unknown functions, this will be cured in an elegant way.

We now apply the splitting of the integral to the original kernel of Eq. (5.94) using the split Simpson’s rule described in Table 5.11. The results are shown in Table 5.12. For comparison we also tabulate the results for the pure composite trapezoidal and Simpson’s rule (without splitting the integral).

| N_R | $1/h$ | $\Sigma(0)$ Split Simp | $\Sigma(0)$ trapez | $\Sigma(0)$ Simpson’s |
|-------|-------|---------------------------|-----------------------|--------------------------|
| 32 | 4 | 17.444 | 246.741 | 587.681 |
| 64 | 8 | 72.730 | 121.505 | 219.550 |
| 128 | 16 | 83.790 | 93.557 | 120.363 |
| 256 | 32 | 86.236 | 88.075 | 94.905 |
| 512 | 64 | 86.768 | 87.093 | 88.778 |

Table 5.12: $\Sigma(0)$ versus number of radial integration panels N_R and grid density $1/h$ using the split Simpson’s rule and the pure composite trapezoidal and Simpson’s rule for $\alpha = 2.086$, $\kappa^2 = 100$.

For equal values of N_R , the result of the split Simpson’s rule is better than the results achieved with the other methods, given that the correct answer for $\Sigma(0) \approx 87.009$.

5.6.7 Heuristic improvement of the split Simpson’s rule

We now make an interesting observation starting from the error formulae on the integral evaluation. Recall the error formula, Eq. (5.172), for the composite trapezoidal rule with grid spacing h ,

$$I - I_h = E_{trap} = -\frac{b-a}{12}h^2 f^{(2)}(\xi), \quad a < \xi < b, \quad (5.186)$$

where I is the exact integral value and I_h represents the approximate value of the integral computed with a composite trapezoidal rule with grid spacing h . If we perform two independent integral evaluations with grid spacings h_1 and h_2 , and divide their respective errors using

Eq. (5.186) we get:

$$\frac{I - I_{h_1}}{I - I_{h_2}} = \frac{h_1^2 f^{(2)}(\xi_1)}{h_2^2 f^{(2)}(\xi_2)}. \quad (5.187)$$

If the second derivative of $f(x)$ varies slowly we can put $f^{(2)}(\xi_1) \approx f^{(2)}(\xi_2)$ and Eq. (5.187) becomes,

$$\frac{I - I_{h_1}}{I - I_{h_2}} \approx \left(\frac{h_1}{h_2}\right)^2, \quad (5.188)$$

and thus,

$$I \approx \frac{(h_2/h_1)^2 I_{h_1} - I_{h_2}}{(h_2/h_1)^2 - 1}. \quad (5.189)$$

If we take $h_1 = h$ and $h_2 = 2h$, this expression gives,

$$I \approx \frac{4I_h - I_{2h}}{3}. \quad (5.190)$$

This last equations tells us that we can get an improved integral evaluation, if we know the evaluations of the integral with some number of panels and for half this number of panels. If we apply this to an integral evaluation using three points, x_0 , x_1 and x_2 , this yields,

$$\begin{aligned} I &\approx \frac{1}{3} \left[\left(4\frac{h}{2}(f_0 + 2f_1 + f_2) - h(f_0 + f_2)\right) \right] \\ &\approx \frac{h}{3}(f_0 + 4f_1 + f_2), \end{aligned}$$

which is exactly Simpson's rule Eq. (5.159). Thus, using the trapezoidal rules with N and $N/2$ panels we can construct some rule with a higher degree of precision, i.e. Simpson's rule.

From the error formula Eq. (5.186) we can also compute,

$$\begin{aligned} \frac{I_{h_2} - I_{h_1}}{I_{h_3} - I_{h_2}} &= \frac{(I_{h_2} - I) - (I_{h_1} - I)}{(I_{h_3} - I) - (I_{h_2} - I)} \\ &= \frac{h_2^2 f^{(2)}(\xi_2) - h_1^2 f^{(2)}(\xi_1)}{h_3^2 f^{(2)}(\xi_3) - h_2^2 f^{(2)}(\xi_2)} \\ &\approx \frac{h_2^2 - h_1^2}{h_3^2 - h_2^2}, \end{aligned}$$

which allows us to estimate the improvement of the integral evaluation with successive doubling of the number of panels. If we take $h_3 = h/2$, $h_2 = h$, $h_1 = 2h$, then,

$$\frac{I_h - I_{2h}}{I_{h/2} - I_h} \approx 4. \quad (5.191)$$

Although the previous relations were derived for integral evaluations, we can check if the numerical solution of the integral equation follow some analogous relations. From the trapezoidal

results of Table 5.12 for $\Sigma(0)$ we indeed find that,

$$\frac{\Sigma_0(\text{trap}, h) - \Sigma_0(\text{trap}, 2h)}{\Sigma_0(\text{trap}, h/2) - \Sigma_0(\text{trap}, h)} \approx 4, \quad (5.192)$$

which means that Eq. (5.191) gets propagated from the integral evaluations to the solution of the integral equation.

For curiosity we can also check if a relation analogous to Eq. (5.190) can be derived from Table 5.12, using the final solution of the integral equation rather than the individual integral values. We rather surprisingly see that:

$$\Sigma_0(\text{split}, h) \approx \frac{4\Sigma_0(\text{trap}, h) - \Sigma_0(\text{trap}, h/2)}{3}. \quad (5.193)$$

This tells us that the results of the split Simpson's rule can be approximated by combining the results from the trapezoidal rule for the same number of panels and for half this number of panels. Eqs. (5.192, 5.193) seem to be a feature of the h^2 accuracy of the composite trapezoidal rule.

In analogy with this, we now study the behaviour of Simpson's rule. Using the error formulae Eq. (5.174),

$$E_{Simp} = -\frac{b-a}{180} h^4 f^{(4)}(\xi), \quad a < \xi < b, \quad (5.194)$$

for two different evaluations using grid spacings h_1 and h_2 . If the fourth derivative of f varies slowly, we can write,

$$\frac{I - I_{h_1}}{I - I_{h_2}} \approx \left(\frac{h_1}{h_2}\right)^4, \quad (5.195)$$

and thus,

$$I \approx \frac{(h_2/h_1)^4 I_{h_1} - I_{h_2}}{(h_2/h_1)^4 - 1}. \quad (5.196)$$

Using this for $h_1 = h$ and $h_2 = 2h_1$ yields,

$$I \approx \frac{16I_h - I_{2h}}{15}. \quad (5.197)$$

Analogously to Eq. (5.191), we have,

$$\frac{I_{h_2} - I_{h_1}}{I_{h_3} - I_{h_2}} \approx \frac{h_2^4 - h_1^4}{h_3^4 - h_2^4}, \quad (5.198)$$

and for $h_3 = h/2$, $h_2 = h$, $h_1 = 2h$,

$$\frac{I_h - I_{2h}}{I_{h/2} - I_h} \approx 16. \quad (5.199)$$

Nevertheless, Table 5.12 shows that the rate of convergence of the split Simpson’s rule, when N_R is increased does not follow Eq. (5.199) but tends to be the same as for the trapezoidal rule,

$$\frac{\Sigma_0(\text{split}, h) - \Sigma_0(\text{split}, 2h)}{\Sigma_0(\text{split}, h/2) - \Sigma_0(\text{split}, h)} \approx 4 . \tag{5.200}$$

This is probably because there are always two trapezoidal rules involved in the calculation using the split rules and the error propagation keeps the global degree of precision down to that of the trapezoidal rule.

The previous observations can be used to construct a heuristic method to improve the split Simpson’s solution on the integral equation. Eqs. (5.192, 5.193, 5.200) suggest the following improvement:

$$\Sigma_0(\text{Improved split}, h) \approx \frac{4\Sigma_0(\text{split}, h) - \Sigma_0(\text{split}, h/2)}{3} . \tag{5.201}$$

The application of Eq. (5.201) to the results of Table 5.12 are tabulated in Table 5.13.

| N_R | $1/h$ | $\Sigma(0)$ Split Simp | $\Sigma(0)$ Improved split Simp |
|-------|-------|---------------------------|------------------------------------|
| 32 | 4 | 17.444 | |
| 64 | 8 | 72.730 | 91.159 |
| 128 | 16 | 83.790 | 87.477 |
| 256 | 32 | 86.236 | 87.051 |
| 512 | 64 | 86.768 | 86.945 |

Table 5.13: $\Sigma(0)$ versus number of radial integration panels N_R and grid density $1/h$ using the split Simpson’s rule (from Table 5.12) and the improved split Simpson’s rule of Eq. (5.201) for $\alpha = 2.086$, $\kappa^2 = 100$.

5.7 Critical coupling in the 1-loop approximation to Π

We will now apply the previously discussed method to the integral equation, Eq. (5.94), describing the dynamical fermion mass generation in QED, in the 1-loop approximation to the vacuum polarization. In Fig. 5.3 we plot the 1-loop behaviour of $\mathcal{G}(x)$ used as input in Eq. (5.94). The Σ -equation is solved for various values of α using the improved split Simpson’s rule and Newton’s iterative method. In Fig. 5.4 we show a typical plot of the dynamical mass function $\Sigma(x)$ for $\alpha = 2.086$, $\kappa^2 = 0.01$ and $\Lambda^2 = 1e10$.

In Fig. 5.5 we plot the evolution of $\Sigma(0)$, which is representative for the scale of the dynamically generated fermion mass, versus the coupling strength α . For small α there is no fermion mass

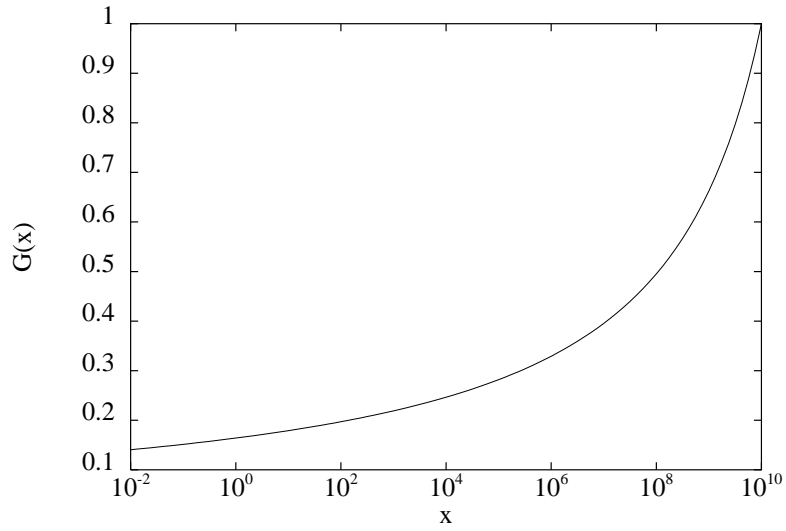


Figure 5.3: 1-loop photon renormalization function $\mathcal{G}(x)$ as a function of the photon momentum x for $\alpha = 2.086$. $\kappa^2 = 0.01$, $\Lambda^2 = 1e10$.

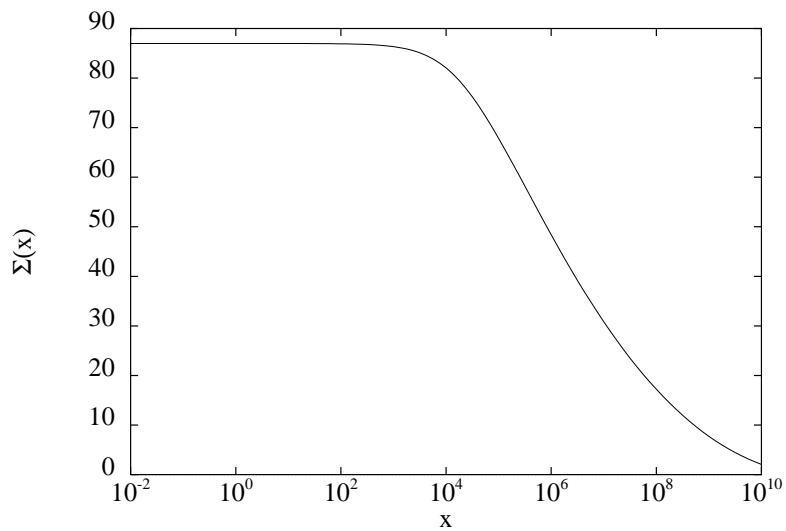


Figure 5.4: Dynamical mass function $\Sigma(x)$ as a function of the fermion momentum x for $\alpha = 2.086$ in the 1-loop approximation to \mathcal{G} . $\kappa^2 = 0.01$, $\Lambda^2 = 1e10$.

generation. At a certain value of the coupling, called the critical coupling, α_c , fermion mass generation sets in. The generated fermion mass increases further with increasing values of α . To pin down the value of α_c numerically, we start from some large value of the coupling and decrease it till the mass generation disappears. From this we find $\alpha_c = 2.08432$.

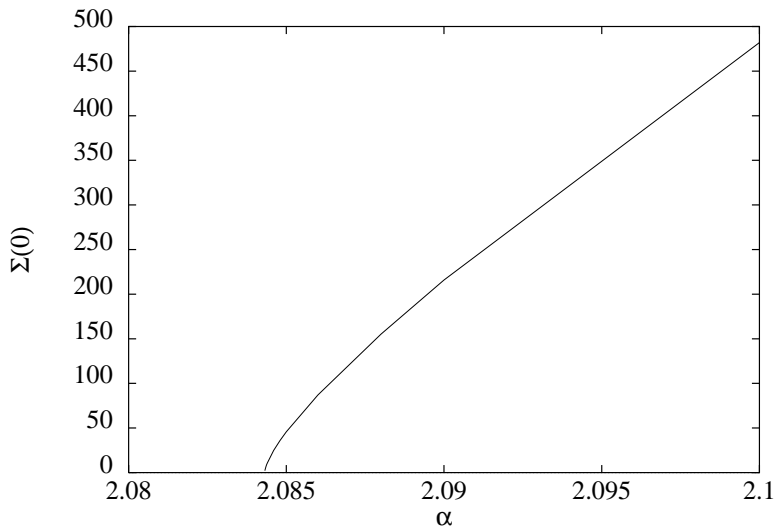


Figure 5.5: Dynamically generated mass $\Sigma(0)$ versus coupling α in the 1-loop approximation to \mathcal{G} . $\kappa^2 = 0.01$, $\Lambda^2 = 1e10$.

In this chapter we have set up the numerical framework to solve non-linear integral equations. We have applied this to a single integral equation for the dynamical mass Σ , corresponding to a specific truncation of the Schwinger-Dyson equations describing fermion mass generation in QED. In the next chapter we will relax some of the simplifications introduced in this chapter and will investigate the behaviour of the coupled set of integral equations for Σ and \mathcal{G} .

Chapter 6

Solving the coupled (Σ, \mathcal{G}) -system: first attempt

6.1 Numerical method to solve the coupled (Σ, \mathcal{G}) -system

In this chapter we are going to extend the study started in the previous chapter by including the photon equation in our procedure instead of approximating the vacuum polarization by its 1-loop approximation.

We recall the integral equations, Eqs. (2.59, 2.60, 2.68), derived with the bare vertex approximation. In the Landau gauge and with zero bare mass these equations are:

$$\frac{\Sigma(x)}{\mathcal{F}(x)} = \frac{3\alpha}{2\pi^2} \int dy \frac{y\mathcal{F}(y)\Sigma(y)}{y + \Sigma^2(y)} \int d\theta \sin^2 \theta \frac{\mathcal{G}(z)}{z} \quad (6.1)$$

$$\begin{aligned} \frac{1}{\mathcal{F}(x)} &= 1 + \frac{\alpha}{2\pi^2 x} \int dy \frac{y\mathcal{F}(y)}{y + \Sigma^2(y)} \\ &\times \int d\theta \sin^2 \theta \mathcal{G}(z) \left(\frac{3\sqrt{xy} \cos \theta}{z} - \frac{2xy \sin^2 \theta}{z^2} \right) \end{aligned} \quad (6.2)$$

$$\begin{aligned} \frac{1}{\mathcal{G}(x)} &= 1 + \frac{2N_f \alpha}{3\pi^2 x} \int dy \frac{y\mathcal{F}(y)}{y + \Sigma^2(y)} \int d\theta \sin^2 \theta \frac{\mathcal{F}(z)}{z + \Sigma^2(z)} \\ &\times \left[(n-2)y - 2ny \cos^2 \theta + (n+2)\sqrt{xy} \cos \theta + (n-4)\Sigma(y)\Sigma(z) \right] \end{aligned} \quad (6.3)$$

where $z \equiv x + y - 2\sqrt{xy} \cos \theta$.

Although we will generally set $n = 4$ in Eq. (6.3) throughout this work to avoid the quadratic divergence in the vacuum polarization integral, as explained in Section 2.5, we will use an alternative procedure in this chapter, taking $n = 0$, which corresponds to the operator $\mathcal{P}_{\mu\nu} = g_{\mu\nu}$ in Eq. (2.61), in order to investigate the results obtained by Kondo, Mino and Nakatani in

Ref. [20]. Setting $n = 0$ in Eq. (6.3) yields:

$$\frac{1}{\mathcal{G}(x)} = 1 - \frac{4N_f\alpha}{3\pi^2x} \int dy \frac{y\mathcal{F}(y)}{y + \Sigma^2(y)} \int d\theta \sin^2\theta \frac{\mathcal{F}(z)}{z + \Sigma^2(z)} [y - \sqrt{xy} \cos\theta + 2\Sigma(y)\Sigma(z)]. \quad (6.4)$$

The vacuum polarization integral in Eq. (6.4) contains a quadratic divergence which can be removed explicitly by imposing :

$$\lim_{x \rightarrow 0} \frac{x}{\mathcal{G}(x)} = 0, \quad (6.5)$$

to ensure a massless photon. If we write the photon renormalization function as :

$$\mathcal{G}(x) = \frac{1}{1 + \Pi(x)}, \quad (6.6)$$

Eq. (6.5) can be satisfied by defining a renormalized vacuum polarization $\Pi(x)$:

$$x\tilde{\Pi}(x) = x\Pi(x) - \lim_{x \rightarrow 0} x\Pi(x). \quad (6.7)$$

This is the procedure adopted by Kondo et al. [20]. They solve numerically the coupled set of integral equations for the dynamical fermion mass $\Sigma(x)$ and the photon renormalization function $\mathcal{G}(x)$ in the case of zero bare mass, $m_0 \equiv 0$. The calculations are performed in the Landau gauge ($\xi = 0$) with the bare vertex approximation, i.e. $\Gamma^\mu(k, p) \equiv \gamma^\mu$. As a further approximation they decouple the \mathcal{F} -equation by putting $\mathcal{F}(x) \equiv 1$. While the quadratic divergence in the vacuum polarization is removed by imposing Eq. (6.7), the fact that the Ward-Takahashi identity is not satisfied, when dynamical mass is generated, makes the results procedure dependent. The main improvement with respect to Section 5.3.2 is that we now determine the photon renormalization function $\mathcal{G}(x)$ using the photon Schwinger-Dyson equation instead of using the 1-loop perturbative result.

The coupled integral equations for Σ and \mathcal{G} obtained using these approximations, in Euclidean space and introducing an ultraviolet cutoff Λ^2 on the radial integrals, are given by :

$$\Sigma(x) = \frac{3\alpha}{2\pi^2} \int_0^{\Lambda^2} dy \frac{y\Sigma(y)}{y + \Sigma^2(y)} \int_0^\pi d\theta \sin^2\theta \frac{\mathcal{G}(z)}{z} \quad (6.8)$$

and, performing the subtraction, Eq. (6.7), on Eq. (6.4):

$$\begin{aligned} \frac{1}{\mathcal{G}(x)} = & 1 - \frac{4N_f\alpha}{3\pi^2x} \int_0^{\Lambda^2} dy \frac{y}{y + \Sigma^2(y)} \int_0^\pi d\theta \sin^2\theta \\ & \times \left\{ \frac{y - \sqrt{xy} \cos\theta + 2\Sigma(y)\Sigma(z)}{z + \Sigma^2(z)} - \frac{y + 2\Sigma^2(y)}{y + \Sigma^2(y)} \right\}. \end{aligned} \quad (6.9)$$

Recall that in QED the momentum dependence of the coupling comes wholly from the photon renormalization function, so solutions for $\mathcal{G}(x)$ give the running of the coupling. Kondo et al. solve this coupled set of non-linear integral equations, Eqs. (6.8, 6.9), for $N_f = 1$ and find a symmetry breaking phase for α greater than some critical coupling $\alpha_c \approx 2.084$.

We now describe how to solve the coupled set of integral equations Eqs. (6.8, 6.9) for $\Sigma(x)$ and $\mathcal{G}(x)$. As in the previous chapter we will replace the integral equations by a set of non-linear algebraic equations (see Section 5.3.2). For the purpose of numerical integration we introduce an ultraviolet cutoff Λ^2 and an infrared cutoff κ^2 and change variables to the logarithm of momentum squared, $t = \log_{10} y$. We then evaluate the integrals by some quadrature rule and consider the resulting equations only for external momenta equal to the integration nodes,

$$\Sigma_i = \frac{3\alpha \ln 10}{2\pi^2} \sum_{j=0}^N w_j \frac{x_j^2 \Sigma_j}{x_j + \Sigma_j^2} \sum_{k=0}^M w'_k \sin^2 \theta_k \frac{\mathcal{G}(z_k)}{z_k} \quad (6.10)$$

$$\frac{1}{\mathcal{G}_i} = 1 - \frac{4N_f \alpha \ln 10}{3\pi^2 x_i} \sum_{j=0}^N w_j \frac{x_j^2}{x_j + \Sigma_j^2} \sum_{k=0}^M w'_k \sin^2 \theta_k \times \left\{ \frac{x_j - \sqrt{x_i x_j} \cos \theta_k + 2\Sigma_j \Sigma(z_k)}{z_k + \Sigma^2(z_k)} - \frac{x_j + 2\Sigma_j^2}{x_j + \Sigma_j^2} \right\}, \quad (6.11)$$

where the equidistant logarithmic nodes are distributed as,

$$t_i = \log_{10} \kappa^2 + \frac{i}{N} \left(\log_{10} \Lambda^2 - \log_{10} \kappa^2 \right), \quad i = 0, \dots, N. \quad (6.12)$$

The corresponding momenta squared of the external particle and the radial integration nodes are

$$x_i = 10^{t_i}, \quad i = 0, \dots, N. \quad (6.13)$$

The angular integration nodes are

$$\theta_k = \frac{k\pi}{M}, \quad k = 0, \dots, M, \quad (6.14)$$

such that the momenta squared of the angular integration nodes are given by

$$z_k = x_i + x_j - 2\sqrt{x_i x_j} \cos \theta_k, \quad k = 0, \dots, M. \quad (6.15)$$

The unknowns of the system of non-linear algebraic equations are the function values at the radial integration nodes,

$$\begin{aligned} \Sigma_i &= \Sigma(x_i) \\ \mathcal{G}_i &= \mathcal{G}(x_i) \end{aligned} \quad i = 0, \dots, N. \quad (6.16)$$

However, the collocation method cannot yet be applied to Eqs. (6.10, 6.11) as the equations do not only refer to the unknown functions at the radial integration nodes x_i . The angular parts of Eqs. (6.10, 6.11) contain the function values $\Sigma(z_k)$ and $\mathcal{G}(z_k)$ where the momentum z_k defined in Eq. (6.15) is not one of the quadrature nodes x_i as it also depends on the angle between the external momentum and the internal momentum. Therefore $\Sigma(z_k)$ and $\mathcal{G}(z_k)$ are not one of the components Σ_i, \mathcal{G}_i of Eq. (6.16) which are the solution vectors of the problem and the collocation method cannot be applied directly. To compute the angular parts of Eqs. (6.10, 6.11) we have to interpolate the values of $\Sigma(z_k)$ and $\mathcal{G}(z_k)$. A straightforward choice is to perform a linear interpolation on the logarithmic scale between the function values at the surrounding integration nodes x_i and x_{i+1} , where $z_k \in [x_i, x_{i+1}]$:

$$\begin{aligned}\Sigma(z_k) &= \Sigma_i + \frac{\log_{10} z_k - \log_{10} x_i}{\log_{10} x_{i+1} - \log_{10} x_i} (\Sigma_{i+1} - \Sigma_i) \\ \mathcal{G}(z_k) &= \mathcal{G}_i + \frac{\log_{10} z_k - \log_{10} x_i}{\log_{10} x_{i+1} - \log_{10} x_i} (\mathcal{G}_{i+1} - \mathcal{G}_i) .\end{aligned}\tag{6.17}$$

After using these interpolation rules for $\Sigma(z_k)$ and $\mathcal{G}(z_k)$ in Eqs. (6.10, 6.11) the system of non-linear equations now only depends on the function values Σ_i and \mathcal{G}_i of Eq. (6.16) so that the collocation method can be applied.

We then have to solve this system of non-linear equations using some appropriate numerical technique. From the discussion in the previous chapter it is clear that Newton's iterative procedure is the right choice for this. However the full implementation of this method on the system of equations is very tedious and requires a large amount of computing time and memory allocation. A major consumption of computer time will come from the computation of the angular integrals in Eqs. (6.10, 6.11). Because the kernels of the angular integrals depend on the unknown functions, the angular integrals have to be recalculated for *each* iteration in Newton's method using the new approximations for Σ and \mathcal{G} . Furthermore, Newton's method requires the partial derivatives of the non-linear equations with respect to the function values Σ_i and \mathcal{G}_i . As these are present in the radial and angular integrals, the computation of the derivatives will use a huge amount of computer time and memory allocation. Because these resources are limited we will settle for some compromise.

We therefore introduce a hybrid method between Newton's method and the natural iterative procedure based on the observation that the kernel of the angular integrals in the Σ -equation,

Eq. (6.10), is a function of $\mathcal{G}(z)$ but is independent of Σ , while the kernel of the angular integrals of the \mathcal{G} -equation, Eq. (6.11), is a function of $\Sigma(z)$ and has no dependency on \mathcal{G} . In this hybrid method we apply Newton's method on the Σ -equation for a given \mathcal{G} , but the coupling between the Σ and \mathcal{G} equations is solved using a global natural iterative procedure. We now give more details about the program flow of this method shown in Fig. 6.1.

Let us start from some initial guess Σ_0 and \mathcal{G}_0 for the unknown vectors of function values at the quadrature points x_i . This could for example be the 1-loop perturbative approximation for \mathcal{G} and some arbitrary, realistic function for the dynamical mass Σ . We now describe how to derive new approximations $(\Sigma_{\mathbf{n}+1}, \mathcal{G}_{\mathbf{n}+1})$ starting from the current approximations $(\Sigma_{\mathbf{n}}, \mathcal{G}_{\mathbf{n}})$. We first compute the angular integrals $(\Theta_n)_{ij}$,

$$(\Theta_n)_{ij} = \sum_{k=0}^M w'_k \sin^2 \theta_k \frac{\mathcal{G}_n(z_k)}{z_k}, \quad (6.18)$$

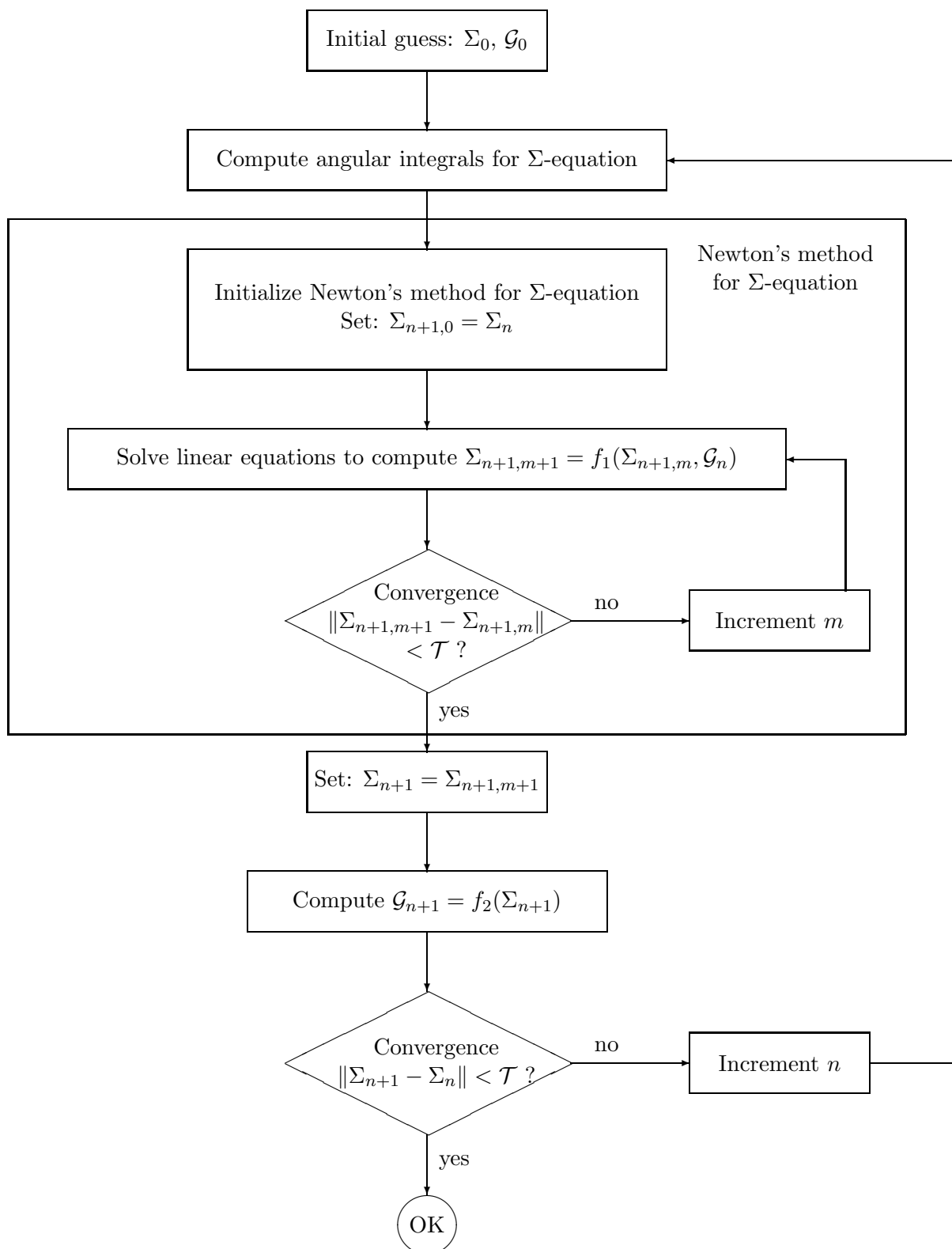
of the Σ -equation, Eq. (6.10), using $\mathcal{G}_{\mathbf{n}}$ and the interpolation rule Eq. (6.17).

Then, Eq. (6.10) becomes:

$$(\Sigma_{n+1})_i - \frac{3\alpha \ln 10}{2\pi^2} \sum_{j=0}^N w_j \frac{x_j^2 (\Sigma_{n+1})_j (\Theta_n)_{ij}}{x_j + (\Sigma_{n+1})_j^2} = 0, \quad i = 0, \dots, N. \quad (6.19)$$

Eq. (6.19) describes a system of non-linear algebraic equations determining the solution vector $\Sigma_{\mathbf{n}+1}$ computed from $\mathcal{G}_{\mathbf{n}}$. This equation is very similar to Eq. (5.102) and can be solved using Newton's iterative method. The iterative method starts from an initial guess $\Sigma_{\mathbf{n}+1,0}$, for which $\Sigma_{\mathbf{n}}$ seems an obvious but in no way necessary choice. At each iteration step the method requires the solution of a linear set of equations, Eq. (5.142), to compute $\Sigma_{\mathbf{n}+1, \mathbf{m}+1}$ from the previous solution $\Sigma_{\mathbf{n}+1, \mathbf{m}}$. Because we only improve Σ in this part of the calculation, the angular integrals Θ remain unchanged throughout Newton's method. The iterations of the Newton method will be repeated till two successive approximations $\Sigma_{\mathbf{n}+1, \mathbf{m}+1}$ and $\Sigma_{\mathbf{n}+1, \mathbf{m}}$ are sufficiently close, this approximation will be identified as $\Sigma_{\mathbf{n}+1}$.

Once the Newton method has converged, the function $\Sigma_{\mathbf{n}+1}$ is used to compute a new approximation to $\mathcal{G}_{\mathbf{n}+1}$ using the photon equation, Eq. (6.11), and the interpolation rule, Eq. (6.17). Note that the integral in this equation does only depend on Σ and so we need not apply any iterative procedure to compute $\mathcal{G}_{\mathbf{n}+1}$, all we have to do is evaluate the double sum in Eq. (6.11), corresponding to the two dimensional integrals of Eq. (6.9). This provides the end-point of one global iteration where the new approximations $(\Sigma_{\mathbf{n}+1}, \mathcal{G}_{\mathbf{n}+1})$ has been constructed from the

Figure 6.1: Program flow to solve the coupled (Σ, \mathcal{G}) -system.

previous approximation $(\Sigma_{\mathbf{n}}, \mathcal{G}_{\mathbf{n}})$. The whole procedure is iterated till the new solutions for Σ and \mathcal{G} satisfy a global convergence criterion.

As before the part computed using Newton's method is solved very efficiently. The coupling of the \mathcal{G} -iteration on the other hand slows down the whole procedure as the angular integrals for both equations have to be recalculated for every main iteration. Fortunately the \mathcal{G} -equation seems to converge relatively rapidly in this hybrid iteration scheme, i.e. after a few iterations, so that the overall computing time remains reasonable.

In the next section we will show the results obtained with this method and discuss how the photon quadratic divergence, which is easily removed theoretically, could effectively be cancelled numerically.

6.2 Numerical cancellation of the photon quadratic divergence

In this section we apply the previously developed method to determine the critical coupling and study the behaviour of the photon renormalization function of the coupled (Σ, \mathcal{G}) -system. A numerical solution to this problem has also been recently presented in Ref. [20] by Kondo, Mino and Nakatani. As in Ref. [57], we discuss the peculiar behaviour they find for the photon renormalization function \mathcal{G} at intermediate low momentum. For $N_f = 1$ we find a symmetry breaking phase for α greater than some critical coupling $\alpha_c \approx 2.084$. In Figs. 6.2, 6.3 we display the results for a value of $\alpha = 2.086$, close to its critical value. The dynamical mass function, $\Sigma(x)$, is illustrated in Fig. 6.2.

Fig. 6.3 shows the photon renormalization function, $\mathcal{G}(x)$, found from the solution of the coupled (Σ, \mathcal{G}) -system and this is compared with its 1-loop approximation. To allow the comparison with the 1-loop result the vacuum polarization is renormalized such that $\tilde{\Pi}(\Lambda^2) = 0$.

One observes that at high momenta the self-consistent $\mathcal{G}(x)$ follows the 1-loop result very nicely. For decreasing momenta the effect of the dynamically generated mass comes into play and the value of $\mathcal{G}(x)$, and hence that of the running coupling, seems to stabilize for a while, as one could expect. Then, surprisingly, at some lower momentum there is a sudden fall in $\mathcal{G}(x)$, which drops below the 1-loop value and almost vanishes completely. This is a rather strange behaviour for the running coupling at low momenta. This decrease corresponds to the vacuum polarization integral of Eq. (6.9) becoming large. We will show that this sharp decrease is an artefact of the method used by Kondo et al. [20] to remove the quadratic divergence in the vacuum polarization.

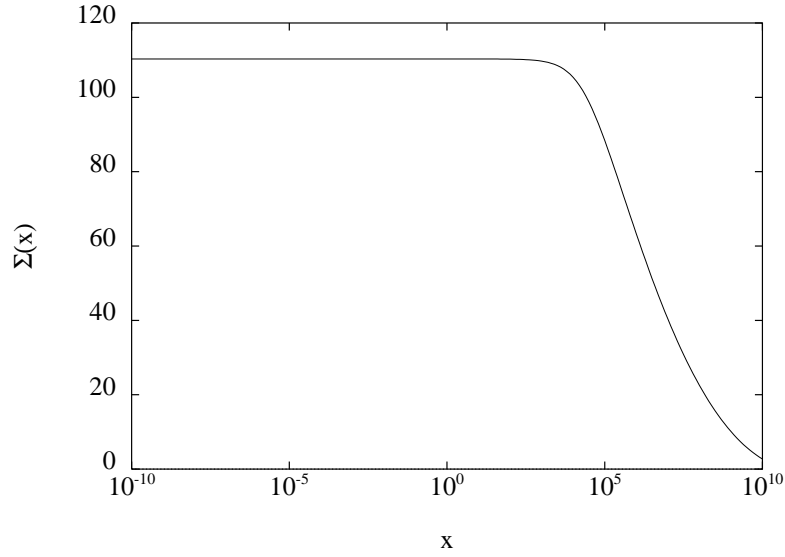


Figure 6.2: Dynamical mass function $\Sigma(x)$, as a function of momentum x for $N_f = 1$ and $\alpha = 2.086$ as calculated in a self-consistent way as in Ref. [20] ($\Lambda^2 = 1e10$).

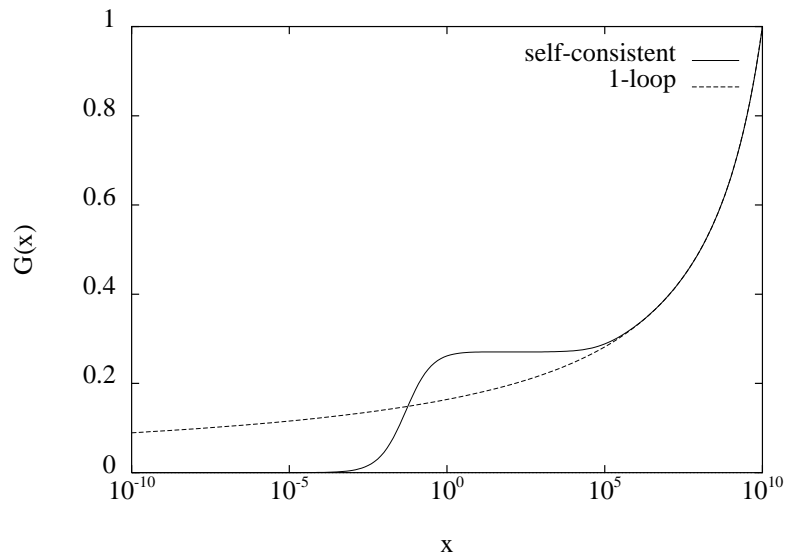


Figure 6.3: Photon renormalization function $\mathcal{G}(x)$, as a function of momentum x for $N_f = 1$ and $\alpha = 2.086$ as calculated in a self-consistent way as in Ref. [20] and in 1-loop approximation ($\Lambda^2 = 1e10$).

We also discuss how this can be avoided in numerical studies of the Schwinger-Dyson equations. To solve the problem numerically we have to make additional assumptions about the ultraviolet behaviour of $\Sigma(x)$ and $\mathcal{G}(x)$. These arise from the need to handle loop momenta beyond the ultraviolet (UV) cutoff. If in Eqs. (6.8, 6.9) $0 \leq x, y \leq \Lambda^2$, then the momentum in the angular integration, $z = x + y - 2\sqrt{xy} \cos \theta$, will lie in the interval $0 \leq z \leq 4\Lambda^2$. Therefore, the angular integrals need values of Σ and \mathcal{G} at momenta above the UV-cutoff, i.e. outside the *physical momentum region*. Therefore one will have to extrapolate Σ and \mathcal{G} outside this region. In their work, Kondo et al. [20] define :

$$\Sigma(x > \Lambda^2) \equiv 0 \quad (6.20)$$

$$\Pi(x > \Lambda^2) \equiv 0 \Rightarrow \mathcal{G}(x > \Lambda^2) \equiv 1. \quad (6.21)$$

Both dynamical mass and vacuum polarization vanish above the UV-cutoff and the theory then behaves as a free theory. Although this assumption seems reasonable, Eq. (6.20) introduces a jump discontinuity in the dynamical mass function at $x = \Lambda^2$ because $\Sigma(\Lambda^2) \neq 0$ for $\alpha > \alpha_c$ (see Fig. 6.2), while Eq. (6.21) introduces a relatively sharp kink in the photon renormalization function at that point (see Fig. 6.3).

A more detailed investigation shows that the step in the photon renormalization function found by Kondo et al. is an artefact of the way they renormalize the quadratic divergence in the vacuum polarization integral, Eq. (6.9), combined with the presence of the jump discontinuity in the dynamical mass function, Eq. (6.20), as we now explain.

From the angular integrand of the \mathcal{G} -equation, Eq. (6.9) , we define f_θ as :

$$f_\theta = \frac{y - \sqrt{xy} \cos \theta + 2\Sigma(y)\Sigma(z)}{z + \Sigma^2(z)} - \frac{y + 2\Sigma^2(y)}{y + \Sigma^2(y)}. \quad (6.22)$$

Both terms in Eq. (6.22) cancel exactly at $x = 0$ to remove the quadratic singularity. Of course the description of the real world has to be such that the approximate cancellation of the quadratically divergent terms at low x becomes exact at $x = 0$ in a continuous way.

To investigate this, we now look analytically at the behaviour of f_θ at low x , for some arbitrary value of y and θ . We can write z as:

$$z = y + \delta y \quad (6.23)$$

where we define:

$$\delta y = x - 2\sqrt{xy} \cos \theta, \quad (6.24)$$

and we know δy is small if x is small. Furthermore, we also write $\Sigma(z)$ as:

$$\Sigma(z) = \Sigma(y) + \delta\Sigma. \quad (6.25)$$

Substituting Eqs. (6.23), (6.25) in the expression for the angular integrand f_θ , Eq. (6.22), yields:

$$f_\theta \approx \frac{y - \sqrt{xy} \cos \theta + 2\Sigma^2(y) + 2\delta\Sigma\Sigma(y)}{y + \Sigma^2(y) + \delta y + 2\delta\Sigma\Sigma(y) + \delta\Sigma^2} - \frac{y + 2\Sigma^2(y)}{y + \Sigma^2(y)}. \quad (6.26)$$

Performing a Taylor expansion of the denominator of the first term, we get (neglecting terms of $\mathcal{O}(\delta y)^2, \delta\Sigma^2$):

$$\begin{aligned} f_\theta &\approx \frac{1}{y + \Sigma^2(y)} \left[-\sqrt{xy} \cos \theta + 2\delta\Sigma\Sigma(y) - (\delta y + 2\delta\Sigma\Sigma(y)) \frac{y - \sqrt{xy} \cos \theta + 2\Sigma^2(y)}{y + \Sigma^2(y)} \right] \\ &\approx \mathcal{O}(x, \sqrt{xy} \cos \theta, \delta\Sigma). \end{aligned} \quad (6.27)$$

If $\Sigma(z)$ is smooth, we can make a Taylor expansion of $\Sigma(z)$ around $\Sigma(y)$:

$$\Sigma(z) = \Sigma(y) + \delta y \Sigma'(y) + \mathcal{O}(\delta y)^2, \quad (6.28)$$

and $\delta\Sigma$ of Eq. (6.25) is,

$$\delta\Sigma = \delta y \Sigma'(y) + \mathcal{O}(\delta y)^2. \quad (6.29)$$

In this case, Eq. (6.27) becomes,

$$f_\theta \approx \mathcal{O}(x, \sqrt{xy} \cos \theta) \quad (6.30)$$

and it is clear that the angular integrand f_θ is continuous for all $\theta \in [0, \pi]$ and goes to zero in a continuous way when x goes to zero. From Eq. (6.27) we see that the same argument holds even when Σ is continuous, but not necessarily smooth, at $z = \Lambda^2$.

Now let us look at the angular integrand f_θ in the approximation of Kondo et al. [20] when x is small but y is very large, indeed larger than $y_0 = (\Lambda - \sqrt{x})^2$. Then, for values of θ greater than $\theta_0(y) = \arccos((x + y - \Lambda^2)/2\sqrt{xy})$ we will have $z > \Lambda^2$. If we now use Kondo et al.'s extrapolation, Eq. (6.20), then $\Sigma(z > \Lambda^2) = 0$ and the angular integrand Eq. (6.22), now becomes :

$$f_\theta = \frac{y - \sqrt{xy} \cos \theta}{z} - \frac{y + 2\Sigma^2(y)}{y + \Sigma^2(y)}, \quad \text{for } z > \Lambda^2. \quad (6.31)$$

For small x , and $z > \Lambda^2$ (corresponding to $y > y_0$ and $\theta > \theta_0(y)$) we have,

$$f_\theta \approx -\frac{\Sigma^2(y)}{y + \Sigma^2(y)} + \mathcal{O}(x, \sqrt{xy} \cos \theta), \quad (6.32)$$

while for small x and $z \leq \Lambda^2$ we still have the expected behaviour of Eq. (6.30),

$$f_\theta \approx \mathcal{O}(x, \sqrt{xy} \cos \theta). \quad (6.33)$$

From Eqs. (6.32, 6.33) we see that as soon as x deviates from zero, the angular integrands for $y > y_0$ contain a jump discontinuity at $\theta = \theta_0(y)$, and part of the angular integrand will not vanish continuously when $x \rightarrow 0$. In fact the angular integral I_θ will receive an extra contribution δI_θ when y is larger than $y_0 = (\Lambda - \sqrt{x})^2$:

$$\begin{aligned} \delta I_\theta(y > y_0) &= -\frac{\Sigma^2(y)}{y + \Sigma^2(y)} \int_{\theta_0(y)}^{\pi} d\theta \sin^2 \theta \\ &= -\frac{\Sigma^2(y)}{y + \Sigma^2(y)} \left(\frac{\pi}{2} - \frac{\theta_0(y)}{2} + \frac{\sin 2\theta_0(y)}{4} \right). \end{aligned} \quad (6.34)$$

Substituting Eq. (6.34) in Eq. (6.9) we see that the vacuum polarization receives an extra contribution $\delta \Pi(x)$:

$$\delta \Pi(x) = \frac{4N_f \alpha}{3\pi^2 x} \int_{y_0}^{\Lambda^2} dy \frac{y \Sigma^2(y)}{(y + \Sigma^2(y))^2} \left(\frac{\pi}{2} - \frac{\theta_0(y)}{2} + \frac{\sin 2\theta_0(y)}{4} \right). \quad (6.35)$$

Writing $\sqrt{y} = \Lambda + \sqrt{x} \cos \psi$, so that $\theta_0 \simeq \psi$ for $x \ll \Lambda^2$, we have, using the mean value theorem :

$$\delta \Pi(x) \simeq \frac{8N_f \alpha}{3\pi^2} \frac{\Lambda^3 \Sigma^2(\Lambda^2)}{\sqrt{x}(\Lambda^2 + \Sigma^2(\Lambda^2))^2} \int_{\pi/2}^{\pi} d\psi \sin \psi \left(\frac{\pi}{2} - \frac{\psi}{2} + \frac{\sin 2\psi}{4} \right), \quad (6.36)$$

so that :

$$\delta \Pi(x) \simeq \frac{8N_f \alpha}{9\pi^2} \frac{\Sigma^2(\Lambda^2)}{\sqrt{x}\Lambda}. \quad (6.37)$$

Because of the $1/\sqrt{x}$ this change in $\Pi(x)$ would be noticeable at very small values of x . However, this analytic calculation does not explain the sharp decrease of $\mathcal{G}(x)$ at intermediate low momenta we and Kondo et al. [20] find (see Fig. 6.3).

To understand why this happens we have to consider how the numerical program computes the extra contribution, Eq. (6.35), to the vacuum polarization integral. As shown in Eq. (6.11), the integrals of Eq. (6.9) are approximated by a finite sum of integrand values at momenta uniformly spread on a logarithmic scale. For small x , the extra contribution is entirely concentrated at the uppermost momentum region of the radial integral with $y \in [y_0, \Lambda^2]$. There the numerical integration program will have only one grid point x_i (Eq. (6.13)) situated in the interval $[y_0, \Lambda^2]$ for any realistic grid distribution. This point will lie at $x_N = \Lambda^2$ if we use a closed $(N+1)$ -point

quadrature formula. Therefore the integral will be approximated by the value of the integrand at Λ^2 times a weight factor $W(\Lambda^2) = w\Lambda^2$ (w is $\mathcal{O}(1)$) :

$$\delta\Pi(x) \approx \frac{4N_f\alpha}{3\pi^2} \frac{W(\Lambda^2)\Lambda^2\Sigma^2(\Lambda^2)}{x(\Lambda^2 + \Sigma^2(\Lambda^2))^2} \left(\frac{\pi}{2} - \frac{\theta_0(\Lambda^2)}{2} + \frac{\sin 2\theta_0(\Lambda^2)}{4} \right). \quad (6.38)$$

For small x we have $\theta_0(\Lambda^2) \approx \pi/2$ and the extra contribution to the vacuum polarization will be :

$$\delta\Pi(x) \approx \frac{N_f\alpha w}{3\pi} \frac{\Sigma^2(\Lambda^2)}{x}. \quad (6.39)$$

This will effectively add a huge correction to the vacuum polarization at low x . This has been extensively checked numerically and shown to be completely responsible for the sudden decrease in the photon renormalization function $\mathcal{G}(x)$ at low momenta. To reproduce our previous analytic result of Eq. (6.37) numerically, the integration grid would have to be tuned unnaturally fine to include more points in the region $[y_0, \Lambda^2]$. Without such tuning one has the result of Eq. (6.39). Then $x\Pi(x)$ does not vanish continuously as $x \rightarrow 0$. Instead, for $x > 0$, $x\Pi(x) \approx N_f\alpha w\Sigma^2(\Lambda^2)/3\pi$ and so as soon as x is non-zero the cancellation of the quadratic divergence disappears suddenly and not gradually as the physical world requires. Eq. (6.39) tells us that the step in \mathcal{G} (see Fig. 6.3), is due to an unsuccessful numerical cancellation of the quadratic divergence in the vacuum polarization integral $\Pi(x)$. It is significant for the sensitivity of the problem that, against all expectations, the high momentum behaviour of $\Sigma(x)$, where its value is quite small, plays such a major role in the behaviour of $\mathcal{G}(x)$ at low x . This will even become more apparent in the following discussion.

It is natural to expect that the function Σ from the physical world will be smooth. To improve on the discontinuous extrapolation rule Eq. (6.20), we can replace it by the following simple extrapolation rule :

$$\Sigma(x > \Lambda^2) = \Sigma(\Lambda^2) \frac{\Lambda^2}{x}. \quad (6.40)$$

This will get rid of the jump discontinuity in the dynamical mass function, leaving instead a very slight kink. Although $\Sigma(x)$ is not yet smooth at $x = \Lambda^2$ it now is continuous. When solving the integral equations using this extrapolation rule, the step in the photon renormalization function at intermediate low momenta disappears, only to be replaced by a singularity as can be seen in Fig. 6.4.

However, the new singularity in \mathcal{G} is not as worrying as it may seem at first sight. If we recall

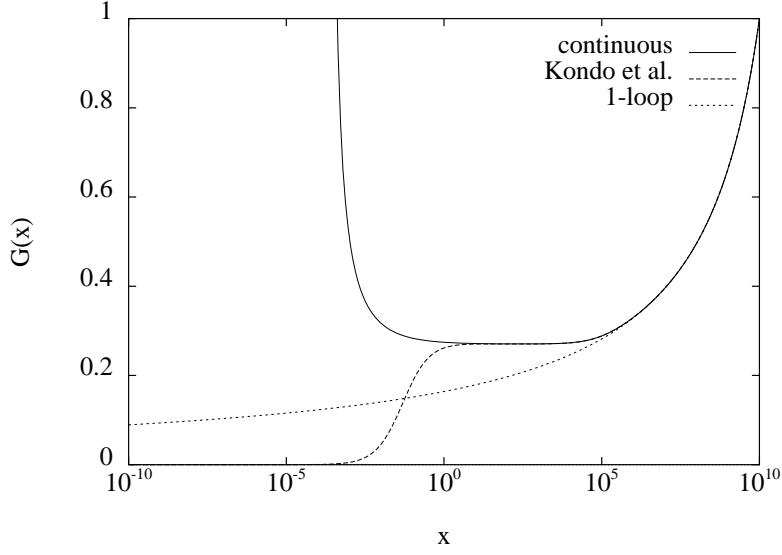


Figure 6.4: Photon renormalization function $\mathcal{G}(x)$, as a function of momentum x for $N_f = 1$ and $\alpha = 2.086$ as calculated in a self-consistent way with a continuous extrapolation for Σ , with the jump discontinuity in Σ as in Ref. [20] and in 1-loop approximation ($\Lambda^2 = 1e10$).

Eq. (6.6),

$$\mathcal{G}(x) = \frac{1}{1 + \Pi(x)},$$

we see that the singularity in \mathcal{G} corresponds to $\Pi(x) \rightarrow -1$. A closer numerical investigation shows that this is due to the inadequacy of the interpolations, Eq. (6.17), to compute the angular integrals in Eq. (6.11). The functions $\Sigma(x)$ and $\mathcal{G}(x)$ constructed with these interpolation rules are in fact piecewise linear polynomials (on logarithmic scale) with interpolation points x_i . Although these functions are continuous, they are not smooth and this leads to cancellation mismatches in the angular integrals of the \mathcal{G} -equation and thus to unphysical singularities in \mathcal{G} .

This points the way to a possible solution of this problem: we want smooth approximations to the functions in order to get a realistic, physical answer to the problem.

To study the validity of this statement without completely modifying the numerical program straight away, we just add one more step at the very end of the previous calculation. There we used the collocation method to construct the system of non-linear equations, Eqs. (6.10, 6.11), enhanced with the interpolation rules, Eq. (6.17), and extrapolation rules, Eqs. (6.40, 6.21). This system of equations was then solved to determine the unknown function values Σ_i and \mathcal{G}_i at the quadrature nodes of the radial integrals.

Starting from this solution vector Σ_i we now construct a smooth polynomial approximation $\tilde{\Sigma}(x)$ using, for instance, Chebyshev polynomials to replace the piecewise linear construction achieved previously with the interpolation rule Eq. (6.17). The Chebyshev approximation to $\Sigma(x)$ can be written as,

$$\tilde{\Sigma}(x) = \sum_{j=0}^{N-1} a_j T_j(x). \quad (6.41)$$

As will be shown in Section 7.2, the coefficients a_j can be easily determined provided we know the function values $\Sigma(y_j)$ at the N distinct roots y_j of the Chebyshev polynomial $T_N(x)$ of degree N . The function values $\Sigma(y_j)$, needed to determine a_j , can be approximated by applying the interpolation rule Eq. (6.17) on the solution vector Σ_i . The polynomial approximation $\tilde{\Sigma}(x)$ coincides with the interpolated, piecewise linear, dynamical mass function $\Sigma(x)$ at the N points y_j ,

$$\tilde{\Sigma}(y_j) = \Sigma(y_j), \quad j = 1, \dots, N. \quad (6.42)$$

Note that the interpolation points y_j of the new smoothed function $\tilde{\Sigma}(x)$ do not coincide with the original collocation points x_i of the collocation method, and thus, $\tilde{\Sigma}(x_i) \neq \Sigma_i$.

We now use the smooth function $\tilde{\Sigma}(x)$ of Eq. (6.41) to compute numerically the integral evaluations in Eq. (6.11), and determine \mathcal{G} . As we see in Fig. 6.5, the smoothing of Σ has the desired effect on the behaviour of \mathcal{G} . The singularity disappears and is replaced by a flat line down into the infrared. This agrees with our physical intuition about the behaviour of the running of the coupling, when fermion mass is generated.

In this chapter we have seen that the proper numerical cancellation of the quadratic divergence in the vacuum polarization requires the dynamical mass function $\Sigma(x)$ to be smooth. This ensures that the cancellation of the quadratic divergence takes place smoothly as $x \rightarrow 0$.

From the previous discussion we conclude that the collocation method, where the unknowns of the problem are the function values at the radial integration nodes, has definite drawbacks. Because the unknown functions are also present in the angular integrals, we have to complement the method with some appropriate interpolation and extrapolation rules. The function Σ constructed with these rules will not be smooth and therefore \mathcal{G} will behave unphysically. Furthermore, as mentioned in the previous chapter, the use of a single fixed set of radial integration points in the collocation method, and the kink in the radial integrand forcing us to split the integral in two, reduces the accuracy of the integration rules.

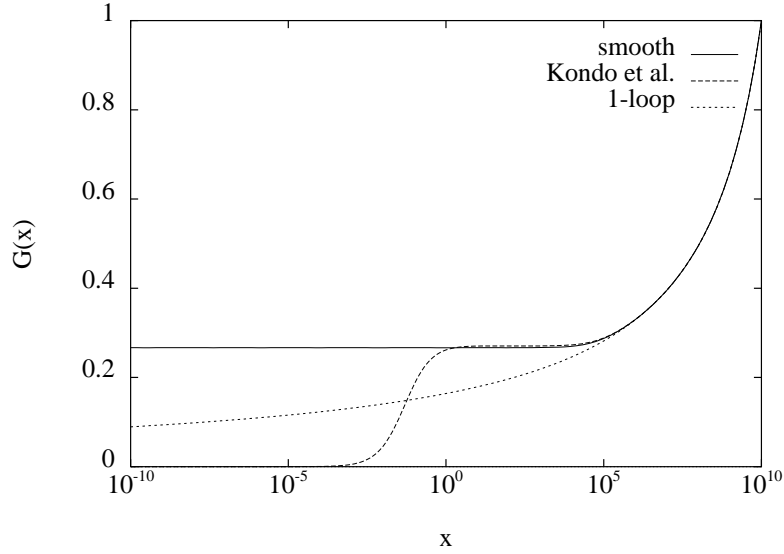


Figure 6.5: Photon renormalization function $\mathcal{G}(x)$, as a function of momentum x for $N_f = 1$ and $\alpha = 2.086$ as calculated in a self-consistent way with a smoothed approximation to Σ , with the jump discontinuity in Σ as in Ref. [20] and in 1-loop approximation ($\Lambda^2 = 1e10$).

To avoid these problems it is therefore preferable to search for smooth solutions for the dynamical mass function $\Sigma(x)$, the fermion wavefunction renormalization $\mathcal{F}(x)$ and the photon renormalization function $\mathcal{G}(x)$. In the next chapter we are going to develop the formalism to approximate the unknown functions by a smooth, polynomial expansion instead of discretizing the function at the radial integration points.

Chapter 7

Chebyshev expansion method

In the previous chapters we solved the integral equations using the collocation method. This method discretizes the unknown functions at the nodes of the quadrature rule used to evaluate the integrals. However we gathered enough evidence supporting the need to develop an alternative procedure where these functions are smoothly approximated, for example by the use of some polynomial expansion. For various reasons one of the favoured polynomial approximations of functions is the expansion in Chebyshev polynomials.

7.1 Chebyshev polynomials

The Chebyshev polynomial of degree n is denoted $T_n(x)$, and is given by the explicit formula [41],

$$T_n(x) = \cos(n \arccos x) . \quad (7.1)$$

Although this looks trigonometric at first glance, the use of trigonometric expressions in Eq. (7.1) gives the following polynomial forms,

$$\begin{aligned} T_0(x) &= 1 \\ T_1(x) &= x \\ T_2(x) &= 2x^2 - 1 \\ T_3(x) &= 4x^3 - 3x \\ T_4(x) &= 8x^4 - 8x^2 + 1 \\ &\vdots \end{aligned} \quad (7.2)$$

In general one can derive the following recursion relation:

$$T_{n+1}(x) = 2xT_n(x) - T_{n-1}(x), \quad n \geq 1. \quad (7.3)$$

We plot the first few Chebyshev polynomials $T_n(x)$, $n=0, \dots, 4$ in Fig. 7.1.

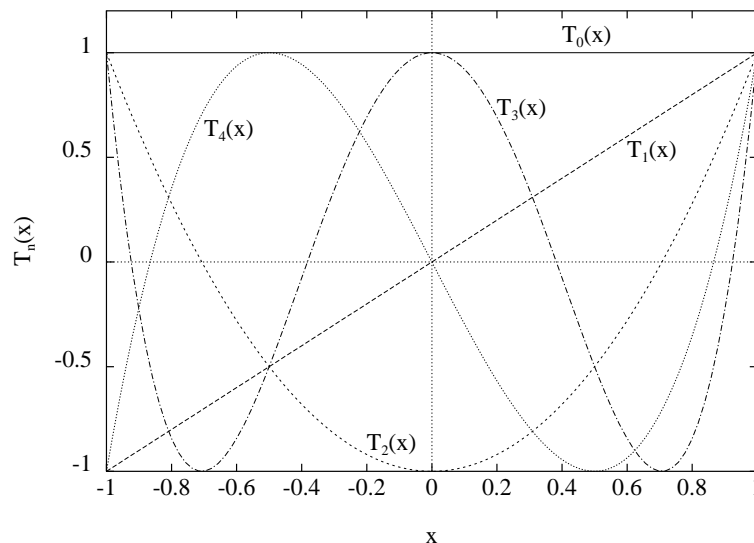


Figure 7.1: Chebyshev polynomials $T_n(x)$ for $n=0, \dots, 4$.

The polynomial $T_n(x)$ has n zeros in the interval $[-1, 1]$ at

$$x = \cos\left(\frac{(k-1/2)\pi}{n}\right), \quad k = 1, \dots, n. \quad (7.4)$$

$T_n(x)$ also has $n+1$ extrema in $[-1, 1]$ located at

$$x = \cos\left(\frac{k\pi}{n}\right), \quad k = 0, \dots, n. \quad (7.5)$$

All the minima have a value $T_n(x) = -1$, while the maxima all have a value $T_n(x) = 1$.

The Chebyshev polynomials are orthogonal in the interval $[-1, 1]$ over a weight $\sqrt{1-x^2}$,

$$\int_{-1}^1 dx \frac{T_i(x)T_j(x)}{\sqrt{1-x^2}} = \begin{cases} 0 & i \neq j \\ \pi/2 & i = j \neq 0 \\ \pi & i = j = 0 \end{cases}. \quad (7.6)$$

In addition to the continuous orthogonality relation Eq. (7.6), the Chebyshev polynomials also satisfy a discrete orthogonality relation. If x_k are the n zeros of $T_n(x)$ given by Eq. (7.4), $k = 1, \dots, n$, and if $i, j < n$, then

$$\sum_{k=1}^n T_i(x_k)T_j(x_k) = \begin{cases} 0 & i \neq j \\ n/2 & i = j \neq 0 \\ n & i = j = 0 \end{cases}. \quad (7.7)$$

7.2 Chebyshev approximation

We now want to determine the coefficients c_j of the polynomial approximation to an arbitrary function $f(x)$,

$$f(x) \approx \sum_{j=0}^{N-1} 'c_j T_j(x) \equiv \sum_{j=0}^{N-1} c_j T_j(x) - \frac{c_0}{2}, \quad (7.8)$$

such that the approximation becomes *exact* at the N zeros of $T_N(x)$.

For these zeros we then have

$$f(x_k) = \sum_{j=0}^{N-1} 'c_j T_j(x_k), \quad k = 1, \dots, N. \quad (7.9)$$

Multiply both sides with $T_i(x_k)$ where $i < N$ and sum over all zeros of $T_N(x)$:

$$\sum_{k=1}^N T_i(x_k) f(x_k) = \sum_{j=0}^{N-1} 'c_j \sum_{k=1}^N T_i(x_k) T_j(x_k). \quad (7.10)$$

Using the orthogonality relation Eq. (7.7) yields:

$$\sum_{k=1}^N T_i(x_k) f(x_k) = \frac{N}{2} c_i. \quad (7.11)$$

The coefficients c_j of Eq. (7.8) are

$$c_j = \frac{2}{N} \sum_{k=1}^N T_j(x_k) f(x_k). \quad (7.12)$$

If we substitute the expression (7.4) for the zeros of $T_N(x)$ this becomes:

$$c_j = \frac{2}{N} \sum_{k=1}^N T_j \left[\cos \left(\frac{(k-1/2)\pi}{N} \right) \right] f \left[\cos \left(\frac{(k-1/2)\pi}{N} \right) \right]. \quad (7.13)$$

Substituting the definition Eq. (7.1) for the Chebyshev polynomial $T_j(x)$ the coefficients can be computed as

$$c_j = \frac{2}{N} \sum_{k=1}^N \cos \left(\frac{j(k-1/2)\pi}{N} \right) f \left[\cos \left(\frac{(k-1/2)\pi}{N} \right) \right]. \quad (7.14)$$

The Chebyshev expansion is often used because the error generated by replacing the function by its expansion is smeared out over the complete interval.

7.3 Evaluation of Chebyshev approximation

To evaluate a Chebyshev approximation of a function using a set of Chebyshev coefficients c_j , we could use the recurrence relation Eq. (7.3) to evaluate the successive values of $T_j(x)$ and then sum up these contributions multiplied by their respective coefficient. However, there is a more efficient way to evaluate a sum of polynomials using *Clenshaw's recurrence formula*.

Suppose we want to evaluate the polynomial sum

$$f(x) \equiv \sum_{j=0}^N c_j F_j(x), \quad (7.15)$$

where the polynomials $F_j(x)$ obey a recurrence relation of the kind,

$$F_{n+1}(x) = \alpha(n, x)F_n(x) + \beta(n, x)F_{n-1}(x). \quad (7.16)$$

Define the quantities d_j by the following recurrence relation:

$$d_j = \alpha(j, x)d_{j+1} + \beta(j+1, x)d_{j+2} + c_j, \quad j = N, N-1, \dots, 1 \quad (7.17)$$

where $d_{N+2} = d_{N+1} = 0$.

Then *Clenshaw's recurrence formula* to compute $f(x)$ defined in Eq. (7.15) is

$$f(x) = \beta(1, x)F_0(x)d_2 + F_1(x)d_1 + F_0(x)c_0. \quad (7.18)$$

If we apply Clenshaw's formula to the Chebyshev polynomials obeying the recurrence relation Eq. (7.3), the function approximation Eq. (7.8) is given by

$$\begin{aligned} d_{N+1} &= d_N = 0 \\ d_j &= 2xd_{j+1} - d_{j+2} + c_j, \quad j = N-1, N-2, \dots, 1 \\ f(x) &= xd_1 - d_2 + \frac{c_0}{2}. \end{aligned} \quad (7.19)$$

The Chebyshev polynomials define a polynomial approximation over the interval $[-1, 1]$. To approximate a function $f(x)$ over an arbitrary interval $[a, b]$ we introduce a change of variable

$$s \equiv \frac{x - \frac{1}{2}(b+a)}{\frac{1}{2}(b-a)}, \quad (7.20)$$

so that,

$$x \in [a, b] \mapsto s \in [-1, 1]. \quad (7.21)$$

The Chebyshev approximation will now be

$$f(x) \approx \sum_{j=0}^{N-1} 'c_j T_j(s), \quad (7.22)$$

where x is mapped into s using Eq. (7.20).

7.4 Chebyshev expansions for Σ , \mathcal{F} and \mathcal{G} .

For the specific case of the numerical solution of the Schwinger-Dyson equations, we have already pointed out in the previous chapters that a convenient variable to perform the numerical integrations is $t = \log_{10} x$. Therefore we will consider $\Sigma(x)$, $\mathcal{F}(x)$ and $\mathcal{G}(x)$ as functions of t , defined over the interval $t \in [\log_{10} \kappa^2, \log_{10} \Lambda^2]$. According to Eq. (7.20) the Chebyshev polynomials, used to construct the Chebyshev expansions, will be written as function of the new variable s defined as

$$s = \frac{\log_{10} x - \frac{1}{2}(\log_{10} \Lambda^2 + \log_{10} \kappa^2)}{\frac{1}{2}(\log_{10} \Lambda^2 - \log_{10} \kappa^2)}, \quad (7.23)$$

or

$$s \equiv \frac{\log_{10}(x/\Lambda\kappa)}{\log_{10}(\Lambda/\kappa)}. \quad (7.24)$$

We will define the Chebyshev expansions of the unknown functions as:

$$\Sigma(x) \equiv \sum_{j=0}^{N_{\Sigma}-1} 'a_j T_j(s) \quad (7.25)$$

$$\mathcal{F}(x) \equiv \sum_{j=0}^{N_{\mathcal{F}}-1} 'b_j T_j(s) \quad (7.26)$$

$$\mathcal{G}(x) \equiv \sum_{j=0}^{N_{\mathcal{G}}-1} 'c_j T_j(s), \quad (7.27)$$

where s is defined by Eq. (7.24).

In principle the number of Chebyshev polynomials N_{Σ} , $N_{\mathcal{F}}$, $N_{\mathcal{G}}$ used to approximate the functions will be chosen so that the error on the three functions is comparable.

We now mention some of the advantages of using the Chebyshev expansion to approximate the unknown functions. First of all, it guarantees the smoothness of the solutions and in doing so it should also ensure the correct cancellation of the quadratical divergence in the vacuum polarization integral. Related to this is the fact that the Chebyshev expansions are extremely useful to handle the two-dimensional integrals because the function values can be computed at

any value of $x \in [a, b]$. There is no need for any complementary interpolation method anymore. Furthermore, because we can compute the function values at any point it allows us to use whatever quadrature rule we want, we are not bound anymore to use the same set of equidistant integration points for all the individual equations in the system of non-linear equations. We can now freely choose a different, optimal set of points for each integration.

7.5 Σ -equation and Chebyshev expansion

We will now use the Chebyshev expansion for Σ to construct an alternative method for solving the integral equation to replace the previously used collocation method.

Let us recall the Σ -equation Eq. (5.98),

$$\Sigma(x) = \frac{3\alpha \ln 10}{2\pi^2} \int_{\log_{10} \kappa^2}^{\log_{10} \Lambda^2} dt \frac{y^2 \Sigma(y)}{y + \Sigma^2(y)} \int d\theta \frac{\sin^2 \theta}{z(1 + \frac{N_f \alpha}{3\pi} \ln \frac{\Lambda^2}{z})}, \quad x \in [\kappa^2, \Lambda^2] \quad (7.28)$$

where $y = 10^t$ and $z = x + y - 2\sqrt{xy} \cos \theta$.

We will now look for an approximate solution $\Sigma(x)$ to Eq. (7.28) which can be written as a Chebyshev expansion,

$$\Sigma(x) = \sum_{j=0}^{N_\Sigma-1} a_j T_j(s(x)) \quad (7.29)$$

where $x \in [\kappa^2, \Lambda^2]$ and, from Eq. (7.24),

$$s(x) = \frac{\log_{10}(x/\Lambda\kappa)}{\log_{10}(\Lambda/\kappa)}. \quad (7.30)$$

The integral equation Eq. (7.29) contains N_Σ unknown Chebyshev coefficients a_j . To determine these coefficients we need at least N_Σ constraints. These constraints are obviously found by imposing that Eq. (7.29) should be satisfied at M different values of x (where $M \geq N_\Sigma$).

$$\Sigma_i = \frac{3\alpha \ln 10}{2\pi^2} \int_{\log_{10} \kappa^2}^{\log_{10} \Lambda^2} dt \frac{y^2 \Sigma(y)}{y + \Sigma^2(y)} \int d\theta \frac{\sin^2 \theta}{z(1 + \frac{N_f \alpha}{3\pi} \ln \frac{\Lambda^2}{z})}, \quad i = 1, \dots, M, \quad (7.31)$$

where $\Sigma_i = \Sigma(x_i)$ using the Chebyshev expansion Eq. (7.29).

If $M = N_\Sigma$, Eq. (7.31) is a system of N_Σ non-linear equations with N_Σ unknowns. If $M > N_\Sigma$ the system of equations will be overconstrained and the coefficients can be determined by *minimizing* the error between the right and left hand sides of the complete system of M equations. Such a minimization procedure is quite tedious for a non-linear problem and does not have any advantage compared to solving the system of equations when $M = N_\Sigma$ [58]. In practice we will

choose the N_Σ external momenta to be located at the N_Σ zeros of the Chebyshev polynomial T_{N_Σ} ,

$$s_i = \cos\left(\frac{(i-1/2)\pi}{N_\Sigma}\right), \quad i = 1, \dots, N_\Sigma, \quad (7.32)$$

and from Eq. (7.30) the external momenta x_i are given by ,

$$x_i = \Lambda \kappa \left(\frac{\Lambda}{\kappa}\right)^{s_i}. \quad (7.33)$$

In contrast to the use of the expansion method to solve linear integral equations, the non-linearity of Eq. (7.31) does not allow us to take the expansion coefficients a_j out of the integrals. To make further progress in the numerical solution of Eq. (7.31), we have to approximate the integrals of Eq. (7.31) by some suitable quadrature rules. The quadrature rule R_i , the number of integration nodes and the position of the nodes can vary depending on the external momentum x_i . The actual choice of the quadrature rule will be discussed in a later section. Eq. (7.31) can now be written as:

$$\Sigma_i = \frac{3\alpha \ln 10}{2\pi^2} \sum_{k=0}^{(N_R)_i} w_{ik} \frac{y_{ik}^2 \Sigma_{ik}}{y_{ik} + \Sigma_{ik}^2} \sum_{\ell=0}^{N_\theta} w'_\ell \frac{\sin^2 \theta_\ell}{z_\ell \left(1 + \frac{N_f \alpha}{3\pi} \ln \frac{\Lambda^2}{z_\ell}\right)}, \quad i = 1, \dots, N_\Sigma, \quad (7.34)$$

where $\Sigma_{ik} = \Sigma(y_{ik})$, $y_{ik} = 10^{t_{ik}}$, t_{ik} are the $(N_R)_i + 1$ integration nodes and w_{ik} the weights corresponding to the integration rule R_i . The photon momentum in the angular part is given by $z_\ell = x_i + y_{ik} - 2\sqrt{x_i y_{ik}} \cos \theta_\ell$.

The angular part of Eq. (7.34) is independent of the unknown function Σ . We define:

$$\Theta_{ik} \equiv \sum_{\ell=0}^{N_\theta} w'_\ell \frac{\sin^2 \theta_\ell}{z_\ell \left(1 + \frac{N_f \alpha}{3\pi} \ln \frac{\Lambda^2}{z_\ell}\right)}. \quad (7.35)$$

Substituting Eq. (7.35) in Eq. (7.34) yields:

$$\Sigma_i = \frac{3\alpha \ln 10}{2\pi^2} \sum_{k=0}^{(N_R)_i} w_{ik} \frac{y_{ik}^2 \Theta_{ik} \Sigma_{ik}}{y_{ik} + \Sigma_{ik}^2}, \quad i = 1, \dots, N_\Sigma. \quad (7.36)$$

Eqs. (7.36, 7.29) form a system of N_Σ non-linear algebraic equations, where the N_Σ Chebyshev coefficients are the unknowns. To solve this system of equations, we will again use Newton's method, developed in Section 5.4. We apply Eqs. (5.127, 5.126, 5.118) to Eqs. (7.36, 7.29).

Newton's iterative method will provide successive approximations \mathbf{a}_n to the vector of Chebyshev coefficients \mathbf{a} solving Eq. (7.36). Each iteration step requires the solution of a linear set of equations:

$$J(\mathbf{a}_n) \Delta_{n+1} = \mathbf{f}(\mathbf{a}_n). \quad (7.37)$$

Once the solution $\Delta_{\mathbf{n}+1}$ of Eq. (7.37) has been computed, the new approximation $\mathbf{a}_{\mathbf{n}+1}$ is determined from

$$\mathbf{a}_{\mathbf{n}+1} = \mathbf{a}_{\mathbf{n}} - \Delta_{\mathbf{n}+1}. \quad (7.38)$$

To construct the system of linear equations, Eq. (7.37), we rewrite Eq. (7.36) as

$$f_i(\mathbf{a}) \equiv \Sigma_i - \frac{3\alpha \ln 10}{2\pi^2} \sum_{k=0}^{(N_R)_i} w_{ik} \frac{y_{ik}^2 \Theta_{ik} \Sigma_{ik}}{y_{ik} + \Sigma_{ik}^2} = 0, \quad i = 1, \dots, N_\Sigma, \quad (7.39)$$

where Σ_i, Σ_{ik} are functions of \mathbf{a} . The matrix of derivatives J is defined as

$$J_{ij}(\mathbf{a}) \equiv \frac{\partial f_i(\mathbf{a})}{\partial a_j}. \quad (7.40)$$

Substituting Eq. (7.39) in Eq. (7.40) yields

$$\begin{aligned} J_{ij}(\mathbf{a}) &= \frac{\partial}{\partial a_j} \left(\Sigma_i - \frac{3\alpha \ln 10}{2\pi^2} \sum_{k=0}^{(N_R)_i} w_{ik} \frac{y_{ik}^2 \Theta_{ik} \Sigma_{ik}}{y_{ik} + \Sigma_{ik}^2} \right) \\ &= \frac{\partial \Sigma_i}{\partial a_j} - \frac{\partial}{\partial a_j} \left(\frac{3\alpha \ln 10}{2\pi^2} \sum_{k=0}^{(N_R)_i} w_{ik} \frac{y_{ik}^2 \Theta_{ik} \Sigma_{ik}}{y_{ik} + \Sigma_{ik}^2} \right). \end{aligned} \quad (7.41)$$

From the Chebyshev expansion Eq. (7.29) and the definition Eq. (7.8) we know that

$$\frac{\partial \Sigma_i}{\partial a_j} = T_j(s_i) - \frac{1}{2} \delta_{j0} \equiv \tilde{T}_j(s_i). \quad (7.42)$$

Applying the chain rule and substituting Eq. (7.42) in Eq. (7.41) gives,

$$\begin{aligned} J_{ij}(\mathbf{a}) &= \tilde{T}_j(s_i) - \frac{3\alpha \ln 10}{2\pi^2} \sum_{k=0}^{(N_R)_i} w_{ik} \frac{\partial \Sigma_{ik}}{\partial a_j} \frac{\partial}{\partial \Sigma_{ik}} \left(\frac{y_{ik}^2 \Theta_{ik} \Sigma_{ik}}{y_{ik} + \Sigma_{ik}^2} \right) \\ &= \tilde{T}_j(s_i) - \frac{3\alpha \ln 10}{2\pi^2} \sum_{k=0}^{(N_R)_i} w_{ik} \tilde{T}_j(r_{ik}) \frac{y_{ik}^2 \Theta_{ik} (y_{ik} - \Sigma_{ik}^2)}{(y_{ik} + \Sigma_{ik}^2)^2}, \end{aligned} \quad (7.43)$$

where r_{ik} maps y_{ik} on the interval $[-1,1]$ using Eq. (7.30).

After substitution of Eqs. (7.39, 7.43) in Eq. (7.37) the linear system of algebraic equation to be solved at each iteration step in Newton's method is

$$\begin{aligned} \sum_{j=0}^{N_\Sigma-1} \left[\tilde{T}_j(s_i) - \frac{3\alpha \ln 10}{2\pi^2} \sum_{k=0}^{(N_R)_i} w_{ik} \tilde{T}_j(r_{ik}) \frac{y_{ik}^2 \Theta_{ik} (y_{ik} - \Sigma_{ik}^2)}{(y_{ik} + \Sigma_{ik}^2)^2} \right]_{\mathbf{a}=\mathbf{a}_{\mathbf{n}}} (\Delta_{\mathbf{n}+1})_j \\ = \left[\Sigma_i - \frac{3\alpha \ln 10}{2\pi^2} \sum_{k=0}^{(N_R)_i} w_{ik} \frac{y_{ik}^2 \Theta_{ik} \Sigma_{ik}}{y_{ik} + \Sigma_{ik}^2} \right]_{\mathbf{a}=\mathbf{a}_{\mathbf{n}}}, \quad i = 1, \dots, N_\Sigma. \end{aligned} \quad (7.44)$$

7.6 Splitting the integral

To evaluate the integrals of Eq. (7.31) we have to introduce some appropriate quadrature rule. Following the discussion in Section 5.6 we know that in order to preserve the accuracy of rules with a high degree of precision, the integrand has to be sufficiently smooth. Because of the kink in the radial integrand it is therefore necessary to split the radial integrals in two parts:

$$\Sigma_i = \int_{\log_{10} \kappa^2}^{\log_{10} x_i} dt K(x_i, y) + \int_{\log_{10} x_i}^{\log_{10} \Lambda^2} dt K(x_i, y), \quad i = 1, \dots, N_\Sigma, \quad (7.45)$$

where the total radial integrand is

$$K(x, y) = \frac{3\alpha \ln 10}{2\pi^2} \frac{y^2 \Sigma(y)}{y + \Sigma^2(y)} \Theta(x, y) \quad (7.46)$$

and the angular integral $\Theta(x, y)$ is defined as:

$$\Theta(x, y) = \int d\theta \frac{\sin^2 \theta}{z(1 + \frac{N_f \alpha}{3\pi} \ln \frac{\Lambda^2}{z})}, \quad (7.47)$$

with $z = x + y - 2\sqrt{xy} \cos \theta$.

We then choose a suitable quadrature rule to evaluate both integrals in Eq. (7.45). The resulting system of non-linear algebraic equations is still given by Eq. (7.36) and will be solved using the method described in the previous section.

7.7 Gaussian quadrature

The quadrature rule in Eq. (7.34) can again be chosen to be a composite Newton-Cotes rule with equidistant points as in Section 5.6, but, because of the polynomial expansion of $\Sigma(x)$ we are now free to use other methods.

In the Newton-Cotes formulae the integration nodes are equidistant and the weights are determined to maximize the degree of precision of the integration rule. In a more general class of integration rules, we determine not only the weights of the function values at the different integration nodes, but also the location of these nodes such that the degree of precision becomes maximal. This allows us to achieve a higher degree of precision than the Newton-Cotes rules with an equal number of integration points. Such methods are known as the *Gaussian* integration rules [56, 41]. The n-point Gaussian quadrature evaluates the integral

$$\int_a^b w(x) f(x) dx = \sum_{j=1}^n w_j f(x_j) + E_n\{f\}. \quad (7.48)$$

such that its degree of precision is $2n - 1$.

One can show in general that the quadrature formula, Eq. (7.48), has degree of precision at most $2n - 1$. This maximum degree of precision is attained iff the n nodes x_j are the zeros of $p_n(x)$, the n^{th} orthogonal polynomial with respect to the weight $w(x)$ over $[a, b]$.

Orthogonal polynomials with respect to a specified weight function $w(x)$ over $[a, b]$ obey the relation:

$$\int_a^b w(x)p_i(x)p_j(x) dx = 0 \quad \text{if } i \neq j. \quad (7.49)$$

The Gaussian quadrature with weight $w(x) \equiv 1$ over the interval $[-1, 1]$ is known as the *Gauss-Legendre* quadrature rule, which can be written as

$$\int_{-1}^1 f(x) dx = \sum_{j=1}^n w_j f(x_j) + E_n\{f\}. \quad (7.50)$$

The orthogonal polynomials with respect to the weight $w(x) \equiv 1$ over $[-1, 1]$ are the *Legendre* polynomials $P_n(x)$. They can be built by imposing the orthogonality relation

$$\int_{-1}^1 P_i(x)P_j(x) dx = 0 \quad \text{if } i \neq j \quad (7.51)$$

and are normalized by

$$\int_{-1}^1 P_n^2(x) dx = \frac{2}{2n + 1}. \quad (7.52)$$

The Legendre polynomials can be computed with the help of Rodrigues' formula:

$$P_n(x) = \frac{1}{2^n n!} \frac{d^n}{dx^n} (x^2 - 1)^n, \quad (7.53)$$

or by using the recurrence relation,

$$(n + 1)P_{n+1}(x) = (2n + 1)xP_n(x) - nP_{n-1}(x). \quad (7.54)$$

The abscissas of the quadrature, Eq. (7.50), are the roots of the Legendre polynomial $P_n(x)$. The coefficients of the Gauss-Legendre quadrature formula, Eq. (7.50), over the interval $[-1, 1]$ are given by:

$$w_j = \frac{2}{(1 - x_j^2)[P_n'(x_j)]^2}. \quad (7.55)$$

One can prove that the coefficients w_j in the Gauss-Legendre quadrature formulae are always positive. This is important for the numerical accuracy of the method because roundoff errors are not generally magnified in this case.

The error term of the Gauss-Legendre quadrature over $[-1,1]$ is:

$$E_n\{f\} = \frac{2^{2n+1}(n!)^4}{(2n+1)[(2n)!]^3} f^{(2n)}(\xi), \quad -1 < \xi < 1. \quad (7.56)$$

To compute an integral over an arbitrary interval, the Gauss-Legendre will be adapted as

$$\int_a^b f(y) dy = \frac{b-a}{2} \sum_{j=1}^n w_j f\left(\frac{b+a}{2} + \frac{b-a}{2}x_j\right) + E_n\{f\}. \quad (7.57)$$

where w_j and x_j are the weights and nodes of the Gauss-Legendre quadrature over the interval $[-1,1]$, Eq. (7.50).

The error term is now

$$E_n\{f\} = \frac{(b-a)^{2n+1}(n!)^4}{(2n+1)[(2n)!]^3} f^{(2n)}(\xi), \quad a < \xi < b. \quad (7.58)$$

7.8 Gaussian quadrature and the integral equations

If we look back at the solution method used to solve the integral equations, we can ask ourselves if we could have used the Gaussian quadrature to evaluate the integrals in the collocation method. We have indeed tried this method, but the results obtained were much worse than those obtained with the Newton-Cotes formula. Indeed, if we use a Gaussian formula with N nodes x_j , we will construct a system of non-linear equations where the unknowns are the function values Σ_j at the integration nodes, which are now unequally spaced. Although this problem is solvable in the same way as before the accuracy obtained is rather poor because the high degree of precision of the Gaussian rule requires the integrand to be sufficiently smooth. This condition is obviously not satisfied as the integrand has a kink. Although we encountered the same problem when we used the composite Newton-Cotes formulae when the degree of precision was higher than that of the trapezoidal rule, we were able to improve the accuracy by splitting the integration region in two at the kink, so that each of the two integrations has a smooth integrand. Unfortunately we cannot apply this method to the Gaussian quadrature because the integration nodes are unequally spaced. If we want to apply Gaussian quadratures to the equation with external momentum x_i , we choose N_1 Gaussian nodes in the interval $[\kappa^2, x_i]$ and N_2 Gaussian nodes in the interval $[x_i, \Lambda^2]$. Therefore we will have a set of $N_1 + N_2$ integration nodes y_j , being the roots of the Legendre polynomials $P_{N_1}(x)$ and $P_{N_2}(x)$. The reason why the collocation method fails is that the position of the $N_1 + N_2$ nodes changes with that of the kink: the integration nodes will be different for each external momentum and the collocation method is not applicable.

However, when we introduce the Chebyshev expansion for the unknown functions the situation is completely different. After splitting the integral at $y = x$ we can use a Gaussian quadrature with any number of nodes N_1, N_2 on the intervals because the integrand can be computed at any point in the interval $[\kappa^2, \Lambda^2]$. The integral equation, Eq. (7.45), for Σ will be replaced by the system of non-linear equations

$$\Sigma_i = \sum_{j=1}^{(N_1)_i} w_{1ij} K(x_i, y_{1ij}) + \sum_{j=1}^{(N_2)_i} w_{2ij} K(x_i, y_{2ij}), \quad i = 1, \dots, N_\Sigma, \quad (7.59)$$

where the nodes y_{1ij}, y_{2ij} and the weights w_{1ij}, w_{2ij} are defined according to Eq. (7.57) and $K(x, y)$ is defined in Eq. (7.46). Remember that as before it is the variable $t \equiv \log_{10} y$, where $t \in [\log_{10} \kappa^2, \log_{10} \Lambda^2]$, which is mapped on the interval $[-1, 1]$ to apply the Gauss-Legendre quadrature.

Concatenating the two arrays of node locations y_{1ij} and y_{2ij} into one array y_{ij} and the weight arrays w_{1ij} and w_{2ij} into w_{ij} , we can rewrite Eq. (7.59) as

$$\Sigma_i = \sum_{j=1}^{(N_R)_i} w_{ij} K(x_i, y_{ij}), \quad i = 1, \dots, N_\Sigma, \quad (7.60)$$

where $(N_R)_i = (N_1)_i + (N_2)_i$.

The system of equations, Eq. (7.60), is similar to the system, Eq. (7.36), for which Newton's method was developed in Section 7.5. Therefore Eq. (7.60) will be solved by Newton's iteration method, Eq. (7.44).

Although we also considered the use of a two-dimensional adaptive integration method, we did not retain this method. Its advantage is that it only computes function values at positions which depend on the behaviour of the integrand, minimizing the number of function evaluations. Furthermore, the integration routine returns an integral value satisfying a requested minimum accuracy. However, the method is not efficient to evaluate integrals as part of an integral equation. The variable location of the function values to be evaluated does not allow us to compute parts of the integrands beforehand and to store them for multiple, future use. Moreover, the main problem resides in the use of Newton's method, which requires the knowledge of the derivatives of the integral with respect to the Chebyshev coefficients. The use of an adaptive method makes it extremely hard and inefficient to compute these derivatives. It seems therefore that a higher order method with a priori determined integration nodes and weights, as in the Gaussian quadrature, is the best choice of integral evaluation for the solution of integral equations with the Chebyshev expansion method.

In the next chapter we will apply the Chebyshev expansion method to solve the coupled integral equations of unquenched QED in the bare vertex approximation for various approximations to the $(\Sigma, \mathcal{F}, \mathcal{G})$ -system of integral equations.

Chapter 8

Numerical results with Chebyshev expansion method

In this chapter we will apply the Chebyshev expansion method to determine the critical coupling above which fermion mass is generated dynamically in unquenched QED in the bare vertex approximation. We will consider various approximations to the coupled $(\Sigma, \mathcal{F}, \mathcal{G})$ -system. First we will decouple the \mathcal{G} equation by using the 1-loop approximation to the vacuum polarization. In a next section we will revisit the coupled (Σ, \mathcal{G}) -system which was discussed previously in Chapter 6 and was the motivation to introduce the Chebyshev expansion method. Finally we will treat the complete system of coupled integral equations for Σ , \mathcal{F} and \mathcal{G} .

8.1 The 1-loop approximation

We first simplify the $(\Sigma, \mathcal{F}, \mathcal{G})$ -system of coupled integral equations by approximating the vacuum polarization by its 1-loop result. The \mathcal{G} -equation then decouples from the coupled (Σ, \mathcal{F}) -system describing the dynamical generation of fermion mass. We recall Eqs. (5.80, 5.81),

$$\frac{\Sigma(x)}{\mathcal{F}(x)} = \frac{3\alpha}{2\pi^2} \int dy \frac{y\mathcal{F}(y)\Sigma(y)}{y + \Sigma^2(y)} \int d\theta \sin^2 \theta \frac{\mathcal{G}(z)}{z} \quad (8.1)$$

$$\begin{aligned} \frac{1}{\mathcal{F}(x)} &= 1 + \frac{\alpha}{2\pi^2 x} \int dy \frac{y\mathcal{F}(y)}{y + \Sigma^2(y)} \\ &\times \int d\theta \sin^2 \theta \mathcal{G}(z) \left(\frac{3\sqrt{xy} \cos \theta}{z} - \frac{2xy \sin^2 \theta}{z^2} \right) \end{aligned} \quad (8.2)$$

where $z \equiv x + y - 2\sqrt{xy} \cos \theta$ and the 1-loop approximation to $\mathcal{G}(z)$ is given by:

$$\mathcal{G}(z) = \frac{1}{1 + \frac{N_f \alpha}{3\pi} \ln \frac{\Lambda^2}{z}}. \quad (8.3)$$

As discussed in Chapter 4 many other authors have used the same approximation to determine the critical coupling of unquenched QED. We will consider the three main variants encountered in the literature. Firstly, we consider the LAK-approximation to remove the angular dependence of the vacuum polarization; this automatically yields $\mathcal{F}(x) = 1$ and leaves us the Σ -equation alone to solve. In another approximation we keep the full angular dependence in the vacuum polarization but approximate $\mathcal{F}(x) \equiv 1$, which should be reasonable in the Landau gauge, and solve the Σ -equation. Finally we will solve the coupled (Σ, \mathcal{F}) -system in the 1-loop approximation to the vacuum polarization.

8.1.1 The LAK-approximation

An often used variant to the 1-loop calculation is often referred to as the LAK-approximation (in analogy to Landau, Abrikosov and Khalatnikov [48]) to the vacuum polarization:

$$\Pi(z) = \Pi(\max(x, y)), \quad (8.4)$$

where $z = x + y - 2\sqrt{xy}\cos\theta$. This approximation has been often introduced to allow the angular integrals to be computed analytically [13, 14]. Furthermore, the angular integral of the \mathcal{F} -equation, Eq. (8.2), vanishes in the Landau gauge when introducing the LAK-approximation and $\mathcal{F}(x) = 1$.

The mass equation, Eq. (8.1), now becomes

$$\Sigma(x) = \frac{3\alpha}{2\pi^2} \int dy \frac{y\Sigma(y)}{y + \Sigma^2(y)} \mathcal{G}(\max(x, y)) \int d\theta \frac{\sin^2\theta}{z}. \quad (8.5)$$

The angular integral can be computed analytically and is given in Appendix A. Substituting Eq. (A.1) into Eq. (8.5) gives

$$\Sigma(x) = \frac{3\alpha}{4\pi} \int dy \frac{y\Sigma(y)}{y + \Sigma^2(y)} \frac{\mathcal{G}(\max(x, y))}{\max(x, y)}. \quad (8.6)$$

with $\mathcal{G}(z)$ given by Eq. (8.3).

Eq. (8.6) will be solved following the solution pattern for the Chebyshev expansion method developed in Chapter 7. Change the integration variable from y to $t = \log_{10} y$. Then, split the integral in two at $y = x$, where the radial integrand obviously has a kink. Consequently, replace the integrals by a quadrature formula using a Gauss-Legendre quadrature with $(N_1)_i = (N_2)_i = 120$ nodes on every radial integral. The resulting system of non-linear equations is:

$$\Sigma_i = \frac{3\alpha \ln 10}{4\pi} \sum_{j=1}^{(N_R)_i} w_{ij} \frac{y_{ij}^2 \Sigma_{ij}}{y_{ij} + \Sigma_{ij}^2} \frac{\mathcal{G}(\max(x_i, y_{ij}))}{\max(x_i, y_{ij})}, \quad i = 1, \dots, N_\Sigma. \quad (8.7)$$

This system can then be solved with a Newton's method analogous to the one described in Section 7.5 to determine the coefficients a_j , $j = 1, \dots, N_\Sigma$ of the Chebyshev expansion for $\Sigma(x)$. In practice we choose $N_\Sigma = 50$, such that the error due to the approximation of $\Sigma(x)$ by a Chebyshev expansion is negligible.

The numerical results of Eq. (8.7) are summarized in Figs. 8.1 for $N_f = 1$ and Fig. 8.2 for $N_f = 2$ where we show the evolution of the generated fermion mass with changing coupling α . The critical couplings are $\alpha_c(N_f = 1) = 1.99953$ and $\alpha_c(N_f = 2) = 2.75233$.

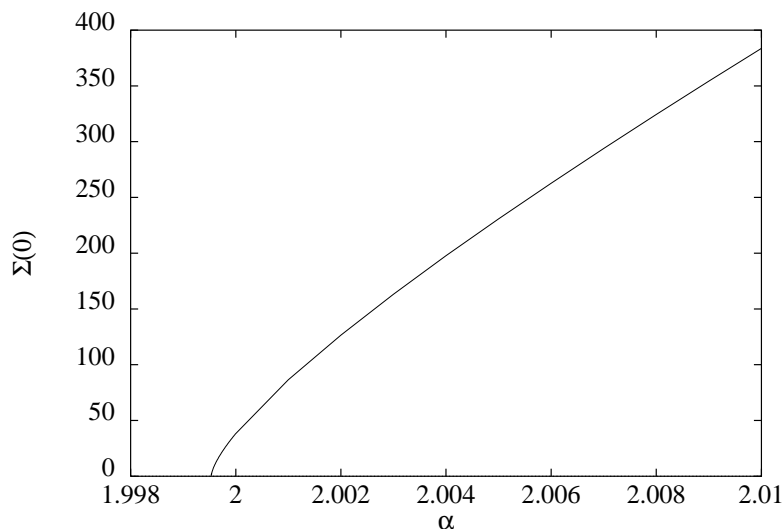


Figure 8.1: Generated fermion mass $\Sigma(0)$ versus coupling α for $N_f = 1$ in the 1-loop LAK approximation to Π .

8.1.2 The $\mathcal{F} \equiv 1$ approximation

In this section we approximate the system of equations, Eqs. (8.1, 8.2), by setting $\mathcal{F}(x) \equiv 1$, which is thought to be a good approximation in the Landau gauge, and solve the remaining Σ -equation which is:

$$\Sigma(x) = \frac{3\alpha}{2\pi^2} \int dy \frac{y\Sigma(y)}{y + \Sigma^2(y)} \int d\theta \frac{\sin^2 \theta}{z \left(1 + \frac{N_f \alpha}{3\pi} \ln \frac{\Lambda^2}{z}\right)}. \quad (8.8)$$

The numerical method to solve this equation has been derived in Chapter 7. We saw in Eq. (7.60) that the Chebyshev expansion method requires us to solve the following system of non-linear

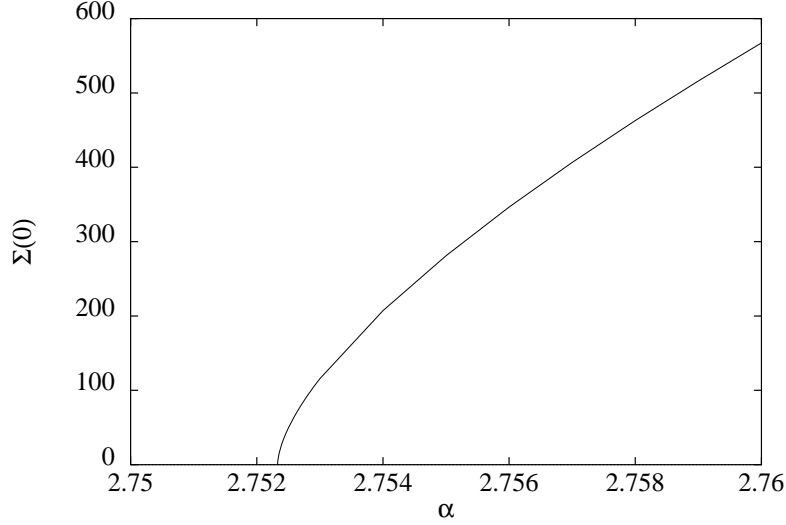


Figure 8.2: Generated fermion mass $\Sigma(0)$ versus coupling α for $N_f = 2$ in the 1-loop LAK approximation to Π .

algebraic equations for the Chebyshev coefficients a of the Chebyshev expansion for $\Sigma(x)$:

$$\Sigma_i = \frac{3\alpha \ln 10}{2\pi^2} \sum_{j=1}^{(N_R)_i} w_{ij} \frac{y_{ij}^2 \Sigma_{ij}}{y_{ij} + \Sigma_{ij}^2} \Theta(x_i, y_{ij}) \quad , \quad i = 1, \dots, N_\Sigma. \quad (8.9)$$

with

$$\Theta(x, y) = \int d\theta \frac{\sin^2 \theta}{z(1 + \frac{N_f \alpha}{3\pi} \ln \frac{\Lambda^2}{z})}. \quad (8.10)$$

To solve Eq. (8.9), we first choose a set of values $(N_1)_i, (N_2)_i, i = 1, \dots, N_\Sigma$, fixing the Gaussian quadrature rule to be used on each single radial integral. In practice we opted for $(N_1)_i = (N_2)_i = 120$ nodes on each interval $[\log_{10} \kappa^2, \log_{10} x_i]$ and $[\log_{10} x_i, \log_{10} \Lambda^2]$ for all i to yield sufficient accuracy. For each rule we then compute and store the corresponding locations and weights of the integration nodes.

Then, the angular integrals $\Theta(x_i, y_{ij})$, Eq. (8.10), are computed for $i = 1, \dots, N_\Sigma$ and $j = 1, \dots, (N_1)_i + (N_2)_i$, using some appropriate quadrature formula. We will use a Gaussian quadrature rule with $(N_\theta)_{ij}$ nodes to evaluate the angular integrals. In practice we will choose the same number of nodes N_θ for all the angular integrals. The angular integrals are evaluated by

$$\Theta(x_i, y_{ij}) = \sum_{k=0}^{N_\theta} w_k \frac{\sin^2 \theta_k}{z_k(1 + \frac{N_f \alpha}{3\pi} \ln \frac{\Lambda^2}{z_k})}, \quad (8.11)$$

where $z_k = x_i + y_{ij} - 2\sqrt{x_i y_{ij}} \cos \theta_k$. The locations θ_k and weights w_k of the Gaussian quadrature are determined by Eq. (7.57) for a Gaussian quadrature with N_θ points over the interval $[0, \pi]$. In practice we take $N_\theta = 32$ to give us sufficient accuracy.

After the angular integrals have been computed and stored, we apply Newton's method to Eq. (8.9) as described in Section 7.5 to find the solution vector of Chebyshev coefficients a_j , $j = 1, \dots, N_\Sigma$ defining the Chebyshev approximation to $\Sigma(x)$. As in Section 8.1.1 we will again take $N_\Sigma = 50$.

We now summarize the main results computed from Eq. (8.9) with the above described method. The results are quite similar to the ones obtained with the collocation method in Section 5.7. We show the evolution of the generated fermion mass with changing coupling α in Fig. 8.3 for one flavour, $N_f = 1$. The critical coupling is $\boxed{\alpha_c(N_f = 1) = 2.08431}$, which is in total agreement with the results obtained with the collocation method and the improved Simpson's rule. However, the results show that we need much fewer integration nodes using the Gauss-Legendre quadrature than we do using Simpson's rule to obtain equal accuracy.

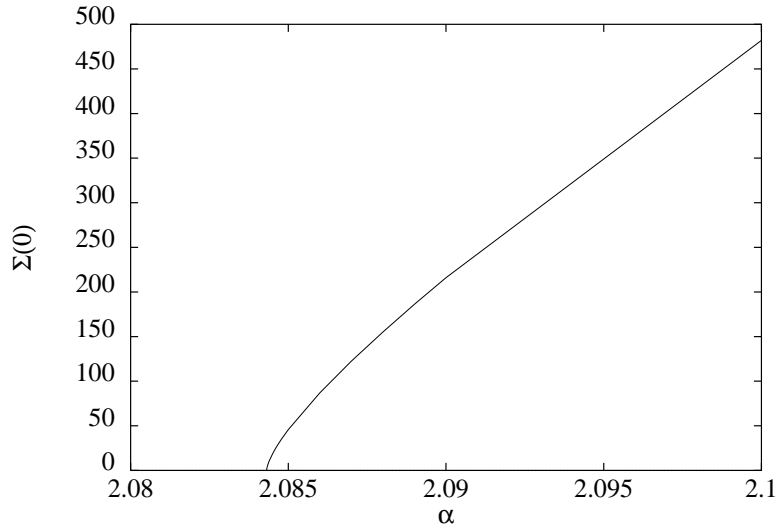


Figure 8.3: Generated fermion mass $\Sigma(0)$ versus coupling α for $N_f = 1$ in the 1-loop approximation to Π and $\mathcal{F} \equiv 1$.

We performed a similar calculation for two flavours, $N_f = 2$. The evolution of the generated fermion mass is shown in Fig. 8.4. The critical coupling is $\boxed{\alpha_c(N_f = 2) = 2.99142}$.

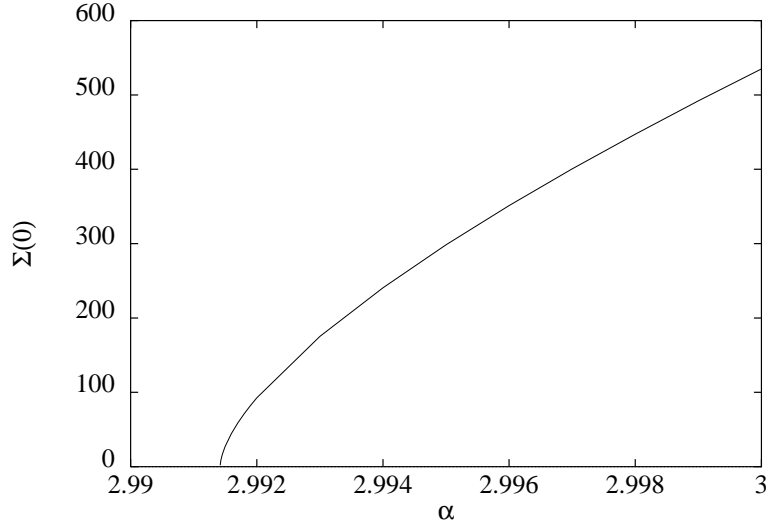


Figure 8.4: Generated fermion mass $\Sigma(0)$ versus coupling α for $N_f = 2$ in the 1-loop approximation to Π and $\mathcal{F} \equiv 1$.

8.1.3 The coupled (Σ, \mathcal{F}) -system

A further improvement on the calculation in the 1-loop approximation to the vacuum polarization is to solve the coupled system of fermion equations (8.1, 8.2) for Σ and \mathcal{F} . We have seen in Section 5.4 how such a coupled system can be solved using Newton's method.

We are looking for approximate solutions to Eqs. (8.1, 8.2), which can be written as the following Chebyshev expansions:

$$\Sigma(x) \equiv \sum'_{j=0}^{N_\Sigma-1} a_j T_j(s(x)) \quad (8.12)$$

$$\mathcal{F}(x) \equiv \sum'_{j=0}^{N_\mathcal{F}-1} b_j T_j(s(x)) \quad (8.13)$$

where $s(x)$ satisfies Eq. (7.24) and where the sum \sum' is defined in Eq. (7.8).

To solve the problem numerically we will again go through the following steps. Change the integration variable from y to $t = \log_{10} y$. Then, select N_Σ external momenta where we impose that Eq. (8.1) has to be satisfied and $N_\mathcal{F}$ external momenta where Eq. (8.2) has to be satisfied. We then split the radial integrals in two at $x = y$ to avoid integrating numerically over the kink. Consequently we introduce the quadrature rules to evaluate the integrals. We will again use the Gauss-Legendre quadrature to solve the radial and angular integrals. We now evaluate and

store the angular integrals,

$$\Theta_{\Sigma}(x_i, y_{ij}) = \sum_{k=1}^{N_{\theta}} w_k \sin^2 \theta_k \frac{\mathcal{G}(z_k)}{z_k} \quad (8.14)$$

$$\Theta_{\mathcal{F}}(x_i, y_{ij}) = \sum_{k=1}^{N_{\theta}} w_k \sin^2 \theta_k \mathcal{G}(z_k) \left(\frac{3\sqrt{x_i y_{ij}} \cos \theta_k}{z_k} - \frac{2x_i y_{ij} \sin^2 \theta_k}{z_k^2} \right) \quad (8.15)$$

where $z_k = x_i + y_{ij} - 2\sqrt{x_i y_{ij}} \cos \theta_k$ and $\mathcal{G}(z)$ is defined by its 1-loop approximation Eq. (8.3).

By doing so we are left with a system of $N_{\Sigma} + N_{\mathcal{F}}$ non-linear equations to determine the N_{Σ} Chebyshev coefficients a_j , defining the Chebyshev expansion of $\Sigma(x)$, and the $N_{\mathcal{F}}$ Chebyshev coefficients b_j , defining the Chebyshev expansion of $\mathcal{F}(x)$:

$$f_{1,i} \equiv \frac{\Sigma(x_i)}{\mathcal{F}(x_i)} - \frac{3\alpha \ln 10}{2\pi^2} \sum_{j=1}^{(N_R)_i} w_{ij} \frac{y_{ij}^2 \mathcal{F}(y_{ij}) \Sigma(y_{ij})}{y_{ij} + \Sigma^2(y_{ij})} \Theta_{\Sigma}(x_i, y_{ij}) = 0, \quad i = 1, \dots, N_{\Sigma} \quad (8.16)$$

$$f_{2,i} \equiv \frac{1}{\mathcal{F}(x_i)} - 1 - \frac{\alpha \ln 10}{2\pi^2 x_i} \sum_{j=1}^{(N_R)_i} w_{ij} \frac{y_{ij}^2 \mathcal{F}(y_{ij})}{y_{ij} + \Sigma^2(y_{ij})} \Theta_{\mathcal{F}}(x_i, y_{ij}) = 0, \quad i = 1, \dots, N_{\mathcal{F}} \quad (8.17)$$

where $(N_R)_i = (N_1)_i + (N_2)_i$ is the total number of nodes of the two Gauss-Legendre rules used to compute the split radial integrals. This system of non-linear equations will be solved with Newton's iterative method. Each iteration step requires the solution of the following system of linear equations,

$$J(\mathbf{a}_n, \mathbf{b}_n) \Delta_{n+1} = \mathbf{f}(\mathbf{a}_n, \mathbf{b}_n), \quad (8.18)$$

which can be written out as:

$$\sum_{j=0}^{N_{\Sigma}-1} \frac{\partial f_{1,i}(\mathbf{a}_n, \mathbf{b}_n)}{\partial a_j} (\Delta_{a,n+1})_j + \sum_{j=0}^{N_{\mathcal{F}}-1} \frac{\partial f_{1,i}(\mathbf{a}_n, \mathbf{b}_n)}{\partial b_j} (\Delta_{b,n+1})_j = f_{1,i}(\mathbf{a}_n, \mathbf{b}_n), \quad i = 1, \dots, N_{\Sigma} \quad (8.19)$$

$$\sum_{j=0}^{N_{\Sigma}-1} \frac{\partial f_{2,i}(\mathbf{a}_n, \mathbf{b}_n)}{\partial a_j} (\Delta_{a,n+1})_j + \sum_{j=0}^{N_{\mathcal{F}}-1} \frac{\partial f_{2,i}(\mathbf{a}_n, \mathbf{b}_n)}{\partial b_j} (\Delta_{b,n+1})_j = f_{2,i}(\mathbf{a}_n, \mathbf{b}_n), \quad i = 1, \dots, N_{\mathcal{F}}.$$

The partial derivatives in Eq. (8.19) are computed from Eqs. (8.16, 8.17) using the expression (7.42):

$$\begin{aligned} \frac{\partial f_{1,i}(\mathbf{a}, \mathbf{b})}{\partial a_j} &= \frac{\partial}{\partial a_j} \left(\frac{\Sigma(x_i)}{\mathcal{F}(x_i)} - \frac{3\alpha \ln 10}{2\pi^2} \sum_{k=1}^{(N_R)_i} w_{ik} \frac{y_{ik}^2 \mathcal{F}(y_{ik}) \Sigma(y_{ik})}{y_{ik} + \Sigma^2(y_{ik})} \Theta_{\Sigma}(x_i, y_{ik}) \right) \\ &= \frac{\tilde{T}_j(s_i)}{\mathcal{F}(x_i)} - \frac{3\alpha \ln 10}{2\pi^2} \sum_{k=1}^{(N_R)_i} w_{ik} \frac{y_{ik}^2 \mathcal{F}(y_{ik}) (y_{ik} - \Sigma^2(y_{ik})) \tilde{T}_j(r_{ik})}{(y_{ik} + \Sigma^2(y_{ik}))^2} \Theta_{\Sigma}(x_i, y_{ik}) \end{aligned} \quad (8.20)$$

$$\frac{\partial f_{1,i}(\mathbf{a}, \mathbf{b})}{\partial b_j} = \frac{\partial}{\partial b_j} \left(\frac{\Sigma(x_i)}{\mathcal{F}(x_i)} - \frac{3\alpha \ln 10}{2\pi^2} \sum_{k=1}^{(N_R)_i} w_{ik} \frac{y_{ik}^2 \mathcal{F}(y_{ik}) \Sigma(y_{ik})}{y_{ik} + \Sigma^2(y_{ik})} \Theta_{\Sigma}(x_i, y_{ik}) \right)$$

$$= -\frac{\Sigma(x_i)\tilde{T}_j(s_i)}{\mathcal{F}^2(x_i)} - \frac{3\alpha \ln 10}{2\pi^2} \sum_{k=1}^{(N_R)_i} w_{ik} \frac{y_{ik}^2 \tilde{T}_j(r_{ik}) \Sigma(y_{ik})}{y_{ik} + \Sigma^2(y_{ik})} \Theta_{\Sigma}(x_i, y_{ik}) \quad (8.21)$$

$$\begin{aligned} \frac{\partial f_{2,i}(\mathbf{a}, \mathbf{b})}{\partial a_j} &= \frac{\partial}{\partial a_j} \left(\frac{1}{\mathcal{F}(x_i)} - 1 - \frac{\alpha \ln 10}{2\pi^2 x_i} \sum_{k=1}^{(N_R)_i} w_{ik} \frac{y_{ik}^2 \mathcal{F}(y_{ik})}{y_{ik} + \Sigma^2(y_{ik})} \Theta_{\mathcal{F}}(x_i, y_{ik}) \right) \\ &= \frac{\alpha \ln 10}{2\pi^2 x_i} \sum_{k=1}^{(N_R)_i} w_{ik} \frac{2y_{ik}^2 \mathcal{F}(y_{ik}) \Sigma(y_{ik}) \tilde{T}_j(r_{ik})}{(y_{ik} + \Sigma^2(y_{ik}))^2} \Theta_{\mathcal{F}}(x_i, y_{ik}) \end{aligned} \quad (8.22)$$

$$\begin{aligned} \frac{\partial f_{2,i}(\mathbf{a}, \mathbf{b})}{\partial b_j} &= \frac{\partial}{\partial b_j} \left(\frac{1}{\mathcal{F}(x_i)} - 1 - \frac{\alpha \ln 10}{2\pi^2 x_i} \sum_{k=1}^{(N_R)_i} w_{ik} \frac{y_{ik}^2 \mathcal{F}(y_{ik})}{y_{ik} + \Sigma^2(y_{ik})} \Theta_{\mathcal{F}}(x_i, y_{ik}) \right) \\ &= -\frac{\tilde{T}_j(s_i)}{\mathcal{F}^2(x_i)} - \frac{\alpha \ln 10}{2\pi^2 x_i} \sum_{k=1}^{(N_R)_i} w_{ik} \frac{y_{ik}^2 \tilde{T}_j(r_{ik})}{y_{ik} + \Sigma^2(y_{ik})} \Theta_{\mathcal{F}}(x_i, y_{ik}). \end{aligned} \quad (8.23)$$

We now substitute Eqs. (8.16, 8.17, 8.20-8.23) in the system of linear equations Eq. (8.19) and solve it for $(\Delta_{\mathbf{a}, \mathbf{n}+1}, \Delta_{\mathbf{b}, \mathbf{n}+1})$. Then, the new approximations to the Chebyshev coefficients are computed by:

$$\begin{aligned} \mathbf{a}_{\mathbf{n}+1} &= \mathbf{a}_{\mathbf{n}} - \Delta_{\mathbf{a}, \mathbf{n}+1} \\ \mathbf{b}_{\mathbf{n}+1} &= \mathbf{b}_{\mathbf{n}} - \Delta_{\mathbf{b}, \mathbf{n}+1}. \end{aligned} \quad (8.24)$$

In the program implementing this we choose $N_{\Sigma} = N_{\mathcal{F}} = 50$. The Gauss-Legendre quadratures are performed with $N_{\theta} = 32$ nodes for the angular integrations and $(N_1)_i = (N_2)_i = 120$ nodes for the split radial integrations. The evolution of the generated mass for the coupled (Σ, \mathcal{F}) -system for $N_f = 1$ is shown in Fig. 8.5. The value of the critical coupling is $\boxed{\alpha_c(N_f = 1) = 1.67280}$.

Typical plots of the dynamical mass function $\Sigma(x)$ and the fermion wavefunction renormalization $\mathcal{F}(x)$ are shown in Fig. 8.6 and Fig. 8.7 for $\alpha = 1.678, 1.676, 1.674$.

Fig. 8.8 shows the generated fermion mass versus coupling for $N_f = 2$. The value of the critical coupling is $\boxed{\alpha_c(N_f = 2) = 2.02025}$.

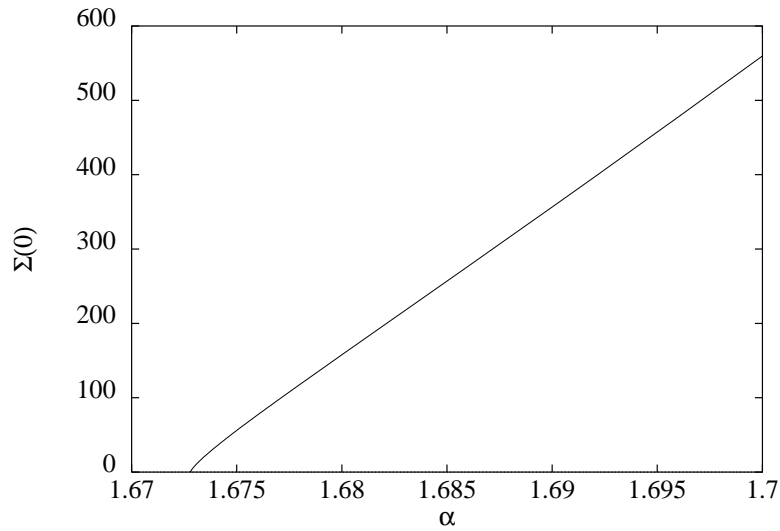


Figure 8.5: Generated fermion mass $\Sigma(0)$ versus coupling α for the coupled (Σ, \mathcal{F}) -system, for $N_f = 1$ in the 1-loop approximation to Π .

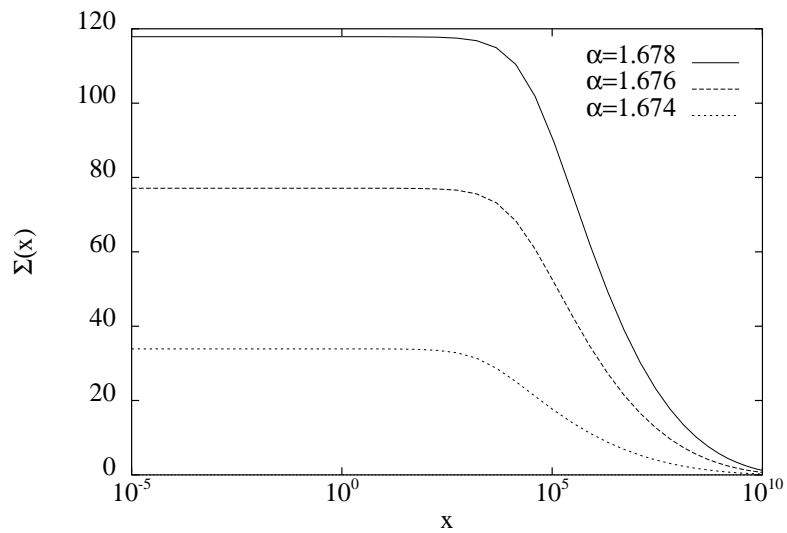


Figure 8.6: Dynamical fermion mass $\Sigma(x)$ versus momentum squared x for the coupled (Σ, \mathcal{F}) -system, for $N_f = 1$ in the 1-loop approximation to Π , for $\alpha = 1.678, 1.676, 1.674$.

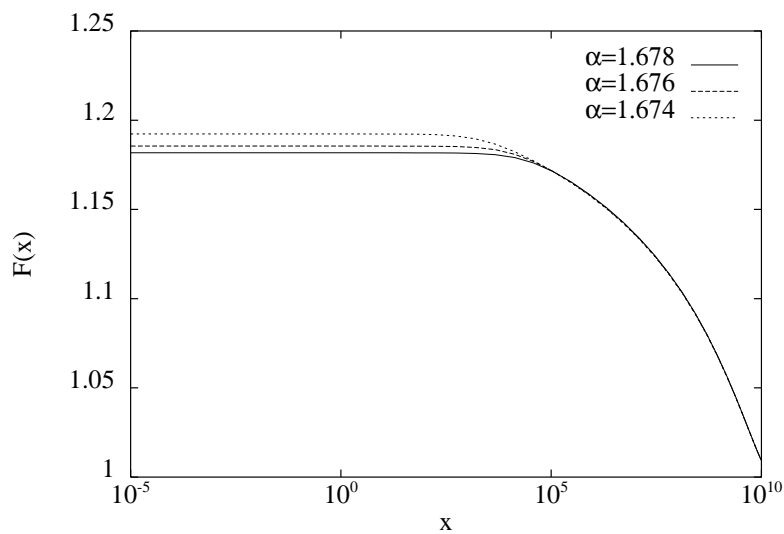


Figure 8.7: Fermion wavefunction renormalization $\mathcal{F}(x)$ versus momentum squared x for the coupled (Σ, \mathcal{F}) -system, for $N_f = 1$ in the 1-loop approximation to Π , for $\alpha = 1.678, 1.676, 1.674$.

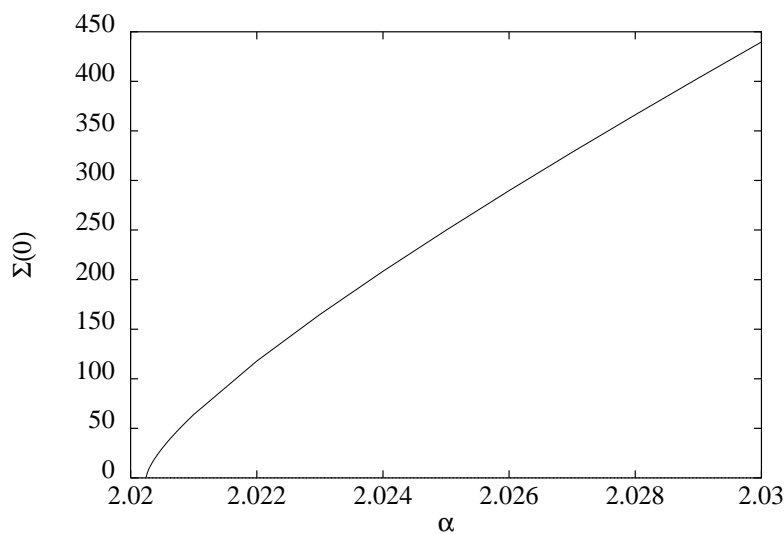


Figure 8.8: Generated fermion mass $\Sigma(0)$ versus coupling α for the coupled (Σ, \mathcal{F}) -system, for $N_f = 2$ in the 1-loop approximation to Π .

8.1.4 Summary

In Table 8.1 we compare the various results obtained for the critical coupling α_c in the 1-loop approximation to the vacuum polarization in the Landau gauge. It is clear that the inclusion of the \mathcal{F} -equation affects the value of the critical coupling. We note a decrease of α_c by about 20% for $N_f = 1$ and by more than 30% for $N_f = 2$.

| Approximation | $\alpha_c(N_f = 1)$ | $\alpha_c(N_f = 2)$ |
|-------------------------|---------------------|---------------------|
| LAK | 1.99953 | 2.75233 |
| $\mathcal{F} \equiv 1$ | 2.08431 | 2.99142 |
| (Σ, \mathcal{F}) | 1.67280 | 2.02025 |

Table 8.1: Critical coupling α_c for $N_f = 1$ and $N_f = 2$ for various approximations to the (Σ, \mathcal{F}) -system in the 1-loop approximation to the vacuum polarization.

In Table 8.2 we compare our results with those found in the literature as discussed in Chapter 4 for the LAK-approximation and in the $\mathcal{F} \equiv 1$ approximation. From Table 8.2.A we see that in the LAK-approximation all the analytical and numerical calculations agree extremely well. The largest deviation for $N_f = 1$ is found in the analytical calculation Ref. [14] and is only about 2%. For the $\mathcal{F} \equiv 1$ approximation only numerical work has been done as the angular integrals cannot be computed analytically. The deviation between previously published work and our calculation is at most 0.5% for $N_f = 1$ and almost 6% for $N_f = 2$ as can be seen in Table 8.2.B. For the coupled (Σ, \mathcal{F}) -system no evaluation of the critical coupling has been found in the literature. There is only a qualitative assessment in Ref. [16] to verify that the approximation $\mathcal{F} \equiv 1$ is justified. However, as we noted above, we found in our numerical calculation that the critical coupling does change considerably by including the corrections to \mathcal{F} in the calculation.

| (A) | Ref. | $\alpha_c(N_f = 1)$ | $\alpha_c(N_f = 2)$ |
|-----|------|---------------------|---------------------|
| | JCRB | 1.99953 | 2.75233 |
| | [13] | 1.99972 | 2.71482 |
| | [14] | 1.95 | |
| | [16] | 1.9989 | 2.7517 |
| | [17] | 1.999534163 | |
| | [50] | 1.9995 | |

| (B) | Ref. | $\alpha_c(N_f = 1)$ | $\alpha_c(N_f = 2)$ |
|-----|------|---------------------|---------------------|
| | JCRB | 2.08431 | 2.99142 |
| | [16] | 2.0728 | 2.8209 |
| | [20] | 2.084 | |

Table 8.2: Comparison of our numerical results (JCRB) with those found in the literature for the critical coupling in the 1-loop approximation to the vacuum polarization, for $N_f = 1, 2$: (A) in the LAK-approximation, (B) in the $\mathcal{F} \equiv 1$ -approximation.

8.2 Coupled (Σ, \mathcal{G}) -system: revisited

We now take a new look at the solution of the coupled (Σ, \mathcal{G}) -system which was discussed previously in Chapter 6. There we solved this system of equations using the collocation method and found that we encountered difficulties cancelling the photon quadratic divergence properly. It was then suggested that with some smooth approximations to the functions Σ and \mathcal{G} we could prevent these problems. In this section we are going to investigate how the approximation of Σ and \mathcal{G} by Chebyshev expansions affects the numerical cancellation of the quadratic divergence.

In contrast to Chapter 6, we now use the conventional operator $\mathcal{P}_{\mu\nu} = g_{\mu\nu} - 4q_\mu q_\nu / q^2$ to derive the photon equation, as motivated in Section 2.5.2. Although the vacuum polarization is then theoretically free of quadratic divergences, this does not ensure that it will be automatically so numerically. Setting $\mathcal{F} \equiv 1$, the coupled system of integral equations, Eqs. (2.59, 2.69), in the Landau gauge and with zero bare mass, becomes:

$$\Sigma(x) = \frac{3\alpha}{2\pi^2} \int dy \frac{y\Sigma(y)}{y + \Sigma^2(y)} \int d\theta \sin^2 \theta \frac{\mathcal{G}(z)}{z} \quad (8.25)$$

$$\frac{1}{\mathcal{G}(x)} = 1 + \frac{4N_f\alpha}{3\pi^2 x} \int dy \frac{y}{y + \Sigma^2(y)} \int d\theta \sin^2 \theta \frac{y(1 - 4\cos^2 \theta) + 3\sqrt{xy} \cos \theta}{z + \Sigma^2(z)}. \quad (8.26)$$

In analogy to Eqs. (6.10, 6.11), after having changed variables with $t = \log_{10} y$, we replace the integral equations by a system of non-linear equations by introducing quadrature rules to evaluate the integrals numerically:

$$\Sigma(x_i) = \frac{3\alpha \ln 10}{2\pi^2} \sum_{j=1}^{(N_R)i} w_{ij} \frac{y_{ij}^2 \Sigma(y_{ij})}{y_{ij} + \Sigma^2(y_{ij})} \Theta_\Sigma(x_i, y_{ij}), \quad i = 1, \dots, N_\Sigma \quad (8.27)$$

$$\frac{1}{\mathcal{G}(x_i)} = 1 + \frac{4N_f\alpha \ln 10}{3\pi^2 x_i} \sum_{j=1}^{(N_R)i} w_{ij} \frac{y_{ij}^2}{y_{ij} + \Sigma^2(y_{ij})} \Theta_\mathcal{G}(x_i, y_{ij}), \quad i = 1, \dots, N_\mathcal{G} \quad (8.28)$$

where

$$\Theta_\Sigma(x_i, y_{ij}) = \sum_{k=1}^{N_\theta} w'_k \sin^2 \theta_k \frac{\mathcal{G}(z_k)}{z_k} \quad (8.29)$$

$$\Theta_\mathcal{G}(x_i, y_{ij}) = \sum_{k=1}^{N_\theta} w'_k \sin^2 \theta_k \frac{y_{ij}(1 - 4\cos^2 \theta_k) + 3\sqrt{x_i y_{ij}} \cos \theta_k}{z_k + \Sigma^2(z_k)} \quad (8.30)$$

and $z_k = x_i + y_{ij} - 2\sqrt{x_i y_{ij}} \cos \theta_k$.

The unknowns of the system of equations are the coefficients a_j and c_j of the Chebyshev expan-

sions for $\Sigma(x)$ and $\mathcal{G}(x)$:

$$\Sigma(x) \equiv \sum_{j=0}^{N_{\Sigma}-1} 'a_j T_j(s(x)) \quad (8.31)$$

$$\mathcal{G}(x) \equiv \sum_{j=0}^{N_{\mathcal{G}}-1} 'c_j T_j(s(x)), \quad (8.32)$$

where $s(x)$ is defined by Eq. (7.24).

Instead of being equidistant as in Chapter 6 the logarithms of the external momenta in Eqs. (8.27, 8.28), mapped to the interval $[-1, 1]$, now correspond to the roots of the Chebyshev polynomials $T_{N_{\Sigma}}(x)$ and $T_{N_{\mathcal{G}}}(x)$ as shown in Eqs. (7.32, 7.33).

The evaluation of the kernels in the radial and angular integrals is straightforward as the functions $\Sigma(x)$ and $\mathcal{G}(x)$ can be computed at any point in the interval $[\log_{10} \kappa^2, \log_{10} \Lambda^2]$.

In analogy with the discussion in Chapter 6, the coupled system of non-linear algebraic equations will be solved by the method described by the program flow, Fig. 8.9 which is similar to Fig. 6.1.

We start from an initial guess \mathbf{a}_0 and \mathbf{c}_0 to the Chebyshev coefficients. To derive the approximation $\mathbf{a}_{\mathbf{n}+1}$, $\mathbf{c}_{\mathbf{n}+1}$ from $\mathbf{a}_{\mathbf{n}}$, $\mathbf{c}_{\mathbf{n}}$ we apply the following procedure. Keeping the coefficients $\mathbf{c}_{\mathbf{n}}$ fixed, we compute the angular integrals, Eq. (8.29), of the Σ -equation using the Chebyshev expansion, Eq. (8.32), for \mathcal{G} . After substituting the values of these angular integrals in Eq. (8.27), this equation will represent a set of non-linear algebraic equations for the unknown $\mathbf{a}_{\mathbf{n}+1}$, which is analogous to Eq. (7.36). This set of equations can be solved by applying Newton's iterative procedure to the Chebyshev expansion method as described in Section 7.5. This will involve successive solutions of linear systems of equations.

We then compute the angular integrals, Eq. (8.30), of the \mathcal{G} -equation using the Chebyshev expansion for $\Sigma(x)$ with coefficients $\mathbf{a}_{\mathbf{n}+1}$. Then, these angular integrals are substituted into the \mathcal{G} -equation, Eq. (8.28). Taking the reciprocal of this equation and substituting the Chebyshev expansion, Eq. (8.32), for $\mathcal{G}(x)$ yields:

$$\sum_{j=0}^{N_{\mathcal{G}}-1} 'c_j T_j(s(x_i)) = \left[1 + \frac{4N_f \alpha \ln 10}{3\pi^2 x_i} \sum_{j=1}^{(N_R)_i} w_{ij} \frac{y_{ij}^2}{y_{ij} + \Sigma^2(y_{ij})} \Theta_{\mathcal{G}}(x_i, y_{ij}) \right]^{-1}, \quad i = 1, \dots, N_{\mathcal{G}}. \quad (8.33)$$

This is a system of $N_{\mathcal{G}}$ linear equations for the $N_{\mathcal{G}}$ Chebyshev coefficients c_j with known right hand sides which can easily be solved numerically. In this way we have constructed a new set of Chebyshev coefficients $\mathbf{a}_{\mathbf{n}+1}$, $\mathbf{c}_{\mathbf{n}+1}$. We repeat the whole procedure till convergence has been

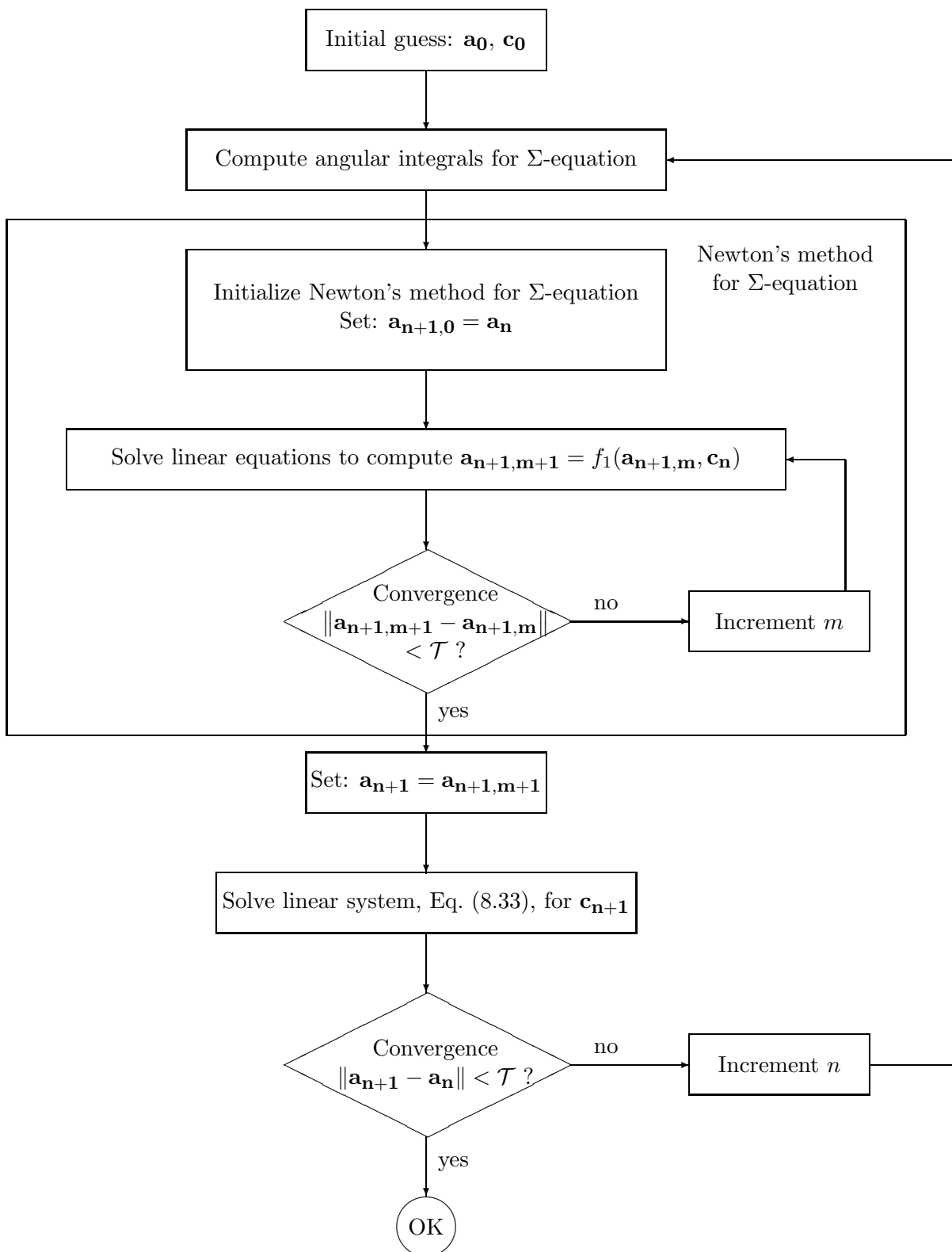


Figure 8.9: Program flow to solve the coupled (Σ, \mathcal{G}) -system using the Chebyshev expansion method.

reached.

We now show the main results obtained with this method. As before the numbers of Chebyshev polynomials in the expansions are $N_\Sigma = N_G = 50$, while the number of radial integration nodes for the Gauss-Legendre rule are taken to be $(N_R)_i = (N_1)_i + (N_2)_i$ with $(N_1)_i = (N_2)_i = 120$ and for the angular integrals $N_\theta = 32$.

The evolution of the generated fermion mass $\Sigma(0)$ versus the coupling α is shown in Fig. 8.10. The critical coupling is found to be $\alpha_c(N_f = 1) = 2.55523$. Although this could seem in

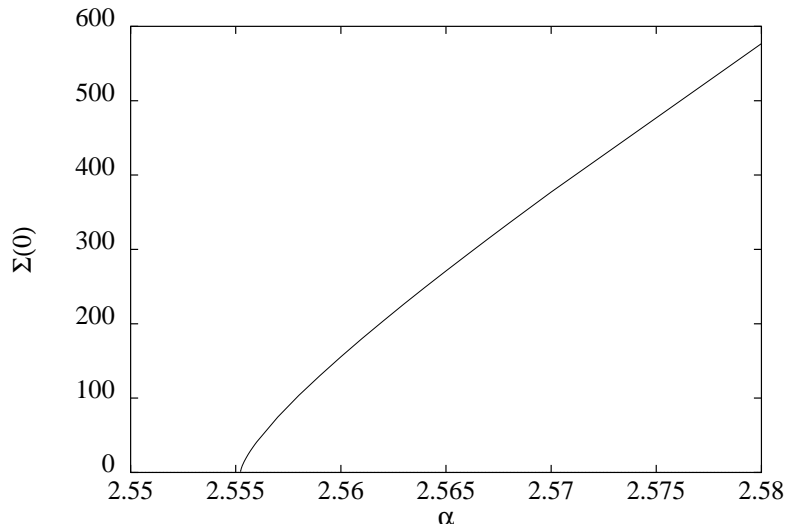


Figure 8.10: Generated fermion mass $\Sigma(0)$ versus coupling α for the coupled (Σ, \mathcal{G}) -system, for $N_f = 1$.

contradiction with the results of Chapter 6 where $\alpha_c(N_f = 1) \approx 2.084$, this is only apparently so. In Chapter 6 we followed the treatment of Kondo et al. [20] and renormalized the coupling such that $\alpha(\Lambda^2) = \alpha$. As the renormalization was not performed consistently on all the quantities under consideration we will leave the coupling unrenormalized in the current method. However, it is clear from the study of dynamical fermion mass generation in quenched QED that the scale of the generated mass depends on the strength of the coupling, which is constant in that case. As we mentioned previously the running of the coupling in unquenched QED is completely determined by the photon renormalization function \mathcal{G} , and the running coupling can be written as $\alpha(x) = \alpha \mathcal{G}(x)$. It is obvious from the Σ -equation, Eq. (8.25), that in unquenched QED the scale of the generated fermion mass will depend on the size and behaviour of the running

coupling. In the 1-loop approximation to \mathcal{G} , Section 8.1, the generated mass scale is related to the value of α , which is also equal to $\alpha(\Lambda^2)$ as the 1-loop corrected \mathcal{G} is there chosen to be $\mathcal{G}(\Lambda^2) = 1$. In order to compare the new calculations with those of Chapter 6 and Section 8.1.2 (where $\mathcal{F} \equiv 1$), we plot $\Sigma(0)$ versus $\alpha(\Lambda^2) = \alpha \mathcal{G}(\Lambda^2)$ using the Chebyshev expansion method for the coupled (Σ, \mathcal{G}) -system and in the 1-loop approximation to \mathcal{G} in Fig. 8.11. Here we see

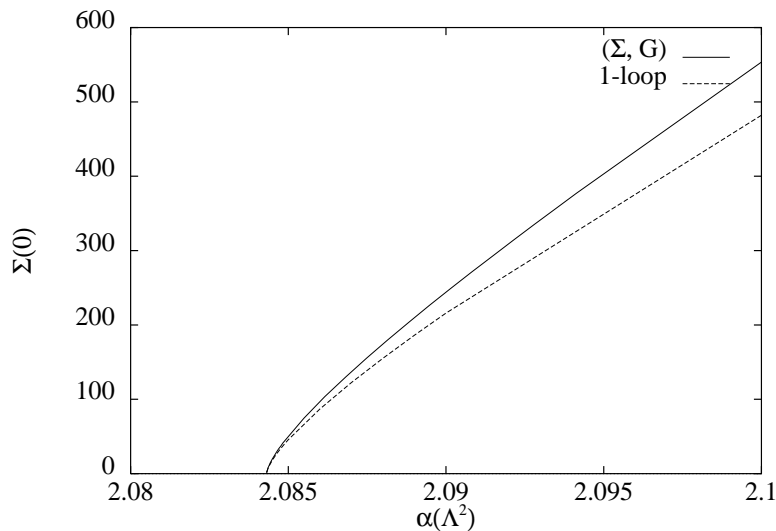


Figure 8.11: Generated fermion mass $\Sigma(0)$ versus running coupling $\alpha(\Lambda^2)$ for the coupled (Σ, \mathcal{G}) -system and in the 1-loop approximation to \mathcal{G} , for $N_f = 1$.

that the critical coupling at the UV-cutoff for the (Σ, \mathcal{G}) -system is $\boxed{\alpha_c(\Lambda^2, N_f = 1) = 2.08431}$, which is consistent with the calculation of Chapter 6 and the results of Kondo et al. [20] and moreover is identical to the value found previously in the 1-loop approximation with $\mathcal{F} \equiv 1$ in Section 8.1.2. From Fig. 8.11 we see that the generation of fermion mass starts at the same value $\alpha(\Lambda^2) = 2.08431$ for both approximations, but this mass evolves differently for increasing coupling. This is easy to explain as the \mathcal{G} -equation, Eq. (8.26), derived for $\mathcal{F} \equiv 1$, can be solved analytically at the critical point, where $\Sigma(x) = 0$. $\mathcal{G}(x)$ is then identical to its 1-loop approximation, hence the same value of the critical coupling. For larger couplings the generated mass function will alter the behaviour of $\mathcal{G}(x)$ and so the evolution of the generated mass scale will differ between the (Σ, \mathcal{G}) -system and the 1-loop approximation. In another study of the coupled (Σ, \mathcal{G}) -system with $\mathcal{F} \equiv 1$, Atkinson et al. [19] introduce the LAK-approximation on the vacuum polarization and on the mass function to compute the angular integrals analytically,

and simplify some of the remaining integrals to derive a differential equation which is then solved numerically. With these approximations they find $\alpha_c = 2.100286$, which only deviates about 0.8% from our, more accurate, solution.

Typical plots of the dynamical fermion mass $\Sigma(x)$ for various values of the bare coupling α are shown in Fig. 8.12. The corresponding running couplings, $\alpha(x) = \alpha\mathcal{G}(x)$, are shown in Fig. 8.13.

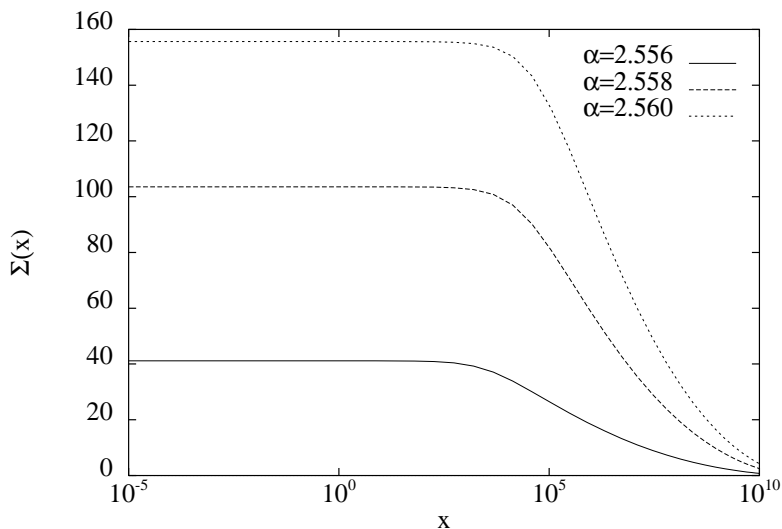


Figure 8.12: Dynamical fermion mass $\Sigma(x)$ versus momentum squared x for the coupled (Σ, \mathcal{G}) -system, for $N_f = 1$ and $\alpha = 2.556, 2.558, 2.56$.

As expected from the discussion of Chapter 6, we indeed see that any unphysical behaviour in the running coupling has now been removed: the quadratic divergence has been cancelled properly.

The results of fermion mass generation for two flavours ($N_f = 2$) are shown in Fig. 8.14. Here we show the evolution of $\Sigma(0)$ versus the value of the running coupling at the UV-cutoff, $\alpha(\Lambda^2)$ for the coupled (Σ, \mathcal{G}) -system and in the 1-loop approximation to \mathcal{G} . The critical coupling at the UV-cutoff is $\alpha_c(\Lambda^2, N_f = 2) = 2.99142$.

If we consider the number of flavours N_f in the Schwinger-Dyson equations as an arbitrary parameter, its values do not necessarily need to be integer but can take non-integer values. We compute the critical coupling for various number of flavours, $0 < N_f \leq 2$, and plot the results in Fig. 8.15. It is reassuring to see the smooth evolution of the critical coupling from $\alpha_c = \pi/3$ for quenched QED ($N_f = 0$) to the above mentioned values for unquenched QED with $N_f = 1, 2$.

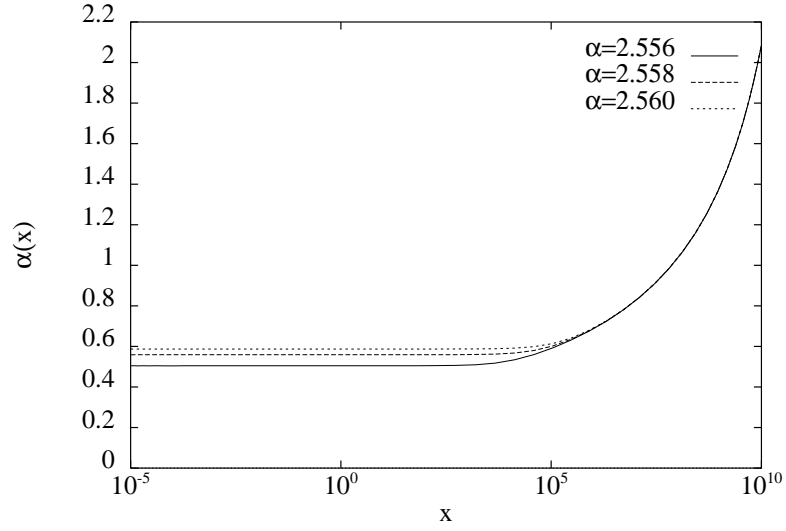


Figure 8.13: Running coupling $\alpha(x)$ versus momentum squared x for the coupled (Σ, \mathcal{G}) -system, for $N_f = 1$ and $\alpha = 2.556, 2.558, 2.56$.

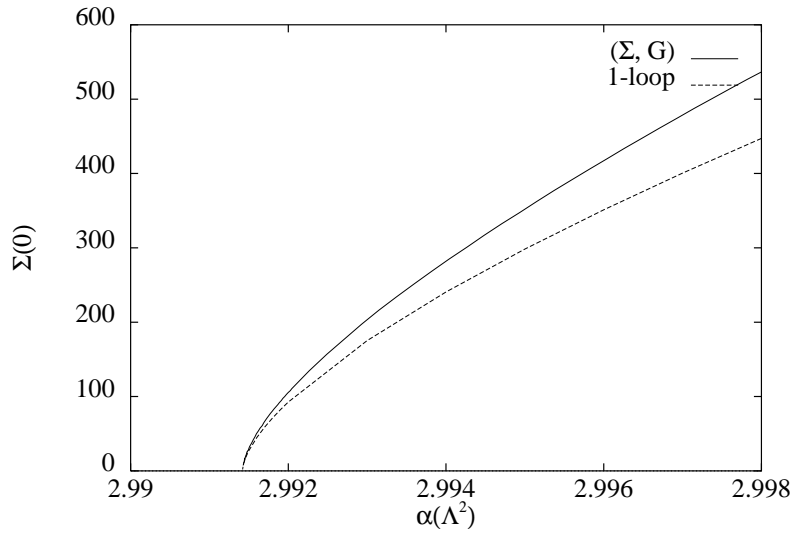


Figure 8.14: Generated fermion mass $\Sigma(0)$ versus running coupling $\alpha(\Lambda^2)$ for the coupled (Σ, \mathcal{G}) -system and in the 1-loop approximation to \mathcal{G} , for $N_f = 2$.

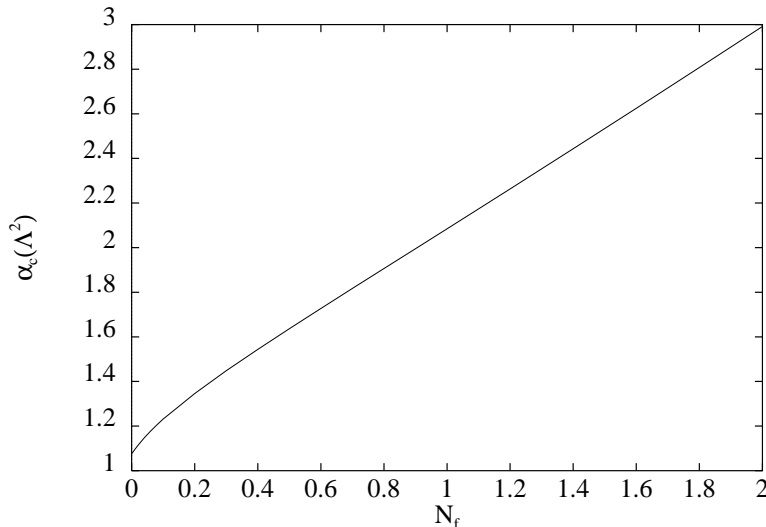


Figure 8.15: Critical coupling $\alpha_c(\Lambda^2)$ versus number of flavours N_f for the coupled (Σ, \mathcal{G}) -system.

There is one more remark which has to be made. When we compare the current method with that from Chapter 6, we note that the interpolation problems have completely disappeared thanks to the use of the Chebyshev expansions of Σ and \mathcal{G} . Nevertheless, one could argue that the need to extrapolate remains. It is known that a polynomial expansion built on a certain interval, here $[\kappa^2, \Lambda^2]$, can only be used reliably for values of the argument in that interval. However we can check that for values, which only lie slightly outside the interval, the function approximations remain realistic. If not, one could always introduce some continuous extrapolation as proposed in Eq. (6.40). Furthermore, the use of the Gaussian quadrature formulae, in contrast to that of Newton and Cotes, has eliminated any problem produced by the extrapolation method. Because the Gaussian rules are open rules, the endpoints of the integration interval are not integration nodes and no extrapolation needs to be made for small values of the external photon momentum, where the mismatch in the cancellation of the quadratic divergence appeared in Chapter 6, and thus, this problem will not occur with the current procedure.

In this section we have shown how the use of the Chebyshev expansion method has enabled us to cancel the quadratic divergence of the vacuum polarization integral properly. We have consistently solved the coupled system of equations for the dynamical fermion mass Σ and the photon renormalization function \mathcal{G} and determined the critical coupling α_c above which fermion mass is generated dynamically.

In the next section we will relax the condition on the fermion wavefunction renormalization, $\mathcal{F} \equiv 1$, to improve the study further and will consider the system of three coupled equations for Σ , \mathcal{F} and \mathcal{G} , still in the bare vertex approximation.

8.3 Coupled (Σ , \mathcal{F} , \mathcal{G})-system

As a logical extension of the study presented in the previous section we now consider the solution of the system of three coupled non-linear integral equations for Σ , \mathcal{F} and \mathcal{G} . To solve this problem we will use ideas developed in Sections 8.2 and 8.1.3.

We recall the three integral equations describing Σ , \mathcal{F} and \mathcal{G} , Eqs. (2.59, 2.60, 2.69), in the Landau gauge and with zero bare mass:

$$\frac{\Sigma(x)}{\mathcal{F}(x)} = \frac{3\alpha}{2\pi^2} \int dy \frac{y\mathcal{F}(y)\Sigma(y)}{y + \Sigma^2(y)} \int d\theta \sin^2 \theta \frac{\mathcal{G}(z)}{z} \quad (8.34)$$

$$\begin{aligned} \frac{1}{\mathcal{F}(x)} &= 1 + \frac{\alpha}{2\pi^2 x} \int dy \frac{y\mathcal{F}(y)}{y + \Sigma^2(y)} \\ &\times \int d\theta \sin^2 \theta \mathcal{G}(z) \left(\frac{3\sqrt{xy} \cos \theta}{z} - \frac{2xy \sin^2 \theta}{z^2} \right) \end{aligned} \quad (8.35)$$

$$\begin{aligned} \frac{1}{\mathcal{G}(x)} &= 1 + \frac{4N_f \alpha}{3\pi^2 x} \int dy \frac{y\mathcal{F}(y)}{y + \Sigma^2(y)} \\ &\times \int d\theta \sin^2 \theta \frac{\mathcal{F}(z)}{z + \Sigma^2(z)} \left[y(1 - 4 \cos^2 \theta) + 3\sqrt{xy} \cos \theta \right] \end{aligned} \quad (8.36)$$

where $z = x + y - 2\sqrt{xy} \cos \theta$.

As previously, we derive a system of non-linear algebraic equations in the following way. Introduce an ultraviolet cutoff, Λ^2 , and an infrared cutoff, κ^2 and change variables from y to $t \equiv \log_{10} y$. Then, consider the integral equations at respectively, N_Σ , $N_\mathcal{F}$ and $N_\mathcal{G}$ external momenta x_i , which are chosen to be the roots of the Chebyshev polynomial of corresponding degree. Finally, replace the integrals by Gauss-Legendre quadrature rules. This yields:

$$\frac{\Sigma(x_i)}{\mathcal{F}(x_i)} - \frac{3\alpha}{2\pi^2} \sum_{j=1}^{(N_R)_i} w_{ij} \frac{y_{ij}^2 \mathcal{F}(y_{ij}) \Sigma(y_{ij})}{y_{ij} + \Sigma^2(y_{ij})} \Theta_\Sigma(x_i, y_{ij}) = 0, \quad i = 1, \dots, N_\Sigma \quad (8.37)$$

$$\frac{1}{\mathcal{F}(x_i)} - 1 - \frac{\alpha}{2\pi^2 x_i} \sum_{j=1}^{(N_R)_i} w_{ij} \frac{y_{ij}^2 \mathcal{F}(y_{ij})}{y_{ij} + \Sigma^2(y_{ij})} \Theta_\mathcal{F}(x_i, y_{ij}) = 0, \quad i = 1, \dots, N_\mathcal{F} \quad (8.38)$$

$$\frac{1}{\mathcal{G}(x_i)} - 1 - \frac{4N_f \alpha}{3\pi^2 x_i} \sum_{j=1}^{(N_R)_i} w_{ij} \frac{y_{ij}^2 \mathcal{F}(y_{ij})}{y_{ij} + \Sigma^2(y_{ij})} \Theta_\mathcal{G}(x_i, y_{ij}) = 0, \quad i = 1, \dots, N_\mathcal{G} \quad (8.39)$$

with

$$\Theta_{\Sigma}(x_i, y_{ij}) = \sum_{k=1}^{N_{\theta}} w'_k \sin^2 \theta_k \frac{\mathcal{G}(z_k)}{z_k} \quad (8.40)$$

$$\Theta_{\mathcal{F}}(x_i, y_{ij}) = \sum_{k=1}^{N_{\theta}} w'_k \sin^2 \theta_k \mathcal{G}(z_k) \left(\frac{3\sqrt{x_i y_{ij}} \cos \theta_k}{z_k} - \frac{2x_i y_{ij} \sin^2 \theta_k}{z_k^2} \right) \quad (8.41)$$

$$\Theta_{\mathcal{G}}(x_i, y_{ij}) = \sum_{k=1}^{N_{\theta}} w'_k \sin^2 \theta_k \frac{\mathcal{F}(z_k)}{z_k + \Sigma^2(z_k)} \left[y_{ij}(1 - 4 \cos^2 \theta_k) + 3\sqrt{x_i y_{ij}} \cos \theta_k \right] \quad (8.42)$$

where $z_k = x_i + y_{ij} - 2\sqrt{x_i y_{ij}} \cos \theta_k$. The unknowns of the system of equations are the Chebyshev coefficients a_j , b_j and c_j of the following expansions:

$$\Sigma(x) \equiv \sum_{j=0}^{N_{\Sigma}-1} 'a_j T_j(s(x)) \quad (8.43)$$

$$\mathcal{F}(x) \equiv \sum_{j=0}^{N_{\mathcal{F}}-1} 'b_j T_j(s(x)) \quad (8.44)$$

$$\mathcal{G}(x) \equiv \sum_{j=0}^{N_{\mathcal{G}}-1} 'c_j T_j(s(x)) \quad (8.45)$$

where s is defined by

$$s(x) \equiv \frac{\log_{10}(x/\Lambda\kappa)}{\log_{10}(\Lambda/\kappa)}. \quad (8.46)$$

According to Section 5.4 the convergence rate of the numerical method used to solve this system of equations will be quadratic if we use Newton's method. However, as mentioned in Section 6.1, it is not convenient to implement Newton's method on the complete system of equations. Newton's method is an iterative procedure where at each step a system of linear equations has to be solved to derive new approximations $(\mathbf{a}_{\mathbf{n}+1}, \mathbf{b}_{\mathbf{n}+1}, \mathbf{c}_{\mathbf{n}+1})$ from $(\mathbf{a}_{\mathbf{n}}, \mathbf{b}_{\mathbf{n}}, \mathbf{c}_{\mathbf{n}})$. This means that the angular integrals, Eqs. (8.40, 8.41, 8.42), have to be recalculated at each iteration step. However, the main objection to this method is that Newton's method requires the derivatives of the left hand sides of Eqs. (8.37, 8.38, 8.39) to be taken with respect of the Chebyshev coefficients a_j , b_j and c_j . The implementation of this method would use a very large amount of memory space and running the program would consume much computing time. Therefore, this procedure has not been implemented here, although it remains an important objective for future work, in order to enhance the consistency and accuracy of the method, if some more powerful computer infrastructure is available. In the meantime we will use a hybrid method with the aim of retaining the advantages of the quadratic convergence rate of Newton's method, while keeping the needs for memory storage and computing time reasonably small. The program flow of this method, which we explain in more detail below, is shown in Fig. 8.16.

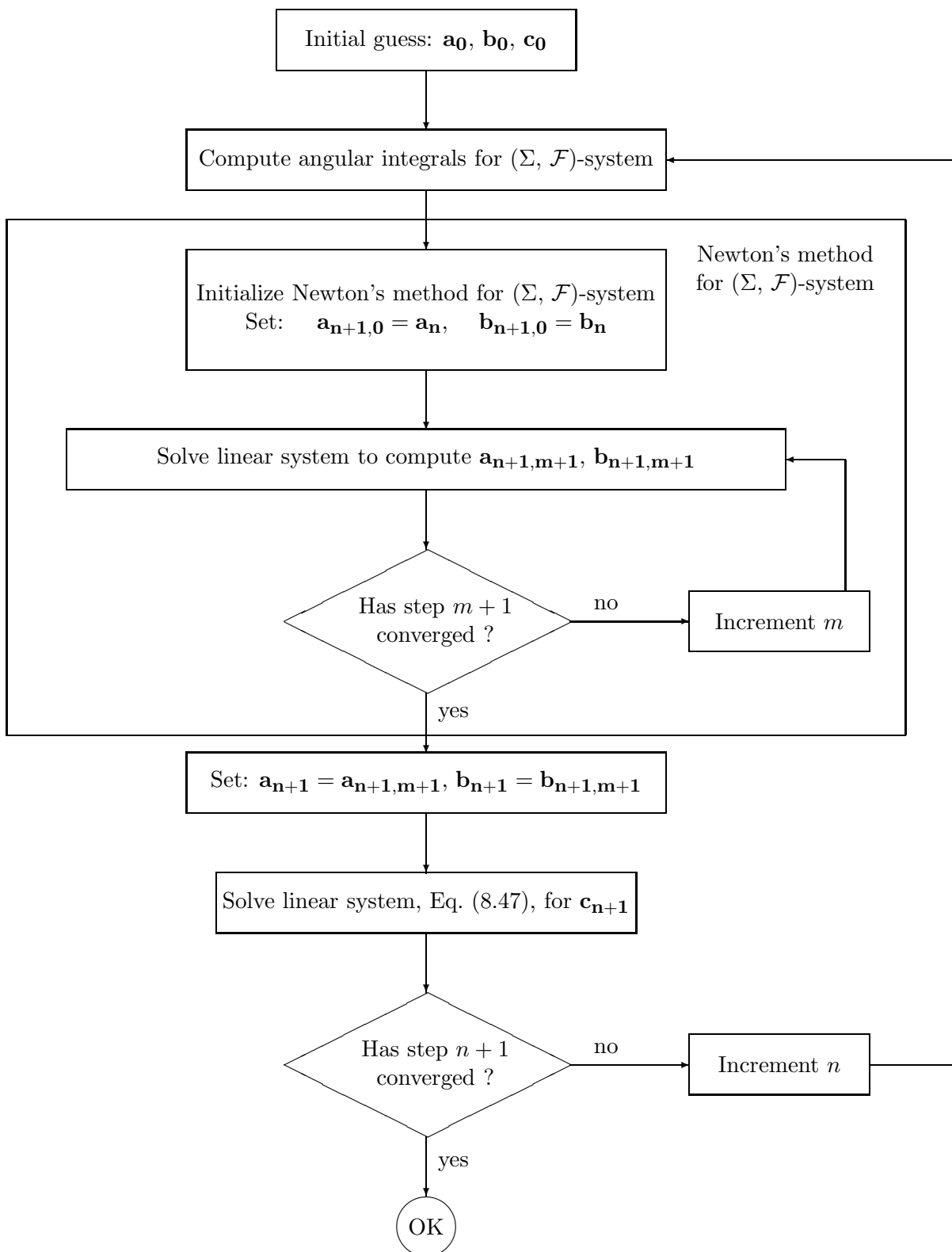


Figure 8.16: Program flow to solve the coupled $(\Sigma, \mathcal{F}, \mathcal{G})$ -system using the Chebyshev expansion method.

To start the program we introduce an initial guess for the Chebyshev coefficients. These initial guesses can be the results of a previous calculation or be derived from some reasonable choice for the unknown functions (e.g. $\mathcal{F}(x) = 1$, one-loop approximation for $\mathcal{G}(x)$). Starting from these values we apply the following iterative procedure till convergence is reached. We describe the $(n + 1)^{th}$ iteration step, supposing we know the n^{th} approximations $\mathbf{a}_n, \mathbf{b}_n, \mathbf{c}_n$. From Eqs. (8.40, 8.41) we compute the angular integrals for the Σ - and \mathcal{F} -equations, using the Chebyshev coefficients \mathbf{c}_n to compute the necessary \mathcal{G} -values with Eq. (8.45). Now, Eqs. (8.37, 8.38) form an independent system of non-linear equations determining the new approximations $\mathbf{a}_{n+1}, \mathbf{b}_{n+1}$. This system of equations can be very efficiently solved using Newton's iterative method, as shown in Section 8.1.3. Starting from some initial values, which can be chosen to be $\mathbf{a}_n, \mathbf{b}_n$, each iteration determines $\mathbf{a}_{n+1,m+1}, \mathbf{b}_{n+1,m+1}$ from $\mathbf{a}_{n+1,m}, \mathbf{b}_{n+1,m}$ by solving a system of linear equations till convergence is reached. The final iterate gives the new approximations $\mathbf{a}_{n+1}, \mathbf{b}_{n+1}$. We now substitute those Chebyshev coefficients in the expansions Eqs. (8.43, 8.44) to compute the angular integrals Eq. (8.42). To determine the new values \mathbf{c}_{n+1} , we will take the reciprocal of Eq. (8.39) and substitute the expansion Eq. (8.45), yielding:

$$\sum_{j=0}^{N_G-1} 'c_j T_j(s(x_i)) = \left[1 + \frac{4N_f \alpha}{3\pi^2 x_i} \sum_{j=1}^{(N_R)_i} w_{ij} \frac{y_{ij}^2 \mathcal{F}(y_{ij})}{y_{ij} + \Sigma^2(y_{ij})} \Theta_{\mathcal{G}}(x_i, y_{ij}) \right]^{-1}, \quad i = 1, \dots, N_G, \quad (8.47)$$

with Σ and \mathcal{F} defined by the expansions Eqs. (8.43, 8.44) using the coefficients $\mathbf{a}_{n+1}, \mathbf{b}_{n+1}$. Eq. (8.47) represents a linear system for the Chebyshev coefficients \mathbf{c}_{n+1} , which can easily be solved by standard numerical techniques. In this way we have determined the new sets of Chebyshev coefficients $\mathbf{a}_{n+1}, \mathbf{b}_{n+1}$ and \mathbf{c}_{n+1} from $\mathbf{a}_n, \mathbf{b}_n$ and \mathbf{c}_n . The whole procedure is iterated till the convergence criterion is satisfied. The final iterates are approximate solutions \mathbf{a}, \mathbf{b} and \mathbf{c} to the non-linear system, Eqs. (8.37, 8.38, 8.39) within the required accuracy.

The results of the program are achieved by requesting a final relative accuracy of 0.001. For the Chebyshev expansions, we take $N_{\Sigma} = N_{\mathcal{F}} = N_{\mathcal{G}} = 50$. The Gauss-Legendre integrations are performed with $(N_R)_i = (N_1)_i + (N_2)_i$, where $(N_1)_i = (N_2)_i = 120$, radial integration points and $N_{\theta} = 32$ angular integration points, which is sufficient to obtain the above mentioned accuracy. The program needs between 3 and 8 global $[(\Sigma, \mathcal{F}), \mathcal{G}]$ -iterations to converge, while each individual Newton's method to solve a (Σ, \mathcal{F}) -system requires between 2 and 8 iterations. The major part of the computing time involves the recalculation of the angular integrals at each global iteration.

The evolution of the generated fermion mass $\Sigma(0)$, is plotted versus $\alpha(\Lambda^2)$, the value of the running coupling at the ultraviolet cutoff, in Fig. 8.17. The critical coupling for the $(\Sigma, \mathcal{F}, \mathcal{G})$ -system is $\boxed{\alpha_c(\Lambda^2, N_f = 1) = 1.74102}$.

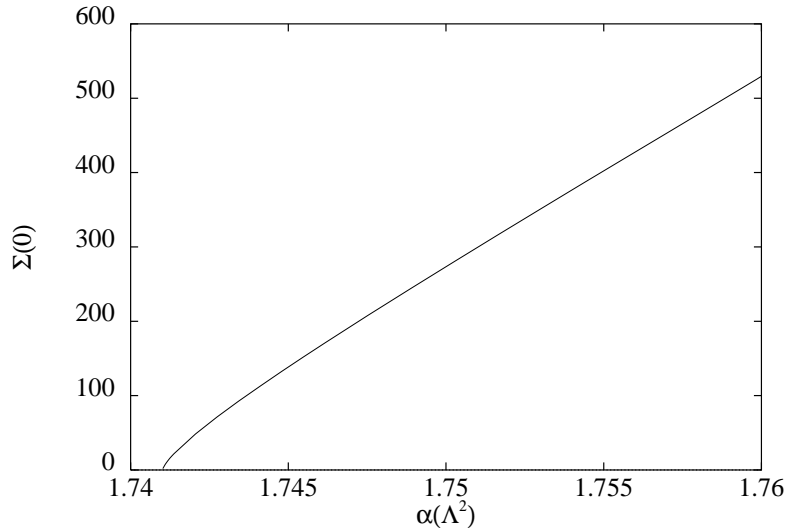


Figure 8.17: Generated fermion mass $\Sigma(0)$ versus running coupling $\alpha(\Lambda^2)$ for the coupled $(\Sigma, \mathcal{F}, \mathcal{G})$ -system, for $N_f = 1$.

Typical plots of $\Sigma(x)$, $\mathcal{F}(x)$ and $\alpha(x) = \alpha \mathcal{G}(x)$ are shown in Fig. 8.18, Fig. 8.19 and Fig. 8.20.

For two flavours, $N_f = 2$, the generated fermion mass $\Sigma(0)$ versus the running coupling $\alpha(\Lambda^2)$ is plotted in Fig. 8.21. The critical coupling is $\boxed{\alpha_c(\Lambda^2, N_f = 2) = 2.22948}$.

If we compare the results of the coupled $(\Sigma, \mathcal{F}, \mathcal{G})$ -system with those of the coupled (Σ, \mathcal{F}) -system in the 1-loop approximation to \mathcal{G} of Section 8.1.3, we note that the critical coupling increases by approximately 4% for $N_f = 1$ and 10% for $N_f = 2$ when we include the \mathcal{G} -equation, Eq. (8.36), in the treatment instead of its 1-loop approximation, Eq. (8.3). On the other hand, if we compare these results with those computed for the (Σ, \mathcal{G}) -system with $\mathcal{F} \equiv 1$ in Section 8.2, we note that the consistent treatment of the \mathcal{F} -equation decreases α_c by 16% for $N_f = 1$ and 25% for $N_f = 2$.

The only other calculation found in the literature treating the three equations simultaneously is that of Rakow [18]. He finds a critical coupling $\alpha_c = 2.25$ for $N_f = 1$, which is quite different from our result with a deviation of almost 30%. Unfortunately the lack of details in that paper

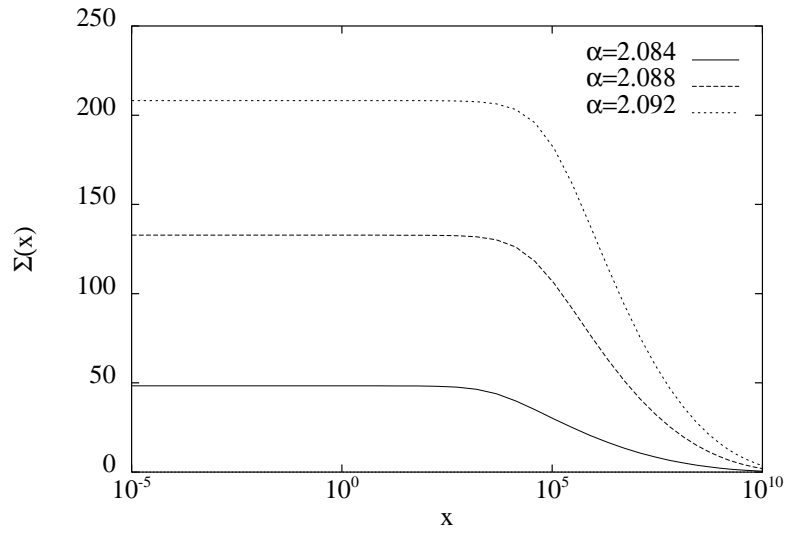


Figure 8.18: Dynamical fermion mass $\Sigma(x)$ versus momentum squared x for the coupled $(\Sigma, \mathcal{F}, \mathcal{G})$ -system, for $N_f = 1$ and $\alpha = 2.084, 2.088, 2.092$.

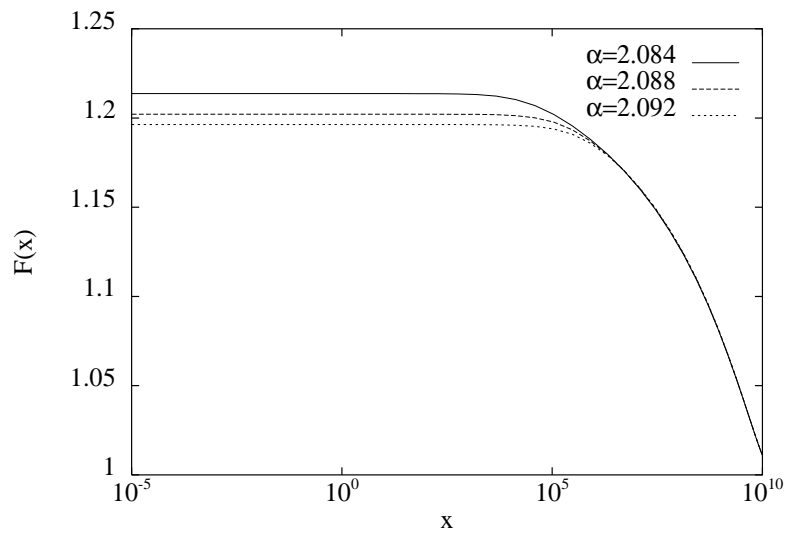


Figure 8.19: Fermion wavefunction renormalization $\mathcal{F}(x)$ versus momentum squared x for the coupled $(\Sigma, \mathcal{F}, \mathcal{G})$ -system, for $N_f = 1$ and $\alpha = 2.084, 2.088, 2.092$.

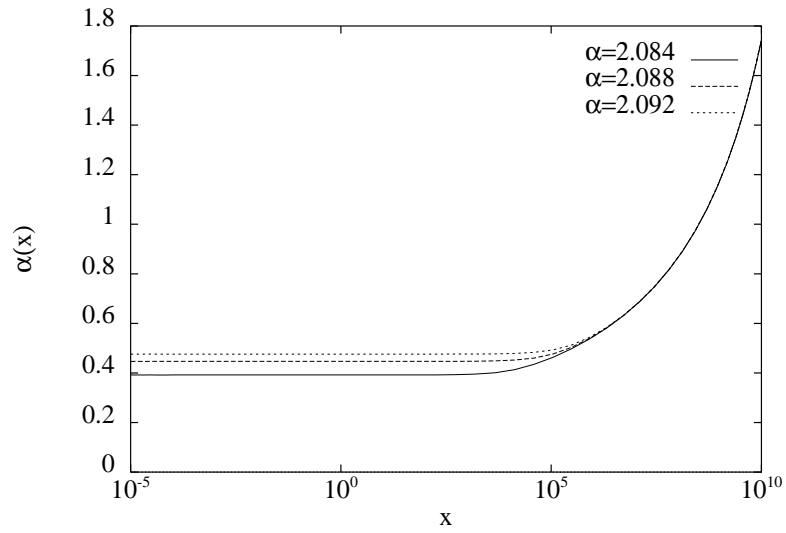


Figure 8.20: Running coupling $\alpha(x)$ versus momentum squared x for the coupled $(\Sigma, \mathcal{F}, \mathcal{G})$ -system, for $N_f = 1$ and $\alpha = 2.084, 2.088, 2.092$.

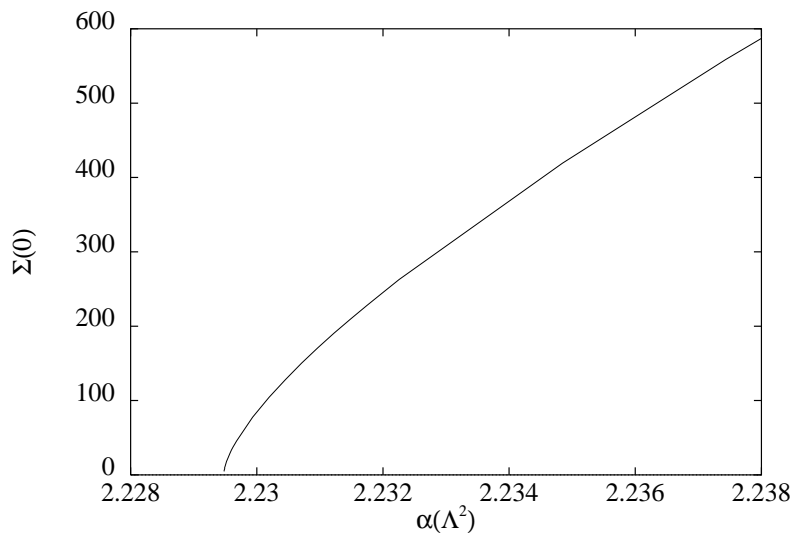


Figure 8.21: Generated fermion mass $\Sigma(0)$ versus running coupling $\alpha(\Lambda^2)$ for the coupled $(\Sigma, \mathcal{F}, \mathcal{G})$ -system, for $N_f = 2$.

does not allow us to deduce where the difference comes from. As explained previously we take the relevant critical coupling to be $\alpha_c(\Lambda^2) = \alpha_c \mathcal{G}(\Lambda^2)$. We believe that only then, calculations with different regularization procedures can be compared. We are very confident about the accuracy of our calculation and we can only guess that Rakow's result should be interpreted in some different way to find agreement. Furthermore, his main result is that the renormalized coupling $\alpha_r \rightarrow 0$ in the critical point which, as he claims, would prove that the renormalized theory is trivial. However, the renormalized coupling is strangely defined in the zero momentum point as $\alpha_r = \alpha \mathcal{G}(0) \mathcal{F}^2(0)$. From plots analogous to Fig. 8.20 we see that for the critical point we have $\alpha_c(0) = \alpha_c \mathcal{G}(0) \rightarrow 0$, as is the case in the massless 1-loop approximation to \mathcal{G} , so that obviously $\alpha_r \rightarrow 0$. However, we do not believe that the infrared behaviour of QED can explain its triviality, but rather it is its ultraviolet behaviour which could, because of the Landau pole. We do not think that Rakow's observation about his renormalized coupling proves the triviality of QED. Intuitively we could say that renormalizing the theory relates the overall evolution of the coupling to the scales of the theory (bare mass and renormalization scale); choosing to renormalize at zero momentum ($\mu^2 = 0$) in the critical point (where $\Sigma(x) = 0$) and taking the continuum limit ($\Lambda \rightarrow \infty$) is in contradiction with this as there are no finite scales available. This will be different if we renormalize at some finite scale and only then will we be able to discuss the triviality of the theory.

8.4 Summary

In this chapter we have seen that dynamical fermion mass generation does occur in unquenched QED with bare vertex approximation for $N_f = 1$ and $N_f = 2$. In Table 8.3 we summarize the various results obtained for the critical coupling for $N_f = 1$ and $N_f = 2$ from the previous sections.

For the 1-loop approximation we compared our results with those found in the literature in Section 8.1.4. We concluded that the various results in the LAK-approximation and the $\mathcal{F} = 1$ approximation agree with each other within good accuracy and that our results are totally in line with the most accurate ones. Furthermore we produced the first critical coupling results for the coupled (Σ, \mathcal{F}) -system. The inclusion of self-energy corrections in \mathcal{F} causes a decrease of α_c by 20% for $N_f = 1$ and 30% for $N_f = 2$.

For the (Σ, \mathcal{G}) -system with $\mathcal{F} \equiv 1$ we found the same critical coupling as Kondo et al. [20].

| System | \mathcal{G} | \mathcal{F} | $\alpha_c(N_f = 1)$ | $\alpha_c(N_f = 2)$ |
|--------------------------------------|---------------|------------------------|---------------------|---------------------|
| Σ | 1-loop, LAK | $\mathcal{F} = 1$ | 1.99953 | 2.75233 |
| Σ | 1-loop | $\mathcal{F} \equiv 1$ | 2.08431 | 2.99142 |
| (Σ, \mathcal{F}) | 1-loop | SD | 1.67280 | 2.02025 |
| (Σ, \mathcal{G}) | SD | $\mathcal{F} \equiv 1$ | 2.08431 | 2.99142 |
| $(\Sigma, \mathcal{F}, \mathcal{G})$ | SD | SD | 1.74102 | 2.22948 |

Table 8.3: Critical coupling α_c for $N_f = 1$ and $N_f = 2$ for various approximations to the $(\Sigma, \mathcal{F}, \mathcal{G})$ -system in the bare vertex approximation. (Column “System” states which coupled system of equations was effectively solved. Columns “ \mathcal{G} ” and “ \mathcal{F} ” tell which approximations were used for these functions, “SD” means that the function is determined self-consistently by the coupled SD-equations in “System”, “LAK” is the Landau-Abrikosov-Khalatnikov approximation of Section 8.1.1.)

However, their erroneous behaviour of $\mathcal{G}(x)$ at intermediate low energy has been corrected thanks to the use of Chebyshev expansions for Σ and \mathcal{G} . The results of Atkinson et al. [19], although less accurate because of additional approximations, still agree very well with our calculation. We also give the first results for $N_f = 2$.

Finally, we have given a detailed description of the consistent and accurate treatment of the complete $(\Sigma, \mathcal{F}, \mathcal{G})$ -system in the bare vertex approximation. From Table 8.3 we see that replacing the 1-loop approximation to \mathcal{G} by the consistent SD-treatment of the \mathcal{G} -equation introduces an increase of α_c by 4% for $N_f = 1$ and 10% for $N_f = 2$. On the other hand, if we consistently add the \mathcal{F} -equation in the (Σ, \mathcal{G}) -system we note a decrease of α_c by 16% for $N_f = 1$ and 25% for $N_f = 2$. We have been unable to make a useful quantitative comparison with Rakow’s work [18] as explained in Section 8.3.

Until now all the calculations have been made in the bare vertex approximation. However, we know that the bare vertex violates the Ward-Takahashi identity relating the QED vertex to the fermion propagator, which is a direct consequence of the gauge invariance of the theory. In the next chapter we will examine the possibility of improving the vertex Ansatz. This is the first time that the study of fermion mass generation in unquenched QED will be taken beyond the bare vertex approximation.

Chapter 9

Improving the vertex Ansatz

In this chapter we are going to investigate the influence of the vertex Ansatz on the dynamical generation of fermion mass. In the previous chapters we have used the bare vertex approximation, $\Gamma^\mu(k, p) = \gamma^\mu$. This vertex Ansatz has the advantage of being very simple and therefore it makes the manipulation of the Schwinger-Dyson equations easier. However, this approximation does not satisfy the Ward-Takahashi identity relating the QED vertex with the fermion propagator, which is a consequence of the gauge invariance of the theory. Therefore, the bare vertex approximation does not ensure that the physical quantities computed with it are gauge invariant as they should be. The Ward-Takahashi identity relating the QED vertex with the fermion propagator determines uniquely the longitudinal part of the vertex [24], called Ball-Chiu vertex. However, the transverse part of the vertex is still arbitrary. Constraints on that part of the vertex can be imposed by requiring the multiplicative renormalizability of the fermion and photon propagator, the absence of kinematical singularities, the reproduction of the perturbative results in the weak coupling limit, gauge invariance of critical coupling, ... [12, 25, 26]. In the next sections we will investigate the generation of fermion mass using improved vertices and highlight the problems which occur when doing so.

9.1 $1/\mathcal{F}$ -corrected vertex

To investigate the influence of the vertex improvement on the dynamical generation of fermion mass we will first introduce a $1/\mathcal{F}$ -corrected vertex defined as:

$$\Gamma^\mu(k, p) = \frac{1}{2} \left[\frac{1}{\mathcal{F}(k^2)} + \frac{1}{\mathcal{F}(p^2)} \right] \gamma^\mu, \quad (9.1)$$

which is just the first term of the Ball-Chiu vertex, Eq. (2.73). The motivation for this vertex Ansatz is that it introduces a wavefunction renormalization dependence in the vertex. However, it avoids the numerical difficulties which can occur with the complete Ball-Chiu vertex because of the difference terms

$$\frac{1}{k^2 - p^2} \left[\frac{1}{\mathcal{F}(k^2)} - \frac{1}{\mathcal{F}(p^2)} \right], \quad \frac{1}{k^2 - p^2} \left[\frac{\Sigma(k^2)}{\mathcal{F}(k^2)} - \frac{\Sigma(p^2)}{\mathcal{F}(p^2)} \right].$$

The coupled integral equations with this vertex Ansatz are easily derived from Eqs. (2.59, 2.60, 2.69) for the bare vertex, as the $1/\mathcal{F}$ -vertex, Eq. (9.1), has the same Dirac structure as the bare vertex and merely introduces a multiplicative factor in each integral where the full vertex is replaced by the vertex Ansatz. The equations, with $m_0 = 0$ and in the Landau gauge, are:

$$\frac{\Sigma(x)}{\mathcal{F}(x)} = \frac{3\alpha}{2\pi^2} \int dy \frac{yA(y, x)\mathcal{F}(y)\Sigma(y)}{y + \Sigma^2(y)} \int d\theta \sin^2 \theta \frac{\mathcal{G}(z)}{z} \quad (9.2)$$

$$\frac{1}{\mathcal{F}(x)} = 1 - \frac{\alpha}{2\pi^2 x} \int dy \frac{yA(y, x)\mathcal{F}(y)}{y + \Sigma^2(y)} \int d\theta \sin^2 \theta \mathcal{G}(z) \left[\frac{2yx \sin^2 \theta}{z^2} - \frac{3\sqrt{yx} \cos \theta}{z} \right] \quad (9.3)$$

$$\frac{1}{\mathcal{G}(x)} = 1 + \frac{4N_f \alpha}{3\pi^2 x} \int dy \frac{y\mathcal{F}(y)}{y + \Sigma^2(y)} \int d\theta \sin^2 \theta \frac{A(y, z)\mathcal{F}(z)}{z + \Sigma^2(z)} \left[y(1 - 4\cos^2 \theta) + 3\sqrt{yx} \cos \theta \right] \quad (9.4)$$

where $A(y, x) = \frac{1}{2} \left[\frac{1}{\mathcal{F}(y)} + \frac{1}{\mathcal{F}(x)} \right]$.

We now solve this system of coupled integral equations using the same method as in Section 8.3. In Fig. 9.1 we show the evolution of the generated fermion mass versus the running coupling at the UV-cutoff, $\alpha(\Lambda^2)$, for $N_f = 1$. The critical coupling is $\boxed{\alpha_c(\Lambda^2, N_f = 1) = 1.90911}$.

Typical plots of $\Sigma(x)$, $\mathcal{F}(x)$ and $\alpha(x) = \alpha \mathcal{G}(x)$ are shown in Fig. 9.2, Fig. 9.3 and Fig. 9.4.

In Fig. 9.5 we plot the generated fermion mass $\Sigma(0)$ versus the running coupling $\alpha(\Lambda^2)$ for $N_f = 2$. The critical coupling is $\boxed{\alpha_c(\Lambda^2, N_f = 2) = 2.59578}$.

If we compare these results with those obtained with the bare vertex approximation in Section 8.3 we note an increase of the critical coupling, $\alpha_c(\Lambda^2)$ by about 10% for $N_f = 1$ and 16% for $N_f = 2$.

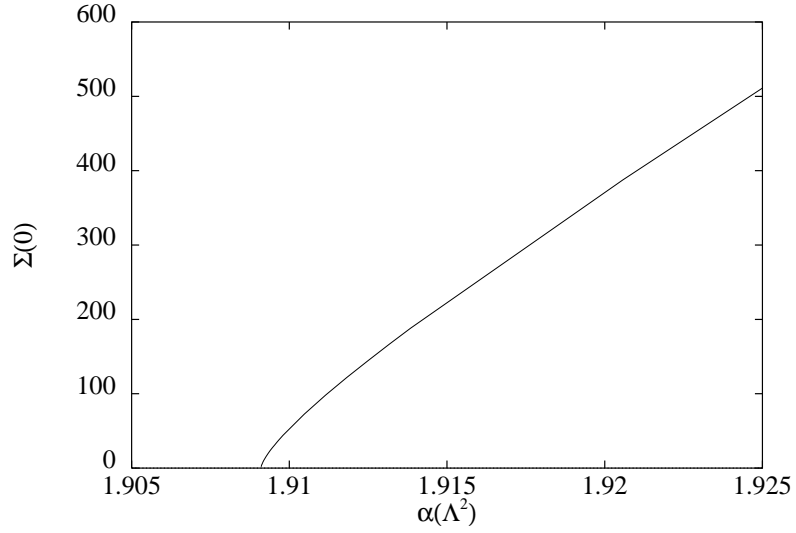


Figure 9.1: Generated fermion mass $\Sigma(0)$ versus running coupling $\alpha(\Lambda^2)$ for the coupled $(\Sigma, \mathcal{F}, \mathcal{G})$ -system with the $1/\mathcal{F}$ -vertex Ansatz, for $N_f = 1$.

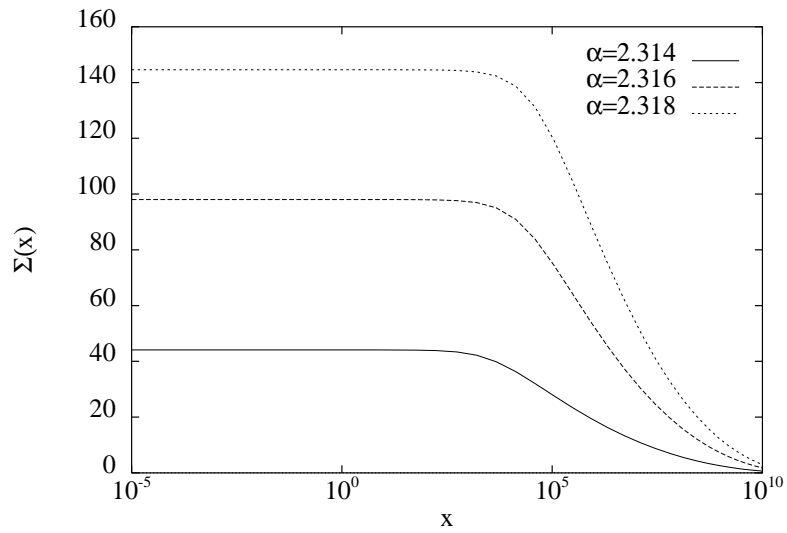


Figure 9.2: Dynamical fermion mass $\Sigma(x)$ versus momentum squared x for the coupled $(\Sigma, \mathcal{F}, \mathcal{G})$ -system with the $1/\mathcal{F}$ -vertex Ansatz, for $N_f = 1$ and $\alpha = 2.314, 2.316, 2.318$.

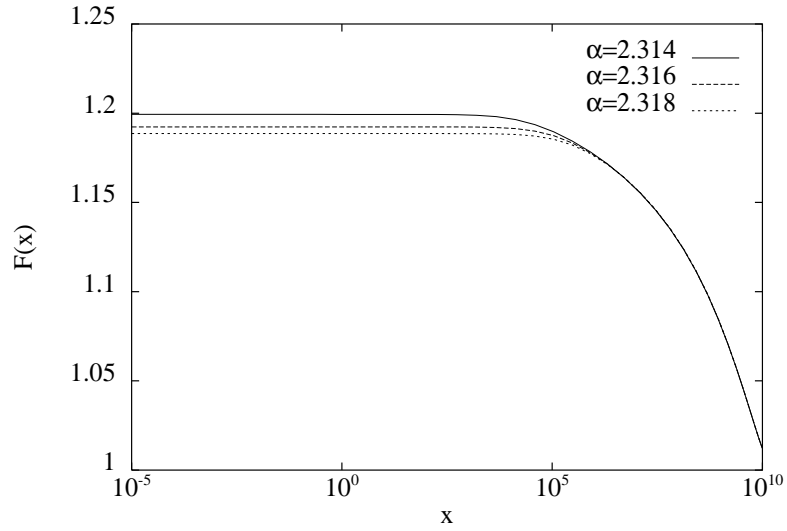


Figure 9.3: Fermion wavefunction renormalization $\mathcal{F}(x)$ versus momentum squared x for the coupled $(\Sigma, \mathcal{F}, \mathcal{G})$ -system with the $1/\mathcal{F}$ -vertex Ansatz, for $N_f = 1$ and $\alpha = 2.314, 2.316, 2.318$.

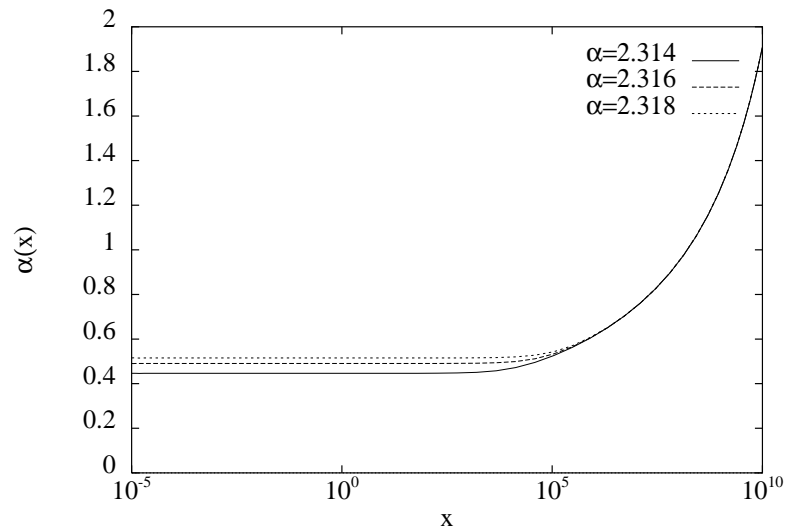


Figure 9.4: Running coupling $\alpha(x)$ versus momentum squared x for the coupled $(\Sigma, \mathcal{F}, \mathcal{G})$ -system with the $1/\mathcal{F}$ -vertex Ansatz, for $N_f = 1$ and $\alpha = 2.314, 2.316, 2.318$.

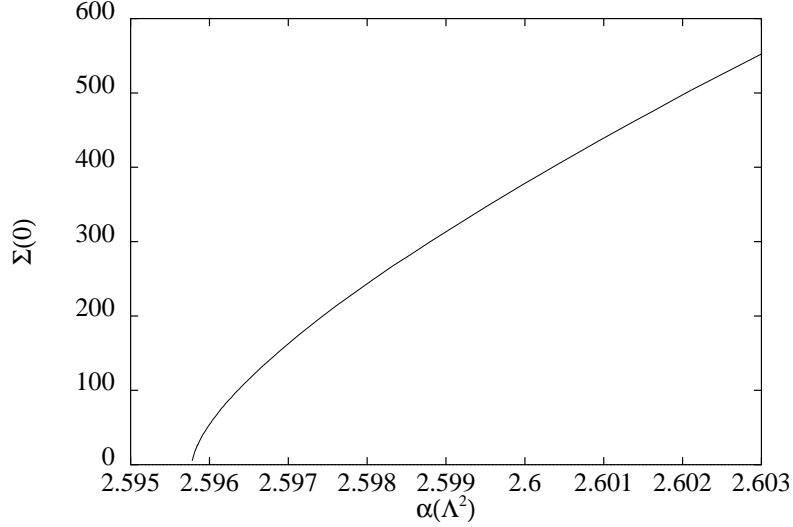


Figure 9.5: Generated fermion mass $\Sigma(0)$ versus running coupling $\alpha(\Lambda^2)$ for the coupled $(\Sigma, \mathcal{F}, \mathcal{G})$ -system with the $1/\mathcal{F}$ -vertex Ansatz, for $N_f = 2$.

9.2 Ball-Chiu vertex

Next we will derive the results using the longitudinal or Ball-Chiu vertex, which satisfies the Ward-Takahashi identity. The Ball-Chiu vertex has been introduced in Eq. (2.73) and is given by:

$$\Gamma_L^\mu(k, p) = \frac{1}{2} \left[\frac{1}{\mathcal{F}(k^2)} + \frac{1}{\mathcal{F}(p^2)} \right] \gamma^\mu + \frac{1}{2} \left[\frac{1}{\mathcal{F}(k^2)} - \frac{1}{\mathcal{F}(p^2)} \right] \frac{(k+p)^\mu (k+p)_\nu}{k^2 - p^2} \quad (9.5)$$

$$- \left[\frac{\Sigma(k^2)}{\mathcal{F}(k^2)} - \frac{\Sigma(p^2)}{\mathcal{F}(p^2)} \right] \frac{(k+p)^\mu}{k^2 - p^2}.$$

The coupled integral equations are easily derived from Eqs. (2.131, 2.132, 2.133) for the Curtis-Pennington vertex, by setting $\tau_6(y, x) = 0$ to remove the transverse part of the vertex. The equations, with $m_0 = 0$ and in the Landau gauge, are:

$$\frac{\Sigma(x)}{\mathcal{F}(x)} = \frac{\alpha}{2\pi^2} \int dy \frac{y\mathcal{F}(y)}{y + \Sigma^2(y)} \int d\theta \sin^2 \theta \mathcal{G}(z) \quad (9.6)$$

$$\times \left\{ \frac{3A(y, x)\Sigma(y)}{z} - \frac{\Sigma(y) - \Sigma(x)}{\mathcal{F}(x)(y-x)} \frac{2yx \sin^2 \theta}{z^2} \right\}$$

$$\frac{1}{\mathcal{F}(x)} = 1 - \frac{\alpha}{2\pi^2 x} \int dy \frac{y\mathcal{F}(y)}{y + \Sigma^2(y)} \int d\theta \sin^2 \theta \mathcal{G}(z) \quad (9.7)$$

$$\times \left\{ A(y, x) \left[\frac{2yx \sin^2 \theta}{z^2} - \frac{3\sqrt{yx} \cos \theta}{z} \right] + [B(y, x)(y+x) - C(y, x)\Sigma(y)] \frac{2yx \sin^2 \theta}{z^2} \right\}$$

$$\begin{aligned}
\frac{1}{\mathcal{G}(x)} &= 1 + \frac{2N_f\alpha}{3\pi^2 x} \int dy \frac{y\mathcal{F}(y)}{y + \Sigma^2(y)} \int d\theta \sin^2 \theta \frac{\mathcal{F}(z)}{z + \Sigma^2(z)} \\
&\times \left\{ 2A(y, z) \left[y(1 - 4\cos^2 \theta) + 3\sqrt{yx} \cos \theta \right] \right. \\
&\quad + B(y, z) \left[(y + z - 2\Sigma(y)\Sigma(z)) (2y(1 - 4\cos^2 \theta) + 3\sqrt{yx} \cos \theta) \right. \\
&\quad \quad \left. \left. + 3(y - z)(y - \Sigma(y)\Sigma(z)) \right] \right. \\
&\quad \left. - C(y, z) \left[(\Sigma(y) + \Sigma(z)) (2y(1 - 4\cos^2 \theta) + 3\sqrt{yx} \cos \theta) + 3(y - z)\Sigma(y) \right] \right\}
\end{aligned} \tag{9.8}$$

where

$$\begin{aligned}
A(y, x) &= \frac{1}{2} \left[\frac{1}{\mathcal{F}(y)} + \frac{1}{\mathcal{F}(x)} \right] \\
B(y, x) &= \frac{1}{2(y-x)} \left[\frac{1}{\mathcal{F}(y)} - \frac{1}{\mathcal{F}(x)} \right] \\
C(y, x) &= -\frac{1}{y-x} \left[\frac{\Sigma(y)}{\mathcal{F}(y)} - \frac{\Sigma(x)}{\mathcal{F}(x)} \right].
\end{aligned} \tag{9.9}$$

9.2.1 Improper cancellation of quadratic divergences

When solving this system of coupled integral equations with the method described in Chapter 8.3 we encounter some serious new problems. Although the solution of Eqs. (9.6, 9.7) does not seem to suffer by the introduction of the Ball-Chiu vertex, the behaviour of the photon equation, Eq. (9.8), however, is somehow erratic. This can be seen in Fig. 9.6 where we plotted the behaviour of $\mathcal{G}(x)$ for $\alpha = 1.921$ with realistic input functions $\Sigma(x)$, $\mathcal{F}(x)$.

To investigate the numerical cancellation of the quadratic divergence we plot the vacuum polarization function $\Pi(x)$ of Eq. (9.8) in Fig. 9.7. From the 1-loop perturbative results for the vacuum polarization we expect the vacuum polarization to be roughly of the order of:

$$\Pi(0) \simeq \frac{N_f\alpha}{3\pi} \ln \frac{\Lambda^2}{\Sigma^2(0)} \approx 2.8 \tag{9.10}$$

for $\alpha = 1.921$, $\Lambda = 1e5$ and $\Sigma(0) = 100$. The very large values of the vacuum polarization at small values of x , in Fig. 9.7, clearly show that the quadratic divergence has not been cancelled correctly. There seems to be a residual linear divergence in the numerical solution. To examine this in more detail, we will investigate the radial integrand, $K_R(x, y)$, of $\Pi(x)$ for small values of x . We can write the vacuum polarization integral of Eq. (9.8) as:

$$\Pi(x) = \int dt K_R(x, y) \tag{9.11}$$

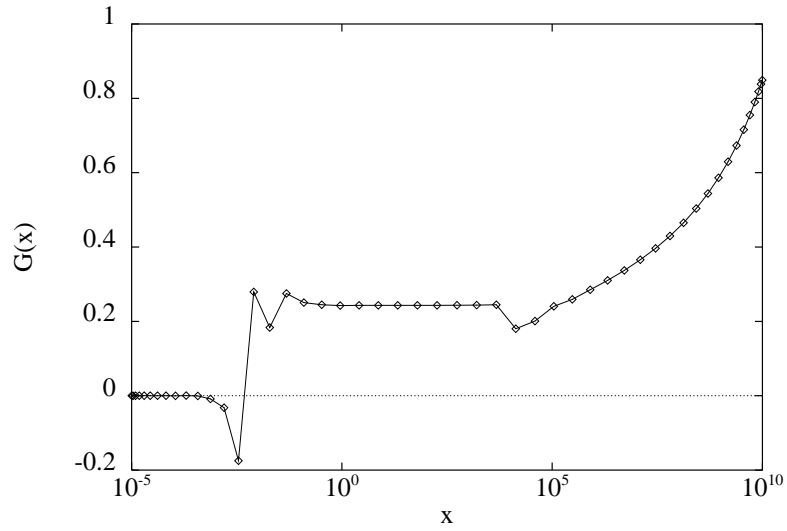


Figure 9.6: Photon renormalization function $\mathcal{G}(x)$ versus momentum squared x from the \mathcal{G} -equation with Ball-Chiu vertex, for $\alpha = 1.921$ and $N_f = 1$.

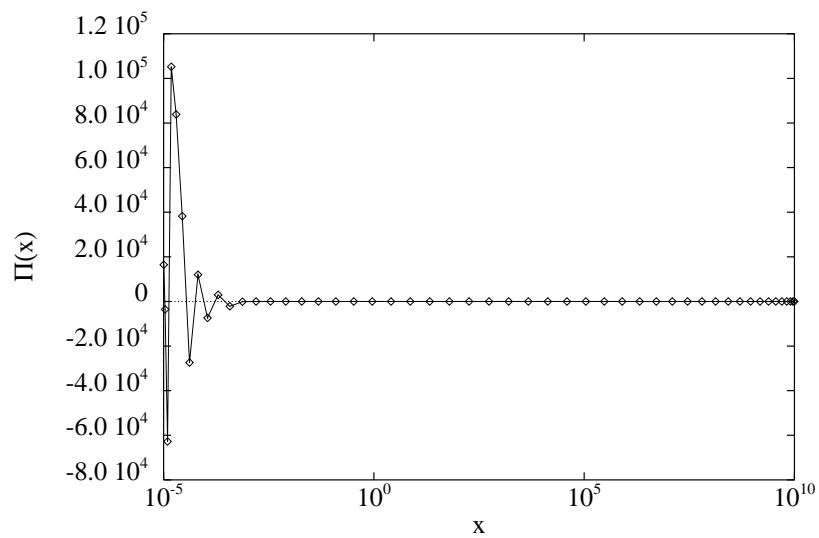


Figure 9.7: Vacuum polarization $\Pi(x)$ versus momentum squared x from the \mathcal{G} -equation with Ball-Chiu vertex, for $\alpha = 1.921$ and $N_f = 1$.

where $t = \log_{10} y$ and the radial integrand $K_R(x, y)$ is defined by:

$$K_R(x, y) = \int d\theta K_\theta(x, y, \theta). \quad (9.12)$$

In Eq. (9.12), the angular integrand $K_\theta(x, y, \theta)$ is given by:

$$K_\theta(x, y, \theta) = \rho(x, y) f_\theta(x, y, \theta). \quad (9.13)$$

where the multiplicative factor $\rho(x, y)$, independent from θ , is:

$$\rho(x, y) = \frac{2N_f \alpha \ln 10}{3\pi^2 x} \frac{y^2 \mathcal{F}(y)}{y + \Sigma^2(y)} \quad (9.14)$$

and the angular function f_θ from is defined as:

$$\begin{aligned} f_\theta(x, y, \theta) = \sin^2 \theta \frac{\mathcal{F}(z)}{z + \Sigma^2(z)} & \left\{ 2A(y, z) \left[y(1 - 4 \cos^2 \theta) + 3\sqrt{yx} \cos \theta \right] \right. \\ & + B(y, z) \left[\left(y + z - 2\Sigma(y)\Sigma(z) \right) \left(2y(1 - 4 \cos^2 \theta) + 3\sqrt{yx} \cos \theta \right) + 3(y - z) \left(y - \Sigma(y)\Sigma(z) \right) \right] \\ & \left. - C(y, z) \left[\left(\Sigma(y) + \Sigma(z) \right) \left(2y(1 - 4 \cos^2 \theta) + 3\sqrt{yx} \cos \theta \right) + 3(y - z)\Sigma(y) \right] \right\} \end{aligned} \quad (9.15)$$

with $z = y + x - 2\sqrt{yx} \cos \theta$.

In Fig. 9.8 we plot the radial integrand $K_R(x_0, y)$, where $x_0 = 1.00856e-05$ is the smallest external momentum value used in the numerical solution of Eqs. (9.6, 9.7, 9.8). There, the integral value is $\Pi(x_0) = 16471.3$. This much too large value seems to be caused by the chaotic behaviour of the radial integrand for large values of momentum. We will, therefore, investigate where this behaviour originates from and examine $K_R(x_0, y)$ in more detail for large values of radial momentum y . For $y_N = 9.96568e+09$, which is the largest radial integration point for the external momentum x_0 , the radial integrand $K_R(x_0, y_N) = -1.82932e+06$.

We now look at the behaviour of the angular integrand $K_\theta(x_0, y_N, \theta)$ where $x_0 = 1.00856e-05$ and $y_N = 9.96568e+09$. We note from Eqs. (9.13, 9.14) that, for such small values of x and large values of y , accuracy problems in the angular function f_θ are magnified enormously, here by a factor $\rho(x_0, y_N) \approx 3e+14$. We plot the angular integrand $K_\theta(x_0, y_N, \theta)$ versus θ in Fig. 9.9.

For the quadratic divergence to cancel, the vacuum polarization integral must satisfy:

$$\lim_{x \rightarrow 0} x \Pi(x) = 0. \quad (9.16)$$

The cancellation of the quadratic divergence occurs if the terms proportional to $1/x$ in the angular integrand, Eq. (9.13), vanish as a result of the angular integrals being equal to zero

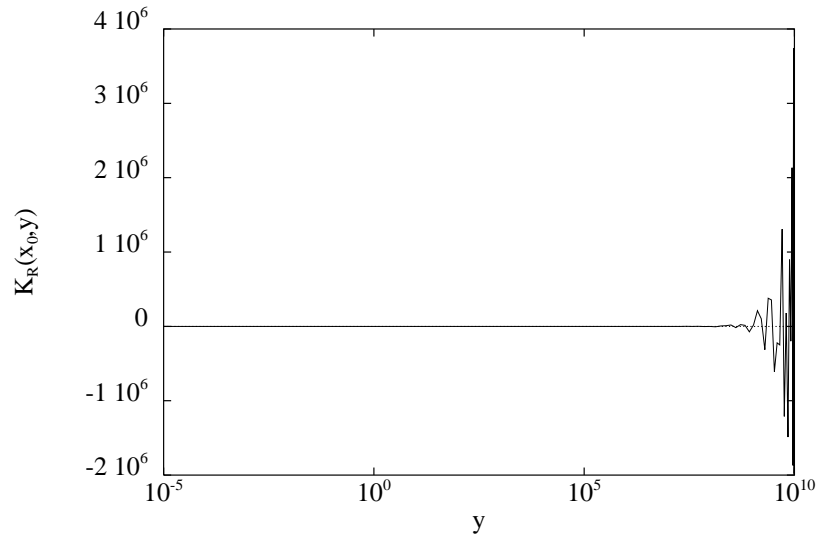


Figure 9.8: Radial integrand $K_R(x_0, y)$, where $x_0 = 1.00856e-05$, versus radial momentum squared y from the \mathcal{G} -equation with Ball-Chiu vertex, for $\alpha = 1.921$ and $N_f = 1$.

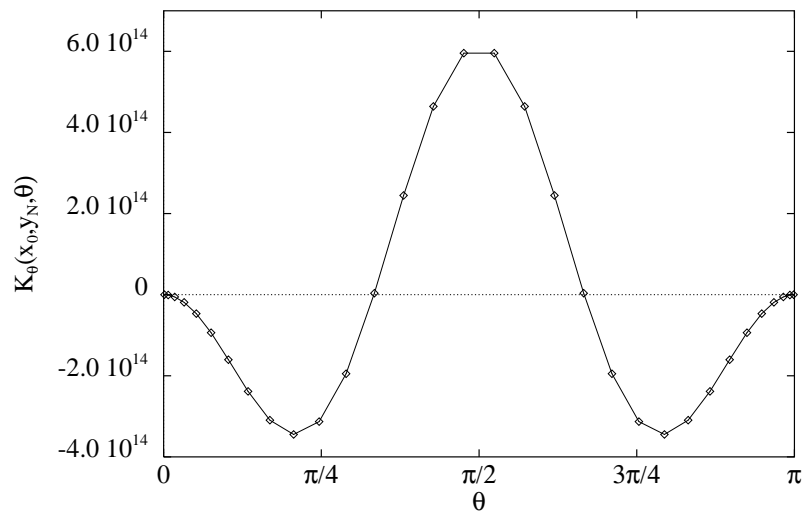


Figure 9.9: Angular integrand $K_\theta(x_0, y_N, \theta)$ for $x_0 = 1.00856e-05$, $y_N = 9.96568e+09$, versus angle θ from the \mathcal{G} -equation with Ball-Chiu vertex, for $\alpha = 1.921$ and $N_f = 1$.

when $x \rightarrow 0$. To investigate if this is achieved numerically, we rewrite the angular function f_θ , Eq. (9.15), as a sum of angular functions which all give individual contributions to the vacuum polarization that are theoretically free of quadratic divergences:

$$f_\theta = \sin^2 \theta (I_A + J_A + I_B + J_B + I_C + J_C) , \quad (9.17)$$

where

$$\begin{aligned} I_A(x, y, \theta) &= \frac{2A(y, z)y\mathcal{F}(z)}{z + \Sigma^2(z)} (1 - 4 \cos^2 \theta) \\ J_A(x, y, \theta) &= \frac{6A(y, z)\mathcal{F}(z)}{z + \Sigma^2(z)} \sqrt{yx} \cos \theta \\ I_B(x, y, \theta) &= \frac{2yB(y, z)\mathcal{F}(z)}{z + \Sigma^2(z)} (y + z - 2\Sigma(y)\Sigma(z)) (1 - 4 \cos^2 \theta) \\ J_B(x, y, \theta) &= \frac{3B(y, z)\mathcal{F}(z)}{z + \Sigma^2(z)} \left[(y + z - 2\Sigma(y)\Sigma(z)) \sqrt{yx} \cos \theta + (y - z)(y - \Sigma(y)\Sigma(z)) \right] \\ I_C(x, y, \theta) &= -\frac{2yC(y, z)\mathcal{F}(z)}{z + \Sigma^2(z)} (\Sigma(y) + \Sigma(z)) (1 - 4 \cos^2 \theta) \\ J_C(x, y, \theta) &= -\frac{C(y, z)\mathcal{F}(z)}{z + \Sigma^2(z)} \left[(\Sigma(y) + \Sigma(z)) 3\sqrt{yx} \cos \theta + 3(y - z)\Sigma(y) \right] . \end{aligned} \quad (9.18)$$

We define the angular integrands $K_{\theta,i}$, $i = 1, \dots, 6$, as:

$$\begin{aligned} K_{\theta,1}(x, y, \theta) &= \rho(x, y) \sin^2 \theta I_A(x, y, \theta) \\ K_{\theta,2}(x, y, \theta) &= \rho(x, y) \sin^2 \theta J_A(x, y, \theta) \\ K_{\theta,3}(x, y, \theta) &= \rho(x, y) \sin^2 \theta I_B(x, y, \theta) \\ K_{\theta,4}(x, y, \theta) &= \rho(x, y) \sin^2 \theta J_B(x, y, \theta) \\ K_{\theta,5}(x, y, \theta) &= \rho(x, y) \sin^2 \theta I_C(x, y, \theta) \\ K_{\theta,6}(x, y, \theta) &= \rho(x, y) \sin^2 \theta J_C(x, y, \theta) \end{aligned} \quad (9.19)$$

and the radial integrands $K_{R,i}$, after angular integration of Eq. (9.19), as:

$$K_{R,i}(x, y) = \int d\theta K_{\theta,i}(x, y, \theta) \quad , \quad i = 1, \dots, 6 . \quad (9.20)$$

The total radial kernel K_R is given by:

$$K_R = K_{R,1} + K_{R,2} + K_{R,3} + K_{R,4} + K_{R,5} + K_{R,6} . \quad (9.21)$$

Although the analytical cancellation of the quadratic divergence for $x \rightarrow 0$ is obvious, this is not ensured to happen numerically. We tabulate the computed values of the individual radial

| | |
|-----------|--------------|
| $K_{R,1}$ | 4.61709e+00 |
| $K_{R,2}$ | 1.44340e+00 |
| $K_{R,3}$ | -1.82932e+06 |
| $K_{R,4}$ | 7.64711e-02 |
| $K_{R,5}$ | -2.35535e-02 |
| $K_{R,6}$ | -3.40508e-09 |

Table 9.1: Radial kernels $K_{R,i}(x_0, y_N)$, for $i = 1, \dots, 6$, with $x_0 = 1.00856e-05$ and $y_N = 9.96568e+09$.

kernels, $K_{R,i}(x_0, y_N)$, with $x_0 = 1.00856e-05$ and $y_N = 9.96568e+09$ in Table 9.1. The main contribution to the radial integrand comes from $K_{R,3}$.

Plots of the various angular integrands $K_{\theta,i}(x_0, y_N, \theta)$, Eq. (9.19), are shown in Fig. 9.10. From this figure nothing suspicious can be detected. This is understandable, from Table 9.1, as the main contribution to the radial integrand comes from $K_{R,3}$ and is of $\mathcal{O}(1e6)$, while the angular integrand $K_{\theta,3}$ has a magnitude of $\mathcal{O}(1e13)$. The problem seems to be hidden as an undiscernible noise in the much larger smooth envelope of the angular integrand.

9.2.2 Small- x expansion of angular functions

To investigate the cancellation of quadratic and linear divergences we need the terms of $K_{\theta,i}$ which are proportional to $1/x$ and $1/\sqrt{x}$. Because of Eq. (9.19) and the $1/x$ -proportionality of $\rho(x, y)$, this corresponds to expanding the angular functions, Eq. (9.18), up to constant terms for the quadratic divergent contributions and to \sqrt{x} for the linear divergent contributions. Therefore we look how the various angular functions, Eq. (9.18), depend on x or $(z - y) = x - 2\sqrt{xy} \cos \theta$ for small x .

To Taylor expand the angular functions, Eq. (9.18), we first Taylor expand their various components up to $\mathcal{O}(z - y)$:

$$\mathcal{F}(z) = \mathcal{F}(y) + (z - y)\mathcal{F}'(y) + \mathcal{O}(z - y)^2 \quad (9.22)$$

$$\Sigma(z) = \Sigma(y) + (z - y)\Sigma'(y) + \mathcal{O}(z - y)^2 \quad (9.23)$$

$$\frac{1}{z + \Sigma^2(z)} = \frac{1}{y + \Sigma^2(y)} - (z - y) \left[\frac{1 + 2\Sigma(y)\Sigma'(y)}{(y + \Sigma^2(y))^2} \right] + \mathcal{O}(z - y)^2 \quad (9.24)$$

$$A(y, z) = \frac{1}{2} \left[\frac{1}{\mathcal{F}(z)} + \frac{1}{\mathcal{F}(y)} \right]$$

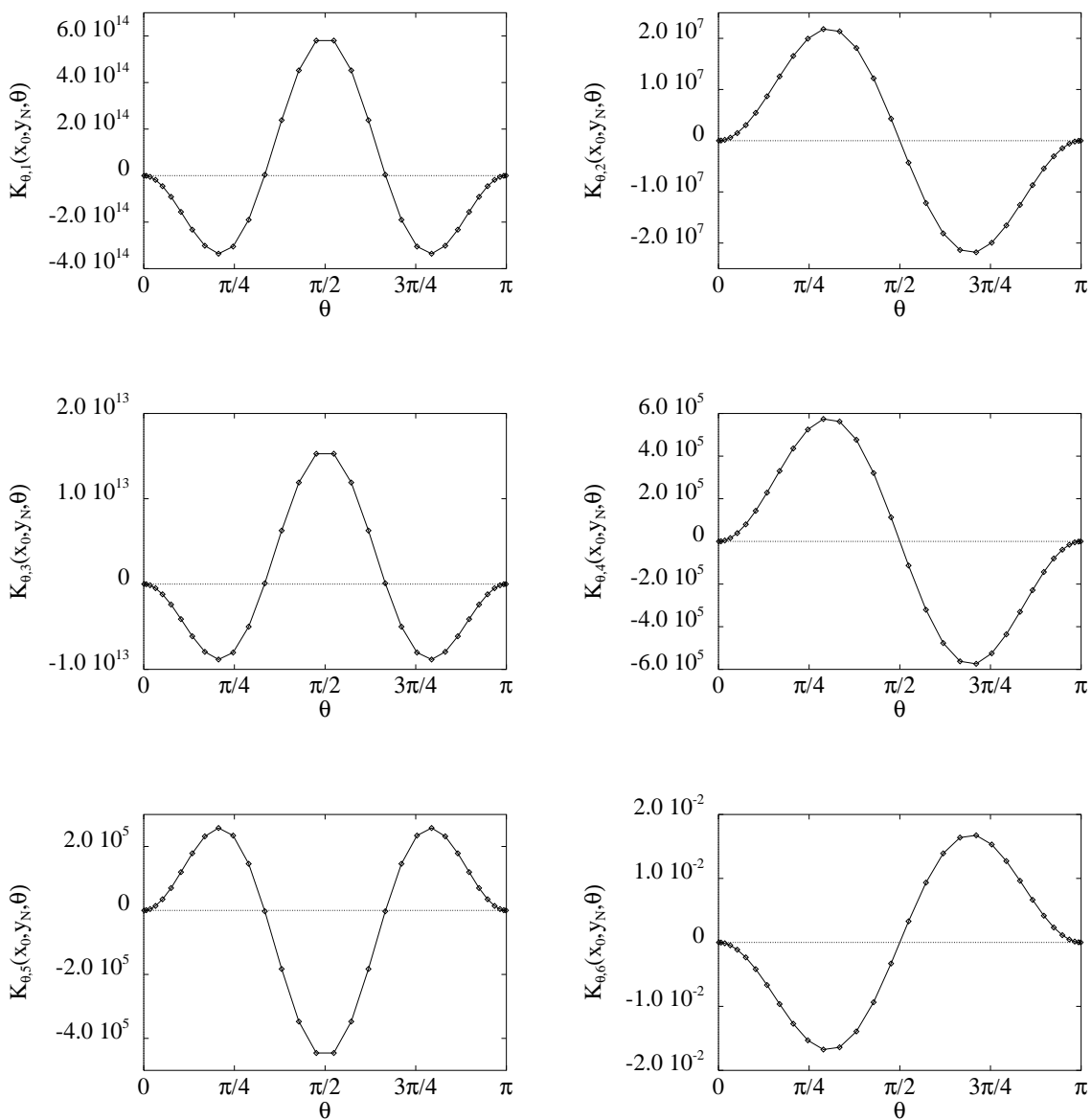


Figure 9.10: Angular integrands $K_{\theta,i}(x_0, y_N, \theta)$, for $i = 1, \dots, 6$, with $x_0 = 1.00856e-05$, $y_N = 9.96568e+09$, versus angle θ from the \mathcal{G} -equation with Ball-Chiu vertex, for $\alpha = 1.921$ and $N_f = 1$.

$$\begin{aligned}
&= \frac{1}{2} \left\{ \frac{1}{\mathcal{F}(y)} + (z-y) \left[\frac{1}{\mathcal{F}(y)} \right]' + \mathcal{O}(z-y)^2 + \frac{1}{\mathcal{F}(y)} \right\} \\
&= \frac{1}{\mathcal{F}(y)} + \frac{z-y}{2} \left[\frac{1}{\mathcal{F}(y)} \right]' + \mathcal{O}(z-y)^2
\end{aligned} \tag{9.25}$$

$$\begin{aligned}
B(y, z) &= \frac{1}{2(z-y)} \left[\frac{1}{\mathcal{F}(z)} - \frac{1}{\mathcal{F}(y)} \right] \\
&= \frac{1}{2(z-y)} \left\{ \frac{1}{\mathcal{F}(y)} + (z-y) \left[\frac{1}{\mathcal{F}(y)} \right]' + \frac{(z-y)^2}{2} \left[\frac{1}{\mathcal{F}(y)} \right]'' + \mathcal{O}(z-y)^3 - \frac{1}{\mathcal{F}(y)} \right\} \\
&= \frac{1}{2} \left[\frac{1}{\mathcal{F}(y)} \right]' + \frac{(z-y)}{4} \left[\frac{1}{\mathcal{F}(y)} \right]'' + \mathcal{O}(z-y)^2
\end{aligned} \tag{9.26}$$

$$\begin{aligned}
C(y, z) &= -\frac{1}{z-y} \left[\frac{\Sigma(z)}{\mathcal{F}(z)} - \frac{\Sigma(y)}{\mathcal{F}(y)} \right] \\
&= -\frac{1}{z-y} \left\{ \frac{\Sigma(y)}{\mathcal{F}(y)} + (z-y) \left[\frac{\Sigma(y)}{\mathcal{F}(y)} \right]' + \frac{(z-y)^2}{2} \left[\frac{\Sigma(y)}{\mathcal{F}(y)} \right]'' + \mathcal{O}(z-y)^3 - \frac{\Sigma(y)}{\mathcal{F}(y)} \right\} \\
&= -\left[\frac{\Sigma(y)}{\mathcal{F}(y)} \right]' - \frac{z-y}{2} \left[\frac{\Sigma(y)}{\mathcal{F}(y)} \right]'' + \mathcal{O}(z-y)^2.
\end{aligned} \tag{9.27}$$

Substituting Eqs. (9.22-9.27) in the angular functions, Eq. (9.18), and gathering together terms of equal power in $(z-y)$ yields:

$$\begin{aligned}
I_A(x, y, \theta) &= \frac{2y}{y + \Sigma^2(y)} (1 - 4 \cos^2 \theta) \\
&+ 2y(z-y)(1 - 4 \cos^2 \theta) \left\{ \frac{1}{2} \frac{\mathcal{F}'(y)}{\mathcal{F}(y)} \frac{1}{y + \Sigma^2(y)} - \frac{1 + 2\Sigma(y)\Sigma'(y)}{(y + \Sigma^2(y))^2} \right\} + \mathcal{O}(z-y)^2
\end{aligned} \tag{9.28}$$

$$\begin{aligned}
I_B(x, y, \theta) &= \frac{2y(y - \Sigma^2(y))\mathcal{F}(y)}{y + \Sigma^2(y)} \left[\frac{1}{\mathcal{F}(y)} \right]' (1 - 4 \cos^2 \theta) \\
&+ 2y(z-y)(1 - 4 \cos^2 \theta) \left\{ \frac{1}{2} \frac{(y - \Sigma^2(y))\mathcal{F}(y)}{y + \Sigma^2(y)} \left[\frac{1}{\mathcal{F}(y)} \right]'' \right. \\
&\quad + \frac{(y - \Sigma^2(y))\mathcal{F}'(y)}{y + \Sigma^2(y)} \left[\frac{1}{\mathcal{F}(y)} \right]' \\
&\quad - \left[\frac{\mathcal{F}(y)(y - \Sigma^2(y))(1 + 2\Sigma(y)\Sigma'(y))}{(y + \Sigma^2(y))^2} \right] \left[\frac{1}{\mathcal{F}(y)} \right]' \\
&\quad \left. + \frac{1}{2} \frac{\mathcal{F}(y)(1 - 2\Sigma(y)\Sigma'(y))}{y + \Sigma^2(y)} \left[\frac{1}{\mathcal{F}(y)} \right]' \right\} + \mathcal{O}(z-y)^2
\end{aligned} \tag{9.29}$$

$$\begin{aligned}
I_C(x, y, \theta) &= \frac{4y\mathcal{F}(y)\Sigma(y)}{y + \Sigma^2(y)} \left[\frac{\Sigma(y)}{\mathcal{F}(y)} \right]' (1 - 4 \cos^2 \theta) \\
&+ 2y(z-y)(1 - 4 \cos^2 \theta) \left\{ \frac{\mathcal{F}(y)\Sigma(y)}{y + \Sigma^2(y)} \left[\frac{\Sigma(y)}{\mathcal{F}(y)} \right]'' + \frac{2\mathcal{F}'(y)\Sigma(y)}{y + \Sigma^2(y)} \left[\frac{\Sigma(y)}{\mathcal{F}(y)} \right]' \right\}
\end{aligned} \tag{9.30}$$

$$-\frac{2\mathcal{F}(y)\Sigma(y)(1+2\Sigma(y)\Sigma'(y))}{y+\Sigma^2(y)}\left[\frac{\Sigma(y)}{\mathcal{F}(y)}\right]'+\frac{\mathcal{F}(y)\Sigma'(y)}{y+\Sigma^2(y)}\left[\frac{\Sigma(y)}{\mathcal{F}(y)}\right]'\Big\}+\mathcal{O}(z-y)^2.$$

Because of the structure of the integrands J_A , J_B , J_C , these have no potentially quadratic divergent terms. However there can be some remnant linear divergent bits, which are proportional to \sqrt{x} . To separate these, we only need the first term in the Taylor expansions of the various components. This gives:

$$J_A(x, y, \theta) = \frac{6\sqrt{yx}\cos\theta}{y+\Sigma^2(y)} + \mathcal{O}(x) \quad (9.31)$$

$$J_B(x, y, \theta) = \frac{3}{2}\left[\frac{1}{\mathcal{F}(y)}\right]'\frac{\mathcal{F}(y)}{y+\Sigma^2(y)}(4\sqrt{yx}\cos\theta-x)(y-\Sigma^2(y)) + \mathcal{O}(x) \quad (9.32)$$

$$J_C(x, y, \theta) = \left[\frac{\Sigma(y)}{\mathcal{F}(y)}\right]'\frac{3\mathcal{F}(y)}{y+\Sigma^2(y)}\left[2\Sigma(y)\sqrt{yx}\cos\theta+(y-z)\Sigma(y)\right] + \mathcal{O}(x). \quad (9.33)$$

It is enlightening to study the behaviour of $K_{\theta,3}(x_0, y_N, \theta)$ in more detail. In Fig. 9.10 we see the nice trigonometric behaviour of the angular kernel as predicted from Eqs. (9.19, 9.29). We now show another plot in Fig. 9.11, where we divide $K_{R,3}(x_0, y_N, \theta)$ by its trigonometric factor $\sin^2\theta(1-4\cos^2\theta)$. As expected from the first term of the Taylor expansion of I_B , Eq. (9.29), the leading order term of the plotted function is now constant in θ . Furthermore, because the integral over θ of the trigonometric part of the leading order term of $K_{R,3}(x_0, y_N)$ vanishes, there is no quadratic divergent contribution to it.

9.2.3 Subtracting the leading order term

To verify that the quadratic divergence is cancelled correctly numerically and that the remaining result is meaningful we now subtract explicitly the value of the angular integrand when $x \rightarrow 0$, i.e. when $z \rightarrow y$. We define:

$$\tilde{K}_\theta(x, y, \theta) = \frac{1}{x}\left[xK_\theta(x, y, \theta) - \lim_{x \rightarrow 0} xK_\theta(x, y, \theta)\right]. \quad (9.34)$$

Formally this should not change the value of the angular integral,

$$K_R(x, y) = \int d\theta K_\theta(x, y, \theta) = \int d\theta \tilde{K}_\theta(x, y, \theta) \quad (9.35)$$

as we can show analytically that:

$$\int d\theta \left[\lim_{x \rightarrow 0} xK_\theta(x, y, \theta)\right] = 0. \quad (9.36)$$

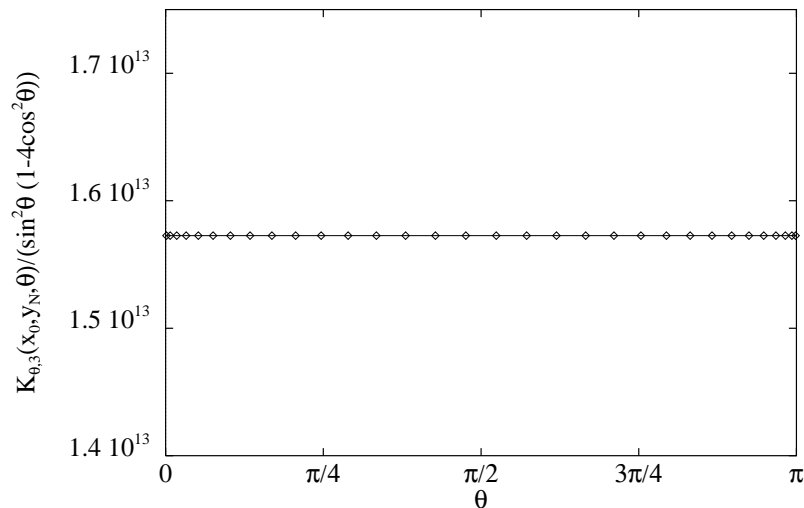


Figure 9.11: Angular integrand $K_{\theta,3}(x_0, y_N, \theta)$ for $x_0 = 1.00856e-05$, $y_N = 9.96568e+09$, versus angle θ from the \mathcal{G} -equation with Ball-Chiu vertex, for $\alpha = 1.921$ and $N_f = 1$ after removing the trigonometric factor $\sin^2 \theta (1 - 4 \cos^2 \theta)$.

Because of the $1/x$ factor in $\rho(x, y)$, Eq. (9.34) corresponds to the subtraction of the terms without any x -dependency in the angular functions $I_A, I_B, I_C, J_A, J_B, J_C$. These are exactly the leading order terms of I_A, I_B and I_C in Eqs. (9.28, 9.29, 9.30), which we will respectively call I_A^0, I_B^0, I_C^0 and are given by:

$$I_A^0(x, y, \theta) = \frac{2y}{y + \Sigma^2(y)} (1 - 4 \cos^2 \theta) \quad (9.37)$$

$$I_B^0(x, y, \theta) = \frac{2y(y - \Sigma^2(y))\mathcal{F}(y)}{y + \Sigma^2(y)} \left[\frac{1}{\mathcal{F}(y)} \right]' (1 - 4 \cos^2 \theta) \quad (9.38)$$

$$I_C^0(x, y, \theta) = \frac{4y\mathcal{F}(y)\Sigma(y)}{y + \Sigma^2(y)} \left[\frac{\Sigma(y)}{\mathcal{F}(y)} \right]' (1 - 4 \cos^2 \theta). \quad (9.39)$$

By subtracting the leading order term, which should vanish anyway after angular integration, we want to explore what happens to the next order in the small- x expansions of I_A, I_B and I_C , Eqs. (9.28, 9.29, 9.30). As there are no potentially quadratic divergences in J_A, J_B, J_C , we do not subtract any contribution from these kernels.

To compute I_B^0 and I_C^0 numerically, we need to take the derivatives of the functions \mathcal{F} and Σ , which are defined as Chebyshev expansions. Consider the Chebyshev expansion of a function

$f(x)$:

$$f(x) = \sum_{j=0}^{N-1} c_j T_j(x) - \frac{c_0}{2}, \quad (9.40)$$

then, its derivative with respect to x is again a Chebyshev expansion:

$$f'(x) = \sum_{j=0}^{N-1} c'_j T_j(x) - \frac{c'_0}{2}, \quad (9.41)$$

where the coefficients c'_j are defined by:

$$c'_{j-1} = c'_{j+1} + 2j c_j, \quad j = N-1, \dots, 1, \quad (9.42)$$

with $c'_N = c'_{N-1} = 0$.

As we expand the functions $\Sigma(x)$, $\mathcal{F}(x)$ and $\mathcal{G}(x)$ in Chebyshev polynomials of $s(x)$, Eq. (7.30), instead of x , the expansion Eq. (9.40) now becomes:

$$g(x) = f(s(x)) = \sum_{j=0}^{N-1} c_j T_j(s(x)) - \frac{c_0}{2} \quad (9.43)$$

where:

$$s(x) = \frac{\log_{10}(x/\Lambda\kappa)}{\log_{10}(\Lambda/\kappa)}. \quad (9.44)$$

and the derivative is now:

$$g'(x) = \frac{dg(x)}{dx} = \frac{ds(x)}{dx} \frac{df(s(x))}{ds} = \frac{f'(s)}{x \ln 10 \log_{10}(\Lambda/\kappa)} \quad (9.45)$$

where $f'(s)$ is defined by Eqs. (9.41, 9.42).

Explicitly cancelling these lowest order terms in Eq. (9.19) will yield the following angular kernels:

$$\begin{aligned} K_{\theta,1}(x, y, \theta) &= \rho(x, y) \sin^2 \theta (I_A - I_A^0) \\ K_{\theta,2}(x, y, \theta) &= \rho(x, y) \sin^2 \theta J_A \\ K_{\theta,3}(x, y, \theta) &= \rho(x, y) \sin^2 \theta (I_B - I_B^0) \\ K_{\theta,4}(x, y, \theta) &= \rho(x, y) \sin^2 \theta J_B \\ K_{\theta,5}(x, y, \theta) &= \rho(x, y) \sin^2 \theta (I_C - I_C^0) \\ K_{\theta,6}(x, y, \theta) &= \rho(x, y) \sin^2 \theta J_C . \end{aligned}$$

| | |
|-----------|----------------|
| $K_{R,1}$ | $-9.45396e-01$ |
| $K_{R,2}$ | $1.44340e+00$ |
| $K_{R,3}$ | $-1.82932e+06$ |
| $K_{R,4}$ | $7.64711e-02$ |
| $K_{R,5}$ | $-2.35535e-02$ |
| $K_{R,6}$ | $-3.40508e-09$ |

Table 9.2: Radial kernels $K_{R,i}(x_0, y_N)$, for $i = 1, \dots, 6$, with $x_0 = 1.00856e-05$ and $y_N = 9.96568e+09$ with explicit cancellation of the quadratic divergence.

After this cancellation we see that the total radial kernel $K_R(x_0, y_N)$, after angular integration is still $K_R(x_0, y_N) = -1.82932e+06$ and the individual radial kernels $K_{R,i}(x_0, y_N)$, for $i = 1, \dots, 6$, are given in Table 9.2.

Although the value of the radial integrands, $K_{R,i}(x_0, y_N)$, shown in Table 9.2 have not changed much compared to those of Table 9.1, the magnitude of the angular integrands, has been reduced as can be seen in Fig. 9.12 for the total angular integrand $K_\theta(x_0, y_N, \theta)$ and in Fig. 9.13 for the partial ones, $K_{\theta,i}(x_0, y_N, \theta)$. However the expected reduction factor of the $\mathcal{O}(\Lambda/\sqrt{x_0})$ has not been achieved for $K_{\theta,3}$ and $K_{\theta,5}$.

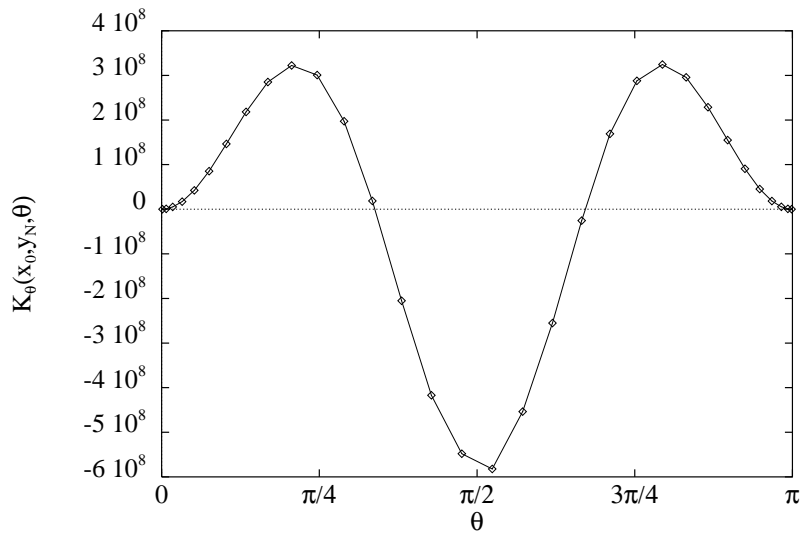


Figure 9.12: Angular integrand $K_\theta(x_0, y_N, \theta)$ for $x_0 = 1.00856e-05$, $y_N = 9.96568e+09$, versus angle θ from the \mathcal{G} -equation with Ball-Chiu vertex, for $\alpha = 1.921$ and $N_f = 1$ with the explicit cancellation of the quadratic divergence.

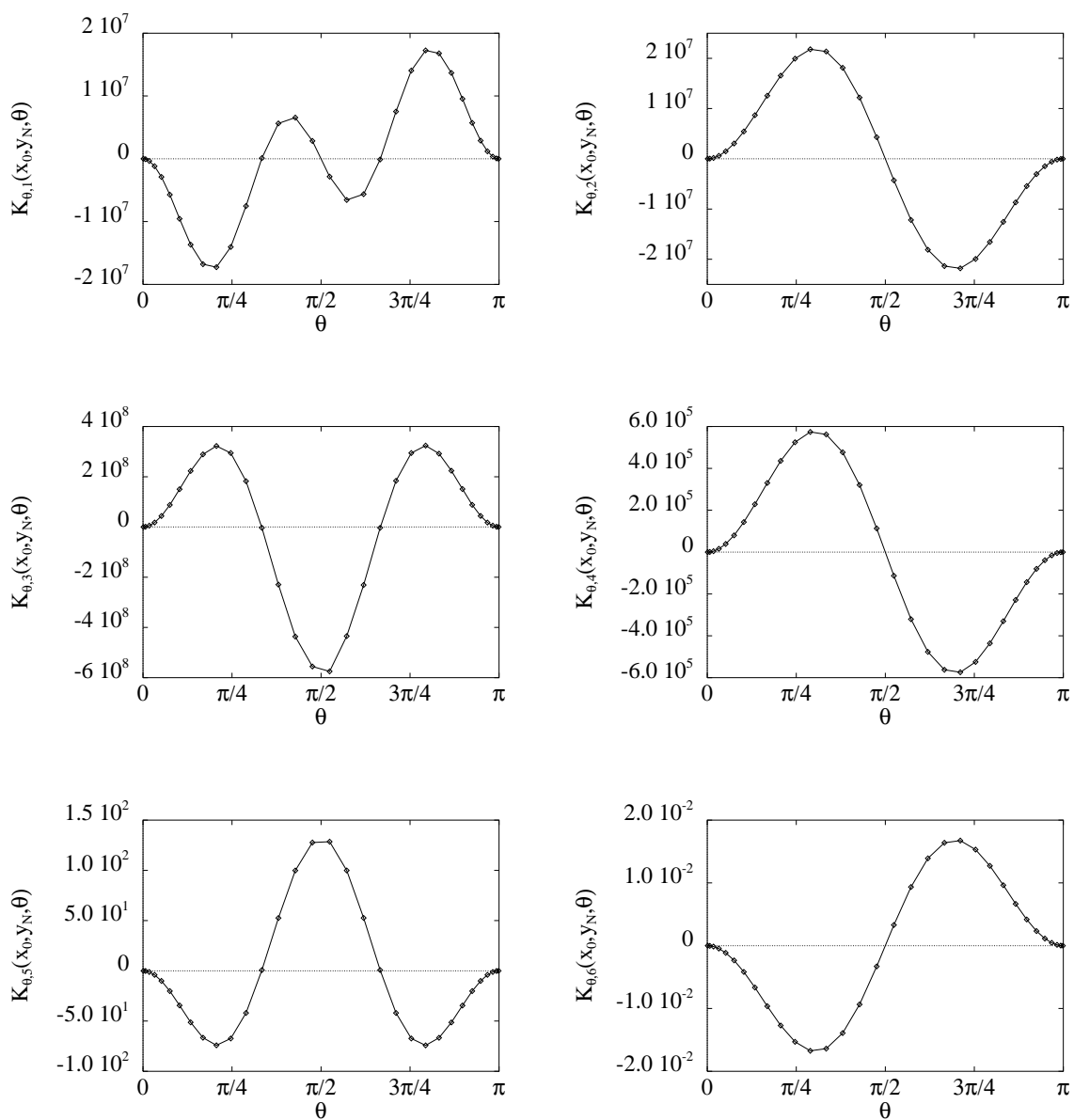


Figure 9.13: Angular integrands $K_{\theta,i}(x_0, y_N, \theta)$, for $i = 1, \dots, 6$, with $x_0 = 1.00856e-05$, $y_N = 9.96568e+09$, versus angle θ from the \mathcal{G} -equation with Ball-Chiu vertex, for $\alpha = 1.921$ and $N_f = 1$ with the explicit cancellation of the quadratic divergence.

From Fig. 9.10 we saw that, to leading order in x , the angular kernels had the correct trigonometric behaviour. However, from Fig. 9.13, it seems that, although $K_{\theta,1}$ seems fine, $K_{\theta,3}$ and $K_{\theta,5}$ do not have the right next-to-leading order behaviour predicted by the expansions, Eqs. (9.29, 9.30), which should be proportional to $\sin^2 \theta(1 - 4 \cos^2 \theta) \cos \theta$. To emphasize this we show in Fig. 9.14 the behaviour of $K_{\theta,3}(x, y, \theta)$ when we remove the $\sin^2 \theta(1 - 4 \cos^2 \theta)$ trigonometric part. Then, we expect the next-to-leading order term to behave as $\cos \theta$. From Fig. 9.14 it is clear that this is not so and that this part of the angular kernel is varying erratically between $-5.95\text{e}+08$ and $-5.7\text{e}+08$.

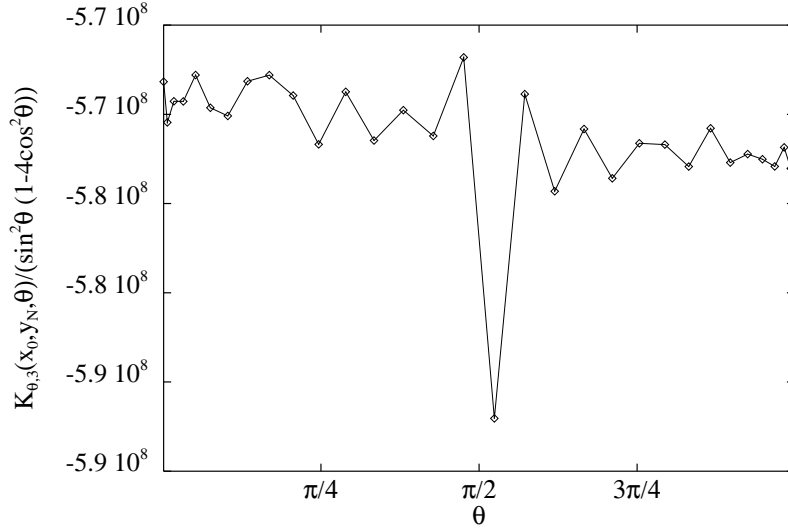


Figure 9.14: Angular integrand $K_{\theta,3}(x_0, y_N, \theta)$ for $x_0 = 1.00856\text{e}-05$, $y_N = 9.96568\text{e}+09$, versus angle θ from the \mathcal{G} -equation with Ball-Chiu vertex, for $\alpha = 1.921$ and $N_f = 1$ after removing the trigonometric factor $\sin^2 \theta(1 - 4 \cos^2 \theta)$.

These results indicate that, for some reason as yet unknown, the numerical accuracy of the \sqrt{x} -term in I_B is not very good. However we need to get this right because these terms will generate a linear divergence in the vacuum polarization, unless their angular integrals vanish to a high degree of precision. From the derivation of the Taylor expansion of I_B , Eq. (9.29), we see that the next-to-leading order term of I_B is achieved by combining the next-to-leading order terms of its various components with the leading order terms, except for $B(y, z)$, for which we need the next-to-next-to-leading order term of the $1/\mathcal{F}(z)$ expansion as shown in Eq. (9.26). Of

course in the numerical program $B(y, z)$ will be computed from:

$$B(y, z) = \frac{1}{2(z-y)} \left[\frac{1}{\mathcal{F}(z)} - \frac{1}{\mathcal{F}(y)} \right]. \quad (9.46)$$

Let us write the Taylor expansion of $1/\mathcal{F}(z)$:

$$\frac{1}{\mathcal{F}(z)} = \frac{1}{\mathcal{F}(y)} + (z-y) \left[\frac{1}{\mathcal{F}(y)} \right]' + \frac{(z-y)^2}{2} \left[\frac{1}{\mathcal{F}(y)} \right]'' + \mathcal{O}(z-y)^3. \quad (9.47)$$

Because of the $(z-y)$ denominator of $B(y, z)$, the third term in $1/\mathcal{F}(z)$ will also contribute to the $(z-y)$ -term in the expansion of $B(y, z)$. However, for small values of x , subsequent terms in the Taylor expansion will decrease by a factor of $\mathcal{O}(\sqrt{x/y})$, which in our case is of $\mathcal{O}(3e7)$. As double precision arithmetic is accurate to about 16 digits, this means that the $(z-y)^2$ contribution of Eq. (9.47) will not be accurate in the numerical evaluation of $1/\mathcal{F}(z)$, and thus, the next-to-leading order $(z-y)$ -term of $B(y, z)$ from Eq. (9.26) will not behave as it should do. The problem is similar for $C(y, z)$.

We will now construct a method to get $B(y, z)$ and $C(y, z)$ with sufficient accuracy by directly evaluating these quantities and cancelling the leading constant term $1/\mathcal{F}(y)$ and $\Sigma(y)/\mathcal{F}(y)$ of their expansions explicitly .

9.2.4 Recurrence formula for difference of Chebyshev expansions

Assume that $f(y)$ is a Chebyshev expansion and we want to compute the difference

$$\begin{aligned} \Delta f &\equiv f(z) - f(y) \\ &= \left[\sum_{j=0}^{N-1} c_j T_j(z) - \frac{c_0}{2} \right] - \left[\sum_{j=0}^{N-1} c_j T_j(y) - \frac{c_0}{2} \right] \\ &= \sum_{j=0}^{N-1} c_j [T_j(z) - T_j(y)] . \end{aligned}$$

From *Clenshaw's* formula, Eq. (7.19), to compute the value of a Chebyshev expansion, we now derive another, original, recurrence formula for the difference of two Chebyshev expansions. Subtracting Eq. (7.19) at two arbitrary points, yields:

$$\begin{aligned} f(z) - f(y) &= \left[zd_1(z) - d_2(z) + \frac{c_0}{2} \right] - \left[yd_1(y) - d_2(y) + \frac{c_0}{2} \right] \\ &= zd_1(z) - yd_1(y) - (d_2(z) - d_2(y)) \end{aligned} \quad (9.48)$$

and

$$\begin{aligned}
d_j(z) - d_j(y) &= [2zd_{j+1}(z) - d_{j+2}(z) + c_j] - [2yd_{j+1}(y) - d_{j+2}(y) + c_j] \\
&= 2(zd_{j+1}(z) - yd_{j+1}(y)) - (d_{j+2}(z) - d_{j+2}(y)).
\end{aligned} \tag{9.49}$$

From Eq. (9.49) it seems logical to look for a recurrence formula for:

$$\begin{aligned}
zd_j(z) - yd_j(y) &= [2z^2d_{j+1}(z) - zd_{j+2}(z) + zc_j] - [2y^2d_{j+1}(y) - yd_{j+2}(y) + yc_j] \\
&= 2(z^2d_{j+1}(z) - y^2d_{j+1}(y)) - (zd_{j+2}(z) - yd_{j+2}(y)) + (z - y)c_j \\
&= 2\left[(z + y)(zd_{j+1}(z) - yd_{j+1}(y)) - zy(d_{j+1}(z) - d_{j+1}(y))\right] \\
&\quad - (zd_{j+2}(z) - yd_{j+2}(y)) + (z - y)c_j.
\end{aligned} \tag{9.50}$$

We now define $\alpha_j(z, y)$ and $\beta_j(z, y)$ as:

$$\begin{aligned}
\alpha_j(z, y) &\equiv \frac{d_j(z) - d_j(y)}{z - y} \\
\beta_j(z, y) &\equiv \frac{zd_j(z) - yd_j(y)}{z - y},
\end{aligned} \tag{9.51}$$

such that Eqs. (9.48, 9.49, 9.50) can be written as the following recurrence relation:

$$\begin{aligned}
\Delta f &\equiv f(z) - f(y) = (z - y)(\beta_1(z, y) - \alpha_2(z, y)) \\
\alpha_j(z, y) &= 2\beta_{j+1}(z, y) - \alpha_{j+2}(z, y) \\
\beta_j(z, y) &= c_j + 2(z + y)\beta_{j+1}(z, y) - 2zy\alpha_{j+1}(z, y) - \beta_{j+2}(z, y)
\end{aligned} \tag{9.52}$$

and $j = N - 1, \dots, 1$, $\beta_{N+1} = \beta_N = \alpha_{N+1} = \alpha_N = 0$.

This recurrence formula ensures that the leading order term of Δf goes as $(z - y)$; the leading order, constant, terms of $f(z)$ and $f(y)$ are automatically cancelled.

Implementing this in our numerical program, to improve the accuracy of the computation of $B(y, z)$ and $C(y, z)$, requires these functions to be written as a difference of Chebyshev expansions. Therefore we will first construct the Chebyshev expansion of the functions $1/\mathcal{F}(x)$ and $\Sigma(x)/\mathcal{F}(x)$ which can easily be done using the known expansions for $\Sigma(x)$ and $\mathcal{F}(x)$. The results achieved with this method are discussed below.

In Fig. 9.15 we compare the new behaviour of the photon renormalization function $\mathcal{G}(x)$ with that of Fig. 9.6. Although we see that for $10^4 < x < 10^7$ and $10^{-2} < x < 1$ the new calculation for $\mathcal{G}(x)$ is much more stable, the smallest x -values still seem to be problematic. As before we

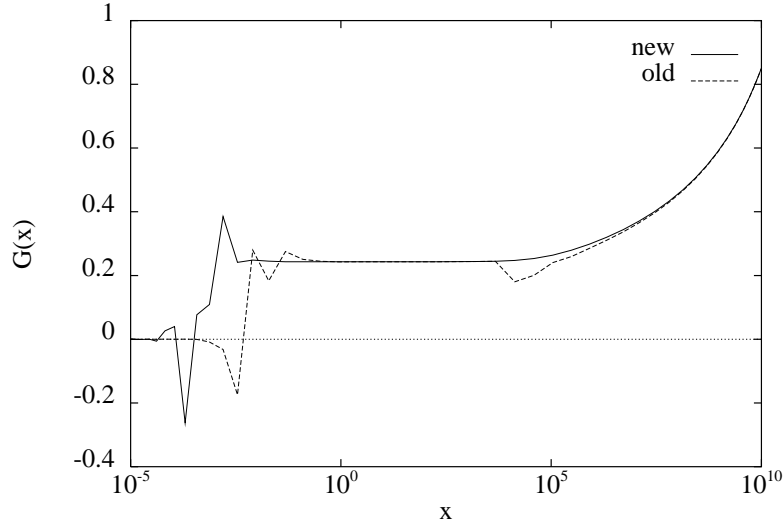


Figure 9.15: Photon renormalization function $\mathcal{G}(x)$ versus momentum squared x from the \mathcal{G} -equation with Ball-Chiu vertex, for $\alpha = 1.921$ and $N_f = 1$ using the Chebyshev subtraction scheme (new) and without it (old).

will look at the various radial and angular integrals to find a clue where the inaccuracy comes from.

The radial kernel $K_R(x_0, y)$, for $x_0 = 1.00856e-05$, is shown in Fig. 9.16. Comparing this with Fig. 9.8 we see that the new improvement has decreased the magnitude of the radial kernel. The value of the radial integrand at $x_0 = 1.00856e-05$ and $y_N = 9.96568e+09$ is $K_R(x_0, y_N) = -834.459$. This value is the integral of the angular kernel, $K_\theta(x_0, y_N, \theta)$, shown in Fig. 9.17.

If we again split the total radial integrand into six parts, $K_{R,i}$, for $i = 1, \dots, 6$, their individual values can be found in Table 9.3. The angular kernels from which these integral values are computed are shown in Fig. 9.18.

From Fig. 9.19 we see that the angular kernel $K_{\theta,3}$ after removal of the trigonometric factor $\sin^2 \theta(1 - 4 \cos^2 \theta)$ tends to the correct $\cos \theta$ -shape. However, the remaining inaccuracy is still responsible for unacceptable instabilities in $\mathcal{G}(x)$ for small x . Next we will introduce the final step to improve this.

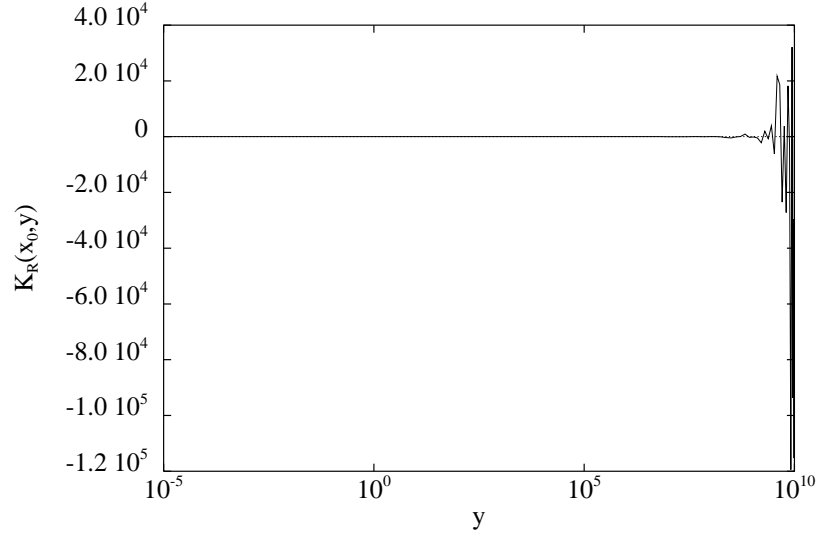


Figure 9.16: Radial integrand $K_R(x_0, y)$ for $x_0 = 1.00856e-05$ versus radial momentum squared y from the \mathcal{G} -equation with Ball-Chiu vertex, for $\alpha = 1.921$ and $N_f = 1$ using the Chebyshev subtraction scheme.

| | |
|-----------|----------------|
| $K_{R,1}$ | $-9.45396e-01$ |
| $K_{R,2}$ | $1.44340e+00$ |
| $K_{R,3}$ | $-8.34999e+02$ |
| $K_{R,4}$ | $4.23751e-02$ |
| $K_{R,5}$ | $2.43633e-05$ |
| $K_{R,6}$ | $-1.61445e-09$ |

Table 9.3: Radial kernels $K_{R,i}(x_0, y_N)$, for $i = 1, \dots, 6$, with $x_0 = 1.00856e-05$ and $y_N = 9.96568e+09$ using the Chebyshev subtraction scheme.

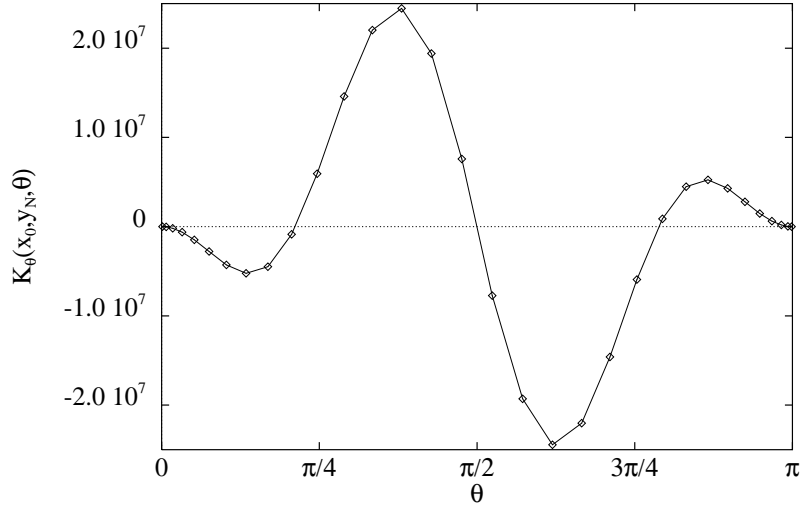


Figure 9.17: Angular integrand $K_\theta(x_0, y_N, \theta)$ for $x_0 = 1.00856e-05$, $y_N = 9.96568e+09$, versus angle θ from the \mathcal{G} -equation with Ball-Chiu vertex, for $\alpha = 1.921$ and $N_f = 1$ using the Chebyshev subtraction scheme.

9.2.5 Alternative logarithm calculation

Using the Chebyshev subtraction scheme Eq. (9.52) we have ensured that the difference of two Chebyshev expansions, $f(z) - f(y)$, has a leading term which will be proportional to $(z - y)$. However, the functions $\Sigma(x)$, $\mathcal{F}(x)$ and $\mathcal{G}(x)$ are expanded in Chebyshev polynomials of $s(x)$ rather than x . Therefore, the Chebyshev subtraction scheme will ensure that the leading term of the differences $f(s(z)) - f(s(y))$ will be proportional to $s(z) - s(y)$. Of course, analytically, $s(z) - s(y)$ itself will be proportional to $(z - y)$ in leading order. However, this is again a possible source of numerical inaccuracy. Remember the definition of $s(x)$:

$$s(x) = \frac{\log_{10}(x/\Lambda\kappa)}{\log_{10}(\Lambda/\kappa)}. \quad (9.53)$$

Then,

$$s(z) - s(y) = \frac{\log_{10}(z/\Lambda\kappa)}{\log_{10}(\Lambda/\kappa)} - \frac{\log_{10}(y/\Lambda\kappa)}{\log_{10}(\Lambda/\kappa)} = \frac{\log_{10}(z/y)}{\log_{10}(\Lambda/\kappa)}. \quad (9.54)$$

From Figs. 9.18, 9.19 we see that the problem resides around $\theta = \pi/2$. We can write,

$$\frac{z}{y} = 1 + \frac{x - 2\sqrt{xy} \cos \theta}{y}$$

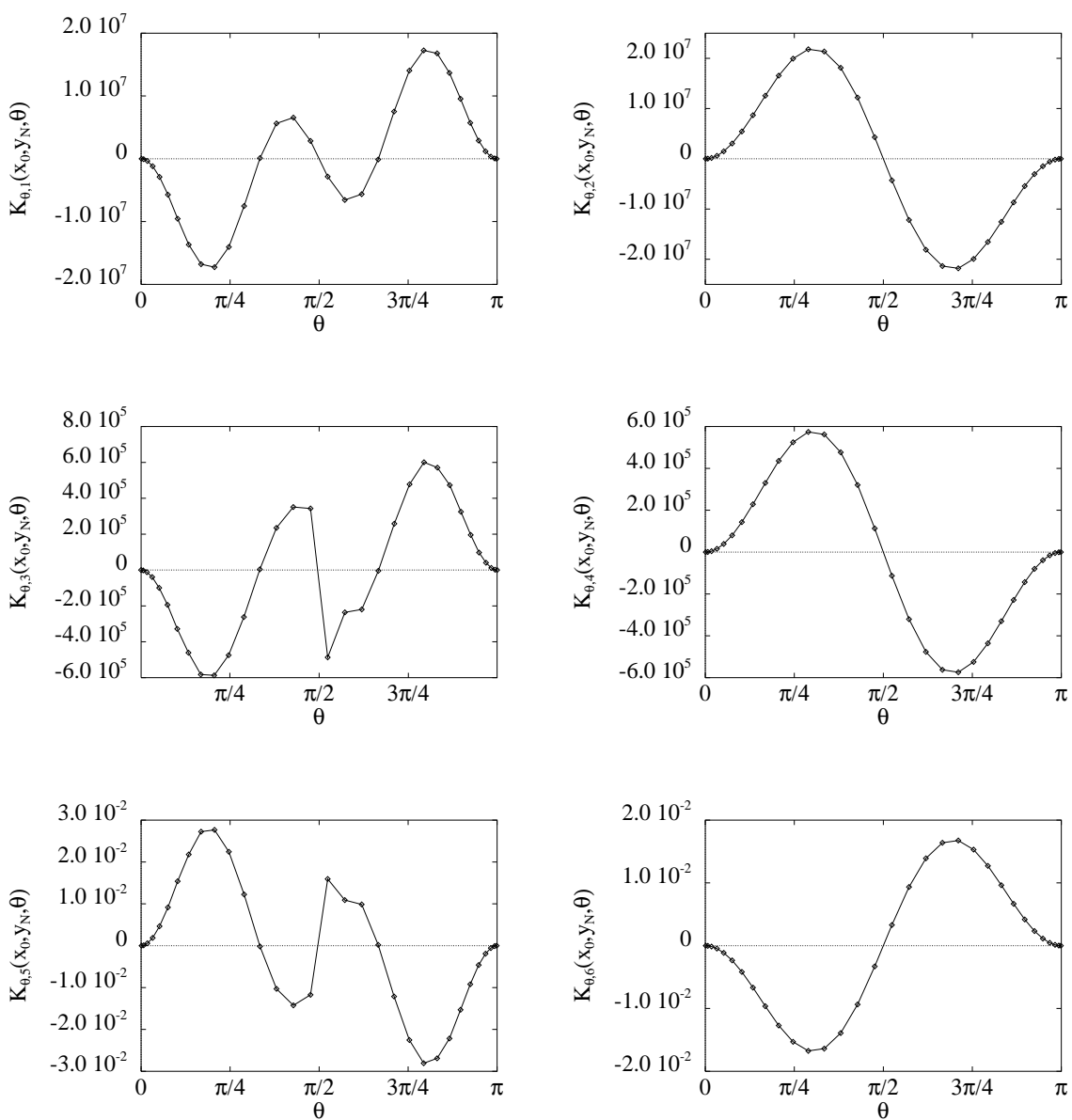


Figure 9.18: Angular integrands $K_{\theta,i}(x_0, y_N, \theta)$, for $i = 1, \dots, 6$, with $x_0 = 1.00856e-05$, $y_N = 9.96568e+09$, versus angle θ from the \mathcal{G} -equation with Ball-Chiu vertex, for $\alpha = 1.921$ and $N_f = 1$ using the Chebyshev subtraction scheme.

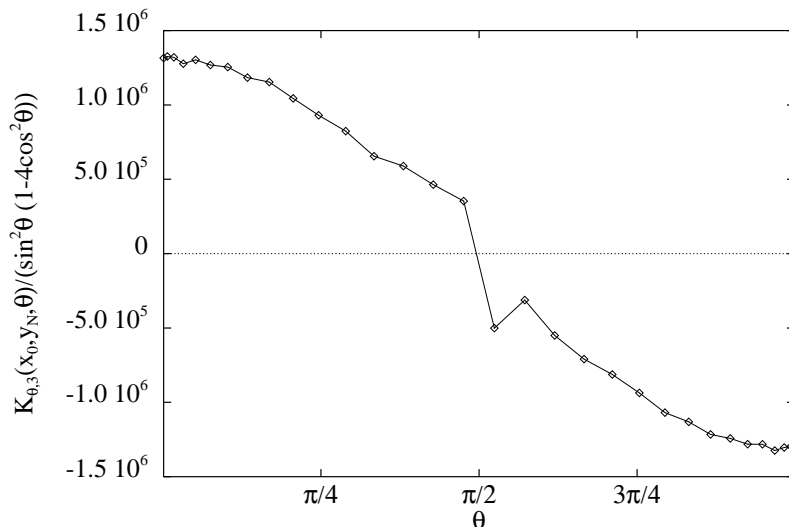


Figure 9.19: Angular integrand $K_{\theta,3}(x_0, y_N, \theta)$ for $x_0 = 1.00856e-05$, $y_N = 9.96568e+09$, versus angle θ from the \mathcal{G} -equation with Ball-Chiu vertex, for $\alpha = 1.921$ and $N_f = 1$ after removing the trigonometric factor $\sin^2 \theta (1 - 4 \cos^2 \theta)$ using the Chebyshev subtraction scheme.

and if x is very small and $\theta \approx \pi/2$, the second term in this last expression will be much smaller than one and its accuracy can be completely lost. However it is exactly this bit of the expression which determines completely the answer of $\log_{10}(z/y)$ and therefore its inaccuracy will be responsible for the incorrect cancellation in the angular integrals. To improve on this we cannot anymore use the logarithm function of the standard mathematical library of the computer; instead we will implement our own routine for values of z very close to y . We will use the following Taylor series [59]:

$$\frac{1}{2} \ln \frac{1+u}{1-u} = u + \frac{u^3}{3} + \frac{u^5}{5} + \frac{u^7}{7} + \dots, \quad -1 < u < 1. \quad (9.55)$$

If we define $u \equiv \frac{z-y}{z+y}$ then,

$$\frac{z}{y} = \frac{1+u}{1-u}. \quad (9.56)$$

Eq. (9.55) ensures that the leading term of $\log_{10}(z/y)$ will be proportional to $(z-y)$. We implement the Taylor series up to u^7 -terms and use it when $|u| < 10^{-3}$, otherwise we use the standard logarithm routine.

In the following figures we will show the various results after this improvement has been implemented. The angular integral $K_{\theta,3}/\sin^2 \theta (1 - 4 \cos^2 \theta)$, after removal of the trigonometric part

is shown in Fig. 9.20 and has the expected $\cos \theta$ behaviour. The influence on the angular inte-

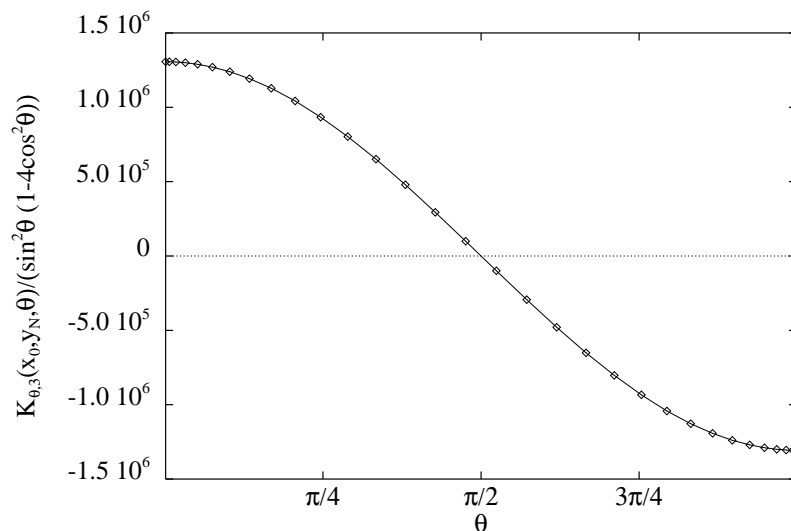


Figure 9.20: Angular integrand $K_{\theta,3}(x_0, y_N, \theta)$ for $x_0 = 1.00856e-05$, $y_N = 9.96568e+09$, versus angle θ from the \mathcal{G} -equation with Ball-Chiu vertex, for $\alpha = 1.921$ and $N_f = 1$ after removing the trigonometric factor $\sin^2 \theta (1 - 4 \cos^2 \theta)$ using the alternative logarithm calculation.

grands with their complete trigonometric behaviour can be seen in Fig. 9.21. The values of these six angular integrals are given in Table 9.4. The total angular integrand is shown in Fig. 9.22 and the integral value is $K_R(x_0, y_N) = 0.524575$ for $x_0 = 1.00856e-05$ and $y_N = 9.96568e+09$.

| | |
|-----------|----------------|
| $K_{R,1}$ | $-9.45396e-01$ |
| $K_{R,2}$ | $1.44340e+00$ |
| $K_{R,3}$ | $-1.30249e-02$ |
| $K_{R,4}$ | $3.95985e-02$ |
| $K_{R,5}$ | $2.63095e-09$ |
| $K_{R,6}$ | $-1.53344e-09$ |

Table 9.4: Radial kernels $K_{R,i}(x_0, y_N)$, for $i = 1, \dots, 6$, with $x_0 = 1.00856e-05$ and $y_N = 9.96568e+09$ using the alternative logarithm calculation.

The radial integrand for $x_0 = 1.00856e-05$ is shown in Fig. 9.23. We see that there is only a very light wriggle left for very large y -values and this does not alter the fundamental behaviour of the vacuum polarization function. The vacuum polarization at $x_0 = 1.00856e-05$ is $\Pi(x_0) = 3.11466$. After performing the radial integrals, the evolution of the vacuum polarization integral $\Pi(x)$ with momentum is shown in Fig. 9.24.

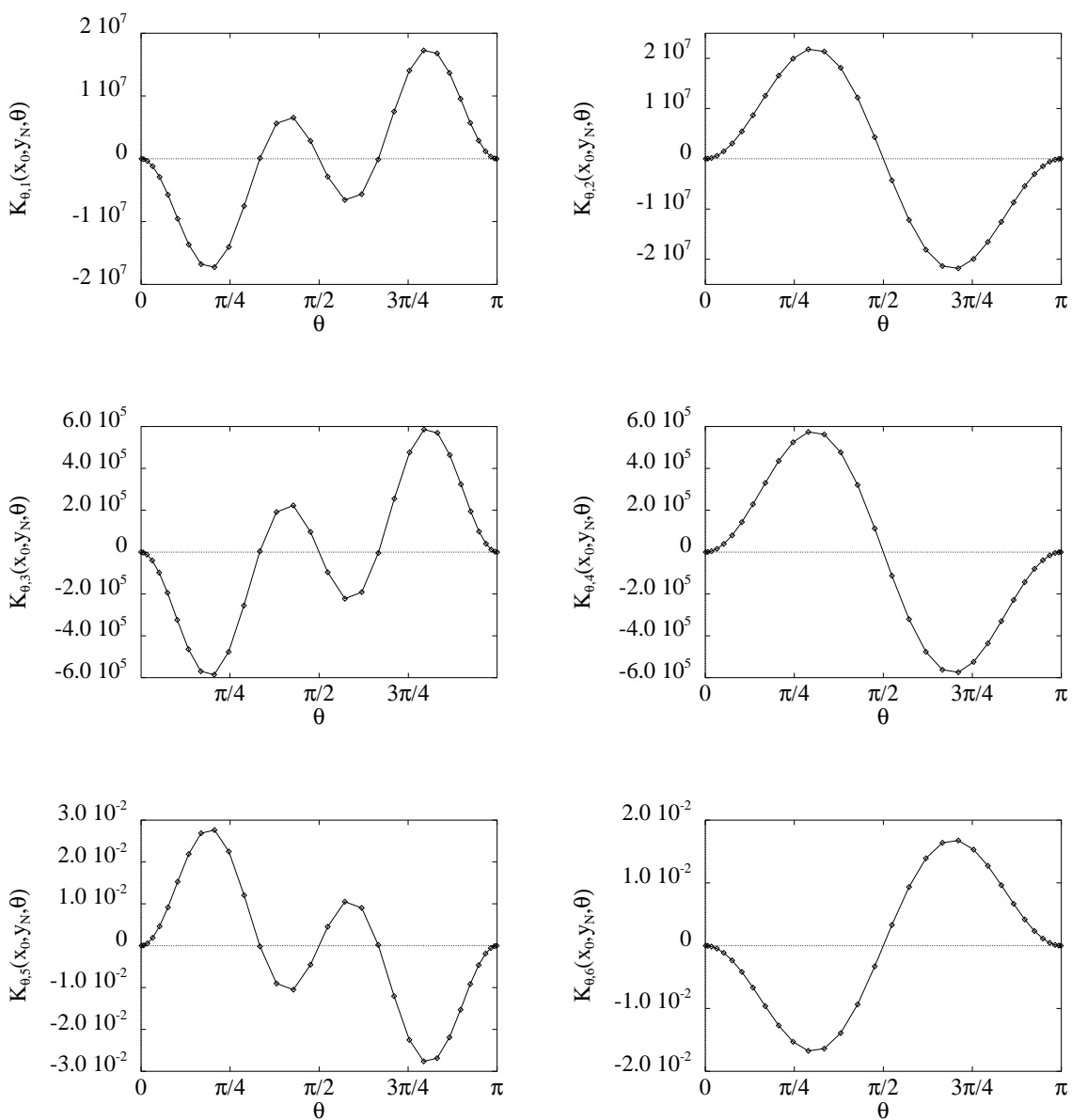


Figure 9.21: Angular integrands $K_{\theta,i}(x_0, y_N, \theta)$, for $i = 1, \dots, 6$, with $x_0 = 1.00856e-05$, $y_N = 9.96568e+09$, versus angle θ from the \mathcal{G} -equation with Ball-Chiu vertex, for $\alpha = 1.921$ and $N_f = 1$ using the alternative logarithm calculation.

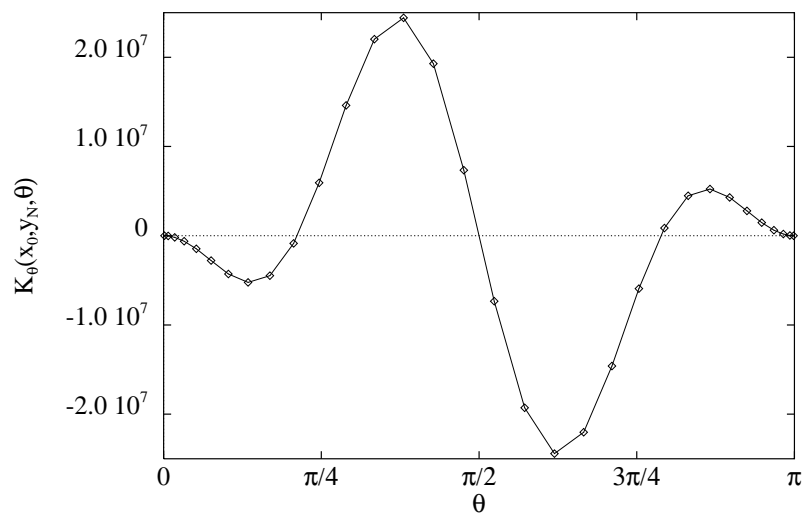


Figure 9.22: Angular integrand $K_\theta(x_0, y_N, \theta)$ for $x_0 = 1.00856e-05$, $y_N = 9.96568e+09$, versus angle θ from the \mathcal{G} -equation with Ball-Chiu vertex, for $\alpha = 1.921$ and $N_f = 1$ using the alternative logarithm calculation.

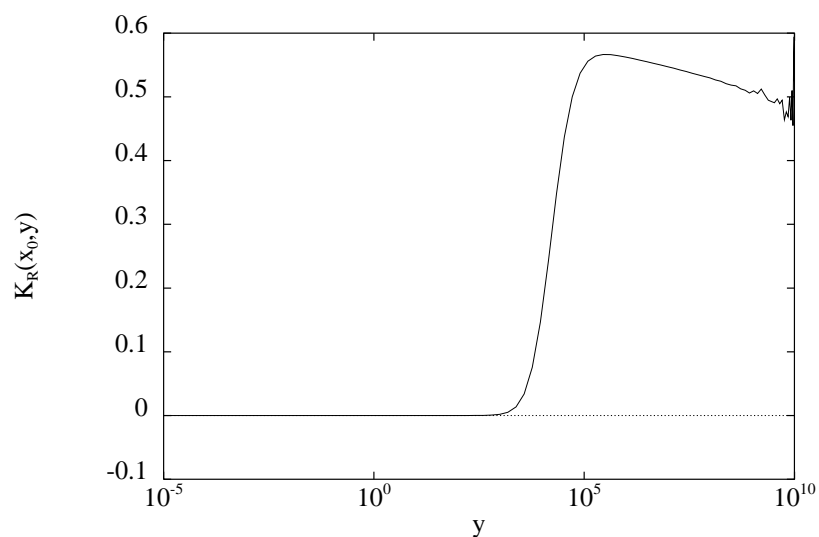


Figure 9.23: Radial integrand $K_R(x_0, y)$ for $x_0 = 1.00856e-05$ versus radial momentum squared y from the \mathcal{G} -equation from the \mathcal{G} -equation with Ball-Chiu vertex, for $\alpha = 1.921$ and $N_f = 1$ using the alternative logarithm calculation.

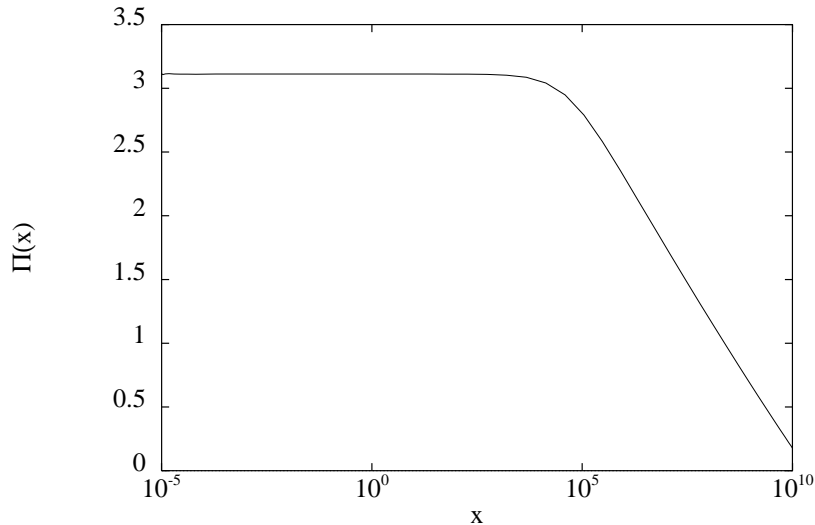


Figure 9.24: Vacuum polarization $\Pi(x)$ versus momentum squared x from the \mathcal{G} -equation with Ball-Chiu vertex, for $\alpha = 1.921$ and $N_f = 1$ using the alternative logarithm calculation.

From the vacuum polarization $\Pi(x)$, we now compute the photon renormalization function $\mathcal{G}(x)$ and plot the result in Fig. 9.25. We see that $\mathcal{G}(x)$ behaves perfectly well now; the unphysicalities due to numerical inaccuracies have been worked away, down to photon momenta of the order $x/\Lambda^2 \approx \mathcal{O}(10^{-15})$.

9.2.6 Numerical results

Having done this, we can now apply the iterative procedure to solve the $(\Sigma, \mathcal{F}, \mathcal{G})$ -system and determine the critical coupling in unquenched QED with Ball-Chiu vertex. The evolution of the generated fermion mass, $\Sigma(0)$, versus the running coupling at the UV-cutoff, $\alpha(\Lambda^2)$ is shown in Fig. 9.26. The critical coupling is $\boxed{\alpha_c(\Lambda^2, N_f = 1) = 1.63218}$. We remark that the program only converges if the starting guesses for the unknown functions are close to the solutions. The logical choice for this is always the solutions of the system of equations for another value of the coupling, which is a little bit larger than the current one. The more difficult it is to achieve convergence, the closer we have to choose the subsequent couplings for which we compute the generated fermion mass. The reason for this convergence problem lies in the global iterative procedure connecting the coupled (Σ, \mathcal{F}) -system to the \mathcal{G} -equation. It is very likely that convergence would be achieved more consistently and we could reach the critical point with fewer computations if

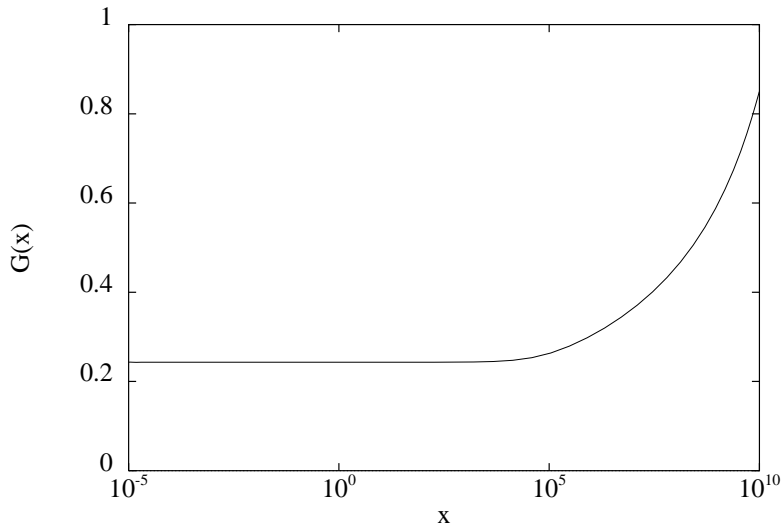


Figure 9.25: Photon renormalization function $\mathcal{G}(x)$ versus momentum squared x from the \mathcal{G} -equation with Ball-Chiu vertex, for $\alpha = 1.921$ and $N_f = 1$ using the alternative logarithm calculation.

the complete $(\Sigma, \mathcal{F}, \mathcal{G})$ -system were treated with Newton's method in a unified way.

Typical plots of $\Sigma(x)$, $\mathcal{F}(x)$ and $\alpha(x) = \alpha \mathcal{G}(x)$ are shown in Fig. 9.27, Fig. 9.28 and Fig. 9.29. From Fig. 9.28 we see that the wavefunction renormalization tends to have a peculiar behaviour with the Ball-Chiu vertex when the coupling is close to its critical value.

For $N_f = 2$ the situation is even more delicate as the procedure initially does not converge for any value of the coupling. To make it converge it is important to start from a realistic set of functions. This can be achieved by using the functions $\Sigma(x)$, $\mathcal{F}(x)$ and $\mathcal{G}(x)$ obtained with the bare vertex approximation for $\alpha = 5$ and using these as starting values to find the results for the Ball-Chiu vertex for the same coupling. We then slowly work our way down to smaller values of the coupling. Unfortunately the program does not converge anymore for $\Sigma(0) < \mathcal{O}(500)$ (for $\Lambda = 1e5$) and further investigation would be needed to understand if this is because of numerical or physical reasons.

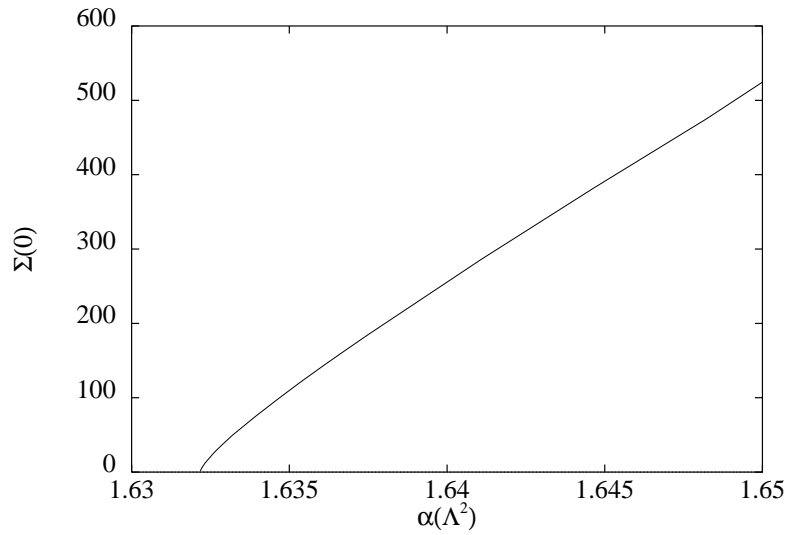


Figure 9.26: Generated fermion mass $\Sigma(0)$ versus running coupling $\alpha(\Lambda^2)$ for the coupled $(\Sigma, \mathcal{F}, \mathcal{G})$ -system with the Ball-Chiu vertex, for $N_f = 1$.

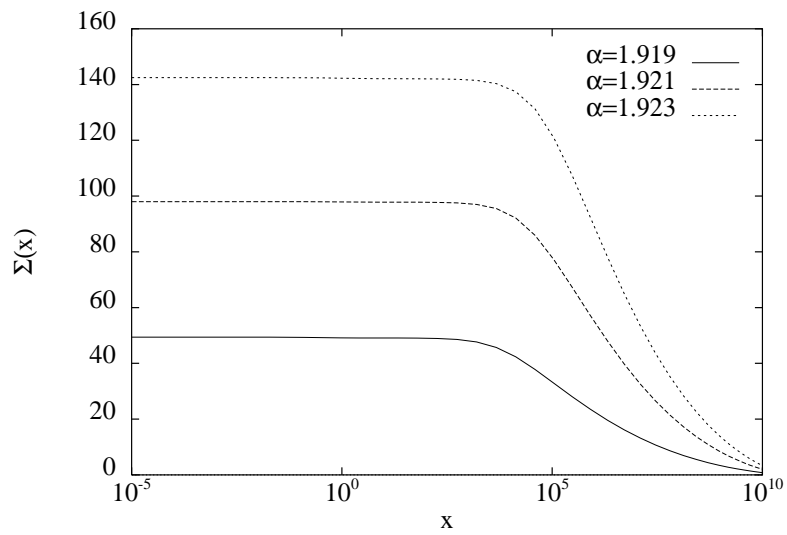


Figure 9.27: Dynamical fermion mass $\Sigma(x)$ versus momentum squared x for the coupled $(\Sigma, \mathcal{F}, \mathcal{G})$ -system with the Ball-Chiu vertex, for $N_f = 1$ and $\alpha = 1.919, 1.921, 1.923$.

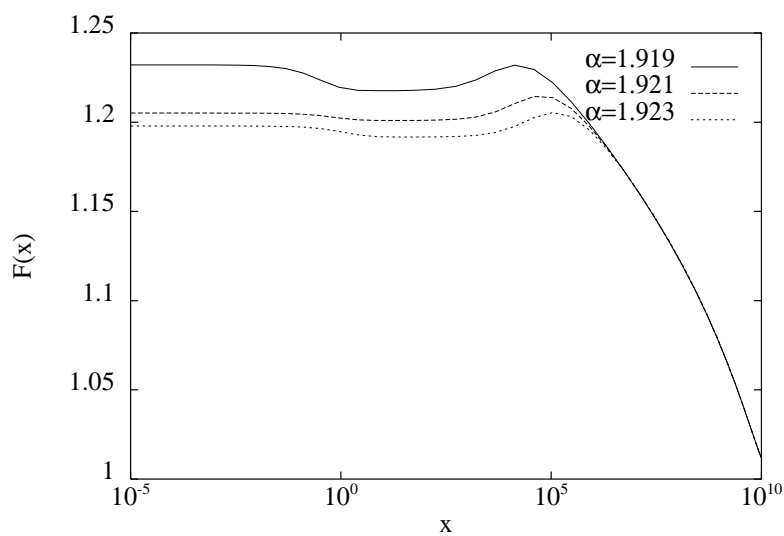


Figure 9.28: Fermion wavefunction renormalization $\mathcal{F}(x)$ versus momentum squared x for the coupled $(\Sigma, \mathcal{F}, \mathcal{G})$ -system with the Ball-Chiu vertex, for $N_f = 1$ and $\alpha = 1.919, 1.921, 1.923$.

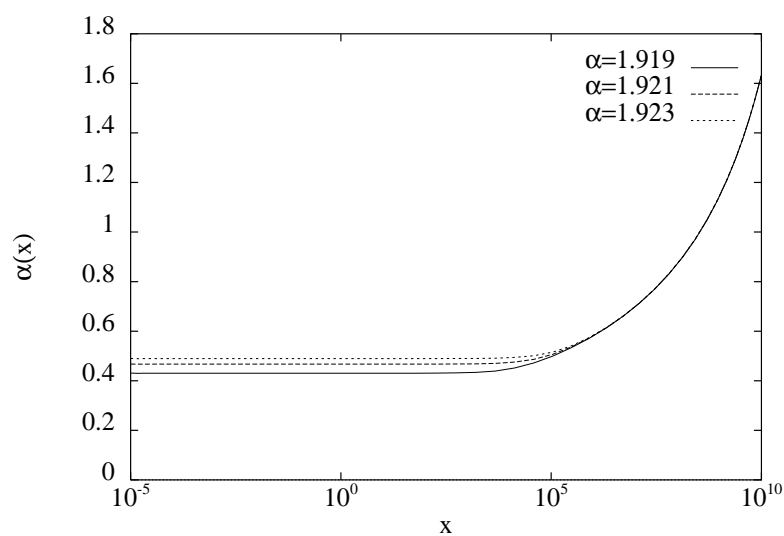


Figure 9.29: Running coupling $\alpha(x)$ versus momentum squared x for the coupled $(\Sigma, \mathcal{F}, \mathcal{G})$ -system with the Ball-Chiu vertex, for $N_f = 1$ and $\alpha = 1.919, 1.921, 1.923$.

9.3 Curtis-Pennington vertex

We recall the Curtis-Pennington vertex Ansatz as introduced in Section 2.6.2:

$$\begin{aligned}
\Gamma_{CP}^\mu(k, p) &= \frac{1}{2} \left[\frac{1}{\mathcal{F}(k^2)} + \frac{1}{\mathcal{F}(p^2)} \right] \gamma^\mu + \frac{1}{2} \left[\frac{1}{\mathcal{F}(k^2)} - \frac{1}{\mathcal{F}(p^2)} \right] \frac{(k+p)^\mu (\not{k} + \not{p})}{k^2 - p^2} \\
&\quad - \left[\frac{\Sigma(k^2)}{\mathcal{F}(k^2)} - \frac{\Sigma(p^2)}{\mathcal{F}(p^2)} \right] \frac{(k+p)^\mu}{k^2 - p^2} \\
&\quad + \frac{1}{2} \left[\frac{1}{\mathcal{F}(k^2)} - \frac{1}{\mathcal{F}(p^2)} \right] \frac{(k^2 + p^2) [\gamma^\mu (k^2 - p^2) - (k+p)^\mu (\not{k} - \not{p})]}{(k^2 - p^2)^2 + (\Sigma^2(k^2) + \Sigma^2(p^2))^2}.
\end{aligned} \tag{9.57}$$

This vertex Ansatz has been used in Section 3.3 and in Ref. [60, 39, 28, 36, 34] to study the behaviour of the fermion propagator and the dynamical generation of fermion mass in quenched QED.

We now want to investigate the possibility of dynamical fermion mass generation in unquenched QED with the Curtis-Pennington vertex. We recall the set of coupled integral equations (in Euclidean space), Eqs. (2.131, 2.132, 2.133) with $m_0 = 0$ and in the Landau gauge:

$$\begin{aligned}
\frac{\Sigma(x)}{\mathcal{F}(x)} &= \frac{\alpha}{2\pi^2} \int dy \frac{y\mathcal{F}(y)}{y + \Sigma^2(y)} \int d\theta \sin^2 \theta \mathcal{G}(z) \\
&\quad \times \left\{ \left[A(y, x) + \tau_6(y, x)(y - x) \right] \frac{3\Sigma(y)}{z} - \frac{\Sigma(y) - \Sigma(x)}{\mathcal{F}(x)(y - x)} \frac{2yx \sin^2 \theta}{z^2} \right\}
\end{aligned} \tag{9.58}$$

$$\begin{aligned}
\frac{1}{\mathcal{F}(x)} &= 1 - \frac{\alpha}{2\pi^2 x} \int dy \frac{y\mathcal{F}(y)}{y + \Sigma^2(y)} \int d\theta \sin^2 \theta \mathcal{G}(z) \\
&\quad \times \left\{ A(y, x) \left[\frac{2yx \sin^2 \theta}{z^2} - \frac{3\sqrt{yx} \cos \theta}{z} \right] \right. \\
&\quad \left. + \left[B(y, x)(y + x) - C(y, x)\Sigma(y) \right] \frac{2yx \sin^2 \theta}{z^2} - \tau_6(y, x)(y - x) \frac{3\sqrt{yx} \cos \theta}{z} \right\}
\end{aligned} \tag{9.59}$$

$$\begin{aligned}
\frac{1}{\mathcal{G}(x)} &= 1 + \frac{2N_f \alpha}{3\pi^2 x} \int dy \frac{y\mathcal{F}(y)}{y + \Sigma^2(y)} \int d\theta \sin^2 \theta \frac{\mathcal{F}(z)}{z + \Sigma^2(z)} \\
&\quad \times \left\{ 2A(y, z) \left[y(1 - 4 \cos^2 \theta) + 3\sqrt{yx} \cos \theta \right] \right. \\
&\quad \left. + B(y, z) \left[(y + z - 2\Sigma(y)\Sigma(z)) (2y(1 - 4 \cos^2 \theta) + 3\sqrt{yx} \cos \theta) \right. \right. \\
&\quad \left. \left. + 3(y - z)(y - \Sigma(y)\Sigma(z)) \right] \right. \\
&\quad \left. - C(y, z) \left[(\Sigma(y) + \Sigma(z)) (2y(1 - 4 \cos^2 \theta) + 3\sqrt{yx} \cos \theta) + 3(y - z)\Sigma(y) \right] \right. \\
&\quad \left. - 3\tau_6(y, z)(y - z)(y - \sqrt{yx} \cos \theta + \Sigma(y)\Sigma(z)) \right\}
\end{aligned} \tag{9.60}$$

where

$$\begin{aligned}
 A(y, x) &= \frac{1}{2} \left[\frac{1}{\mathcal{F}(y)} + \frac{1}{\mathcal{F}(x)} \right] \\
 B(y, x) &= \frac{1}{2(y-x)} \left[\frac{1}{\mathcal{F}(y)} - \frac{1}{\mathcal{F}(x)} \right] \\
 C(y, x) &= -\frac{1}{y-x} \left[\frac{\Sigma(y)}{\mathcal{F}(y)} - \frac{\Sigma(x)}{\mathcal{F}(x)} \right] \\
 \tau_6(y, x) &= \frac{y+x}{2[(y-x)^2 + (\Sigma^2(y) + \Sigma^2(x))^2]} \left[\frac{1}{\mathcal{F}(y)} - \frac{1}{\mathcal{F}(x)} \right].
 \end{aligned}$$

If we now implement the system of coupled integral equations with the Curtis-Pennington vertex, Eqs. (9.58, 9.59, 9.60), the numerical program does not seem to converge. A check of the vacuum polarization integral calculated from realistic input functions is shown in Fig. 9.30.

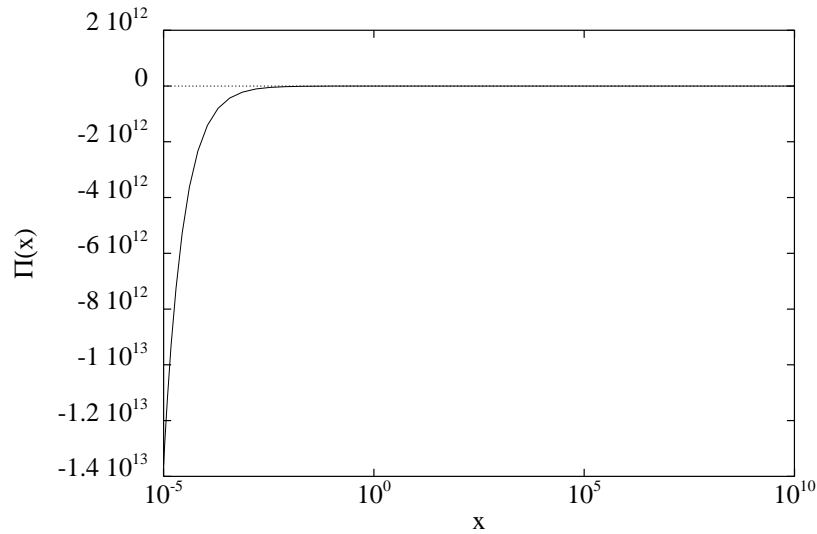


Figure 9.30: Vacuum polarization $\Pi(x)$ versus momentum squared x from the \mathcal{G} -equation with Curtis-Pennington vertex, for $\alpha = 1.921$ and $N_f = 1$.

The huge negative value of the vacuum polarization for decreasing value of momenta is unphysical. It is clear that the CP-vertex gives rise to a quadratic divergence in the vacuum polarization in the massless case. In the case where mass is generated dynamically the situation is more complicated, but Fig. 9.30 shows that the CP-vertex does not give physical results for unquenched QED.

9.4 Hybrid method

In the previous section we have seen that the Curtis-Pennington vertex did not yield physical results when applied to the photon equation. Nevertheless it is useful to use the CP-vertex for the fermion equations as it ensures that the fermion propagator is multiplicatively renormalizable in the quenched case. Therefore we will now introduce a hybrid method where we use the CP-vertex in the fermion equations, yielding Eqs. (9.58, 9.59), and the Ball-Chiu vertex in the photon equation, giving Eq. (9.8), in order to avoid quadratic divergences in the vacuum polarization.

The evolution of the generated fermion mass, $\Sigma(0)$, versus the running coupling, $\alpha_c(\Lambda^2)$, is shown in Fig. 9.31. The value of the critical coupling at the UV-cutoff is $\alpha_c(\Lambda^2, N_f = 1) = 1.61988$. Plots of $\Sigma(x)$, $\mathcal{F}(x)$ and $\alpha(x) = \alpha \mathcal{G}(x)$ are shown in Fig. 9.32, Fig. 9.33 and Fig. 9.34.

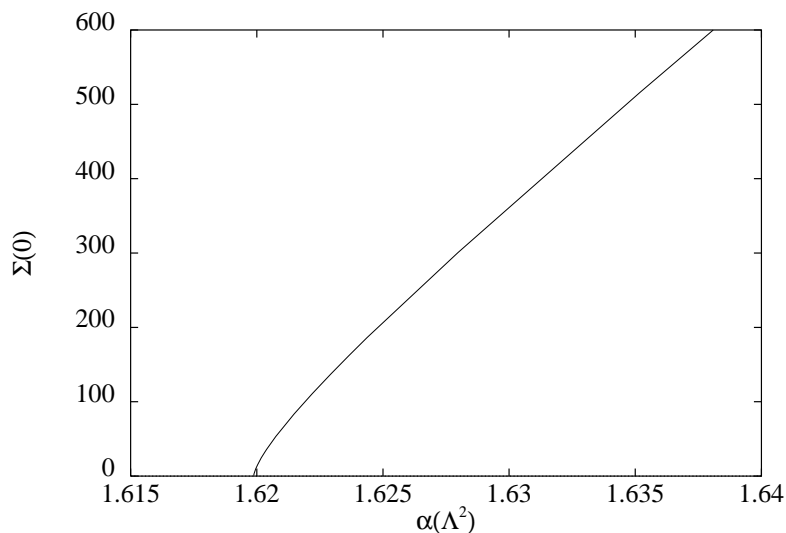


Figure 9.31: Generated fermion mass $\Sigma(0)$ versus running coupling $\alpha(\Lambda^2)$ for the coupled $(\Sigma, \mathcal{F}, \mathcal{G})$ -system with the hybrid method, for $N_f = 1$.

For $N_f = 2$ the generated fermion mass is plotted against the coupling in Fig.9.35. The critical coupling is $\alpha_c(\Lambda^2, N_f = 2) = 2.14429$.

Although for $N_f = 1$, the critical coupling only changes with less than 1% between the Ball-Chiu vertex and the hybrid method, the latter definitely improves the convergence of the numerical method. This is especially true for $N_f = 2$ where we could not locate the critical point with the Ball-Chiu vertex, while it is easily done with the hybrid method.

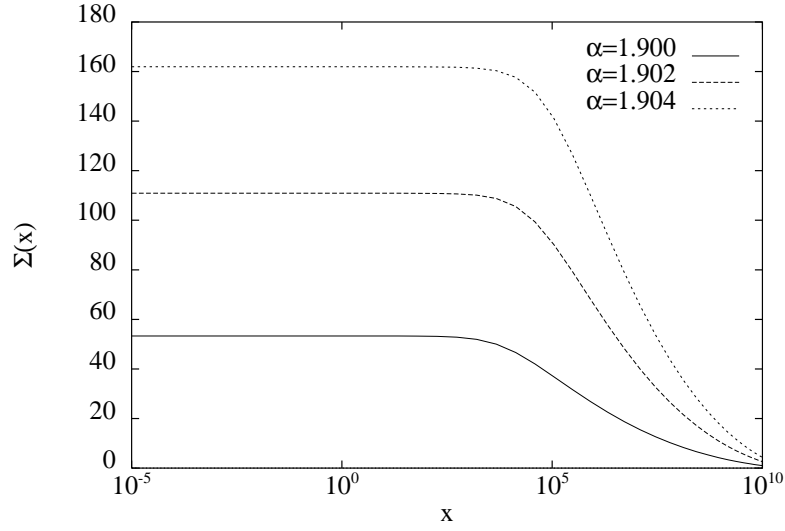


Figure 9.32: Dynamical fermion mass $\Sigma(x)$ versus momentum squared x for the coupled $(\Sigma, \mathcal{F}, \mathcal{G})$ -system with the hybrid method, for $N_f = 1$ and $\alpha = 1.900, 1.902, 1.904$.

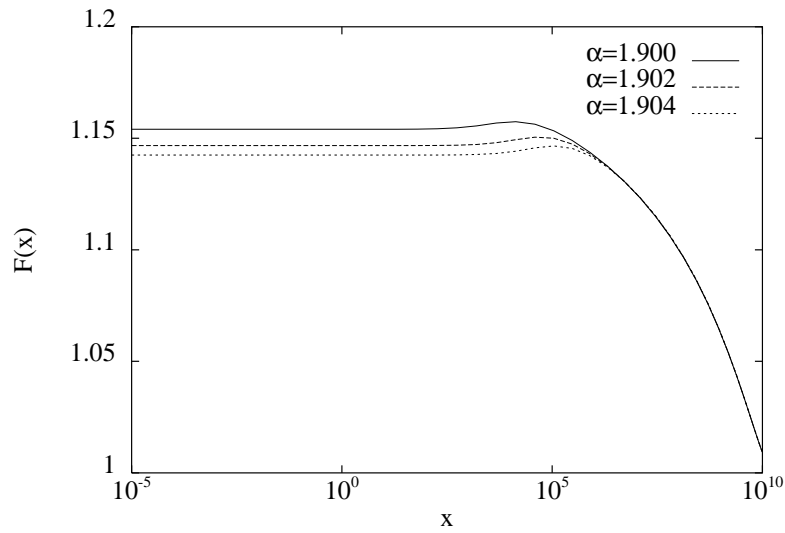


Figure 9.33: Fermion wavefunction renormalization $\mathcal{F}(x)$ versus momentum squared x for the coupled $(\Sigma, \mathcal{F}, \mathcal{G})$ -system with the hybrid method, for $N_f = 1$ and $\alpha = 1.900, 1.902, 1.904$.

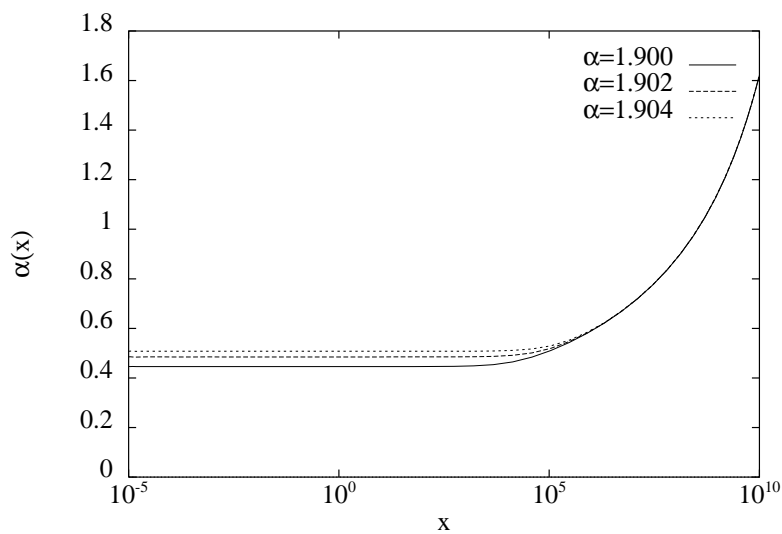


Figure 9.34: Running coupling $\alpha(x)$ versus momentum squared x for the coupled $(\Sigma, \mathcal{F}, \mathcal{G})$ -system with the hybrid method, for $N_f = 1$ and $\alpha = 1.900, 1.902, 1.904$.

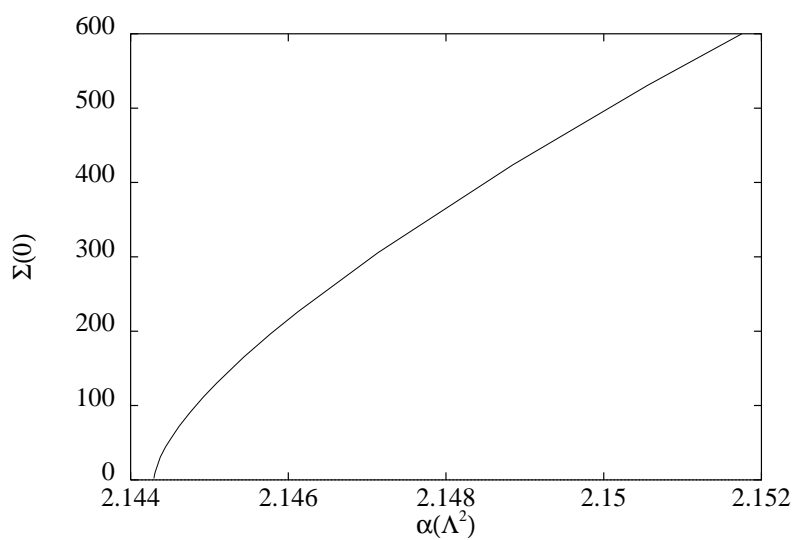


Figure 9.35: Generated fermion mass $\Sigma(0)$ versus running coupling $\alpha(\Lambda^2)$ for the coupled $(\Sigma, \mathcal{F}, \mathcal{G})$ -system with the hybrid method, for $N_f = 2$.

9.5 About the renormalization of the SD equations

In this study we have always used the bare Schwinger-Dyson equations, regularized by an UV-cutoff Λ . From the plots of the running coupling $\alpha(x)$ versus x in the previous result sections, we understand that in the critical point we will be able to define a running critical coupling $\alpha_c(x)$ which depends only on the relative position of x with respect to Λ^2 , i.e. we have a fixed line $\alpha_c(x/\Lambda^2)$. This is shown in Fig. 9.36 where we plot the running coupling $\alpha_c(x/\Lambda^2)$ for α close to the critical point ($\Sigma(0)/\Lambda \approx 1e-5$). Note that if we could go even closer to the critical point we would see that $\alpha_c(x/\Lambda^2) \rightarrow 0$ when $x \rightarrow 0$, as the flat low momentum behaviour of Fig. 9.36 is entirely due to the small generated fermion mass.

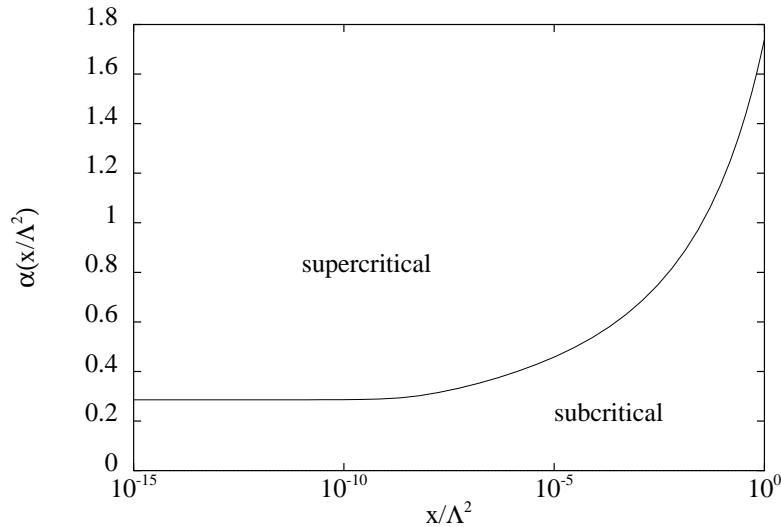


Figure 9.36: Running coupling $\alpha(x/\Lambda^2)$ versus momentum squared x/Λ^2 for the coupled $(\Sigma, \mathcal{F}, \mathcal{G})$ -system, for $N_f = 1$ for $\alpha = 2.0825$.

We now try to relate this intuitively with the physical world, which is described by the renormalized theory. Suppose we fix the value of the coupling at a certain renormalization scale, $\alpha_R(\mu^2)$. If we now look at the generation of fermion mass, the following scenario happens depending on the values of Λ . If we take Λ such that $\alpha_R(\mu^2)$ lies below the critical line in Fig. 9.36, no mass will be generated. When we increase Λ , μ^2/Λ^2 decreases, and as we are traveling from right to left on a horizontal line in Fig. 9.36, $\alpha_c(\mu^2/\Lambda^2)$ decreases such that the renormalized coupling $\alpha_R(\mu^2)$ which started subcritical becomes critical for some critical UV-cutoff Λ_c . If we increase Λ further we enter the supercritical phase where fermion mass is generated. However there is

a serious problem related to the Landau pole. When we shift the renormalized coupling from right to left with respect to the critical line in Fig. 9.36, corresponding to increasing Λ , it is the whole running renormalized coupling which is displaced. If the Landau pole of the running renormalized coupling moves into the integration region $[0, \Lambda]$, the SD equations are not solvable anymore. Therefore, Λ cannot be taken to infinity and the existence of the Landau pole does not allow us to make a consistent discussion of fermion mass generation in renormalized QED. However, if another theory would take over at some scale Ω , we could compare this scale with Λ_c and fermion mass generation could then be possible in a consistent way. A more detailed numerical analysis of the above described scenario could reveal more about this.

9.6 Summary

From the results of this chapter we can conclude that dynamical fermion mass generation does occur in unquenched QED, for $N_f = 1$ and $N_f = 2$. The exact value of the critical coupling is dependent on the vertex Ansatz.

In Table 9.5 we compare the various values obtained for the critical coupling for $N_f = 1$ and $N_f = 2$ in the $(\Sigma, \mathcal{F}, \mathcal{G})$ -system with different vertex approximations in the previous sections and in Section 8.3. The critical coupling varies at most 18% for $N_f = 1$ and 21% for $N_f = 2$.

| vertex | $\alpha_c(N_f = 1)$ | $\alpha_c(N_f = 2)$ |
|-------------------------|---------------------|---------------------|
| bare | 1.74102 | 2.22948 |
| $1/\mathcal{F}$ -vertex | 1.90911 | 2.59578 |
| Ball-Chiu | 1.63218 | — |
| hybrid | 1.61988 | 2.14429 |

Table 9.5: Critical coupling α_c for $N_f = 1$ and $N_f = 2$ for the $(\Sigma, \mathcal{F}, \mathcal{G})$ -system with various vertex approximations.

The study in this chapter has been the very first attempt to introduce an improved vertex in the study of dynamical fermion mass generation in unquenched QED. More work has to be done to construct a vertex Ansatz which ensures the multiplicative renormalizability of the photon propagator in addition to that of the fermion propagator [26]. However, although the vertex approximations used in this work were not designed specifically for unquenched QED, the numerical method developed here will prove very helpful when such vertices will be available. Having achieved the proper numerical cancellation of the quadratic divergence in the vacuum polarization integral with the Ball-Chiu vertex is important as this vertex is the uniquely determined longitudinal part of the QED-vertex, and as such will have to be present in any realistic improvement of the vertex in unquenched QED.

Chapter 10

Conclusions

We have investigated the dynamical generation of fermion mass in QED, using the Schwinger-Dyson equations to approach this non-perturbative phenomenon of quantum field theory. This infinite set of equations was then truncated by introducing various approximations.

Bifurcation analysis was applied to determine the critical point in the Curtis-Pennington approximation to *quenched* QED. We computed the critical coupling, above which fermion mass is generated dynamically, for a large range of the covariant gauge parameter and concluded that the critical coupling has a much smaller dependence on the gauge parameter than in the bare vertex approximation. The critical coupling in the Landau gauge, which is $\alpha_c = \pi/3$ in the bare vertex approximation, becomes $\alpha_c = 0.933667$ with the CP-vertex. Furthermore we have shown that the generated fermion mass follows the Miransky-scaling law in the neighbourhood of the critical point, with the bare vertex as well as with the Curtis-Pennington vertex.

We went on to discuss dynamical fermion mass generation in *unquenched* QED and developed a sophisticated computer program to investigate this numerically. We derived the formalism to solve the coupled system of non-linear integral equations by approximating the integrals by suitable quadrature formulae, paying special attention to the kink in the radial integrand, and solving the resulting system of coupled non-linear algebraic equations with an iteration method. Using Newton's iterative procedure ensured the quadratic convergence of the method.

When applying this method to the coupled equations for the dynamical mass Σ and the photon renormalization function \mathcal{G} , we observed that $\mathcal{G}(x)$ had an unphysical behaviour for intermediate small values of x . A detailed analysis exposed a problem in the numerical cancellation of the quadratic divergence in the vacuum polarization integral. It was suggested that smooth approximations to Σ , \mathcal{F} and \mathcal{G} would be preferable in contrast to the discretized approach used

so far.

Motivated by this observation, we introduced Chebyshev expansions for Σ , \mathcal{F} and \mathcal{G} and adapted the previously developed method to solve the integral equations in the most advantageous way. The introduction of the Chebyshev expansion method proved to be very powerful as the smoothness of the functions is automatically guaranteed, which avoids all interpolation problems. Furthermore higher order numerical quadrature formulae can now be used, enhancing the accuracy and speeding up the calculations.

We went on applying the Chebyshev solution method to various approximations to unquenched QED in the bare vertex approximation. We computed the value of the critical coupling for one and two flavours and compared these with the results found in the literature. First in the 1-loop approximation to \mathcal{G} using three variants: the LAK-approximation, the $\mathcal{F} \equiv 1$ approximation and the coupled (Σ, \mathcal{F}) -system. Then we solved the coupled (Σ, \mathcal{G}) -system for $\mathcal{F} \equiv 1$ and finally we computed the solution to the full $(\Sigma, \mathcal{F}, \mathcal{G})$ -system. Where the calculations had been performed previously we found very good agreement with these results, supporting our claim to have implemented a highly accurate method of solution. Furthermore, it is the first time that values for the critical coupling are produced in a system where the self-energy corrections to the wavefunction renormalization \mathcal{F} are taken into account in a consistent way.

Since the previous calculations have all been performed in the bare vertex approximation, we decided it was important to explore the influence of improved vertices on the dynamical generation of fermion mass in unquenched QED. A first, simple extension to the bare vertex consisted to include a $1/\mathcal{F}$ -fermion wavefunction dependence in the vertex. We observed chiral symmetry breaking and computed the critical coupling for one and two flavours. Then the Ball-Chiu vertex was implemented as this is the correct, non-perturbative, longitudinal part of the QED vertex, uniquely determined by requiring the satisfaction of the Ward-Takahashi identity. Although formally this vertex ensures that the quadratic divergences in the vacuum polarization integral vanish, the precise form of the Ball-Chiu vertex is a source for many numerical accuracy problems affecting the correct numerical cancellation of the quadratic divergence. In a detailed numerical investigation of the kernels of the angular integrals we were able to locate the various sources of inaccuracies in successive steps and to recover the accuracy necessary to cancel the quadratic divergence correctly. Then fermion mass generation was found and the critical coupling was determined. For the Curtis-Pennington vertex we could not find solutions to the integral equations because the transverse part of the vertex intrinsically leads to a quadratic

divergence in the vacuum polarization. Therefore we considered a hybrid method where the Curtis-Pennington vertex is used in the fermion equations and the Ball-Chiu vertex is used on the photon equation to avoid unphysical quadratic divergences. We found dynamical fermion mass generation and determined the value of the critical coupling.

We now give some considerations about future studies. An extension to our investigation would be to implement more sophisticated vertices, which not only satisfy the Ward-Takahashi identities but, also ensure the multiplicative renormalizability of the fermion and photon propagators. This could be done by merging the work performed by A. Kızılersü [26] on the QED-vertex with the numerical program developed here. This is especially wanted if we are to study the fermion mass generation with the renormalized Schwinger-Dyson equations, as these are derived by making explicit use of the multiplicative renormalizability of the fermion and photon propagators.

An important improvement to the numerical program would be to implement Newton's iteration method to solve the complete system of non-linear equations for Σ , \mathcal{F} and \mathcal{G} . As we explained before, limitations on memory and computing time forced us to implement a hybrid method, using Newton's iteration method on the coupled (Σ, \mathcal{F}) -system, while the much slower, natural iterative procedure is used to couple this system to the \mathcal{G} -equation. The use of a single Newton's method on the whole system would surely improve the convergence rate and the accuracy of the solutions, especially if we use more complicated vertices.

All the present results tend to show that the generation of fermion mass sets in, if the QED coupling is sufficiently strong. Although QED with a strong coupling seems fictitious, the experimental situation in heavy ion collisions, where the normal weak coupling QED is submerged in a very strong, rapidly varying background field, could approximate it quite well. An extensive numerical investigation of this situation could teach us more about the possibility of a new phase transition which might already have been discovered experimentally [6, 7]. For this purpose we could start with the same computer program developed here. The major task would be to reformulate the Schwinger-Dyson formalism in the presence of realistic background fields. Interestingly, Gusynin et al. have recently shown in an analytic study [61] that chiral symmetry is spontaneously broken by a constant magnetic field in QED.

Furthermore, there is no reason to restrict the use of the numerical method to the study of QED. For instance, we could add a four-fermion interaction in the original QED Lagrangian.

This is motivated by quenched QED, where the four-fermion operator becomes renormalizable because of its large anomalous dimension and should therefore be included in the theory [29]. It could also be used to study the propagators in non-Abelian theories as QCD. There we could, for instance, study the interplay between the infrared behaviour of the QCD-coupling and the dynamical generated fermion mass to enhance our understanding of confinement.

Finally, we conclude from our study of the coupled Schwinger-Dyson equations for the fermion and photon propagator that fermion mass is generated dynamically in quenched QED and in unquenched QED with one or two flavours, provided the coupling is larger than a critical value which depends on the approximations introduced. We developed a powerful, very accurate numerical method which avoids the many pitfalls encountered in solving the complicated system of non-linear coupled integral equations describing the mass generation. We are convinced that our numerical method will be very valuable for future investigations.

Appendix A

Angular integrals

In this Appendix we derive the following angular integrals:

$$\int_0^\pi d\theta \frac{\sin^2 \theta}{z} = \frac{\pi}{2} \left[\frac{\theta(x-y)}{x} + \frac{\theta(y-x)}{y} \right] \quad (\text{A.1})$$

$$\int_0^\pi d\theta \frac{\sin^2 \theta}{z^2} = \frac{\pi}{2} \left[\frac{\theta(x-y)}{x(x-y)} + \frac{\theta(y-x)}{y(y-x)} \right] \quad (\text{A.2})$$

$$\int_0^\pi d\theta \frac{\sin^4 \theta}{z^2} = \frac{3\pi}{8} \left[\frac{\theta(x-y)}{x^2} + \frac{\theta(y-x)}{y^2} \right] \quad (\text{A.3})$$

$$\int_0^\pi d\theta \frac{\sin^2 \theta \cos \theta}{z} = \frac{\pi}{4\sqrt{yx}} \left[\frac{y}{x} \theta(x-y) + \frac{x}{y} \theta(y-x) \right] \quad (\text{A.4})$$

$$\int_0^\pi d\theta \frac{\sin^2 \theta \cos \theta}{z^2} = \frac{\pi}{2\sqrt{xy}} \left[\frac{y}{x} \frac{\theta(x-y)}{x-y} + \frac{x}{y} \frac{\theta(y-x)}{y-x} \right]. \quad (\text{A.5})$$

To evaluate these angular integrals we will make use of the integral, Eq. (3.665.2) of Ref. [40]:

$$\int_0^\pi d\theta \frac{\sin^{2r} \theta}{(1 + 2a \cos \theta + a^2)^n} = B \left(r + \frac{1}{2}, \frac{1}{2} \right) F \left(n, n-r; r+1; a^2 \right), \quad (\text{A.6})$$

where $\text{Re}(r) > -1/2$, $|a| < 1$.

The beta function can be written as:

$$B(m, n) = \frac{\Gamma(m)\Gamma(n)}{\Gamma(m+n)}, \quad (\text{A.7})$$

while the hypergeometric function $F(\alpha, \beta; \gamma; z)$ is given by Eq. (9.100) of Ref. [40]:

$$\begin{aligned} F(\alpha, \beta; \gamma; z) &= 1 + \frac{\alpha\beta}{\gamma \cdot 1} z + \frac{\alpha(\alpha+1)\beta(\beta+1)}{\gamma(\gamma+1) \cdot 1 \cdot 2} z^2 + \frac{\alpha(\alpha+1)(\alpha+2)\beta(\beta+1)(\beta+2)}{\gamma(\gamma+1)(\gamma+2) \cdot 1 \cdot 2 \cdot 3} z^3 + \dots \\ &= \frac{\Gamma(\gamma)}{\Gamma(\alpha)\Gamma(\beta)} \sum_{n=0}^{\infty} \frac{\Gamma(\alpha+n)\Gamma(\beta+n)}{\Gamma(\gamma+n) n!} z^n. \end{aligned} \quad (\text{A.8})$$

If either α or β is negative the series terminates after a finite number of terms.

We compute the following integral:

$$\begin{aligned} \int_0^\pi d\theta \frac{\sin^2 \theta}{z} &= \int_0^\pi d\theta \frac{\sin^2 \theta}{x+y-2\sqrt{xy}\cos\theta} \\ &= \frac{\theta(x-y)}{x} \int_0^\pi d\theta \frac{\sin^2 \theta}{1-2\sqrt{y/x}\cos\theta+y/x} + (y \leftrightarrow x). \end{aligned} \quad (\text{A.9})$$

Applying Eq. (A.6) with $r = 1$ and $n = 1$ to Eq. (A.9) yields:

$$\int_0^\pi d\theta \frac{\sin^2 \theta}{z} = B\left(\frac{3}{2}, \frac{1}{2}\right) \left[\frac{\theta(x-y)}{x} F\left(1, 0; 2; \frac{y}{x}\right) + (y \leftrightarrow x) \right]. \quad (\text{A.10})$$

Note from Eq. (A.7):

$$B\left(\frac{3}{2}, \frac{1}{2}\right) = \frac{\Gamma\left(\frac{3}{2}\right)\Gamma\left(\frac{1}{2}\right)}{\Gamma(2)} = \frac{\pi}{2} \quad (\text{A.11})$$

because $\Gamma\left(\frac{1}{2}\right) = \sqrt{\pi}$. From Eq. (A.8) we find:

$$F(1, 0; 2; z) = 1. \quad (\text{A.12})$$

Substituting Eqs. (A.11, A.12) in Eq. (A.10) finally yields Eq. (A.1):

$$\int_0^\pi d\theta \frac{\sin^2 \theta}{z} = \frac{\pi}{2} \left[\frac{\theta(x-y)}{x} + \frac{\theta(y-x)}{y} \right].$$

Next we compute:

$$\begin{aligned} \int_0^\pi d\theta \frac{\sin^2 \theta}{z^2} &= \int_0^\pi d\theta \frac{\sin^2 \theta}{(x+y-2\sqrt{xy}\cos\theta)^2} \\ &= \frac{\theta(x-y)}{x^2} \int_0^\pi d\theta \frac{\sin^2 \theta}{(1-2\sqrt{y/x}\cos\theta+y/x)^2} + (y \leftrightarrow x). \end{aligned} \quad (\text{A.13})$$

We now apply Eq. (A.6) with $r = 1$ and $n = 2$ to Eq. (A.13). This gives:

$$\int_0^\pi d\theta \frac{\sin^2 \theta}{z^2} = B\left(\frac{3}{2}, \frac{1}{2}\right) \left[\frac{\theta(x-y)}{x^2} F\left(2, 1; 2; \frac{y}{x}\right) + (y \leftrightarrow x) \right]. \quad (\text{A.14})$$

From Eq. (A.8) we compute:

$$F(2, 1; 2; z) = 1 + z + z^2 + z^3 + \dots = \frac{1}{1-z}. \quad (\text{A.15})$$

Substituting Eqs. (A.11, A.15) in Eq. (A.14) yields Eq. (A.2):

$$\int_0^\pi d\theta \frac{\sin^2 \theta}{z^2} = \frac{\pi}{2} \left[\frac{\theta(x-y)}{x(x-y)} + \frac{\theta(y-x)}{y(y-x)} \right].$$

Next we compute:

$$\begin{aligned} \int_0^\pi d\theta \frac{\sin^4 \theta}{z^2} &= \int_0^\pi d\theta \frac{\sin^4 \theta}{(x+y-2\sqrt{xy}\cos\theta)^2} \\ &= \frac{\theta(x-y)}{x^2} \int_0^\pi d\theta \frac{\sin^4 \theta}{(1-2\sqrt{y/x}\cos\theta+y/x)^2} + (y \leftrightarrow x). \end{aligned} \quad (\text{A.16})$$

Applying Eq. (A.6) with $r=2$ and $n=2$ yields:

$$\int_0^\pi d\theta \frac{\sin^4 \theta}{z^2} = B\left(\frac{5}{2}, \frac{1}{2}\right) \left[F\left(2, 0; 3; \frac{y}{x}\right) \frac{\theta(x-y)}{x^2} + (y \leftrightarrow x) \right]. \quad (\text{A.17})$$

We know that:

$$B\left(\frac{5}{2}, \frac{1}{2}\right) = \frac{\Gamma(\frac{5}{2})\Gamma(\frac{1}{2})}{\Gamma(3)} = \frac{3\pi}{8} \quad (\text{A.18})$$

and

$$F(2, 0; 3; z) = 1, \quad (\text{A.19})$$

such that Eq. (A.17) becomes Eq. (A.3):

$$\int_0^\pi d\theta \frac{\sin^4 \theta}{z^2} = \frac{3\pi}{8} \left[\frac{\theta(x-y)}{x^2} + \frac{\theta(y-x)}{y^2} \right].$$

We now compute:

$$\begin{aligned} \int_0^\pi d\theta \frac{\sin^2 \theta \cos \theta}{z} &= \frac{1}{2\sqrt{xy}} \int_0^\pi d\theta \frac{\sin^2 \theta (x+y-z)}{z} \\ &= \frac{1}{2\sqrt{xy}} \left[(x+y) \int_0^\pi d\theta \frac{\sin^2 \theta}{z} - \int_0^\pi d\theta \sin^2 \theta \right] \end{aligned} \quad (\text{A.20})$$

where we used $z = x + y - 2\sqrt{xy}\cos\theta$.

From Eq. (14.347) of Ref. [59] we know that:

$$\int_0^\pi d\theta \sin^2 \theta = \frac{\pi}{2}. \quad (\text{A.21})$$

Substituting Eqs. (A.1, A.21) in Eq. (A.20) yields:

$$\int_0^\pi d\theta \frac{\sin^2 \theta \cos \theta}{z} = \frac{\pi}{4\sqrt{xy}} \left\{ (x+y) \left[\frac{\theta(x-y)}{x} + \frac{\theta(y-x)}{y} \right] - 1 \right\}, \quad (\text{A.22})$$

which proves Eq. (A.4):

$$\int_0^\pi d\theta \frac{\sin^2 \theta \cos \theta}{z} = \frac{\pi}{4\sqrt{yx}} \left[\frac{y}{x} \theta(x-y) + \frac{x}{y} \theta(y-x) \right].$$

In an analogous way we compute:

$$\begin{aligned} \int_0^\pi d\theta \frac{\sin^2 \theta \cos \theta}{z^2} &= \frac{1}{2\sqrt{xy}} \int_0^\pi d\theta \frac{\sin^2 \theta (x+y-z)}{z^2} \\ &= \frac{1}{2\sqrt{xy}} \left[(x+y) \int_0^\pi d\theta \frac{\sin^2 \theta}{z^2} - \int_0^\pi d\theta \frac{\sin^2 \theta}{z} \right]. \end{aligned} \quad (\text{A.23})$$

We substitute Eqs. (A.2, A.1) in Eq. (A.23), proving Eq. (A.5):

$$\int_0^\pi d\theta \frac{\sin^2 \theta \cos \theta}{z^2} = \frac{\pi}{2\sqrt{xy}} \left[\frac{y}{x} \frac{\theta(x-y)}{x-y} + \frac{x}{y} \frac{\theta(y-x)}{y-x} \right].$$

Bibliography

- [1] Y. Nambu and G. Jona-Lasinio, Phys. Rev. **122** (1961) 345.
- [2] S. Weinberg, Phys. Rev. **D19** (1979) 1277; L. Susskind, Phys. Rev. **D20** (1979) 2619.
- [3] S. Dimopoulos and L. Susskind, Nucl. Phys. **B155** (1979) 237; E. Eichten and K. Lane, Phys. Lett. **90B** (1980) 125.
- [4] B. Holdom, Phys. Lett. **150B** (1985) 301.
- [5] L.D. Landau, *On the quantum theory of fields*. In *Niels Bohr and the development of physics*, ed. W. Pauli, pp.52-69, Pergammon Press Ltd., London, 1955.
- [6] A. Schäfer, J. Phys. G: Nucl. Part. Phys. **15** (1989) 373.
- [7] D.G. Caldi, Comments Nucl. Part. Phys. **19** (1989) 137.
- [8] R. Fukuda and T. Kugo, Nucl. Phys. **B117** (1976) 250.
- [9] P.I. Fomin, V.P. Gusynin, V.A. Miransky, Yu.A. Sitenko, Riv. Nuovo Cimento **5** (1983) 1.
- [10] V.A. Miransky, Sov. Phys. JETP **61** (1985) 905.
- [11] V.A. Miransky, Il Nuovo Cimento **90A** (1985) 149.
- [12] D.C. Curtis and M.R. Pennington, Phys. Rev. **D42** (1990) 4165.
- [13] K-I. Kondo and H. Nakatani, Nucl. Phys. **B351** (1991) 236.
- [14] V.P. Gusynin, Mod. Phys. Lett. **5** (1990) 133.
- [15] K-I. Kondo, Y. Kikukawa and H. Mino, Phys. Lett. **B220** (1989) 270.
- [16] K-I. Kondo and H. Nakatani, Prog. Theor. Phys. **88** (1992) 737.

- [17] J. Oliensis and P.W. Johnson, Phys. Rev. **D42** (1990) 656.
- [18] P.E.L. Rakow, Nucl. Phys. **B356** (1991) 27.
- [19] D. Atkinson, H.J. De Groot and P.W. Johnson, Int. J. Mod. Phys. **A7** (1992) 7629.
- [20] K-I. Kondo, H. Mino and H. Nakatani, Mod. Phys. Lett. **A7** (1992) 1509.
- [21] C. Itzykson and J.-B. Zuber, *Quantum Field Theory*, McGraw-Hill, 1980.
- [22] C.D. Roberts and A.G. Williams, Prog. Part. Nucl. Phys. **33** (1994) 477.
- [23] L.H. Ryder, *Quantum Field Theory*, Cambridge University Press, 1985.
- [24] J.S. Ball, T-W. Chiu, Phys. Rev. **D22** (1980) 2542.
- [25] A. Bashir and M.R. Pennington, Phys.Rev. **D50** (1994) 7679; A. Bashir, *Constructing Vertices in QED*, Ph.D. Thesis, University of Durham, 1995.
- [26] A. Kızılersü, *Gauge Theory Constraints on the Fermion-Boson Vertex*, Ph.D. Thesis, University of Durham, November 1995.
- [27] A. Kızılersü, M. Reenders, M.R. Pennington, Phys. Rev. **D52** (1995) 1242.
- [28] D.C. Curtis and M.R. Pennington, Phys. Rev. **D48** (1993) 4933.
- [29] C.N. Leung, S.T. Love and W.A. Bardeen, Nucl. Phys. **B273** (1986) 649; W.A. Bardeen, C.N. Leung and S.T. Love, Nucl. Phys. **B323** (1989) 493.
- [30] K-I. Kondo, H. Mino and K. Yamawaki, Phys. Rev. **D39** (1989) 2430.
- [31] W.A. Bardeen, S. Love and V.A. Miransky, Phys. Rev. **D42** (1990) 3514.
- [32] A. Kocić, S. Hands, J.B. Kogut and E. Dagotto, Nucl. Phys. **B347** (1990) 217; A. Kocić, J.B. Kogut, M.-P. Lombardo and K.-C. Wang, Nucl. Phys. **397** (1993) 451; M.-P. Lombardo, A. Kocić and J.B. Kogut, hep-lat/9411051.
- [33] J.B. Kogut and J.-F. Lagaë, Nucl. Phys. **B34** (Proc. Suppl.) (1994) 552; hep-lat/9412024.
- [34] D. Atkinson, J.C.R. Bloch, V.P. Gusynin, M.R. Pennington and M. Reenders, Phys.Lett. **B329** (1994) 117.
- [35] Z. Dong, H.J. Munczek and C.D. Roberts, Phys. Lett. **B333** (1994) 536.

- [36] D. Atkinson, V.P. Gusynin and P. Maris, Phys. Lett. **B303** (1993) 157.
- [37] D. Atkinson and M.P. Fry, Nucl. Phys. **B156** (1979) 301.
- [38] D. Atkinson and P.W. Johnson, Phys. Rev. **D35** (1987) 1943.
- [39] D.C. Curtis and M.R. Pennington, Phys. Rev. **D46** (1992) 2663; erratum, Phys. Rev. **D47** (1993) 1729.
- [40] I.S. Gradshteyn and I.M. Ryzhik, *Table of Integrals, Series, and Products*, Academic Press, 1994, 5th ed.
- [41] W.H. Press, B.P. Flannery, S.A. Teukolsky, W.T. Vetterling, *Numerical Recipes in C*, Cambridge University Press, 1988.
- [42] B. Holdom, Phys. Lett. **B213** (1988) 365; Phys. Rev. Lett. **62** (1989) 997.
- [43] P. Rembiesa, Phys. Rev. **D41** (1990) 2009.
- [44] K-I. Kondo, Int. J. Mod. Phys. **A7** (1992) 7239.
- [45] B. Haeri, Jr., Phys. Rev. **D43** (1991) 2701.
- [46] D. Atkinson, P.W. Johnson and K. Stam, Phys. Lett. **B201** (1988) 105.
- [47] M. Abramowitz and I.A. Stegun, *Handbook of Mathematical Functions*, Dover Publications, Inc., New York, 1972.
- [48] L.D. Landau, A. Abrikosov, I. Khalatnikov, Nuovo Cimento Supplement **3** (1956) 80.
- [49] M. Ukita, M. Komachiya and R. Fukuda, Int. J. Mod. Phys. **A5** (1990) 1789.
- [50] K-I. Kondo, T. Iizuka, E. Tanaka and T. Ebihara, Phys. Lett. **B325** (1994) 423.
- [51] K-I. Kondo, Nucl. Phys. **B351** (1991) 259.
- [52] E. Dagotto, A. Kocić and J.B. Kogut, Phys. Rev. Lett. **60** (1988) 772; Phys. Rev. Lett. **61** (1988) 2416.
- [53] A. Kocić, Nucl. Phys. **B34** (Proc. Suppl.) (1994) 123; A. Kocić and J.B. Kogut, Nucl. Phys. **B422** (1994) 593.

- [54] M. Göckeler, R. Horsley, P.E.L. Rakow, G. Schierholz and R. Sommer, Nucl. Phys. **B371** (1992) 713; M. Göckeler, R. Horsley, P.E.L. Rakow, G. Schierholz and H. Stüben, Nucl. Phys. **B34** (Proc. Suppl.) (1994) 527; A.M. Horowitz, Phys. Lett. **B244** (1990) 306; Phys. Rev. **D43** (1991) R2461.
- [55] L.M. Delves and J.L. Mohamed, *Computational methods for integral equations*, Cambridge University Press, 1985.
- [56] E. Isaacson and H.B. Keller, *Analysis of Numerical Methods*, John Wiley & Sons, 1966.
- [57] J.C.R. Bloch and M.R. Pennington, Mod. Phys. Lett. **A10** (1995) 1225.
- [58] C.T.H. Baker, *Expansion Methods*. In *Numerical Solution of Integral Equations*, eds. L.M. Delves and J. Walsh, pp. 80-96, Oxford University Press, 1974.
- [59] M.R. Spiegel, *Mathematical Handbook of Formulas and Tables*, Schaum's Outline Series, McGraw-Hill, 1968.
- [60] D.C. Curtis and M.R. Pennington, Phys. Rev. **D44** (1991) 536.
- [61] V.P. Gusynin, V.A. Miransky and I.A. Shovkovy, UCLA-95-TEP-26, hep-ph/9509320.